Master's thesis

NTNU
Norwegian University of Science and Technology
Faculty of Engineering
Department of Geoscience and Petroleum

Bertil Carlsen

Prospecting a Structurally Complex Marble Occurrence in Vassbygda, Helgeland Nappe Complex, Nordland

Master's thesis in Geology

Supervisor: Espen Torgersen & Bergliot Kulsrud Storruste

January 2021

NTNU
Norwegian University of Science and Technology

BRØNNØY KALK

Bertil Carlsen

Prospecting a Structurally Complex Marble Occurrence in Vassbygda, Helgeland Nappe Complex, Nordland

Master's thesis in Geology
Supervisor: Espen Torgersen & Bergliot Kulsrud Storruste
January 2021

Norwegian University of Science and Technology
Faculty of Engineering
Department of Geoscience and Petroleum

NTNU
Norwegian University of
Science and Technology

Abstract

This thesis provides a detailed multi-disciplinary geological investigation of marble deposits in Vassbygda, Nordland. Along with descriptions of the marble deposits, the thesis also contributes to unravelling the complex structural architecture of the area. Several methods have been used, including geological mapping, petrographical and microscopical analyses, and 3D-modelling using the software Move 3D. The thesis is written in collaboration with Brønnøy Kalk AS.

Vassbygda is located within the Lower nappe of the Helgeland Nappe Complex (HNC) and consists primarily of metasedimentary rocks and intrusions of variable composition. The marble deposits consist of two dominant marble types: a high-quality graphite-spotted marble with minor quartz, feldspar and pyrite impurities, and a silicate-banded marble of varying quality. Ridges of siliciclastic metasedimentary rocks enclose the deposits and define the large-scale structural framework. Sub-vertical quartz dioritic dykes occur throughout the study area, together with migmatization-related leucogranitic sills. Both might pose challenges for future mining operations. The most promising marble deposit is found within Stormarka and consists of excellent-quality marbles with few igneous intrusions.

The area has experienced extensive deformation during two main tectonic events. The first event is seen as isoclinal folding (F_1) of a transposed bedding (S_{0+1}) and the development of a weak axial plane cleavage (S_2) and mineral crenulation lineation (CL_1). F_1 folds are recumbent, with north-west-southeast-trending axes and coincides with the migmatization of the siliciclastic rocks. Garnet geothermobarometry indicates that the migmatization occurred at c. 630-650°C and 4.5-5.0kbar, likely due to dehydration melting of muscovite.

The second event is the over-trusting of the Middle nappe along the Heggfjord-Tosen shear zone. The 1.2km wide shear zone developed a strong mylonitic foliation (S_3) that overprinted S_{0+1} and strongly altered the large-scale geometries of northeastern Vassbygda. The compression also led to refolding of the Vassbygda units about an open F_2 northwest–southeast-trending fold axis. The intricate fold interference pattern and large-scale shear deformation resulted in the complicated present-day geometry.

A region-wide geological 3D model is created based on the structural framework and indicates that the Stormarka marble deposit is confined in a cradle-like structure surrounded by siliciclastic metasedimentary ridges. Drillcore logs suggest that the central Stormarka deposit is at least 265m deep. Volume estimates of the Stormarka deposits with a modelled depth of 200m indicate that the area consists of c. 1.8 billion tonnes of high-grade graphite-spotted marble and c. 305 million tonnes of medium quality banded marble. The northeastern section of the Stormarka deposit contains excellent-quality graphite-spotted marble, estimated at c. 268 million tonnes.

Sammendrag

Denne avhandlingen presenterer en detaljert beskrivelse og forståelse av marmorforekomstene i Vassbygda, Nordland. I tillegg vil denne oppgaven bidra til større forståelse av den strukturelt kompliserte geologien i området. Flere metoder har blitt brukt, inkludert geologisk kartlegging, petrografiske analyser og bergartenes mikroskopiske egenskaper. En 3D-modell har også blitt konstruert med hjelp av programvaren Move 3D. Avhandlingen er skrevet i samarbeid med Brønnøy Kalk AS.

Området befinner seg i Nedre dekke av Helgelandsdekkekomplekset og består hovedsakelig av metasedimentære bergarter og magmatiske intrusjoner. Marmorforekomstene består av to dominerende typer: En høykvalitets grafittspettet marmor med noen få urenheter av kvarts, feltspat og svovelkis, og en silikatbåndet marmor av varierende kvalitet. Marmorforekomstene er omkranset av rygger med silisiklastiske metasedimentære bergarter og er ofte intrudert av subhorisontale kvartsdiorittganger eller migmatisasjonsrelaterte leukogranittiske lagganger, noe som kan bli en utfordring for framtidig gruvedrift i området. Den mest lovende forekomsten ligger i Stormarka og består av en høykvalitets grafittspettet marmor og få magmatiske ganger.

Bergartene har gjennomgått to deformajonsepisoder som har endret områdets geometri betraktelig. Den første episoden er definert av isoklinal folding (F_1) av en transponert sedimentær lagdeling (S_{0+1}), i tillegg til utviklingen av et svakt akseplankløv (S_2) og mineralkrenulasjonslineasjon (CL_1). F_1 er definert av et liggende akseplan med et nordøst-sørvest strøk, og samsvarer i tid med migmatiseringen av de metasedimentære bergartene siden både foliasjons-parallelle og -kuttende leukosomer er observert. Resultater fra granat-geotermobarometri indikerer at migmatiseringen skjedde ved ca. 630-650°C og 4.5-5.0kbar, sannsynlig som et produkt av dehydreringssmelting av muskovitt.

Den andre episoden er introduksjonen av en stor skjærsone som oppsto under overskyvningen av Midtre dekke. Denne 1.2km brede sonen utviklet en sterk mylonittisk foliasjon (S_3) som overskrev S_{0+1} og markant deformerte den storskala geometrien i nordøstre del av Vassbygda. Skjærdeformasjonen foldet området på nytt, denne gangen med en åpen foldefase (F_2) med et nordvest-sørøst stående akseplan. Det intrikate foldeinterferensmønsteret og storskala skjærdeformasjon resulterte i dagens kompliserte geometri.

En regionsdekkende 3D-modell er lagd basert på det strukturelle rammeverket og indikerer at marmorforekomsten i Stormarka ligger i en trau-form omkranset av åsrygger bestående av silisiklastiske metasedimentære bergarter. Kjerneboringer fra området indikerer at forekomsten strekker seg mer enn 265m ned i dypet. Volumestimater av Stormarkaforekomsten med 200m modellert dybde indikerer ca. 1.8 milliarder tonn med høykvalitets grafittspettet marmor og ca. 305 millioner tonn med båndet marmor av medium kvalitet. Den nordøstlige delen av Stormarkaforekomsten består av svært god kvalitet spettet marmor, estimert til ca. 268 millioner tonn.

Acknowledgements

First of all, I would like to give a huge thanks to my primary supervisor, Espen Torgersen, who helped me through this thesis. Your passion and understanding of geology have been a massive inspiration for me, and our conversations have given me an increased interest in structural geology. I am also grateful for the feedback you give me, both during fieldwork and writing, which has helped me improve my work and learn from my mistakes. Apart from geology, you have also been a great mentor who has always believed in me and guided me closely throughout this last year. It was a pleasure to work with you.

Further, I would also like to thank Brønnøy Kalk AS for the opportunity and financial support. It has been very motivating and rewarding to write a thesis that will hopefully help for future explorations. A huge thanks also go out to Bergliot Kulsrud Storruste, Raymond Langfjord and others at Brønnøy Kalk and Norsk Mineral who made this thesis possible. Thank you for the hospitality and support during the summer internship and fieldwork, and thank you for sharing your already obtained data. I hope this thesis will help you unravel some of the challenges of Vassbygda, although I might just have added more pieces to the puzzle.

Several other people also deserve attention for the help they have provided me through this master thesis. First, I would like to thank Øysten Nordgulen, who accompanied Espen and me for three days during the second field season. It was incredibly helpful to have such an expert on the area with me to discuss some of the more thought-provoking observations. Secondly, both the laboratories and personnel at NGU and NTNU deserves a huge thanks for helping me with rock analyses and SEM. Thank you for making sure I still got my results during COVID-19 lockdown, and thanks for being flexible. I would also like to thank the experienced geologists who participated in Høstmøtet 2019. Thanks for giving me positive feedback on my master presentation, and thanks for the conversations and updates from the industry. It was very motivating to continue with my master thesis when I experienced acceptance and interest in my work.

A special thanks to my dearest Siren, who had to deal with my frustrations during the whole process. I appreciate you for being with me, even when I wake you up to nightmares of stereonets and fold analyses. Thank you for your field assistance and for helping me with discussions and proofreading.

Lastly, I want to give a huge thanks to all the clegg (horsefly), deer flies, and stable flies that so kindly kept me company on the hot summer days during my fieldwork. I am forever grateful for your immense hospitality and persistence to show me your favourite areas of the marches of Vassbygda. Your level of friendliness can only be compared to the sheer amount of specimens in your heart-warming community. I hope my blood may serve you well in the future!

Table of Content

List of Figures

List of Tables

List of Abbreviations

AMS	Automatic Mineralogic Systems
APFU	Atoms per formula unit
DEM	Digital Elevation Model
EPMA	Electron Probe Micro-Analyzer
HNC	Helgeland Nappe Complex
HTSZ	Heggfjord–Tosen Shear Zone
NGU	Geological Survey of Norway (Norges Geologiske Undersøkelse)
P.D.G.	Present-day geography
P-T	Pressure- Temperature
REE	Rare-Earth Element
SEM	Scanning Electron Microscope
S–T	Sauren–Torghatten

Mineral Abbreviation

The mineral abbreviations used for this thesis are based on the recommended abbreviation for rock-forming minerals by Whitney and Evans (2010).

Act	Actinolite
Aln	Allanite
Amp	Amphibole (group)
Bt	Biotite
Cal	Calcite
Chl	Chlorite (group)
Di	Diopside
Fsp	Feldspar (group)
Grt	Garnet (group)
Hbl	Hornblende (group)
Pl	Plagioclase
Qz	Quartz
St	Staurolite
Ttn	Titanite
Zo	Zoisite

1 Introduction

Experiences from exploration and modelling of carbonate deposits (Henderson *et al.*, 2019) show that marbles are challenging to prospect due to the often complex fold- and deformational geometry. A 3D model, based on observations such as structural measurements, petrographical descriptions, and drill cores, can be paramount for the visualization and description of a structurally complex marble deposit (Baudino *et al.*, 2010). Advanced software, such as Move 3D, can further apprehend the complex geometry and be used to estimate volumetric properties of a marble deposit (Henderson *et al.*, 2019).

Brønnøy Kalk AS currently runs an open-pit marble quarry at Akselberg, close to Hommelstø in Nordland county (fig. 1.1). Brønnøy Kalk is a subsidiary of Norsk Mineral group and the primary provider of calcite marble to the processing plants run by Hustadmarmor AS. In later years, the question about long term planning for the continuation of marble mining has produced two options: Continue with underground mining at Akselberg when the current open-pit becomes too deep, or opening a new quarry at the marble occurrence in Vassbygda, about 15km southeast of the present quarry (fig. 1.1).

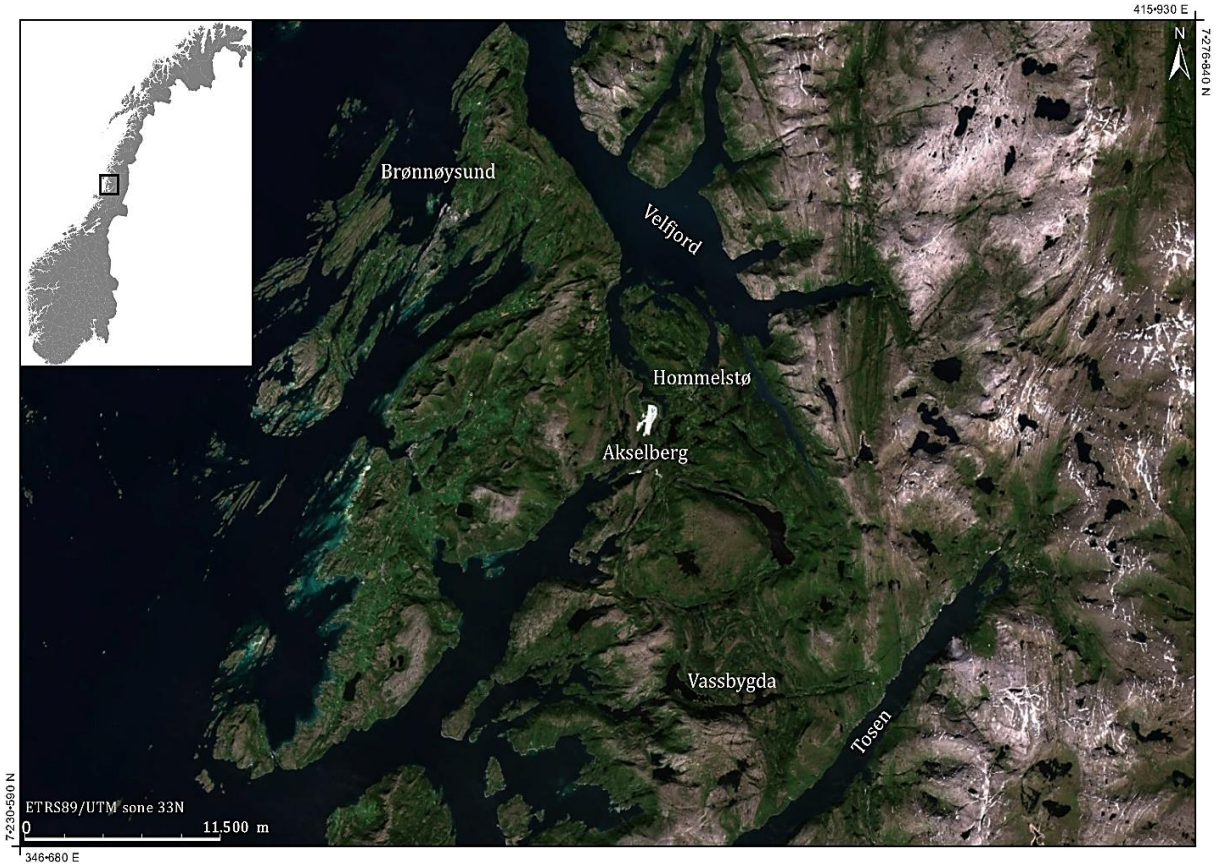

Figure 1.1: Map of the field area and the surrounding areas. Orthophoto from norgeibilder.no

This thesis aims to explore the latter scenario and describe and interpret the structurally complex calcite marble occurrence in Vassbygda. The thesis should provide a better understanding of the geological variations, marble quality, and geometry of the resource, resulting in a 3D model to help establish the complex structural framework of the Vassbygda marble and indicate what may be a good strategy for further exploration. Nevertheless, to fully understand the geometry, the geological evolution of the area is also needed.

The marbles of the Velfjord regions are confined within the Helgeland Nappe Complex (HNC), a stack of pre-Scandian trusted sheets of marine and crustal sediments, penetrated by later volcanic activity, and tectonically deformed by the Scandian Orogeny (Barnes *et al.*, 2007; Thorsnes & Løseth, 1991). The HNC has been extensively studied throughout the last 40 years (Barnes *et al.*, 2007; Gustavson, 1975; Kollung, 1967; McArthur *et al.*, 2014; Nordgulen *et al.*, 1993; Thorsnes & Løseth, 1991; Yoshinobu *et al.*, 2002). However, little research has been conducted on the calcite marbles of the Vassbygda region. Brønnøy Kalk have previously carried out field mapping and coredriling to establish the marble quality and depth extent of the most promising deposits of the region.

Nearby studies of the Sausfjellet pluton (Dumond, 2002; Dumond *et al.*, 2005), the Nordfjellmark area (Thorsnes & Løseth, 1991), and the geological variations of the marbles of the Akselberg – Forbergskog area (Sandøy, 2003) are the only previous works discussing observations relevant to Vassbygda and the marble occurrence. No direct geological exploration of the Vassbygda area, especially the marbles, has been previously undertaken - including detailed geological mapping. However, Dumond (2002) mapped the northern gneisses of Vassbygda and proposed that the rocks were subject to three fold phases with an intricate fold interference pattern.

Several methods were used to map and interpret the geology and geometry of the Vassbygda marbles and surrounding rocks. Two seasons of fieldwork yielded structural observations, petrographical descriptions, and rock samples. Remote sensing techniques using satellite images, forest types, and elevation models were also included in order to determine rock boundaries in densely vegetated areas. A geological map was created together with a 3D-model of the marble occurrence by combining the observations and measurements from the field seasons. In order to understand the geometry of the marble occurrence, a geological and structural evolution was proposed based on observations and calculations of folds, lineations, and kinematic indicators. Chemical and petrographical analysis gave insight into the geological variation of the rocks in the area and evaluated the marble quality. Pressure-temperature estimates using empirical garnet geothermobarometers were also applied to help clarify the metamorphic evolution.

1.1 Geological Background

Before going into detail on the Helgeland Nappe Complex (HNC), it is essential to understand the regional geological setting that led to the formation of the HNC, as well as the basement lithologies and sedimentary sources that resulted in the rocks observed today. This chapter describes the regional geological setting, an introduction to, and the evolution of, the Helgeland nappe stack. This chapter will also present the field area and the previous works done in the Vassbygda area.

1.1.1 Regional Setting

The Caledonian orogeny (the subduction of Baltica beneath Laurentia in Late-Silurian to Early-Devonian times) is the last mountain-forming event in Norway and stretches close to the entire length of the country (fig. 1.2). It forms most of the visible bedrocks that can be observed today. The Caledonian orogeny has been studied in great detail since its conception in the 80s (Gee & Sturt, 1985).

In Late-Cambrian to Ordovician, Laurentia, Baltica, and the minor plate, Avalonia, experienced the first signs of contraction (fig. 1.2) (Cocks & Torsvik, 2002; Gee & Sturt, 1985). This contraction initiated the first increments of the closure of the Iapetus ocean with the appearance of the disputed (Krill & Zwaan, 1987) Finnmarkian continent-cryptic arc – An accretionary event in the Late-Cambrian involving oceanward subduction and local eclogite facies metamorphism (Andréasson, 1994; Essex *et al.*, 1997; Mørk *et al.*, 1988; Roberts, 2003).

Following the Finnmarkian event was the Trondheim event of central Norway (~493–482 Ma): A principal phase of subduction, deformation, and quick ophiolite obduction with related blueschist metamorphism (Eide & Lardeaux, 2002) and plagiogranitic dyke sheets (Roberts, 2003).

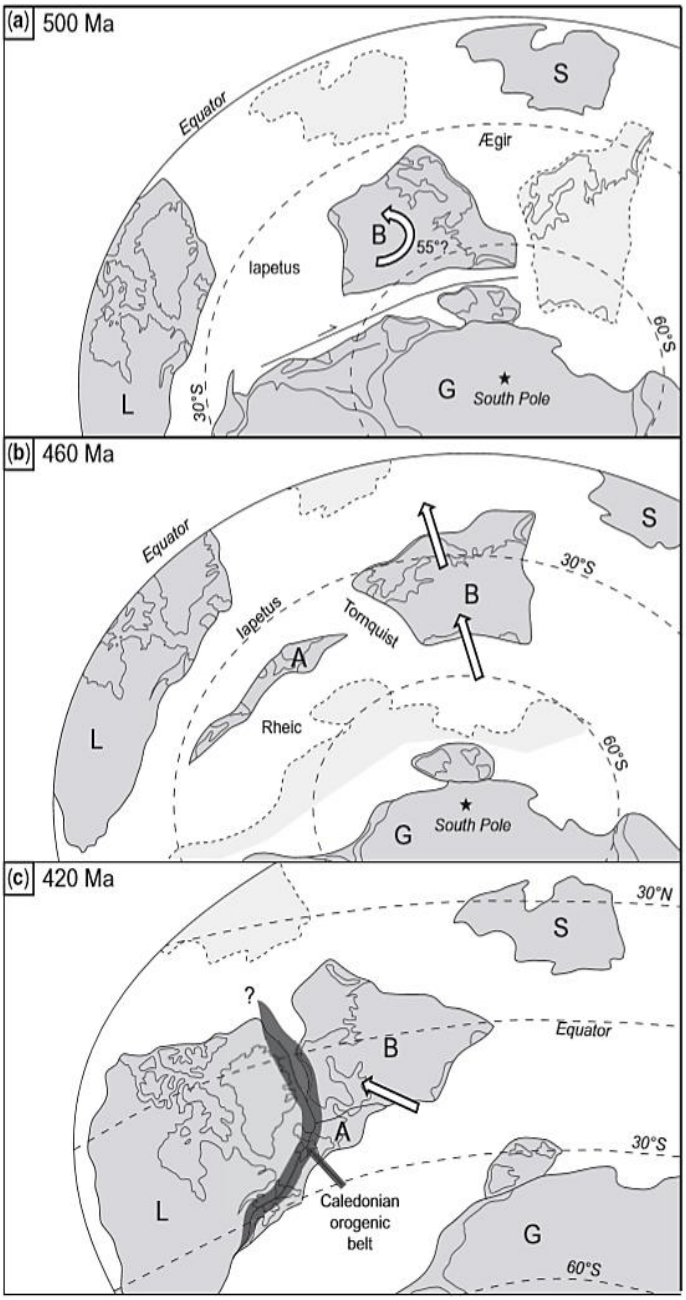

Figure 1.2: The proposed continental drift of Baltica (B), Laurentia (L), Siberia (S), Gondwana (G) and Avalonia (A) during the Late Cambrian to Silurian period by Corfu et al. (2014).

The Taconian event followed thereafter and is observed as Late-Ordovician to Early-Silurian plutons cutting earlier mylonitic foliations (Nordgulen *et al.*, 1993; Sturt & Ramsay, 1994; Yoshinobu *et al.*, 2002). This event is interpreted as arc accretion and involves amphibolite to eclogite metamorphic facies in the Laurentian terranes of Middle- to Late-Ordovician time (as cited in Roberts (2003)).

The final part of the orogeny, and the most prominent in forming the characteristic Caledonian allochtons in Norway and Sweden, is named the Scandian phase (Gee, 1975). This phase was a product of oblique convergence, subduction of the Baltican margin, continent-continent collision, and UHP metamorphism of the Baltican subducting slab (Fossen *et al.*, 2008; Roberts, 2003; Terry *et al.*, 2000).

From the Late Proterozoic through Cambrian, the Baltican margin was dominated by siliciclastic sediments (especially black shales), whereas the Laurentian margin consisted of thick Cambrian to Ordovician carbonate banks (Gee *et al.*, 2008). Carbonates dominated both margins throughout Ordovician, with Baltica showing a transition towards the west into turbidites, indicating early orogenic activity (Gee *et al.*, 2008). Emplaced ophiolites, notably in the Trondheim area, Lyngen and Leka mark this phase with zircon U-Pb isotopes ages of ~500 Ma (Fossen *et al.*, 2008; Pedersen & Furnes, 1991). During the collision between the island arcs and the continental Baltica, swarms of S–Type granites (Trondhjemites) formed from the melting of sedimentary rocks, believed to be of Laurentian origin based on zircon analyses (Fossen *et al.*, 2008). Related magmatism is seen throughout the HNC as large plutons and batholiths (Yoshinobu *et al.*, 2002). However, this magmatism predated the Caledonian orogeny. This is further elaborated in chapter 1.1.3.2.

Recent discussions and interpretations have led to redefinitions of older concepts concerning the formation of the Caledonian mountain range (Corfu *et al.*, 2014). In later years, the allochthon-classification has been proven too rigid for a satisfactory description of the Caledonian rock units. Corfu *et al.* (2014) summarize the current classification of the Caledonian rock units of Central Norway (fig. 1.3).

The central segment (fig. 1.3), in which the HNC lies, is summarized by Corfu *et al.* (2014) and described as consisting of a basal fold-and-thrust belt of Late Neoprotorezoic meta-sediments with mafic dyke swarms and crystalline slivers. Higher-grade meta-sedimentary rocks, amphibolites, and smaller granitic to ultramafic rocks overlay these metasediments (Corfu *et al.*, 2014). Above this are nappes of Palaeozoic oceanic rocks, which are in turn overlain by a nappe stack of Precambrian crust and younger magmatic complexes and turbidites deposits (Corfu *et al.*, 2014).

Following the Caledonian Orogeny, was an extensional period lasting throughout Devonian, where the over-thickened crust formed during the collision began to thin (Séguret *et al.*, 1989). Gravitational collapse of the crust led to the opening of basins along west-vergent detatchement zones and the subsequent unconform sedimentation on top of the exposed basin floor (Gee & Sturt, 1985; Séguret *et al.*, 1989). Devonian detachment zones and basins are characterized by several low angle faults that displaced the basins and basin sediments westward (somewhere close to 50 km) and overprinted many of the eastward shear indicators of the Caledonian Orogeny (Séguret *et al.*, 1989).

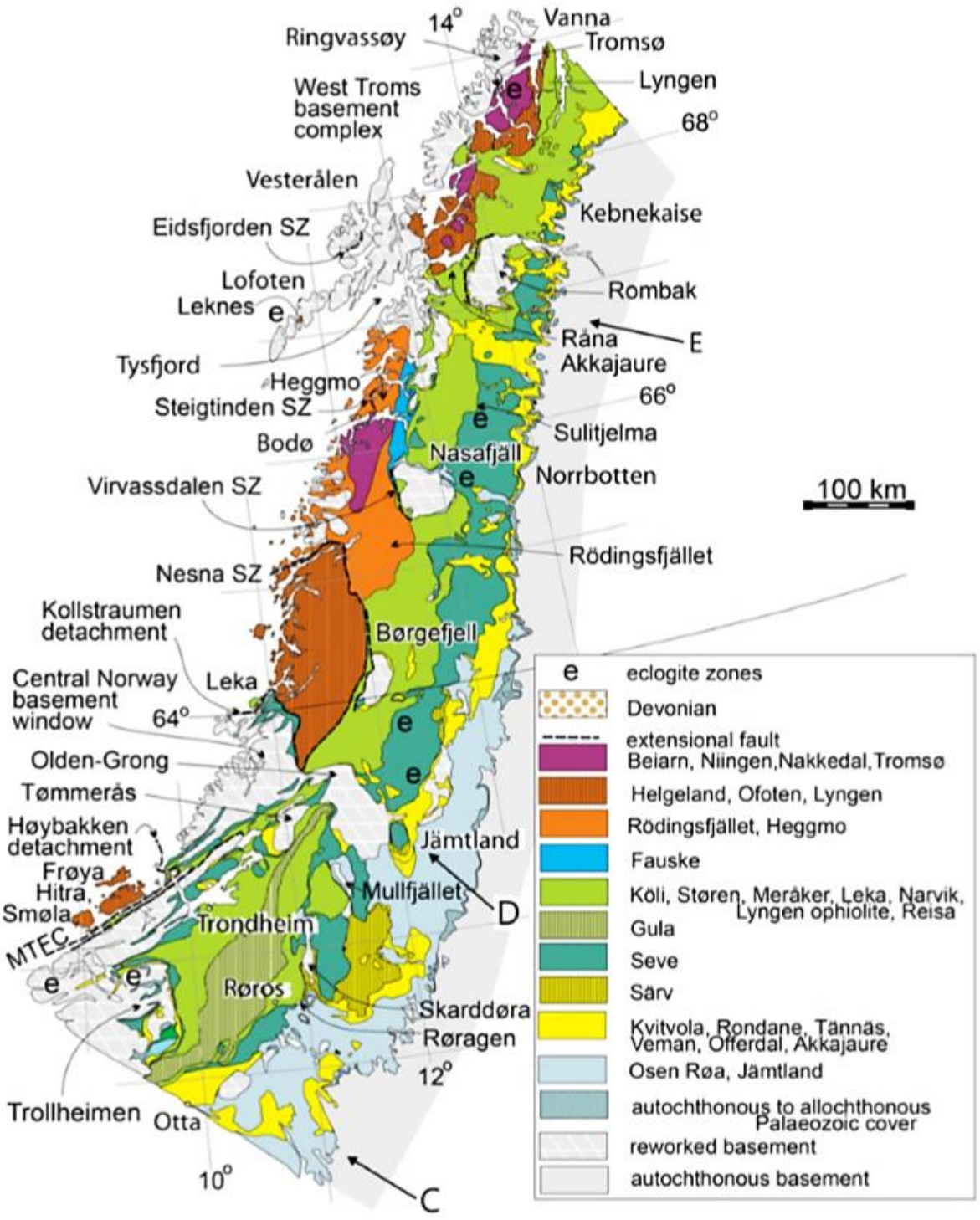

Figure 1.3: Tectonic map of the central segment showing the major lithological units of the Norwegian Caledonides. The HNC is shown in brown and is confined within the Nesna shear zone to the east and north and by the Kollstraumen detachment in the south. Figure from Corfu *et al.* (2014).

1.1.2 Introduction to the Helgeland Nappe Complex

The Helgeland Nappe Complex (HNC), home to the marbles mined by Brønnøy Kalk today, is located in central North Norway and has been studied in extensive detail for over 40 years (Barnes *et al.*, 2007; Barnes & Prestvik, 2000; Barnes *et al.*, 2011; Gustavson, 1975; Kruhl, 1984; McArthur *et al.*, 2014; Ramberg, 1967; Thorsnes & Løseth, 1991; Yoshinobu *et al.*, 2002). The Helgeland Nappe Complex was first described by Gustavson (1973). He used the descriptions of "Helgelandsdekket" (Helgeland Nappe) for the metamorphic rocks that structurally overlay the Rödningsfjellet nappe (a definition first used by I. Ramberg (as cited in Sandøy (2003)). The description was later expanded to include the rocks of the Skålvær region and was renamed to the Helgeland Nappe Complex (Gustavson, 1975).

The HNC is confined to the Uppermost Allochthon (as cited in Barnes *et al.* (2007)) of the Norwegian Caledonides. As mentioned (chapter 1.1.1), the classification of allochthones has, in later years, been proven too rigid for a satisfying description of the Caledonian rocks (Corfu *et al.*, 2014). The southwestern HNC consists of five established nappes in structural descending order: Upper-, Middle-, Lower-, Sauren–Torghatten (S–T)- and Horta nappe (fig. 1.4) (Barnes *et al.*, 2007). These are juxtaposed along east-dipping, west-vergent shear zones (Yoshinobu *et al.*, 2002).

The overall character of the sedimentary rocks of the HNC is metawackes, calc-silicates, interbedded conglomerates, and marble with typical amphibolite facies metamorphism (Barnes *et al.*, 2007). Extensive Migmatization and pluton emplacement is observed throughout the nappe stack, and a full ophiolite sequence is present at the island of Leka (fig. 1.4) (Barnes *et al.*, 2007; McArthur *et al.*, 2014). The HNC overlay highly deforms gneisses which can be seen further south in the Central Norwegian Basement Window (CNBW) (Braathen *et al.*, 2000).

The HNC is the host of the Bindal Batholith, the largest Caledonian batholith in Norway, consisting of more than 50 significant intrusions ranging in age from approximately 480 to 425 Ma (Anderson *et al.*, 2013; Barnes *et al.*, 2007). The batholith results from partial melting of crustal rocks, with an uncertain component of mantle-derived material, giving it a compositional range from granitic to gabbroic (Yoshinobu *et al.*, 2002). Fig. 1.5 correlates some of the plutons to the sedimentary, magmatic, and metamorphic evolution of the HNC.

1.1.2.1 Horta Nappa

Barnes *et al.* (2007) describe the Horta Nappe as the host of the Hortavær igneous complex, with two distinct lithological units. One part of the nappe consists of migmatic quartzofeldspathic gneisses and minor quartzite and marble, and the other part consists of predominantly marble, calc-silicate- gneisses, and -conglomerates (Nordgulen *et al.*, 2011). The western part of the nappe contains locally mingled leucosomes with pillowed quartz-dioritic dykes, dated to c. 480 Ma (Barnes *et al.*, 2007). S-type magmas from the Vega pluton intruded calc-silicate rocks, pelitic sediments, and quartzites, which are also assigned to the Horta Nappe (Barnes *et al.*, 2007). The intruding magmas created migmatites characterized by medium-grained, pale grey, siliceous gneiss, marble, quartzite, and calc-silicate rocks (Barnes *et al.*, 2007).

The nappe is systematically cut by mafic dykes related to the Vega pluton enclaves, which has led to the interpretation that the migmatization of the Horta Nappe co-occurred with the magmatic activity of the Vega pluton at 475 Ma (Barnes *et al.*, 2007). Radiometric dating of leucosomes indicates Ordovician age, meaning that the Horta Nappe underwent high-grade metamorphism

briefly after deposition (Barnes *et al.*, 2007; Nordgulen *et al.*, 2011). Other marbles from the Horta Nappe yield Neoproterozoic ages (Barnes *et al.*, 2007), indicating that the nappe may contain an unconformity that separates Neoprotorezoic rocks from the Ordovician sediment deposition (Nordgulen *et al.*, 2011). Fig. 1.5 summarizes the geological evolution of the Horta Nappe.

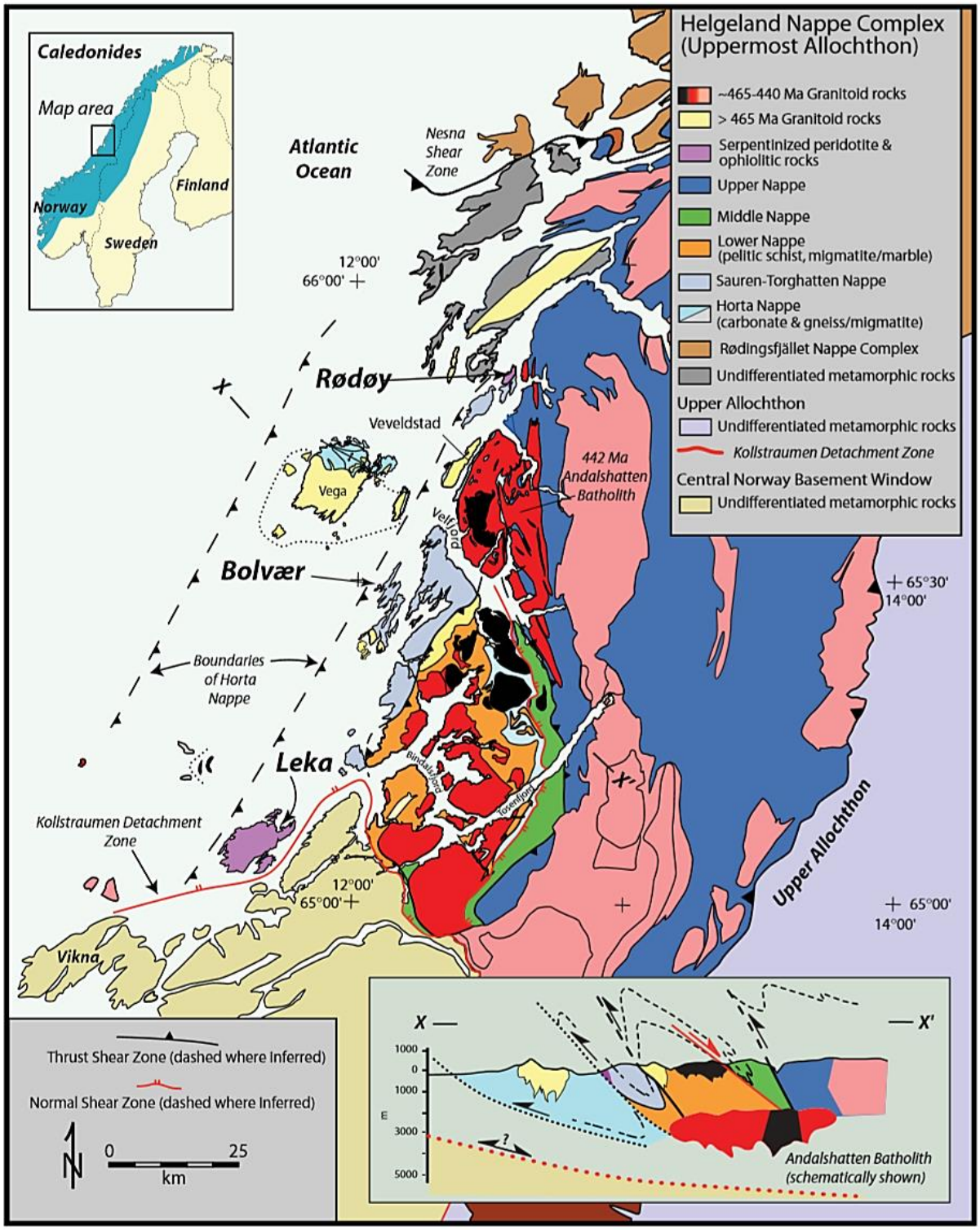

Figure 1.4: Regional map of the Helgeland Nappe Complex, showing the five major nappes and U-Pb dating of plutonic rocks after Anderson *et al.* (2013); Barnes *et al.* (2007). McArthur *et al.* (2014) suggested that Leka should be a part of the Sauren-Torghatten nappe based on the lithological similarities.

1.1.2.2 Sauren–Torghatten Nappe

The ophiolitic basement and associated ophiolite fragments found within the Sauren–Torghatten (S–T) nappe (and the Middle Nappe) are interpreted to have been created during the early stages of intra-oceanic back-arc spreading above a subduction zone (Barnes *et al.*, 2007). Further evidence for a subduction-related source is shown in the rocks' isotopic data: a change to less radiogenic values is observed, which needs incorporation from an isotopically evolved (most likely crustal) source (McArthur *et al.*, 2014).

Weathering and short transportation left basement fragments as coarse polymict conglomerates on top of the remaining basement (McArthur *et al.*, 2014). Today, these fragments are preserved as serpentinite slivers (Nordgulen *et al.*, 2011). The deposition changed from a transitional continent-oceanic source into a predominantly continental source, represented by a change in lithologies from shallow-marine turbidites and marbles to metasandstones (McArthur *et al.*, 2014). Zircon analysis of these S–T sedimentary rocks yields Precambrian ages, similar to that of the Lower Nappe metasedimentary rocks (Barnes *et al.*, 2007). This may indicate that the Lower Nappe was in short proximity to the S–T nappe during Ordovician times and that erosion of the Lower Nappe may be the source of the coarse-grained sediments of the S–T nappe (fig. 1.5) (Barnes *et al.*, 2007).

The Leka ophiolite has been tied to the S–T Nappe based on U-Pb zircon ages and similar metasedimentary sequences (McArthur et al., 2014). The Leka Ophiolite constitutes the island of Leka and the surrounding islets (fig, 1.4) and consists of mafic to ultramafic basement rocks (primarily harzburgite and dunite) unconformably overlain by metasedimentary rocks (Skei group) (Sturt & Ramsay, 1994)). The Skei Group were deposited as conglomerates and sandstones on a deeply eroded substrate of the Leka Ophiolite (Sturt & Ramsay, 1994). The Leka ophiolite sequence is one of several suprasubduction-zone ophiolites in both the Norwegian- and Appalacian Caledonides (Barnes *et al.*, 2007) and reached upper greenschist facies metamorphic grade (McArthur *et al.*, 2014).

1.1.2.3 Lower Nappe

The Lower nappe, home of the Vassbygda units, share similarities with the Horta nappe and the Upper nappe in that it consists almost entirely of metasediments and lack a crystalline basement (Nordgulen *et al.*, 2011). Migmatitic quartzofeldspathic and semi-pelitic gneisses dominate the nappe with minor calc-silicates and marbles (Gustavson, 1973; Nordgulen *et al.*, 2011; Thorsnes & Løseth, 1991). The gneisses are commonly banded with abundant leucosome veins (Barnes & Prestvik, 2000) and usually show a well-developed penetrative foliation (Thorsnes & Løseth, 1991). The marbles in the Lower nappe are pure to banded calcite marble with minor graphite, pyrite, and varying content of silicate minerals (Sandøy, 2003; Thorsnes & Løseth, 1991).

The Lower nappe hosts the dioritic plutonic rocks Velfjord Massifs/Plutons (Barnes *et al.*, 1992; Kollung, 1967), which is interpreted to have intruded after the main phase of deformation and nappe thrusting of the nappe stack (Thorsnes & Løseth, 1991).

The Lower nappe marbles are interpreted to be of Neoprotorezoic age based on chemostratigraphy, with one marble unit being of Ordovician age (Sandøy, 2003). The sedimentary rocks lack zircons younger than 900 Ma, and no direct dating of the migmatization has been achieved (Barnes *et al.*, 2007). However, Yoshinobu *et al.* (2002) indicate an Early-Ordovician age (c. 480Ma) of the migmatization based on inheritance of sediments in younger granites. Furthermore, McArthur *et al.* (2014) concluded that the ranges in zircon U-Pb ages are similar to that in southeast Greenland and could, therefore, indicate that the Lower Nappe was a rifted fragment of Laurentia.

The relationship between the Lower and Middle nappe is described by Thorsnes and Løseth (1991) as a tectonic thrust contact where the Middle nappe was thrust over the Lower nappe. Thorsnes and Løseth (1991) used the sharp transition of the marble of the Lower nappe to the fragmented ophiolite basement of the Middle nappe as an indication of a tectonic contact, alongside the observation of granitic dykes in the marble being increasingly more deformed closer to the contact, but not occurring in the overlying nappe. This also implies that the marbles of the Lower nappe were intruded before the thrusting.

The contact between the Lower and Middle nappe is characterized by a c.1km wide shear zone (Nordgulen *et al.*, 2011), A normal reactivation of the Lower–Middle nappe thrust has been linked to an isothermal decompression event in the contact zone of the host rocks of the Velfjord plutons (Barnes & Prestvik, 2000; Yoshinobu *et al.*, 2002).

1.1.2.4 Middle Nappe

The Middle nappe consists of Late-Cambrian to Ordovician rocks, similar to the S–T nappe (fig. 1.5) (Barnes *et al.*, 2007; Nordgulen *et al.*, 2011; Thorsnes & Løseth, 1991). They are mainly metapelites, calc-silicate rocks, marbles, and interbedded conglomerates (monomict amphibolitic to calcareous and polymict beds) (Nordgulen *et al.*, 2011; Thorsnes & Løseth, 1991). Although the sedimentary rocks are predominantly of Ordovician age, some of the conglomerates are of Precambrian age (Barnes *et al.*, 2007). The Middle nappe and S–T nappe also share the same discontinuous, fragmented, ophiolite basement (Thorsnes & Løseth, 1991). Ultramafic rocks are commonly found at the base of the Middle Nappe, whereas serpentinite slivers are found within the sedimentary section of the S–T nappe (Nordgulen *et al.*, 2011). Sindre (1980) interpreted the ultramafic bodies within the Middle nappe to a depth of 200-350m by gravimetrical analysis.

The metamorphic grade of the Middle nappe is also comparable to that of the S–T nappe with typical amphibolite facies with kyanite-grade zones (Heldal, 2001). However, the S–T nappe difference is that kyanite is replaced by sillimanite in the Middle nappe metasedimentary rocks (Nordgulen *et al.*, 2011). Barnes *et al.* (2007) interpret that the end of the sediment deposition occurred at c. 480 Ma and that the rocks underwent a peak metamorphic event at c. 475 Ma. Some marbles of the Velfjord area yielded Ordovicican ages (Sandøy, 2003), and were tentatively assigned to the Middle nappe by Barnes *et al.* (2007).

Thorsnes and Løseth (1991) establish four phases of deformation in the Middle nappe before the deposition of the overlying sediments on the basement ultramafic rocks:

- The first event (D_1) is defined by porphyroblasts of staurolite and garnet, which overgrown a fine-grained S_1 foliation. The porphyroblast must have grown between D_1 and D_2.
- D_2 was the predominant stage and is observed through the formation of penetrative L-S fabric, isoclinal folds associated with axial planar schistosity (S_2), and stretching lineation. The S_2 foliation is parallel to the thrust plane and imbrication zone in the lower part of the Middle nappe, implying that D_2 was the main thrusting and imbrication event of the middle and lower nappe. D_2 nearly completely overprints all D_1 structures.
- D_3 is represented by open to isoclinal, small to medium-scale folds with an associated L_3 lineation and crenulation cleavage (S_3).
- D_4 consists of gentle to close folds with associated S_4 crenulation cleavage. These folds are only found locally as small-scale structures and were interpreted to be of little regional importance.

1.1.2.5 Upper Nappe

Rocks of the Upper Nappe consists of Late Cambrian to Ordovician calcareous fine-grained metasandstones, pelitic schists, and migmatitic calc-silicate to quartzofeldspathic gneisses (Anderson *et al.*, 2013). The age of the sediments of Upper Nappe is challenging to establish due to sparse zircon data. However, some zircons indicate Cambrian-Ordovician sedimentation ages (Barnes *et al.*, 2007). Migmatization of the Upper nappe is interpreted by U-Pb dating of zircons to c. 480 Ma (Yoshinobu *et al.*, 2002). Barnes *et al.* (2007) further state that, although lithological similar to the Lower Nappe, the different depositional ages of the sediments indicate that the two nappes are not correlated. The sedimentation was shortly followed by high-grade metamorphism and partial melting at c. 480 Ma (Barnes *et al.*, 2007). Subsequent cooling of these rocks has been interpreted to occur from amphibolite facies temperatures around 470 and 474 Ma, as recorded by K/Ar dating of a skarn-zone. (Barnes *et al.*, 2007; James *et al.*, 1993).

The heat from the late magmas of the Bindal Batholith reached biotite dehydration melting at c. 444 Ma, which led to migmatization and formation of diatexite at lower crustal levels (Reid, 2004). This diatexite migrated upwards due to deformation of migmatites at higher crustal levels and may have contributed to the formation of dioritic, granitic, and tonalitic dykes. The final magmatic event of the Upper Nappe is interpreted to be the intrusion of a composite magma at c. 425Ma (Reid, 2004).

1.1.3 Geological Evolution of the Helgeland Nappe Complex

To understand the sedimentary provenance and timing of events within the HNC, dating and structural relationships have proven to yield a better understanding of the geological environment during the sedimentary phases and pluton emplacements (Barnes *et al.*, 2007; McArthur *et al.*, 2014). Following is the geological evolution of the HNC based on the rock descriptions and events described in the previous sub-chapter. This section is divided into the sedimentary provenance, tectonics, and magmatic events that shaped the nappe stack and the emplacement of the HNC to its current position. A summarization of the geological evolution is illustrated in fig. 1.5 and simplifies the evolution described in the following chapters.

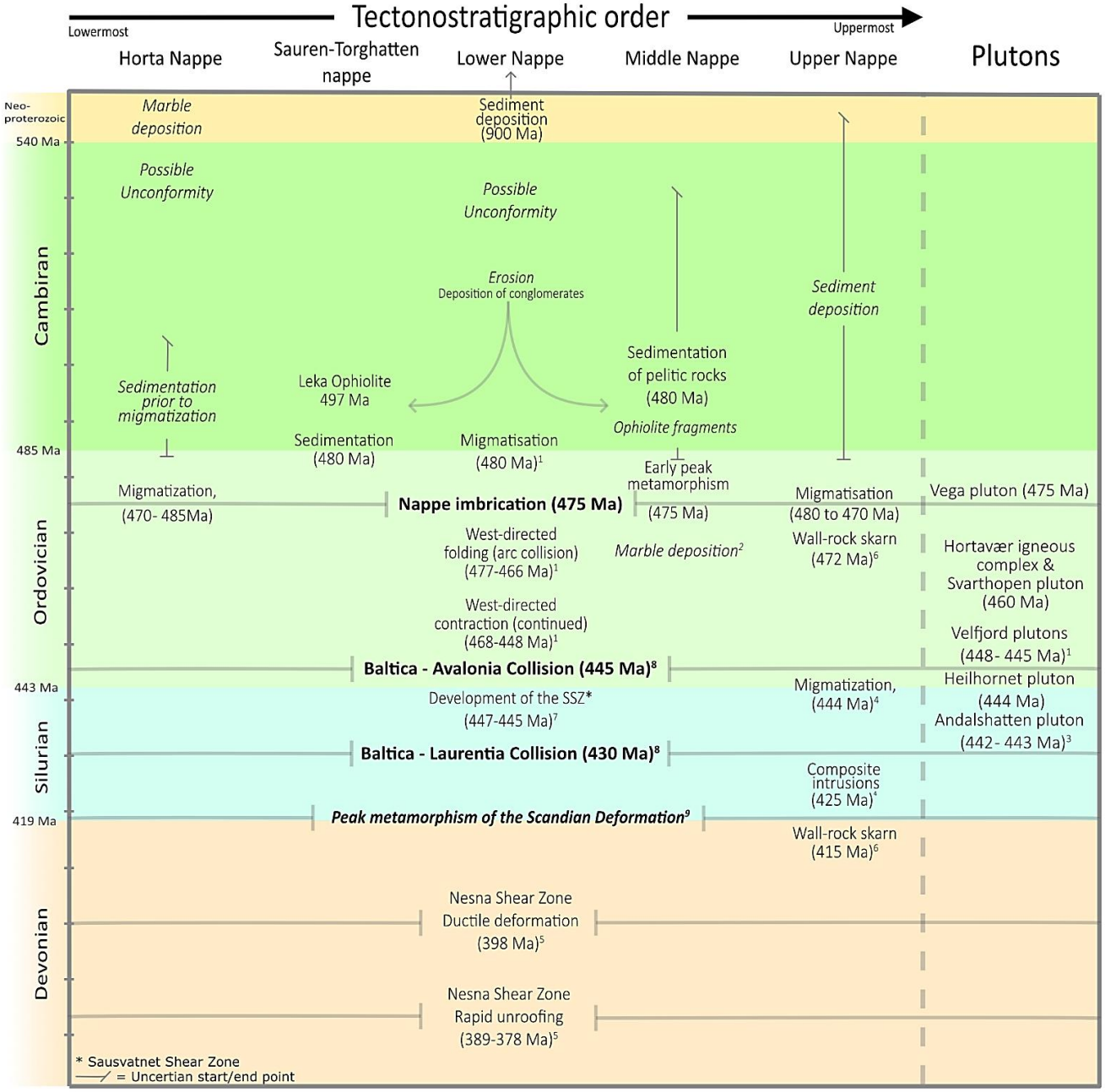

Figure 1.5: Diagram summarising the sedimentary, magmatic, and metamorphic evolution of the Helgeland Nappe Complex and the timing of major regional events. Relative ages are marked as italic writing. All ages are from (Barnes *et al.*, 2007) unless otherwise stated. [1](Yoshinobu *et al.*, 2002), [2] (Sandøy, 2003), marbles placed in the Middle Nappe by Barnes *et al.* (2007), [3]Anderson (2008), [4](Reid, 2004), [5](Eide *et al.*, 2002), [6](James *et al.*, 1993), [7](Dumond *et al.*, 2005) [8](Corfu *et al.*, 2014), [9](Roberts, 2003).

1.1.3.1 Sedimentary Provenance

The regional trends described in chapter 1.1.1 are also evident within the HNC. The Neo-proterozoic rocks of the Lower nappe likely represent a rifted fragment of the Precambrian extensional event and break up of Rodinia (McArthur *et al.*, 2014). The best representation of sedimentary provenance is seen within the S–T nappe, where Late-Precambrian to Early-Cambrian rift basins mark the age of sedimentation of the S–T nappe and the remaining nappes of the HNC (McArthur *et al.*, 2014). Based on the lithological observations described in chapter 1.1.2.2, the Early-Ordovician S–T nappe basin was in such a palaeogeographic position that it could receive material from an exposed oceanic basement, Precambrian sediments from Laurentia, and Cambrian to Early-Ordovician sediments from an unknown source (McArthur *et al.*, 2014). The approach of an ophiolite-floored basement towards a continental margin, with or without increased tectonic activity in the continental regions, may be the source of the coarse-grained sediments (McArthur *et al.*, 2014).

Fig. 1.6 shows the situation in which the S–T stratigraphy could have formed: High-energy sediments from a rift-fragment (possibly the Lower nappe) that covered the ophiolitic crust. These high-energy deposits were later covered by fine-grained deep-marine sediments that gradually changed to more coarse-grained crustal source sediments (Skei group) as the arc collision drew closer (Heldal, 2001; McArthur *et al.*, 2014). These Cambro-Ordovician sediments likely came from a primitive arc that formed in the early stages of the collision; however, this arc is not observed today (McArthur *et al.*, 2014). The Cambrian–Ordovician marbles of the HNC likely formed in marine basins on the Laurentian plate due to similarities with marbles of the New England and Canadian Appalachian mountains (Roberts *et al.*, 2002)

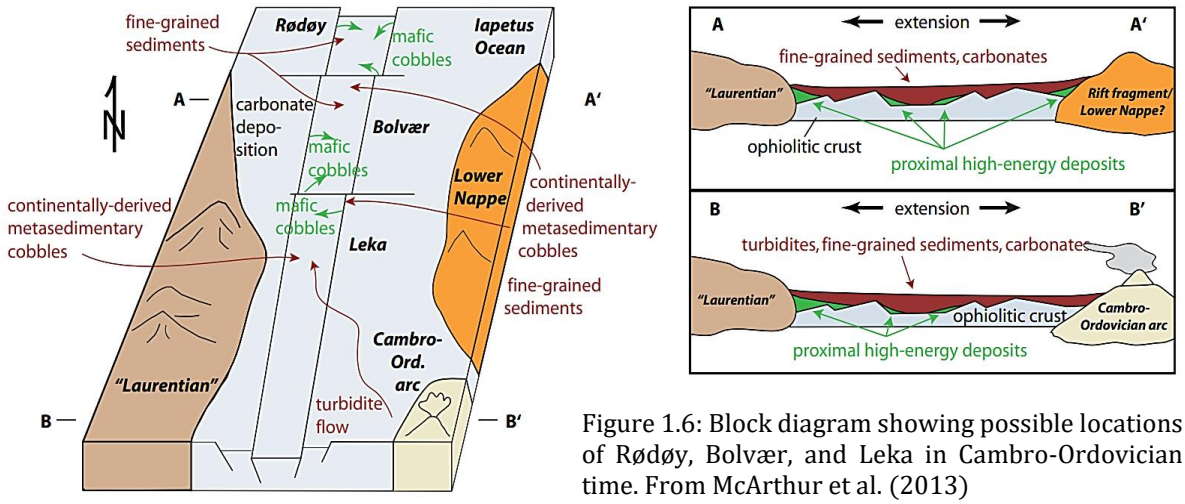

Figure 1.6: Block diagram showing possible locations of Rødøy, Bolvær, and Leka in Cambro-Ordovician time. From McArthur et al. (2013)

The Skei group sediments, which overlay the Leka ophiolite, are interpreted to be of Ordovician age (Barnes *et al.*, 2007; Sturt & Gee, 1986). These sediments have isotopic data that indicate a partial oceanic component, which may suggest that these sediments were derived from the formation of a primitive arc in the closing Iapetus ocean (McArthur *et al.*, 2014). Younger sediments with ages from Neoproterozoic through Early-Ordovician are more difficult to explain since no existing source for these sediments are found within the HNC. However, McArthur *et al.* (2014) propose that they may have formed in relationship to primitive arcs or rift-related events in the Iapetus Ocean.

1.1.3.2 Juxtapositioning, Metamorphism, and Magmatism

Extensive magmatic activity from Late-Cambrian to Silurian is evident in the formation of plutons and migmatization of sediments across the HNC: Melting of the Upper Nappe began c. 480 Ma at 500–700 MPa (20–28 km depth) and around 800 °C, where enough magma was formed to mobilize melt-rich parts and create cross-cutting diatexites (fig. 1.5) (Barnes *et al.*, 2011). This event is almost identical to the partial melting of the Horta- and Lower Nappe, which implies that middle Ordovician metamorphism and crustal melting occurred throughout the HNC due to the amalgamation of the nappes (Barnes *et al.*, 2011). These events combined led to the emplacement of plutons that today are grouped under the Bindal batholith (Yoshinobu *et al.*, 2002). The oldest plutons in the Bindal Batholith are predominantly peraluminous and believed to be emplaced during a regional migmatization event in the Lower Nappe, with later plutons indicating mixed mantle and crustal sources and ranges from granitic to gabbroic in composition (Yoshinobu *et al.*, 2002).

Yoshinobu *et al.* (2002) propose that the Bindal batholith formed during two events, the first during the continent–island arc collision (468-448 Ma) of Baltica and Laurentia, which amalgamated the crust over a subducting slab (eastward dipping in the present geography). The second event occurred c. 448-445 Ma during a reversal in the direction of the subducting slab and resulted in the emplacement of the Velfjord plutons (Barnes *et al.*, 1992; Yoshinobu *et al.*, 2002) (fig. 1.7 B, C).

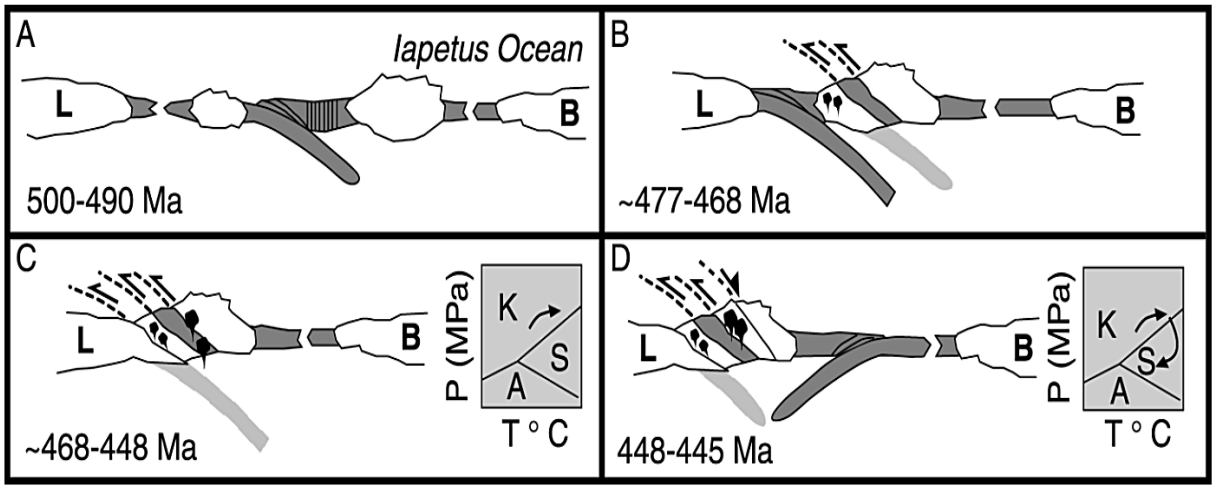

Figure 1.7: Proposed evolution of the Helgeland Nappe Complex during the Ordovician period by Yoshinobu *et al.* (2002): **A**) Proposed continental position of Laurentia (L) and Baltica (B) and the formation of the Leka Ophiolite as a suprasubduction-zone above an east-dipping subduction slab. **B**) First collision and fragmentation of ophiolitic rocks. This also marks the first generation of peraluminous magmas (e.g., The Vega pluton). **C**) The amalgamation of Laurentia and loading of lower nappes prior to 448 Ma. **D**) Exhumation of the Helgeland Nappe Complex (c. 475 Ma), followed by the initiation of west-dipping subduction and the closure of the Iapetus ocean. Metamorphic mineral assemblages and reactions from Barnes and Prestvik (2000). K=kyanite, A=andalusite, S=sillimanite.

One of the earliest plutons in the Bindal batholith is the Vega Pluton that outcrops on the southwestern side of the island of Vega (fig. 1.4) (Nordgulen *et al.*, 1993). It is classified as an S–type diatexite pluton and contains enclaves/xenoliths of gneisses, quartzite, marble, calc-silicate rocks, and mafic magmatic rocks with a paragneissic protolith (Barnes *et al.*, 2007). The pluton is dated to c. 475 Ma and analysis of the enclaves yield close to identical composition as the migmatites of the Horta Nappe (Barnes *et al.*, 2007; Yoshinobu *et al.*, 2002). With these observations, Barnes *et al.* (2007) tentatively assign the Vega pluton to the Horta Nappe.

In the Velfjord region, the batholith consists of the predominantly dioritic plutons that were emplaced in the following order: (1) Akset-Drevli (447.8 $\pm$ 2.3 Ma), (2) Hillstadfjellet (447.0 $\pm$ 3.2 Ma), and (3) Sausfjellet (445 $\pm$ 11 Ma) (Yoshinobu *et al.*, 2002). North of Velfjord lies the Andalshatten pluton (447 $\pm$ 7) (Nordgulen *et al.*, 1993). Barnes and Prestvik (2000) determine the pressures of these plutons to 6-8kbar (20–30 km) based on mineral assemblages and Al-in-hornblendes geobarometry. Outward expansion of the Sausfjellet magma chamber occurred due to contact melting of the host rocks and deflected lithologies and foliation traces near the contact of the intrusions (Dumond *et al.*, 2005).

Barnes and Prestvik (2000) found evidence for an isothermal decompression event (4-5kbar) in the host rock od the Velfjord plutons, which was later related to the rapid exhumation of the HNC and normal reactivation of the Lower–Middle nappe shear zone (fig. 1.7 D) (Yoshinobu *et al.*, 2002).

Andalshatten pluton is a large high-potassium, calc-alkaline composite intrusion that makes up a large part of the Velfjord area and that cuts through four nappes in the HNC (Anderson *et al.*, 2013; Nordgulen *et al.*, 1993). Five distinct rock types make up the pluton and are classified based on their cross-cutting relationship. From oldest to youngest, these are (1) tonalite, (2) hornblende-biotite granite, (3) amphibole-bearing diorite, (4) coarse-grained to megacrystic K-feldspar granodiorite, and (5) schlieren-banded to gneissic granodiorite (Anderson *et al.*, 2013). The Andalshatten batholith is interpreted to be assembled by five distinct batches of magma over 600 ka to 1.7 Ma with recharge events of dioritic magmas (Anderson *et al.*, 2013).

Yoshinobu *et al.* (2002) conclude that the final stage of pluton creation (447 Ma) had to coincide or predate exhumation and extension of the HNC since both contractional and extensional shear zones appear to be cut by the 447 Ma Andalshatten batholith (fig. 1.5).

The S–T and Horta Nappes were presumably juxtaposed by 475 Ma (McArthur *et al.*, 2014). The younger intrusion of the Botnafjellet pluton, which intruded the Neoproterozoic sediments of the Lower Nappe, contains Ordovician age zircons, indicating that the Lower Nappe was thrust onto a younger nappe (possible Horta Nappe) at the time of intrusion (478 Ma) (Barnes *et al.*, 2007). U-Pb age of titanite from the Middle Nappe and the previously mentioned amphibolite skarn implies that cooling below amphibolite condition, likely followed by metamorphism and nappe stacking, occurred ca 475 Ma (fig. 1.5) (Barnes *et al.*, 2007; James *et al.*, 1993; McArthur *et al.*, 2014).

1.1.3.3 Syn- and Post-Scandian Deformation

The structural pattern of the HNC reflects the previously discussed amalgamation of the nappe complex, followed by Early-Silurian magmatism and Scandian nappe translation (see summary in fig 1.5). The Silurian Scandian contractional phase involved the over-thrusting of Caledonian nappe units onto the continental margin of Baltica (Gee & Sturt, 1985). This can be observed as northeast-southwest oriented ductile rock fabrics in the Central Norwegian Basement Window (CNBW), south of the HNC, below the Kollstraumen detachment zone (Nordgulen *et al.*, 2002). Mylonites and shear zones along the base of the HNC also witness the thrusting that occurred during the Scandian event (Roberts *et al.*, 1983). Roberts and Nissen (2006) attribute the change of micro- and macrotexture, mineralogy, and modal properties to a record of the Scandian thrust deformation and a following late-Scandian extensional deformation.

The structural relationship between the nappes is described by Barnes *et al.* (2007) as reactivated shear zones with top-to-the-west vergence. In order to understand when the juxtaposition of the HNC ended, radiometric dating of the shear zones, structural evidence, and pluton emplacements are used. The latest plutons were emplaced during the Early-Silurian period and seemingly cut the structural relationships (top-to-the-west vergence shear zones) of the nappes (Yoshinobu *et al.*, 2002). Yoshinobu *et al.* (2002) therefore conclude that the juxtaposition of nappes, pluton emplacement, and exhumation must have followed closely in time and before the main Scandian orogeny. The pre-Caledonian east-directed nappe thrusting is commonly attributed to the Finnmarikan phase of the Scandian Orogeny (Andréasson, 1994); however, Yoshinobu *et al.* (2002) conclude that the HNC was not a part of the Finnmarkian phase, but somewhat more similar to the Taconic deformation of the northeast United States and Canada. They hypothesized that the HNC represents an orphaned allochthonous arc sequence, stranded on top of Baltica during the final breakup of Pangea.

The HNC shows little evidence of the Scandian deformation, indicating that the nappe complex remained at relatively high crustal levels following the metamorphism and plutonism of the Early-Silurian period (Nordgulen *et al.*, 2002). Therefore, it is difficult to establish the direct structural evolution of the HNC after the nappe amalgamation of Early-Ordovician.

Today, the Helgeland Nappe Complex is confined by two large scale fault zones (fig. 1.8). In the south, the Kollstraumen detachment marks the transition onto the CNBW. The CNBW shows similarities to the Western Gneiss Region and consist of predominately Precambrian (1.80 to 1.79 Ga (Skår, 2002)) gneisses and granitic rocks with kinematic indicators of the Devonian extensional period and infolded parts of thrust sheets (Braathen *et al.*, 2002; Skilbrei & Olesen, 2005). South of the CNBW lies the Høybakken detachment zone (Braathen *et al.*, 2000; Braathen *et al.*, 2002; Osmundsen *et al.*, 2006). The eastern and northern part of the HNC is confined within the Nesna shear zone, described below. Fig. 1.8 links the Nesna shear zone with the proto-Høybakken detachment, indicating that the Kollstraumen detachment had to occur at a later stage than the Early-Devonian Nesna-Høybakken deformation (Braathen *et al.*, 2002; Osmundsen *et al.*, 2003).

The Kollstraumen Detatchemt zone is characterized by a medium-grained ductile fabric indicating top-to-the-east-northeast shear (Nordgulen *et al.*, 2002). Folding of the underlying CNBW is observed as east-northeast-plunging fold axes of open, possible decapitated, or synchronous shear folds (Braathen *et al.*, 2002; Nordgulen *et al.*, 2002). The folds are near parallel to the stretching direction and normal to the south-southeast thrust direction of the Caledonian Orogeny (Nordgulen *et al.*, 2011). This is evidence for an overlap of extensional and contractional regimes

in the middle crust during the latest-Scandian deformation (Braathen *et al.*, 2002; Eide *et al.*, 2002), similar to that of the Devonian deformation of the Møre area (Nordgulen *et al.*, 2002).

Nordgulen *et al.* (2002) obtained U-Pb ages of 436 and 430 Ma from dykes in the rocks of the CNBW, which was interpreted together with structural evidence to overlap with the earliest phase of Scandian contractional deformation. U-Pb ages of c. 401–402 Ma obtained from titanite and monazite from the same dykes coincided with pegmatite formation in central Norway and was interpreted to represent the latest exhumation event of the CNBW (Nordgulen *et al.*, 2002).

The Nesna shear zone defines the northern part of the HNC. K-feldspar samples yield evidence of an Early to Late-Devonian (398 Ma) top-to-the-west-southwest ductile extension and footwall unroofing, followed by a later event of rapid unroofing during the Early-Carboniferous (389 to 378 Ma) (fig. 1.5) (Eide *et al.*, 2002). The Devonian period documents an evolving strain field for the central Scandinavian Caledonides where the upper crustal levels experienced contraction parallel to the orogen direction, whereas middle to lower crustal areas experienced contraction normal to the extension (Eide *et al.*, 2002). A sinistral shear component is also observed in the developing Devonian strain field, which marks the final oblique convergence of the Baltica-Laurentia collision (Eide *et al.*, 2002). The Early-Carboniferous deformation and unroofing are linked to activity on steeper ductile-brittle extensional faults that cut the older low-angle detachments and shear zones (Eide *et al.*, 2002).

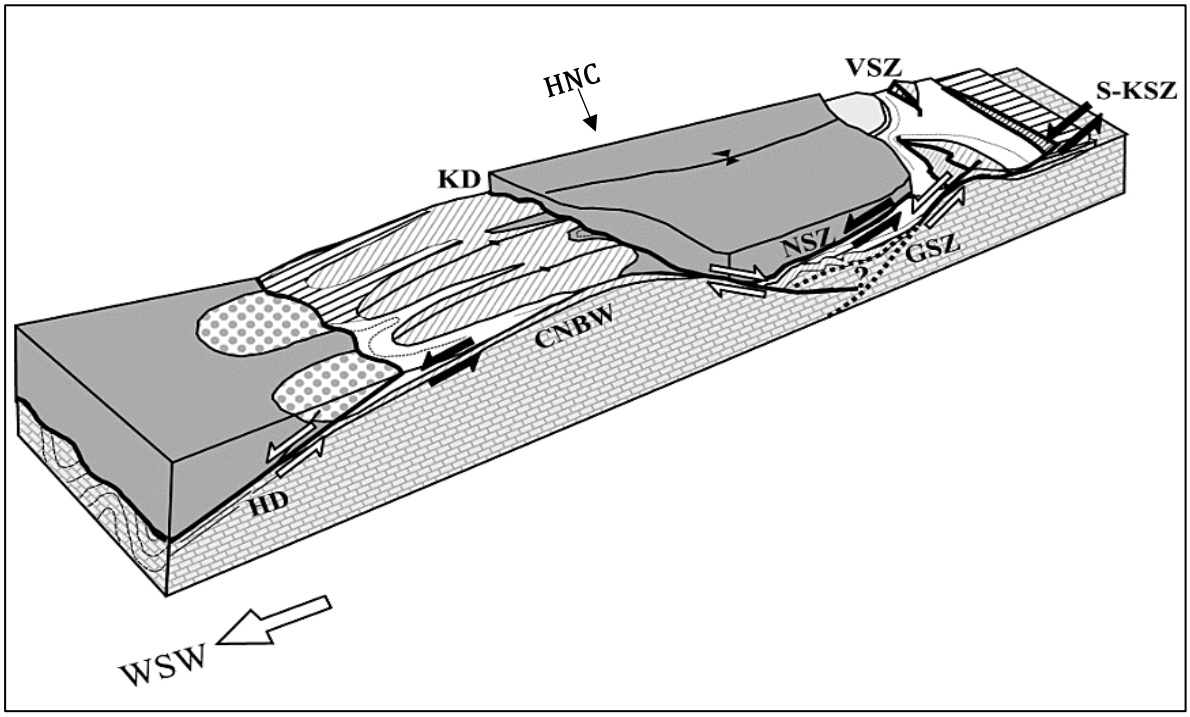

Figure 1.8: Block diagram with kinematic indicators of the faults in and around the Helgeland Nappe Complex (**HNC**) with the Kollstraumen detachment (**KD**) defining the southern border of the nappe complex, and the Nesna shear zone (**NSZ**) confining the eastern and northern parts. South of the HNC, Fennoscandian basement is exposed in the Central Norwegian Basement Window (**CNBW**). Other extensional structures in the region are the extensional Virvassdal shear zone (**VSZ**) and the Gaukarelv shear zone (**GSZ**). Høybakken detachment (**HD**) marks the southern exposure of the CNBW. The footwall of the GSZ contains back-warping by an earlier generation of faults, called the Seve–Köli shear zone (**S-KSZ**). Figure from Osmundsen *et al.* (2003).

1.1.4 Introduction to the Field Area: Vassbygda

The field area for this thesis is a 4x7 km rectangle in Vassbygda (fig. 1.9). The Vassbygda area consists of the uppermost rocks of the Lower nappe and is dominated by a lowland of dense spruce forest with less densely foliated ridges and hills (fig. 1.10). Steep mountains enclose the lowland in the west (Hardangsfjellet), south (Stortuva), and east (Nordfjellmarka) (fig. 1.9 and 1.10)). Two connected lakes (Stor- and Fjellvatnet) dominate the southern part of the area with a smaller lake, Godvatnet, on the central west side.

The area has seen relatively little scientific work compared to the rest of the nappe stack. Following is a brief summary of the relevant observations from the works by Sandøy (2003), Dumond (2002), Dumond *et al.* (2005) Thorsnes and Løseth (1991), and others which describe areas and observations related to, or close by the field area. These works form the closest regional geological framework for this thesis.

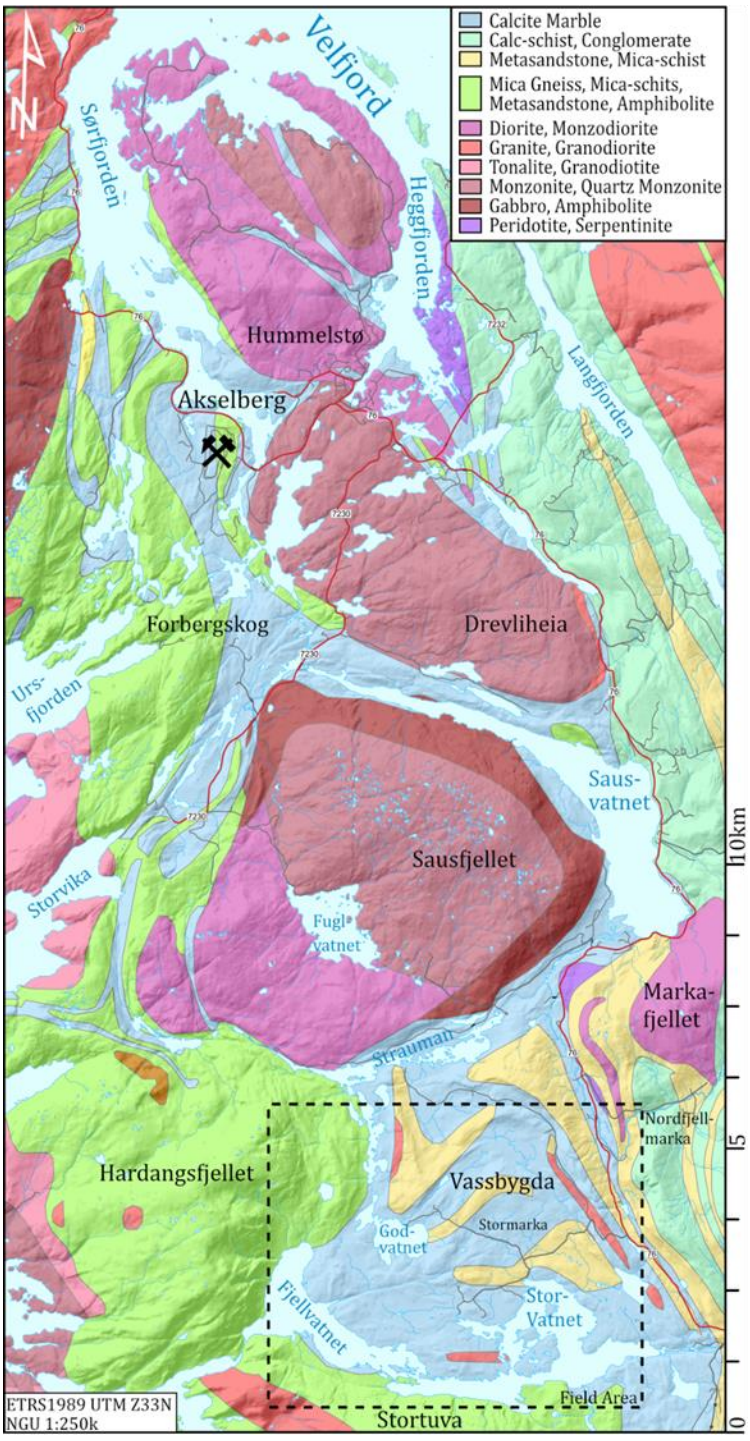

Figure 1.9: Geological map of Vassbygda, the northern Saus carbonates and the current open-pit mine at Akselberg. The dashed line box marks the approximate field area. Rock units from NGU's digital 1:250 000 bedrock map.

The current geological map of Vassbygda is the 1:250 000 bedrock map from the Geological Survey of Norway (NGU) (fig. 1.9) and is based on the map by Gustavson (1981). This area of the HNC was first described as consisting of three central rock units: Metasedimentary gneisses, granitoid intrusions, and marbles with varying content of siliciclastic sediments and graphite (Kollung, 1967).

The siliciclastic metasedimentary rocks of the Vassbygda area lack a detailed description and is only mentioned as "Quartzofeldspathic heterogenous gneisses" by Gustavson (1981). In contrast, the marbles are extensively described. The most detailed desc-riptions of marbles are found in the Dr. Eng. thesis of Sandøy (2003), where he describes the mineralogical variations of the "Saus

Carbonates" north of the Sausfjellet Pluton. The Saus carbonates are interpreted as a continuous belt of marble stretching from Velfjord (fig. 1.9) in the north, through Vassbygda, and continuing S-SW over Tosen and towards Terråkfjellet (Gustavson, 1981; Nordgulen *et al.*, 1990; Nordgulen *et al.*, 1989; Sandøy, 2003). Sandøy (2003) used samples from Forbergskog and the open-pit mine at Akselberg (fig. 1.9) to describe the Saus Carbonates based on their colour and mineralogic composition. Overall, these marbles are relatively impure compared to other Velfjord marble deposits and often contain siliciclastic mineral assemblages. Graphite-spotted and banded marbles contain poorly developed zones of silicate minerals, usually diopside, plagioclase, tremolite, phlogopite, and titanite with minor quartz, chlorite, pyrrhotite, graphite and fluorite (Sandøy, 2003). The marbles of the area have not been definitively assigned to any nappe due to inconsistent structural evidence and limited isotope analysis (Barnes *et al.*, 2007; Sandøy, 2003). However, Sandøy (2003) obtained $^{87}Sr/^{86}Sr$ ratios that indicated a likely depositional age of 590-650 Ma of the Saus carbonates: indicating an affinity to the Neo-proterozoic deposition of the Lower nappe.

Sandøy (2003) undertook a sizeable structural exploration of the geometry of the Saus carbonates. He described the main structural features of the Akselberg–Forbergskog area (fig. 1.9) to consist of parallel planar east-wards dipping layers, which in reality is large overturned isoclinal folds with relatively long limbs compared to the hinge zones. He based his interpretation on the appearance of cm-scale parasitic folds, drag-folded siliciclastic metasediments, and boudinaged intrusions observed on

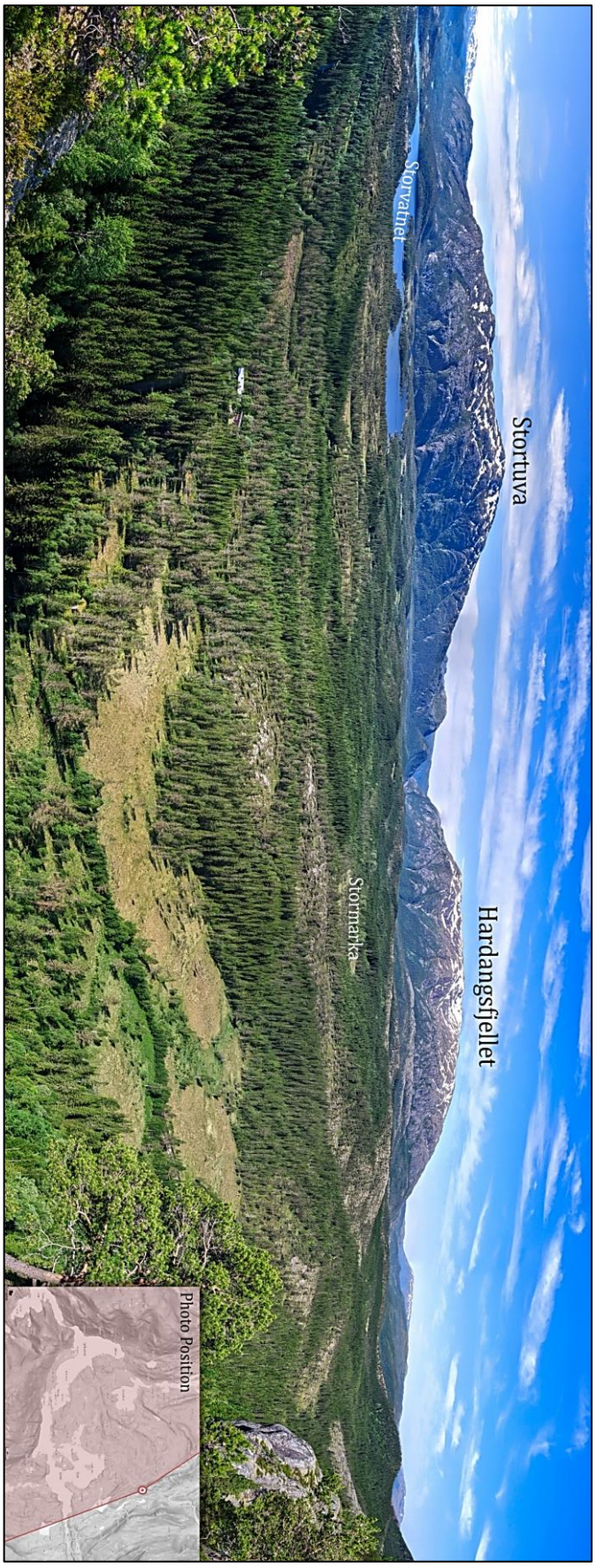

Figure 1.10: Overview of Vassbygda. Picture location and field of view (red area) are shown in the lower right section.

the surface. The folded structures were observed as synform-antiform pairs, which have later been refolded. Similarly, a result of an original fold with a north or north-northwest fold axis being superimposed by a folding event with an east-northeast fold axis into a type 2 fold interference pattern (Ramsay & Huber, 1987; Sandøy, 2003).

Dumond (2002) describes the structural observations of Vassbygda to be dominated by cm-scale psammitic layers (S_1) in quartzofeldspathic gneisses that are folded into open to tight folds. Further, isoclinal to tight folds in muscovite + biotite schists shows a well-developed crenulation cleavage (S_2), with some leucosomes occurring in shear bands (S_3) that cuts all older structures (Dumond, 2002). He separated the structures of the Vassbygda region into a northern and southern segment based on their structural position and the orientation of axial planar fabrics and lineations in each segment. Dumond (2002) interpreted three main phases of folding in these segments: A km-scale isoclinal recumbent F_1 fold refolded into tight F_2 folds along east to northeast-dipping axial planes. Finally, moderately SW-dipping girdles define the third phase with shallowly to moderately northeast-plunging beta axis (Dumond, 2002). In contrast to Sandøy (2003), Dumond (2002) argued that the Vassbygda region represents a type 3 fold interference pattern (Ramsay & Huber, 1987) that formed before the emplacement of the Sausfjellet pluton.

Thorsnes and Løseth (1991) investigated the Nordfjellmark area, east of Vassbygda (see fig. 1.9 for location) and proposed a tectonostratigraphic model for the Middle nappe. The transition from the Lower nappe to the Middle nappe is not directly observed in the Vassbygda area, however, the appearance of serpentinized ultramafic rocks close to Tosenveien (fig. 1.9) is believed to be the first sign of the Middle nappe in the area (Thorsnes & Løseth, 1991). The tectonostratigraphic order of the Velfjord-Nord-fjellmark area proposed by (Thorsnes & Løseth, 1991) is summarized in Table 1.1.

Table 1.1: Tectonostratigraphic model of the Velfjord–Nordfjellmark area from (Thorsnes & Løseth, 1991).

Tectonostratigraphic Order	Nappe	Rock Unit	Unit Name
----Upper----	Upper		Late Igneous Rocks
		Mica gneiss	
	Middle	Marble, green psammite, staurolite schist	Nordlian marble
		Polymict calcareous conglomerate	Langfjord conglomerate
		Calcareous schist with lenses of conglomerate	Buøya schist
		Polymict mafic to calcareous conglomerate	Storvika conglomerate
		Calcareous schist, banded psammites, and marble	Nordfjellmark schist
		Polymict mafic conglomerate	Åsnes conglomerate
		Calcareous, hornblende-rich or quartz-rich psammites	Gløman Psammite
		Metagabbro	Igneous basement
----Lower----	Lower	Granitic dykes	
		Mica gneiss, Ca-silicate gneiss	
		Marble	

Dumond (2002) and Dumond *et al.* (2005) studied the midcrustal emplacement of the dioritic Sausfjellet pluton (445 ± 11 Ma) into the metasedimentary rocks of the Velfjord area (fig. 1.9). They concluded that the pluton was emplaced in at least two stages, one gabbroic and one dioritic, and that it is surrounded by a ~1km wide structural aureole consisting of pluton-bounding folds and shear zones. Dumond (2002) also described small intrusions of a deformed two-mica leucogranite in the southeastern portion of the Vassbygda region.

2 Methods

This thesis incorporates many methods to understand the geology of the Vassbygda, including a detailed structural framework, description and mapping of the marble deposits, metamorphic conditions, and deformations of the rocks. The methods span from fieldwork, microscopical analysis, petrographical descriptions, electron microscope analysis, and pressure-temperature (P-T) estimates.

2.1 Field Work

Mapping of the rock units was an essential part of this thesis since little activity in terms of geological mapping had been done in the Vassbygda area. Two seasons of fieldwork were carried out over two years. The first season of fieldwork consisted of one week with assistance from supervisors in June of 2019. I was lucky and had the opportunity to occasionally work in my field area during the remaining summer of 2019 since I partook in a summer internship at Brønnøy Kalk. During the internship, mapping of marble quality was prioritized. During the off-season, a draft of the geological map was made to choose areas to explore during the next fieldwork season selectively.

The second period of field mapping was in June 2020 with the assistance of supervisors and with the help of Ø. Nordgulen (NGU), who accompanied us for three days. Brønnøy Kalk provided lodging close to their quarry at Akselberg, Velfjord. It was a 30min drive to reach the field area for both field seasons. The mapping was primarily done on foot. However, the large lakes and waterways in the area were mapped with a canoe for reaching inaccessible areas (fig. 2.1). The canoe was also used to map along the well-exposed shorelines of Stor- and Fjellvatnet (fig. 2.2).

Figure 2.1: Picture of an eager field geologist embarking on a day of mapping from the canoe. Photo: Siren Ånestad

The mapping was done digitally using an iPad, with the software "Field Move" by Petroleums Experts. Field Move proved to be very intuitive to use and made the mapping very effective. Detailed observation of folds, lineations, and other tectonic indicators was noted in the Field Move software, along with descriptions of rock units or other field observations. This meant an efficient mapping with data being added in real-time to the iPad, making it possible to review the measurement and create stereonet plots in the field. The compass on the iPad was not accurate enough for proper measurements, so a Brunton GEO Pocket Transit compass was used for measurements. All planar measurements were noted as dip/dip-direction, whereas line measurements were noted as plunge→trend.

An enormous advantage of using digital mapping was the positioning tool, GPS, and imported background map in challenging terrains. The field area consists of varied flora and topography, from fully exposed ridges to thickly forested areas. In the latter areas, the GPS-location of the iPad was crucial to determine position accurately. The software can import and use different background maps, which made it possible to add detailed topographical maps for offline use in remote areas. One of the used background maps was a hillshade made from LiDAR data collected in 2014. These data were available as DEMs from hoydedata.no and made it possible to "see through" the thick vegetation and observe only the topographical factors of the field area.

2.2 Sample Collection and Preparation

Rock samples were collected during the two field seasons and processed for analyses using both the laboratory at the Geological Survey of Norway (NGU) and the Department of Geoscience and Petroleum at NTNU.

Samples were collected from representative lithologies that frequently occur throughout the field area. Exceptional or uncommon rocks or outcrops were also described but not sampled in order to conserve analysis for the typical rock types in the field area. Rocks were sampled by breaking off fresh surfaces with a hammer or sledgehammer. The goal was a large fist-sized chunk – enough material for chemical analyses and polishing of thin sections. The rock was marked with a sample number (BC-01, BC-02, …) and put in canvas bags with the same numbering. Also, corresponding GPS-location and a hand-sample description were created in the "Field Move" software on the iPad. The first field season yielded 13 samples, including two oriented samples that were orientated from clear mineral lineations. The Plunge/plunge azimuth was noted to orient the samples when polished to thin-sections. The lineation was marked as an arrow on the samples and was carried over to the polished surface. However, one of these orientated samples (BC-07) lost its indication arrow during polishing and could therefore not be used for kinematic analysis.

The second field season yielded an additional six samples, giving a total of 19, although only BC-16 of the second season samples was made into a thin section due to time constraints and long waiting time at the laboratory at NGU. A map of all sample locations is seen in fig. 2.2. The samples were brought to NGU and sawed into two pieces using a diamond-bladed rock saw: One for chemical analyses and one for thin section polishing. All weathered surfaces were removed during the sawing to avoid contamination of analyses. The rocks were then delivered to the lab at NGU for chemical testing and NTNU for 30µm polished thin-section preparation.

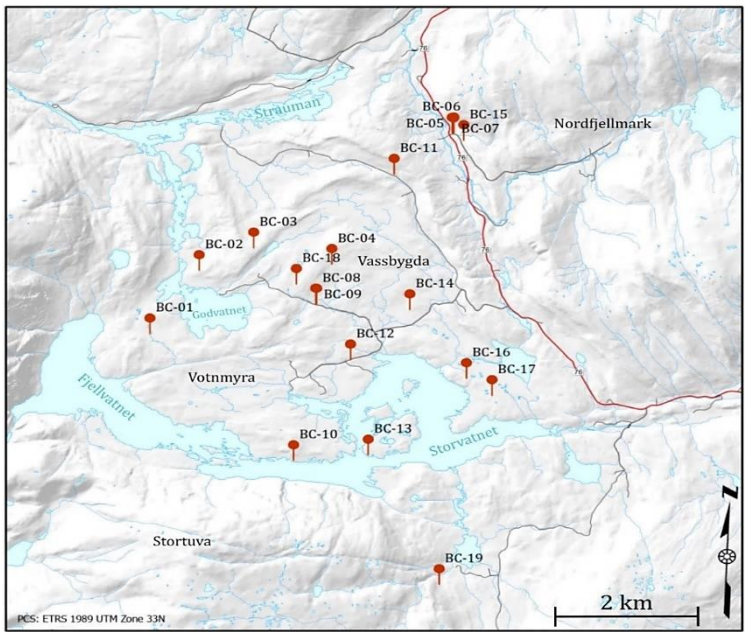

Figure 2.2: Map of sample locations: Background map form norgeskart.no

2.3 Optical and Electron Microscopy

2.3.1 Transmitted- and Reflected Light Microscopy

Optical microscopy was carried out at NTNU using a Nikon Eclipse E600 petrographical microscope and the "Spots" software for imaging and measurements. A Zeiss Axiskop 40 and the Zeiss Zen software was also used at NGU. Scans of the thin sections were made using an Olympus microscope and the Olympus Stream software. The optical microscopic analysis prepared the groundwork for further mineralogical analyses. Mineral identification and microstructures and textures were conducted on all 13 thin sections. Mineral identifications were made using the works of Nesse (2011) and Deer *et al.* (1992). Passchier and Trouw (2005); Winter (2001) were used for microstructural and -textural descriptions. The full descriptions from optical microscopy and the field descriptions are found in Appendix A: Petrographical Description.

2.3.2 Scanning Electron Microscope

The scanning electron microscope (SEM) was used for the classification and quantification of mineral phases present.

SEM utilizes an electron beam to scan the surface of the sample to create an image of the compositional contrast between components (minerals) (Reed, 2005). By using an attached X-ray spectrometer, elemental compositions can also be mapped as images or as point analyses (Reed, 2005). The electrons may gather on the surface of the sample and produce artificial results, which means samples must be coated with a thin layer of carbon to ensure sufficient electron conductivity (Reed, 2005).

2.3.2.1 Automatic Mineralogy Systems (AMS)

AMS is a set of tools for the SEM used to identify mineral phases, geometry, mineral associations, and the liberation of mineral grains and other useful functions to characterize samples (Pirrie & Rollinson, 2011). This thesis utilized AMS for the identification and geometric description of the characteristic rocks of the Vassbygda area and to study the quality and mineralogic properties of the marbles.

The AMS analyses were performed with the assistance of Dr. B. Snook at the Department of Geoscience and Petroleum. Four samples were analysed using a Zeiss Sigma 300 field emission SEM and the corresponding Mineralogic (V01.06SP3) software to post-process the acquired data. The samples consisted of one marble (BC-04), one clastic metasedimentary rock (BC-02), and two amphibolite samples (BC-01, 12) from two different field locations. They were chosen based on their abundance in the field area and would give the best average results for the rocks. The goal of AMS-analysis was to give a quantitative distribution of minerals throughout the rocks and characterize the mineral phases, and accurately differentiate and name the rocks. The graphite-spotted marble was especially interesting as the AMS results could indicate the mineral associations of the calcite and a qualitative measure on the distribution of the graphite grains and other impurities. Besides, the impurities' relative position to the calcite grains could estimate the difficulty of removing the impurities.

The mineralogical compositions for the analysis were based on the observable mineral phases from optical microscopy and tables provided by *webminerals.com*. An extra step had to be taken for the analysis of graphite crystals in the marble. Since the thin-sections were coated with carbon, the classification had to be set up to differentiate between the carbon coating and the graphite

mineral phases. This was done by creating a mineral class in the software called “resin”, and one called “graphite” and assigning a set amount of carbon content in each. Tables for the classification of minerals are shown in appendix B. The goal was to classify at least 95% of the area analysed. The remaining <5% are mostly minor mineral phases or slight variations within mineral grains. This was deemed too time-consuming to classify and would likely not give a significantly better result.

Feldspars were classified based on their compositional ratio. Three classes were created: 1) An Albite class with $X_{Or}<0.2$ and $X_{An}<0.3$, 2) A Ca-plagioclase class with $X_{An}>0.3$, and 3) a microcline class with $X_{Or}>0.2$. This ratio was calculated and assigned by the Mineralogic software.

2.4 Geothermobarometry

The electron probe micro-analyzer was used to analyse the chemical composition of selected minerals to be used for P-T estimates using geothermobarometry.

The EPMA is an instrument that utilizes the same basic concepts as the SEM; however, a better spatial resolution of element analysis is achieved by using a focused electron beam (Reed, 2005). The EPMA was used to gather point analyses of the chemical composition of specific minerals to be used in further geothermobarometric calculations. Analyses of the rocks were taken with the assistance of Dr. K. Drivenes using the JEOL JXF-8530F PLUS EPMA at the department of geosciences and petroleum at NTNU.

Thermobarometry relates to the determination of pressure (P) and temperature (T) conditions of mineral assemblages during their formation. This is done by assessing mineral assemblages that describe certain thermodynamic conditions that the rock experienced for some parts of its P-T path (Powell & Holland, 2008). This requires that mineralogical and mineral-chemical equilibrium is preserved. Using experimental data, formulas are created to empirically describe the P-T conditions of a particular mineral assemblage (Powell & Holland, 2008).

Samples BC-01 (quartz diorite) and BC-16 (metagreywacke/mica schist) were selected for EPMA and geothermobarometry based on their mineralogical composition and representative occurrence throughout the field area.

All analyses were performed using 15keV with a 3µm electron beam, except for feldspars, which were analysed with a 5µm beam to lessen the effect of sodium migration. The known-composition standards were analysed once every twenty sample analysis to ensure the accuracy persisted during the operation.

All results from these geothermobarimeters were derived from spreadsheets provided by the author of the publications or created second hand.

2.4.1 Garnet Geothermobarometry

Garnet geothermobarometry is a well-established method for estimating pressure and temperature experienced by metapeleitic rocks (Winter, 2001). Several types of thermobarimeter have been proposed based on the relevant mineral assemblage and are based on the end-member net-transfer reactions between the minerals (Holdaway, 2000; Wu, 2015). The garnet thermobarometers used are listed in Table 2.1 with the corresponding compositional limits and the publication. GB+GBMP (Wu, 2015) and GM+GMPQ (Wu & Zhao, 2006) geothermometers were calculated in addition to the listed geothermobarometers. However, the BC-16 sample was beyond the compositional limits for these calibrations.

Table 2.1: List of all garnet geothermometers and geobarometers used, their mineral assemblage, type (P=pressure, T=temperature), compositional or physical limits, and the corresponding publications. Compositional limits are given in atoms per formula unit.

Abbr.	Minerals	Type	Limits	Publication
GB+ GBAQ	Garnet-biotite+ garnet-biotite-Al_2SiO_5-quartz	P-T	For metapelites in the range of 450–950°C and 1–17 kbar. Compositional limits: $X_{Fe}^{Grt} = 0.36 - 0.91$, $X_{Mg}^{Grt} = 0.02 - 0.46$, $X_{Fe}^{Bt} = 0.11 - 0.62$, $X_{Mg}^{Bt} = 0.15 - 0.78$, $X_{AlVI}^{Bt} = 0.01 - 0.41$, $X_{AlIV}^{Bt} = 0.10 - 0.41$	Holdaway (2000); Wu (2017)
GM+ GMAQ	Garnet-muscovite + garnet-muscovite-Al_2SiO_5-quartz	P-T	For metapelites in the range of 1–12 kbar and 460–760 ºC. Compositional limits: $X_{Fe}^{Ms} = 0.03 – 0.21$, $X_{Mg}^{Ms} = 0.02 – 0.32$ $X_{AlVI}^{Ms} = 1.62 – 1.96$	Wu (2018)
GASP	Garnet -Al_2SiO_5-plagioclase	P	Compositional limits: $X_{An}^{Pl} > 17\%, X_{Gross}^{Grt} > 3\%$	Holdaway (2001)
GBMAQ	Garnet-biotite-muscovite–Al_2SiO_5-quratz	P-T	For metapelites in the range of 0.8-9.2kbar and 530-700°C. Best for Ca-poor garnets or plagioclase.	Wu and Zhao (2007)

2.4.2 Calcic Amphibole Thermobarometry

Amphiboles can be useful in determining the P-T path since the amphibole group minerals occur at a wide range of P-T conditions (Bucher & Grapes, 2011; Winter, 2001). At lower temperatures, hornblendic amphiboles are replaced by sodic-calcic amphiboles at high-pressure conditions and actinolite at lower pressures (greenschist facies) (Bucher & Grapes, 2011). Table 2.2 shows the geothermobarometer used for P-T estimations utilizing the compositions of hornblende and plagioclase. The pressure was estimated from the Al-in-hornblende geobarometer (Anderson & Smith, 1995; Schmidt, 1992), and temperatures were derived from Blundy and Holland (1990); Holland and Blundy (1994). Additional geothermobarometers were tested (Molina *et al.*, 2015; Ridolfi *et al.*, 2010), but were not viable on the composition of the amphiboles present in the sample.

Table 2.2: Table of the amphibole-plagioclase geothermobarometer used. The geothermobarometer utilizes temperature estimates from Blundy and Holland (1990) & Holland and Blundy (1994), and pressure estimations from Anderson and Smith (1995) & Schmidt (1992).

Abbr.	Minerals	Type	Limits	Publication
Hbl-Pl	Hornblende-plagioclase	P-T	Temperature range of 500°–1100°C. Pressure range from 2.5–13 kbar. Plagioclase composition $<An_{92}$, Amphibole composition <7.8 Si apfu.	Anderson and Smith (1995); Blundy and Holland (1990); Holland and Blundy (1994); Schmidt (1992)

2.5 Geophysical Analyses

Geophysical analyses were performed by default at the NGU by M. Osinka. The analysis tested for density, porosity, susceptibility, remanence, and thermal conductivity, although only the magnetic properties and the densities of the rocks were relevant for this thesis. An overview of the parameters and equipment used is listed in table 2.3.

Table 2.3: Geophysical parameters and the equipment used for analysis. Also listed are the ranges of the measurements and the level of uncertainty.

Parameter	Equipment	Range	Level of uncertainty	Unit	Notes
Sample volume, density, Open porosity. EN 1936: 2006 (E))	Sartorius AX 4202	i.a.	0.01	g	Open porosity is given by the relationship between the volume of open pores and the apparent volume of the sample.
Magnetic susceptibility	Proprietary equipment by NGU (2015) • Operating frequency 75 Hz • 120 mm tube diameter	< 100	60% rel	10^{-6} SI	Used on none-conducting samples
		100 - 1000	6% rel		
		1000 - 100000	0.6% rel		
		> 100000	0.1% rel		
Magnetic remanence	FGM3D sensors and FGM3D DT data collecting software (Sensys)	< 50	5% rel	mA/m	With BH600-3-B-Helmholtz coil (Serviciencia) and proprietary mu-metal shield.
		> 50	1% rel		
Thermal Conductivity	C-Therm Tci	1.1 - 29	2.5%* rel	W/mK	Water is used as a contact medium between the sensor and the sample. Heat transfer, k, and effusivity, e, is reported with the Ceramics calibration method. *For control sample Pyroceram Tci. This may be higher for natural samples.

2.6 Chemical Analyses

Chemical analyses are crucial for correctly characterizing the rocks of the area and important for determining the marble quality. A. E Karlsen and C. Fabian performed analyses using X-ray fluorescence (XRF) at NGU for all 13 samples of the first field season. For main element analysis, sample material was first heated to 1000 °C for two hours, and the mass loss on ignition (LOI) was calculated. Then, 0.6g of the sample material was mixed with 4.2g lithium tetraborate ($Li_2B_4O_7$) and melted into a glass tablet. For the trace element analysis, 9.6g sample material was mixed with 2.4g wax and pressed to form the tablet shape. A PANalytical Axios 4kW XRF with Rh X-ray tubes was used for both analyses. Trace element analyses of the 13 samples were also performed using laser ablation inductively coupled plasma mass spectrometry (ICP-MS) by Ø. Skår and T.S. Røhr at NGU using a Thermo Fisher Scientific "ELEMENT XR" with New Wave 193 nm laser. The samples were prepared the same way as for the main element XRF analysis. For more details and detection limits for the chemical analysis, see Appendix C: Chemical Analysis – Methods. Plots of the results were created with the Geochemical Data Toolkit software (Janoušek *et al.*, 2006).

2.7 Chartography and Modelling

As an updated geological map and 3D-model of the Vassygda area were the main focus of this thesis, a wide range of methods were used to achieve this goal. The process started with the collection of previous data from the area, such as field mapping, core logs, and structural observations by Brønnøy Kalk. The gathered data, together with fieldwork and remote sensing, were used to achieve a comprehensive interpretation of the geology and to create a 3D-model using advanced software.

2.7.1 Acquired Data

Brønnøy Kalk has been working on and off with prospecting in the Vassbygda area for several years. However, the focus has been on core drilling and logging of the Stormarka marble deposit. Thirty-two core logs from drill cores drilled between 2013 and 2018 were acquired for this thesis. The drill cores were primarily gathered from Stormarka, with some cores close to Fiskbekken and Mølnvatnet. (fig. 2.3) A total of 7542m were drilled with the cores ranging in length from 50m to 430m. The cores were logged by various employees from Brønnøy Kalk, commonly with a resolution of 5-10cm. This resolution was too high to be represented in the software, so in order to represent the data digitally, a new log was created for each drill core with 10m resolution with the most dominant rock type across the new length interval.

In addition to core logs, data from previous fieldwork (outcrops, measurements, and observations) was acquired and added to the modelling software. This data included work done by A. Kuhn (2010), M. O. Voll and B. K. Storruste (2018), E. Nerhus (2013), and O. Øvereng (2006).

As this master thesis is written in collaboration with Brønnøy Kalk, the rock classification, both for core logs and field observations, is based on the industrial classification seen in Table 2.4. The industrial classification used by Brønnøy Kalk assign marbles based on their quality in terms of whiteness when processed into pigment, mineralogical impurities and grain-size. The three major classes in descending purity are *spotted*, *banded,* and *impure* marble.

The classification used by Brønnøy Kalk provides a good indication of the quality of the marble but is too detailed to be used for a geological interpretation. Therefore, a simplification of the detailed quality-based classification was done to avoid too complicated and often arbitrary boundaries between the different marble types (see chapter 3.2.1 a for detailed descriptions of the marble transitions). The simplification is seen in Table 2.4. Further descriptions of the rock units are seen in chapter 3.2. Some of the challenges with the classification are discussed in chapter 4.2.4.

The quality of the marbles was often noted when mapping. However, the limited time for field mapping and large field area made a detailed mapping of marble quality too time-consuming. Therefore, only changes in macroscopical character and impurities were noted. When accompanied by Siren Ånestad during the summer internship, a handheld GPS was used to map the marble quality according to the codes seen in Table 2.4.

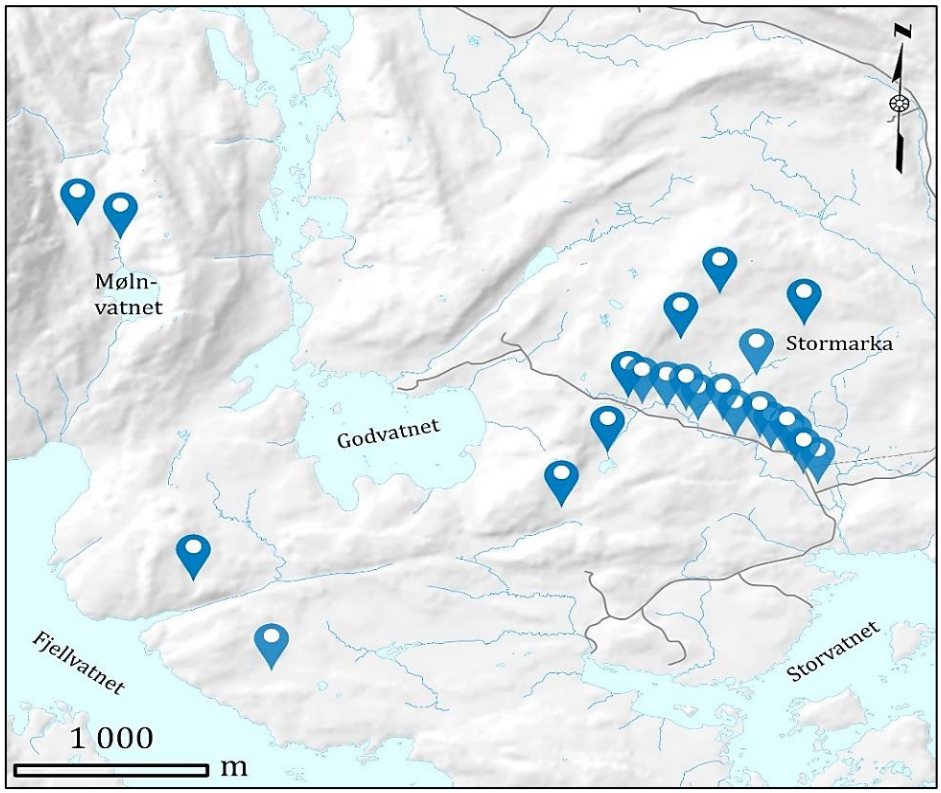

Figure 2.3: Location of drill cores. Background map from norgeskart.no

Table 2.4: The rock classification used by Brønnøy Kalk. The classification codes are shown in grey, with the industrial classification in the right column. In order to simplify the fieldwork, these were reclassified as seen in the left column. ***** Impure marble was also mapped as a siliciclastic metasedimentary rock if rich in silicate minerals. ******White refers to pure calcite marble. *******DOL is often used as a code for everything melanocratic, which may include diabasic dykes, amphibolites/calc-silicates, and skarns.

Field Classification	Standards used by Brønnøy Kalk	
	Code	**Rock Type**
Banded Marble	BAND	Banded Marble
	GREY	Grey Marble
	IMP	Impure Marble*
	SS	Sulphide-spotted Marble
	GM	Mica-marble
Metaarkose/ Metageywacke/ Calc-silicate	SULPH	Massive Sulphides
	GNEISS	Siliciclastic Metasedimentary Rocks
Graphite-Spotted Marble	SPECK	Graphite-spotted Marble
	WHITE	White** Marble
Granite/Diorite or Calc-Silicate Rocks	PEG	Pegmatite / Granite
	DOL	Diabase***

2.7.2 Geological Map

Field observations, outcrop locations, structural measurements, and field photos were directly imported from the iPad into the modelling software, Move 3D. Together with field mapping, some indirect mapping was done by remote sensing of characteristic features based on the underlying rocks.

The generated hillshade image of the DEM dataset was used to map the lithological units based on their topographical contrasts (fig. 2.4 A). This was exceptionally important for the marble occurrences since the densely forested areas yielded few outcrops. Marbles were consistently covered by a thick mixed forest with predominantly Norway spruce.

The characteristic forest cover of the marbles was used as an indirect method of mapping the rock type. The rock units could further be mapped by using measurements of forest types (NIBIO, 2020), together with field observations of which rock types correspond to certain foliage types. Spruce forest usually dominates on marble, whereas mixed and pine forests usually cover siliciclastic sedimentary rocks (fig. 2.4 B).

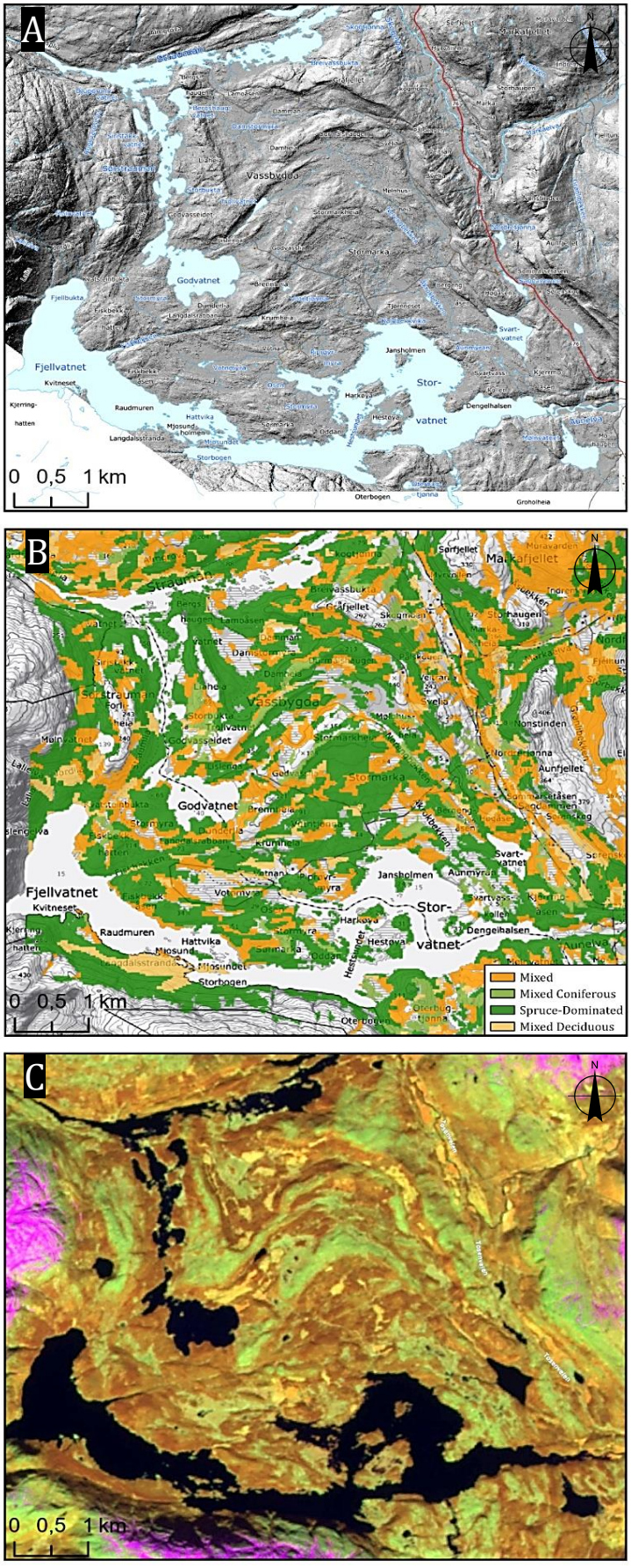

Figure 2.4: Three types of maps used during the creation of the geological map of Vassbygda. **A)** A map using a generated hillshade image from the DEM dataset. **B)** A map showing data on vegetation types provided by laser measurements done by the Norwegian Institute of bioeconomy (NIBIO). The change in vegetation types was used as an indication of changing lithological condition. **C)** A map utilizing the Sentinel-2 satellite data by visualising the terrain by applying a band combination of R: B8A G: B11 B: B04. This differentiates the densely forested areas to the barren edges. Sentinel-2 data from the European Union's Copernicus program. Accessed by the Sentinel Hub EO Browser.

By using the data provided by the Sentinel-2 satellite (Sinergise, 2020), similar distinguishing could be made. It was possible to separate variations in topography, forest types, and general vegetation by combining various frequency bands (fig. 2.4 C). By combining the field data alongside the tools listed above, geological features and rock boundaries were interpreted and drawn as lines in the Move 3D Software. These interpretations were then exported from Move 3D to ArcGis Pro for the final production and visualisation of the geological map.

2.7.3 Structural Analyses and 3D-Modeling

The Move 3D software was used for the primary analysis of the structural data, such as stereonet presentations, contour diagrams, rotation of data, and calculations of mean values and best-fit planes. However, Move 3D lacked features for axial plane calculations, for which the software *Stereonet* (Allmendinger *et al.*, 2011; Cardozo & Allmendinger, 2013) was used. The 3D-model was created to help visualize the marble occurrence of the Vassbygda area with a focus on the Stormarka marble deposits. Move 3D was also used for modelling and data handling for the geological map. This program made it possible to import the field observations and data from the iPad directly. ArcGIS Pro was used for the final map for a better presentation of the results.

Modelling began by using Move 3D's functions to project the 2D rock boundaries onto the DEM- surface. With the lines represented on the topographical surface, cross-sections were created through the most significant structures in the area. The cross-sections were placed as perpendicular to the strike of the rocks as possible (fig. 2.5). The topographical surface (DEM) and the rock boundaries were then marked as intersections on the cross-sections. By using the software's built-in project tool, all dip data within 150m of the section-trace were projected onto the cross-section and adjusted to the corresponding apparent dip angle of the measurements. The drill-core logs were also projected onto the vicinal cross-sections. By using the boundary-intersection as a start-point, the dip data as the tectonic orientation of the rocks, and the core-logs as underground guides, lines representing the continuation of the rocks towards the depth were then drawn.

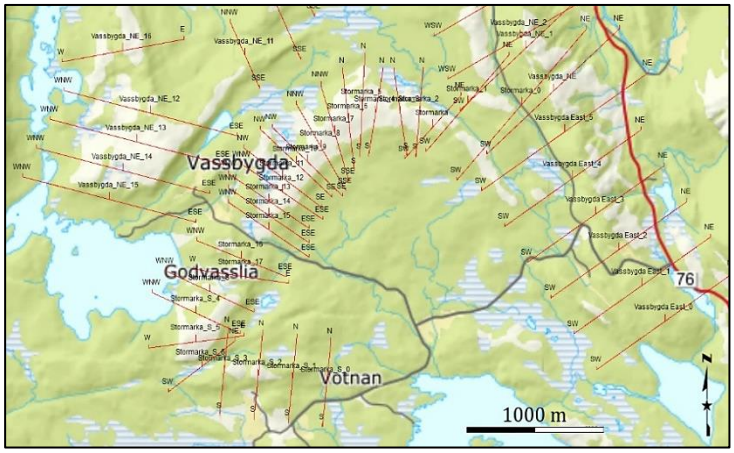

Figure 2.5: Map of cross-sections. The map shows the process of aligning cross-sections to cover the ridges. The profiles are aligned perpendicular to the dip direction of the siliciclastic meta-sedimentary rocks. Background map form norgeskart.no

Cross-sections were placed so that the significant structures had sufficient coverage to combine the cross-sections to a three-dimensional model later. Surfaces were created between the adjacent sections and the lines corresponding to the same rocks by the use of a built-in linear surface tool. A similar tool was used to fill in the spaces between the surfaces to create a rock volume confined to the top of the overlying rock surface. The region-wide 3D-model was made with a depth extent of 500m below sea level. Volume calculations were made using a 200m depth extent to represent the reach of an open-pit quarry better.

3 Results

3.1 Geological Map

The results of outcrop locations and rock types from field mapping are presented in fig. 3.1. It is evident from the figure that the siliciclastic metasedimentary ridges and the shorelines were prioritized due to the abundant outcrops and the ability to follow the rock units to observe transitions and boundaries continuously. Data of rock types and outcrop locations acquired from previous work by Brønnøy Kalk are shown in fig. 3.2 A, whereas structural measurements are shown in fig. 3.2 B. No mapping north of Pålskogen and along the road to Nordfjellmark was done during this thesis. However, measurements from Dumond (2002) and Brønnøy Kalk were used to supplement the northernmost part of the area.

The dataset consisted of 1680 outcrop locations from the fieldwork plus 1243 from Brønnøy Kalk, 815 dip measurements, and 226 lineation measurements. The outcrop observations and structural measurements were used to create and interpret the full geological map seen in fig. 3.3.

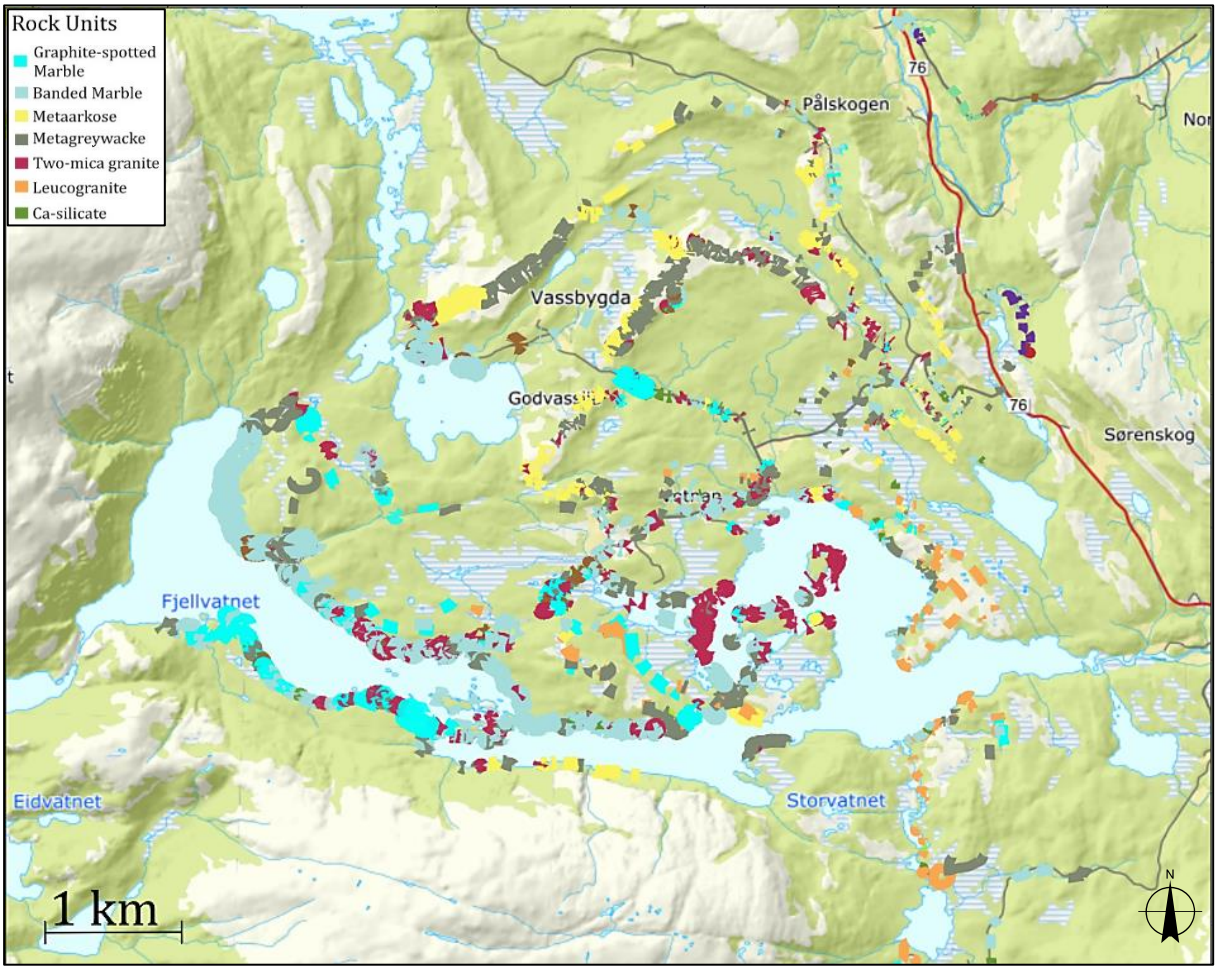

Figure 3.1: Maps of field observations. Each line or dot represents an outcrop with the colour representing the specific rock type. Background map from norgeskart.no

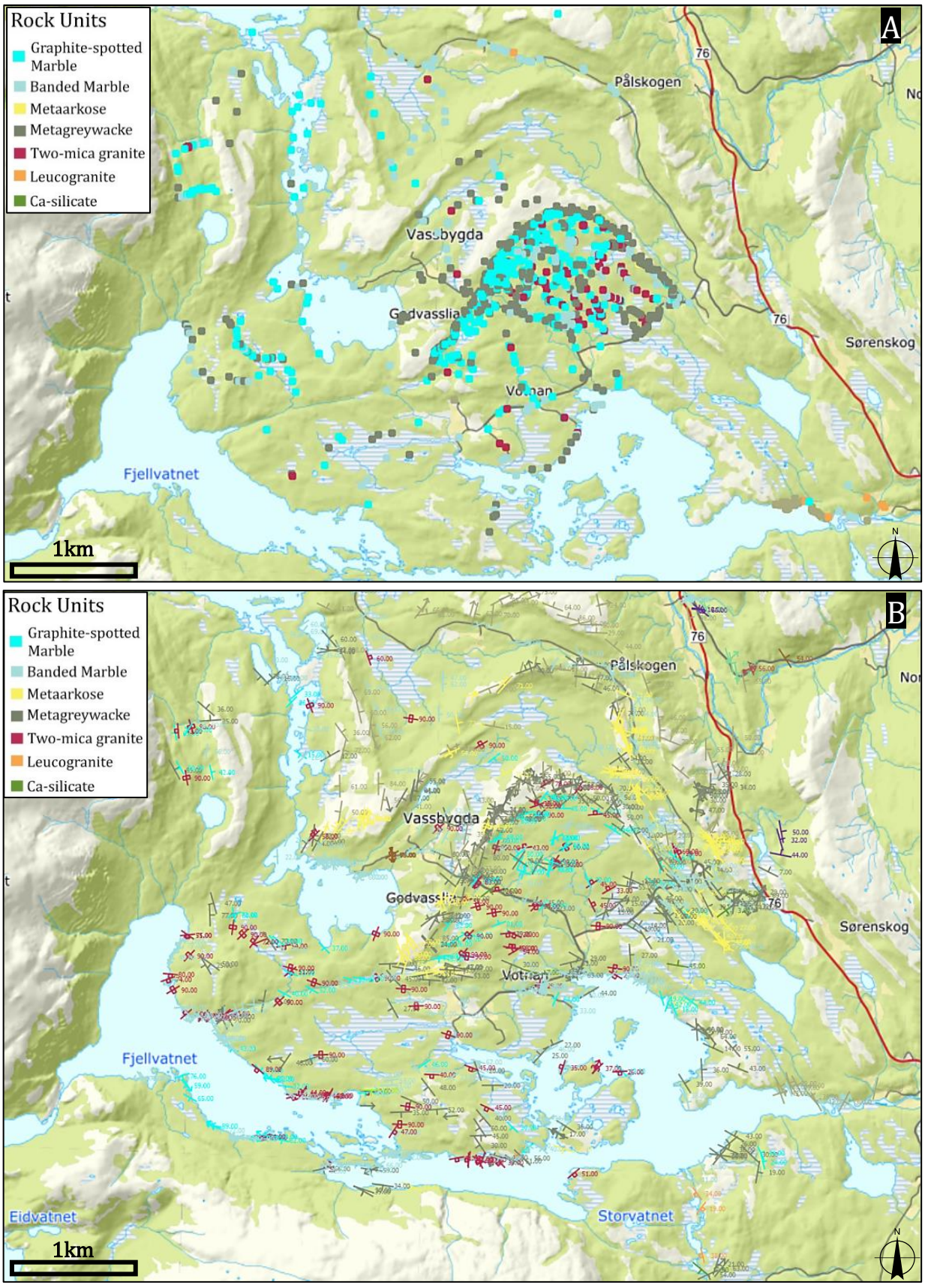

Figure 3.2: . **A**) The acquired data form previous work done by Brønnøy Kalk. The dots represent a GPS-location of an outcrop, and the colour represents the rock type. **B**) Structural measurements obtained from the two field seasons in addition to the acquired dataset from Brønnøy Kalk. Measurements of the siliciclastic metasediments north of Pålskogen from Brønnøy Kalk and Dumond (2002). Map from norgeskart.no

The geological map (fig. 3.3) shows the rock units and structures of the region. Following is a brief description of the most prominent aspects and rock descriptions to indicate the localities and dominance of the units and geometries. For the full descriptions, see the following chapters.

The rocks of the area are seemingly following a north-south trend but are folded or deformed in central Vassbygda. The dominant geometry is the siliciclastic metasedimentary ridges that enclose the banded and graphite-spotted marble. These ridges are folded and pinches out northwest of Svartvatnet. The folding of the Vassbygda metasedimentary rocks is described in chapter 3.7.1 & 3.7.4. Steep mountains of mica-gneisses encircle the lowland of marbles and siliciclastic metasediments.

Layers of high-quality graphite-spotted marble trends north-south from Strauman and are usually sandwiched between siliciclastic ridges and zones of banded marble. The Stormarka marble deposit is surrounded on all sides by siliciclastic metasedimentary ridges and contains a sizeable calc-silicate body. The best quality marble is often located close to the boundary with the siliciclastic metasedimentary ridges or granitic intrusions. This observation makes the Stormarkaa deposit one of the most promising marble occurrences for further exploration (see chapter 4.1.1 for more details).

Since there is no apparent sequential change from the graphite-spotted marble to the banded marble, no exact boundary between them has been drawn. However, zones indicating the overall quality of the marble are shown on the geological map (fig. 3.3). The areas labelled "graphite-spotted marbles" (dark blue) are the areas with the highest density of graphite-spotted marble observations/outcrops and marbles with a similar quality to the graphite-spotted marble (mainly pure calcite marble). The areas labelled banded marble (light blue) are similarly marbles of quality comparable to the banded marble (graphite-banded or siliciclastic bands). Impure marbles are usually confined to transition zones between banded marbles and larger siliciclastic metasedimentary rocks or zones too small to include in the geological map. This combination of marble types was done to represent the geological aspect of the area better, although this was at the expense of a detailed map of marble qualities.

The contact between the Lower and Middle nappe is characterized by a reactivated thrust fault and proximal parallel layers that do not seem to be affected by the same geometry of the Vassbygda ridges. This is interpreted as a large shear zone and named the Heggfjord-Tosen shear zone (HTSZ). The shear deformation is described further in chapter 3.7.2. Small ultramafic lenses occur in the shear zone at the base of the overlying Middle nappe.

The most extensive granitic intrusions are found on the Dengelhalsen peninsula, where leucogranitic sills emanating from the intrusion is seen on all shores of Storvatnet. A smaller porphyric granite is found close to Mellomenget. Although smaller magmatic intrusions dominate the area, these are the only two large enough to be included on the geological map.

The structural complexity of the Vassbygda region gave the areas with few to none outcrops a high degree of uncertainty. Using the topography (DEM), forest types, or satellite imaging, estimations could be made regarding the surface expression of the rocks. The area south-east of Svartvatnet and east of Storvatnet are areas of high uncertainty due to the lack of observations. Here, the overall trend of the rocks measured on the eastern side of Stormarka is believed to continue along the Lower–Middle nappe boundary.

Figure 3.3 (**next page**): Proposed geological map of the Vassbygda region.

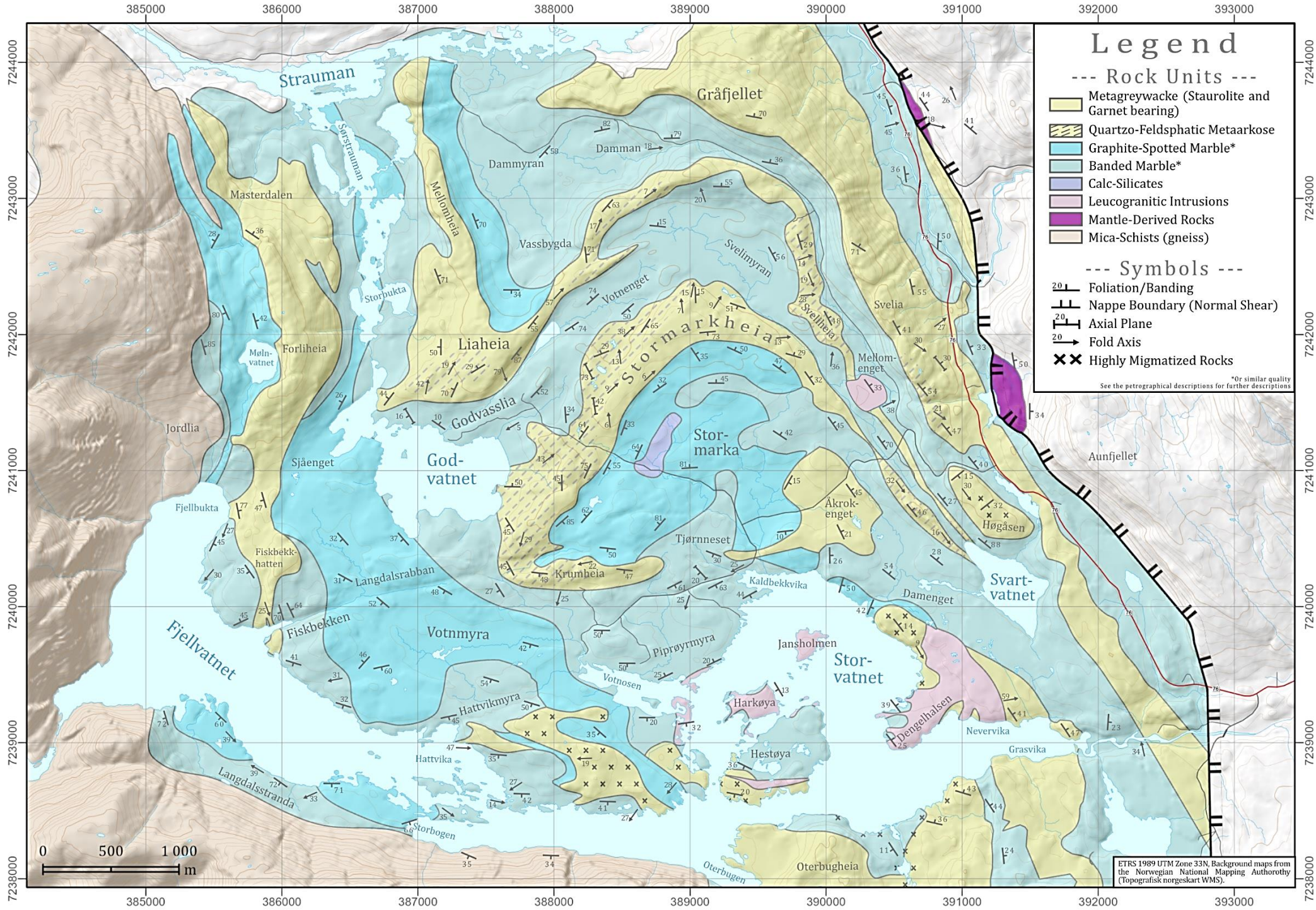
Legend
--- Rock Units ---
Metagreywacke (Staurolite and Garnet bearing)
Quartzo-Feldsphatic Metaarkose
Graphite-Spotted Marble*
Banded Marble*
Calc-Silicates
Leucogranitic Intrusions
Mantle-Derived Rocks
Mica-Schists (gneiss)
--- Symbols ---
Foliation/Banding
Nappe Boundary (Normal Shear)
Axial Plane
Fold Axis
Highly Migmatized Rocks
*Or similar quality
See the petrographical descriptions for further descriptions
Strauman
Søstrauman
Gråfjellet
Damman
Dammyran
Masterdalen
Mellomheia
Vassbygda
Svelimyran
Storbukta
Votnenget
Svelia
Svellheia
Liaheia
Stormarkheia
Mellom-enget
Forliheia
Møln-vatnet
Godvasslia
Jordlia
Stor-marka
Aunfjellet
Sjåenget
God-vatnet
Åkrok-enget
Fjellbukta
Høgåsen
Tjørnneset
Fiskbekk-hatten
Langdalsrabban
Krumheia
Kaldbekkvika
Svart-vatnet
Damenget
Fiskbekken
Votnmyra
Piprøyrmyra
Jansholmen
Fjellvatnet
Stor-vatnet
Votnosen
Harkøya
Hattvikmyra
Dengelhalsen
Nevervika
Hattvika
Hestøya
Grasvika
Langdalsstranda
Storbogen
Oterbugen
Oterbugheia
0 500 1 000 m
ETRS 1989 UTM Zone 33N, Background maps from the Norwegian National Mapping Authorothy (Topografisk norgeskart WMS).
385000
386000
387000
388000
389000
390000
391000
392000
393000
7244000
7243000
7242000
7241000
7240000
7239000
7238000

3.2 Petrographical Descriptions

The rock types of Vassbygda may be divided into two distinct categories: Metasedimentary and igneous rocks. The metasedimentary rocks consist of alternating sequences of siliciclastic and carbonate rocks. These alternating sequences may be as narrow as only a few millimetres, or as broad as several 10s of meters. The large ridges surrounding Vassbygda consist mainly of siliciclastic metasedimentary rocks and appear more coarse-grained than the smaller sequences found within the lowland marbles. Intrusions of plutonic to sub-volcanic rocks appear within the metasedimentary rocks throughout the area. In addition to the two dominant rock categories, several smaller bodies of calc-silicates and ultramafic rocks infrequently occur within the area. In the following sub-chapters, detailed field- and mineralogical descriptions of each significant rock unit are presented.

3.2.1 Marbles

The marbles span a wide range of both physical and mineralogical appearances. The transition between marble type is often abrupt and may change over just a few meters. They may also transition gradually, often observed between the graphite-spotted marble and the banded marble, where the transition maybe 10s of meters. Banded marbles are the most common type and are found throughout the field area. The spotted marbles often occur as zones within the banded marbles. The contacts between other rock units (especially larger siliciclastic metasedimentary or igneous bodies) are often dominated by coarse-grained graphite spotted marble. The marbles are typically white to grey but are usually tainted slight yellow/brown by erosion.

The goal for the industrial processes is a raw material as close to 100% calcite as possible. Sulphides and oxides prove especially bad for the final whiteness of the product. The majority of the marbles contain graphite: The banded marbles commonly contain fine-grained graphite oriented in bands, whereas the graphite-spotted marbles usually contain medium to coarse-grained single crystals or graphite aggregates. However, given the right grain size and geometry, this graphite can be removed during crushing and processing. Sulphide rich marbles are labelled “Sulphide marble” and are regarded as too impure for production into pigment.

The determination and mapping of marble type (and quality) was an essential focus of this thesis in order to provide Brønnøy Kalk with a detailed description of the marble deposits to help clarify the available calcite resource in Vassbygda. The following sub-chapters provides detailed descriptions of the significant marble types found within the field area.

3.2.1.1 Graphite-Spotted Marble

The spotted marble is characterized by medium- to coarse-grained, equigranular, white calcite crystals with grain aggregates (or rarely single laths) of graphite occurring as spots throughout the rock (fig. 3.4 A & B). Some zones contain graphite crystals up to 3cm; however, these are rare. The graphite aggregates are frequently void of any preferred orientation, although some sections close to the transition into banded marble begin to show a preferred orientation to the banding. The calcite grains commonly show type 1 deformation twinning (Burkhard, 1993), as illustrated in fig. 3.4 B. The weathered appearance of the graphite-spotted marble is grey to greyish brown, which usually looks unfavourable with regards to the quality of the marble. A fresh surface is necessary to determine the quality.

Quartz and opaques are common accessory minerals (fig. 3.4 B, quantified by the AMS results: Table 3.6). Sulphides (mainly pyrite, pyrrhotite, and chalcopyrite) may occur as very fine to fine-grained fully-grown single crystals or aggregates (fig. 3.5 B), which is often tricky to distinguish from graphite. Sulphides give the marble a characteristic smell when crushed and could be used together with a slight yellow colour to indicate the presence of fine-grained sulphides. The zones of the spotted marble are dominated by sulphides and are coined "sulphide-spotted marble" by Brønnøy Kalk. These marbles are assigned to the lowest quality due to a yellow discolouration of the final pigment. The marble may also contain white mica, which shows a similar spotted appearance as the graphite-spotted marble (fig. 3.5 A). These marbles are also challenging to differentiate due to the often fine grain-size of the mica crystals. Mica-dominated marbles are commonly named "mica-marble" and are of poor quality due to problematic processing (Storruste, personal communication, 2020).

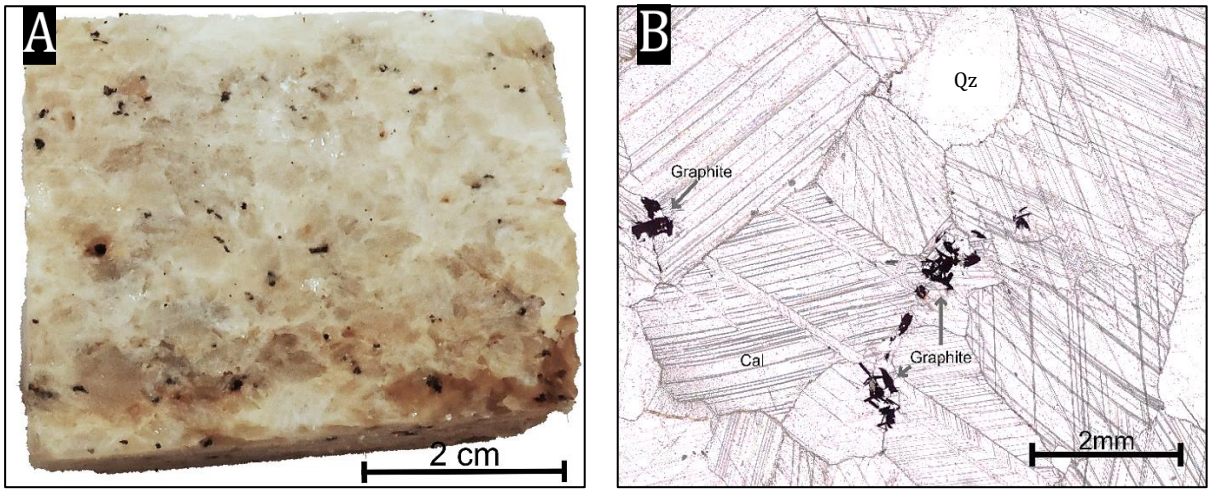

Figure 3.4: Graphite-spotted marble (sample BC-04). **A**) Characteristic hand sample appearance of the medium-grained graphite-spotted marble. **B**) Micrograph of the same rock. Calcite with type 1 deformation twinning (Burkhard, 1993) is the dominant mineral. Laths of graphite and minor quartz crystals are common accessory minerals. The smaller laths of graphite occur along grain boundaries and rarely within calcite grains.

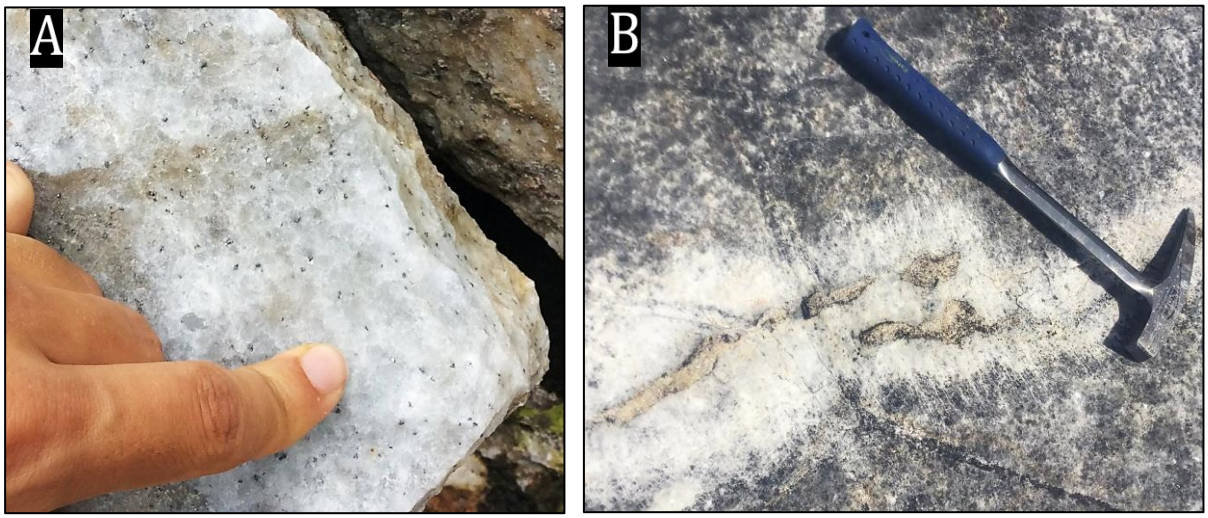

Figure 3.5: Different "spots" in the spotted marble. **A**) Marble with small spots of white mica, often hard to differentiate from the fine-grained graphite. This type is named mica-marble by Brønnøy Kalk. **B**) Large aggregates of sulphide minerals form small, irregular bands in the spotted marble. The grey weathering surface of the marble is not visible close to the sulphide bands. Marbles with a large content of sulphides are named sulphide-spotted marbles by Brønnøy Kalk.

A pure calcite marble without any mesoscopic impurities or graphite crystals is named “white” marble due to the homogenous white colour. This marble is of excellent quality and infrequently occurs throughout the area. Although the mesoscopic appearance of the white marble is homogenous, small silicate minerals can be seen when using a hand lens. The white marble was mapped in the same category as the graphite-spotted marble due to their similar quality and because white marble is often confined to small zones in the graphite-spotted marble. The most massive outcrop of white marble is found on the shore close to Langdalsstranda (fig. 3.3).

A correlation between the grain-size of the graphite-spotted marble and the proximity to magmatic intrusions was observed during the fieldwork: The graphite-spotted marble proximal to the granitic intrusions (especially visible in between the leucogranitic sills surrounding Storvatnet) is consistently coarse-grained, often with large single crystals of graphite or large graphite grain aggregates. The zone of increased grain-size is usually 2-5m and is related to the intrusion size. The correlation between grain-size and proximity to intrusions is present, even if an otherwise fine-grained banded marble dominates the area.

3.2.1.2 Banded Marble

Banded marbles are the most common marble type in the field area. “Banded marble” is the term given to marbles with typical parallel bands of darker colour, as seen in fig. 3.6 A, B & C. The darker bands consist of silicate minerals such as white mica, quartz, feldspar, and calc-silicate minerals. The silicate minerals are commonly aphanitic to fine-grained. Banding also occurs with fine-grained graphite laths. The bands are in the range of a few millimetres up to several dm wide. The banded marble is consistently fine- to medium-grained, often without any visible calcite crystals. However, the banded marble may occur coarse-grained close to, or bordering, magmatic intrusions.

The banded marble commonly shows a brownish-grey colour on fresh surfaces, likely due to the sulphide content, and a dark grey to greyish-blue weathering surface. The silicate bands often protrude from the marble surface, as seen in fig. 3.6 C & D and 3.7 B. Areas between the bands of silicate minerals is often consisting of relatively pure calcite.

The grey to dark grey colour of the banded marble, alongside the small grain-size, makes the appearance similar to that of some Calc-rich siliciclastic metasedimentary rocks. The transition between siliciclastic carbonate-rich rocks and poor quality silica-rich marble was often characterized by a gradual influx of more carbonates/silica, such that the precise rock boundaries were difficult to establish.

A variant of the banded marble is named “grey” based on the homogenous appearance and grey colour. The grey marble is fine-grained, equigranular, and without any mesoscopic impurities. The grey marble occurs sporadically throughout the field area and is always seen as small zones within the banded marble. The grey colour of the rock has not been determined, although theories of trapped gas or microscopic impurities have been proposed (Sandøy, 2003; Storruste, personal communication, 2020).

The layers of silicate minerals are commonly deformed with a dominant isoclinal folding with a typical recumbent or steeply-dipping axial plane (fig. 3.6 B, and 3.7 B & C). The folds in the marble may be rootless, commonly observed within layers with high rheological contrast such as calc-silicate layers or mafic dykes (fig. 3.7 C). In addition, strongly boudinaged or imbricated layers are frequently observed (fig. 3.6 D, 3.7 A). The deformation is mainly observed within the silicate

mineral layers or intrusions in the marble, whereas the marble is seemingly little deformed. The deformation observed within the marble is usually the infilling of boudin necks (fig. 3.7 A). Further elaborations into these structural observations are found in chapter 3.7.

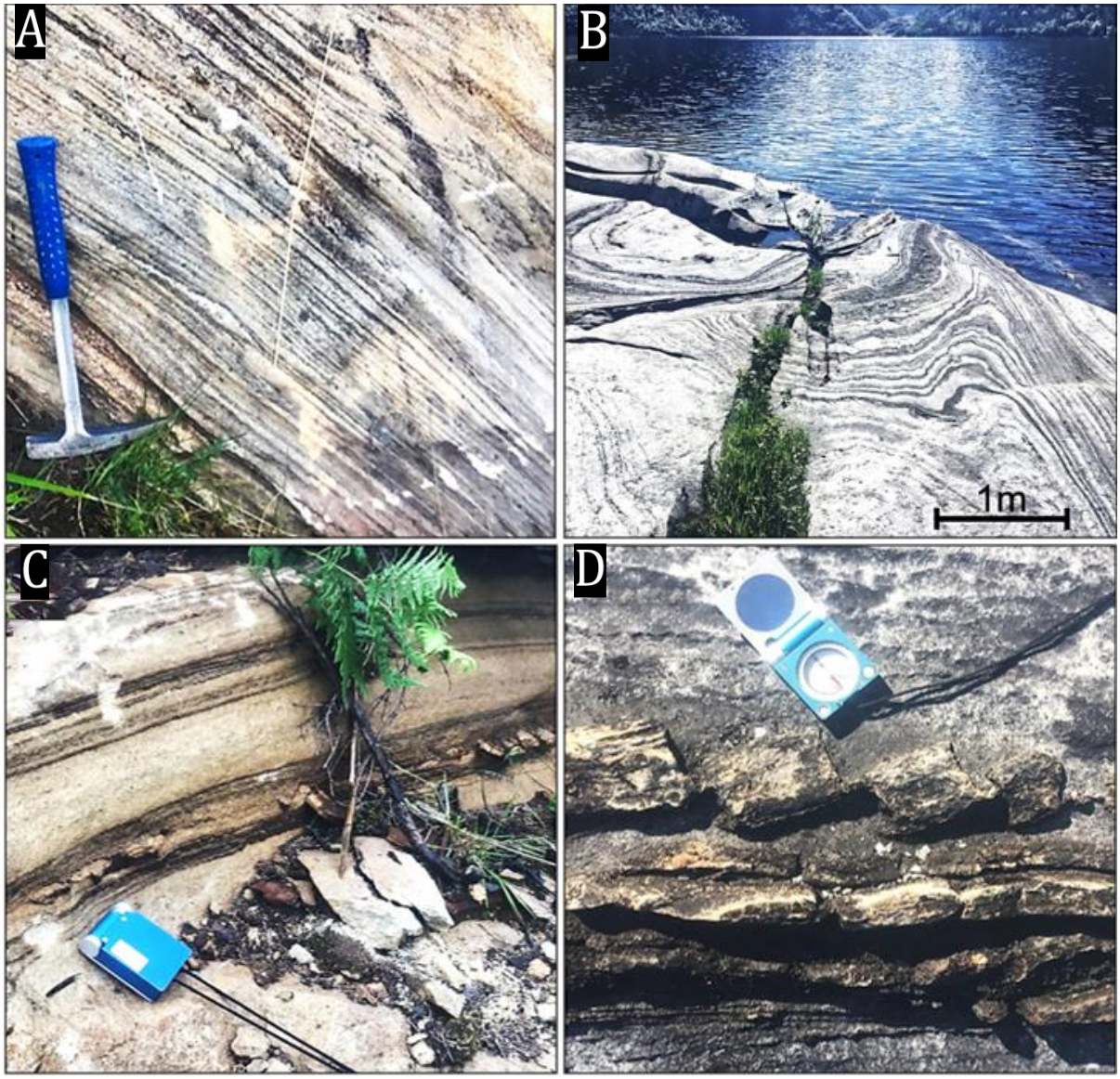

Figure 3.6: Examples of banded marble. **A**) Poor quality banded marble with bands of dark silicate minerals. The appearance can often be confused with some metaarkose rocks. **B**) Layers of siliciclastic sediments folded to tight, shallowly plunging folds within the marble. **C**) Fine-grained banded marble with larger clasts of clastic sediments and fine layers of darker minerals. **D**) Typical imbricated bands or boudins of silicate minerals. Little deformation is observed within the marble.

Figure 3.7: Pictures of typical deformation of siliciclastic sediments or magmatic intrusions in the banded marble. **A**) Bouidinaged layer of siliciclastic sediments with asymmetrical (sigma)clasts. **B**) Small folded layer of silicate minerals. The folds are isoclinal to very tight, often overturned, with shallowly dipping to sub-horizontal fold axes. **C**) Rootless fold of a small mafic intrusion.

The Heggfjord–Tosen shear zone (HTSZ) occurs in the northeastern part of the field area. This zone contains highly deformed marbles (see chapter 3.7.2 for further descriptions). Acid test on these marbles indicates dolomitic composition, which is also confirmed by the chemical analysis (Table 3.2). A highly foliated calc-mylonite also occurs close to the Lower–Middle nappe boundary. The microscopic structures of these marbles show extensive type 2 deformation twinning (Burkhard, 1993) and zones of shape-preferred orientation of carbonate grains (fig. 3.8 A). Silicate layers within this marble are highly deformed, commonly boudinaged and isoclinal folded (fig. 3.40). The folds are often rootless and are often deformed to the point of complete separation of continuous layers, leaving only the hinge zones of folds (fig. 3.7 C). Marbles with the deformed noncontinuous fragments often resemble a conglomerate (fig. 3.8 B). Asymmetric clasts (fig. 3.8 C) are also common in this marble. This calc-mylonite is regarded as the uppermost rock of the Lower nappe and occurs near the contact between the Lower and Middle nappe (Thorsnes & Løseth, 1991). This contact is further described in section 3.7.2.

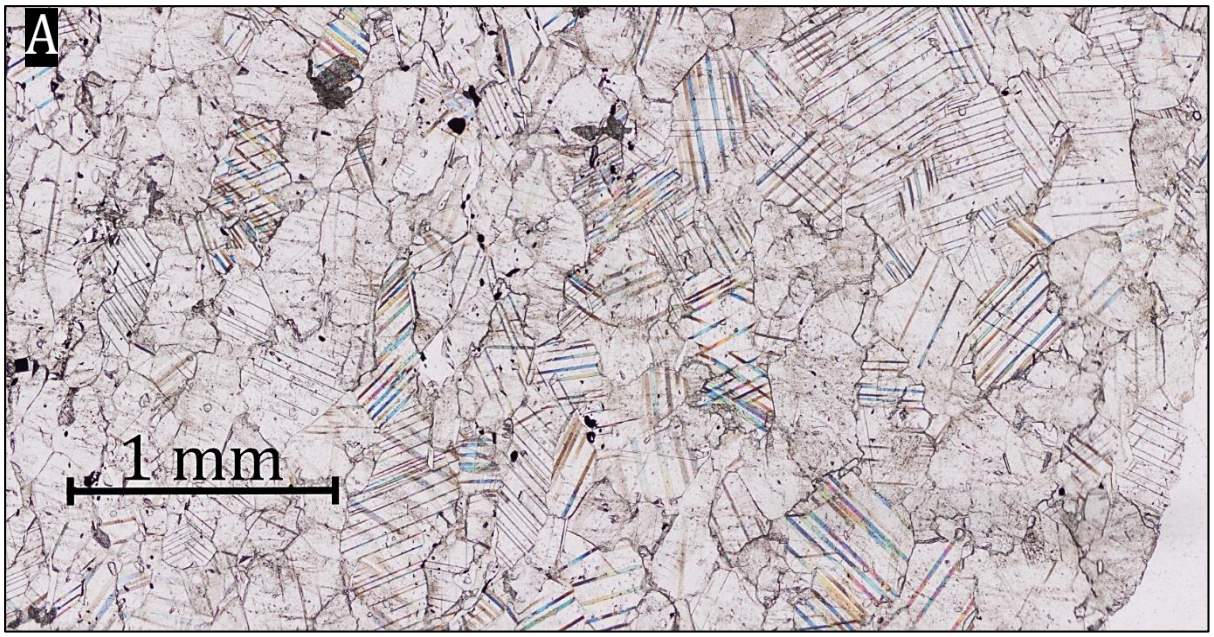

Figure 3.8: **A**) Micrograph (ppl) of the highly deformed marble in the HTSZ. The dolomite/calcite grains show extensive type 2 deformation twinning (Burkhard, 1993). The marble in the shear zone contains only a few grains of sulphides.

B) Highly deformed marble with siliciclastic sequences mangled into resembling a conglomerate. This rock occurs just below the boundary between the Lower and Middle nappe, although similar, less deformed banded marbles can be found throughout the field area. Hammerhead is 16 cm long.

C) Calc-mylonite shear zone close to the contact between the Lower and Middle nappe. Picture taken towards southwest. A sigmoidal clast (~20 cm long) indicates top-to-the southeast normal displacement, although several asymmetrical isoclinal folds close by indicates top-to-the northwest movement (3.40).

3.2.2 Siliciclastic Metasedimentary Rocks

Three different types of siliciclastic metasedimentary rocks are present within Vassbygda: 1) A light grey to grey metaarkose, 2) a dark brown to grey metagreywacke, and 3) a grey to black gneissic mica-schist. The metagreywacke and metaarkose often occur as larger separate lithologies. However, they also occur as smaller layers within each other, or as larger zones with a gradual transition between the two types. Where possible, the rock was mapped either as metagreywacke or metaarkose. However, due to the difficulties of determining the type, or the metagreywacke was chosen on the geological map (fig. 3.3) due to the dominance of this rock. Where possible, the metaarkose-dominated areas were marked as dashed lines on the map.

The gradual and sequential transition between the marbles and the siliciclastic metasedimentary rocks was often challenging to map. The transition is commonly several 10s of meters wide, giving a certain amount of uncertainty of the actual boundaries drawn on the geological map. If the complete transition was seen, the border was drawn in the middle. Hillshade, topography, or the change of forest type were used on poorly exposed areas to establish the transition indirectly. The boundary was placed between two measurements of different rocks if no transition could be seen or interpreted by external factors.

Migmatization is commonly observed in all siliciclastic metasedimentary rocks but is most evident in the metaarkose, where the rock contains both cross-cutting (fig. 3.9 A) and foliation-parallel (fig. 3.9 C) leucosomes. Migmatization is commonly associated with intrusive dykes and sills (fig. 3.9 B). The rock may also appear mostly melted, with only xenoliths remaining in more massive dykes/sills (fig. 3.18).

The leucosomes are fine-grained (often aphanitic) white to pale brown. The small grain-size makes it challenging to observe the mineralogical composition, although some quartz and feldspar grains can be seen in coarser-grained sections. Garnets may occur in leucosomes within mica-rich metasedimentary rocks (fig. 3.17 A). The leucosomes are often deformed and frequently cut by later granitic dykes (fig. 3.9 D).

Optical microscopy revealed that the leucosomes are characterized by zones of plagioclase and quartz that cuts the previous fabric of the rock. They may contain minerals from the host rock as trapped grains– usually muscovite grains or fine needless of sillimanite. A description of the microscopical textures of the leucosomes is seen in fig. 3.12 B & C and described with sample BC-16 in Appendix A.

The amount of migmatization of the siliciclastic metasedimentary rocks was also the cause for uncertain mapping. The highly migmatized rocks were often mapped as the visible host rock with symbols (**X**) marking the high degree of migmatization on the geological map (fig. 3.3). The areas with little to none host rock remaining were mapped as the magmatic leucogranite. This was only observed on a small hill east of Mellomenget and the lager Dengelhalsen intrusion.

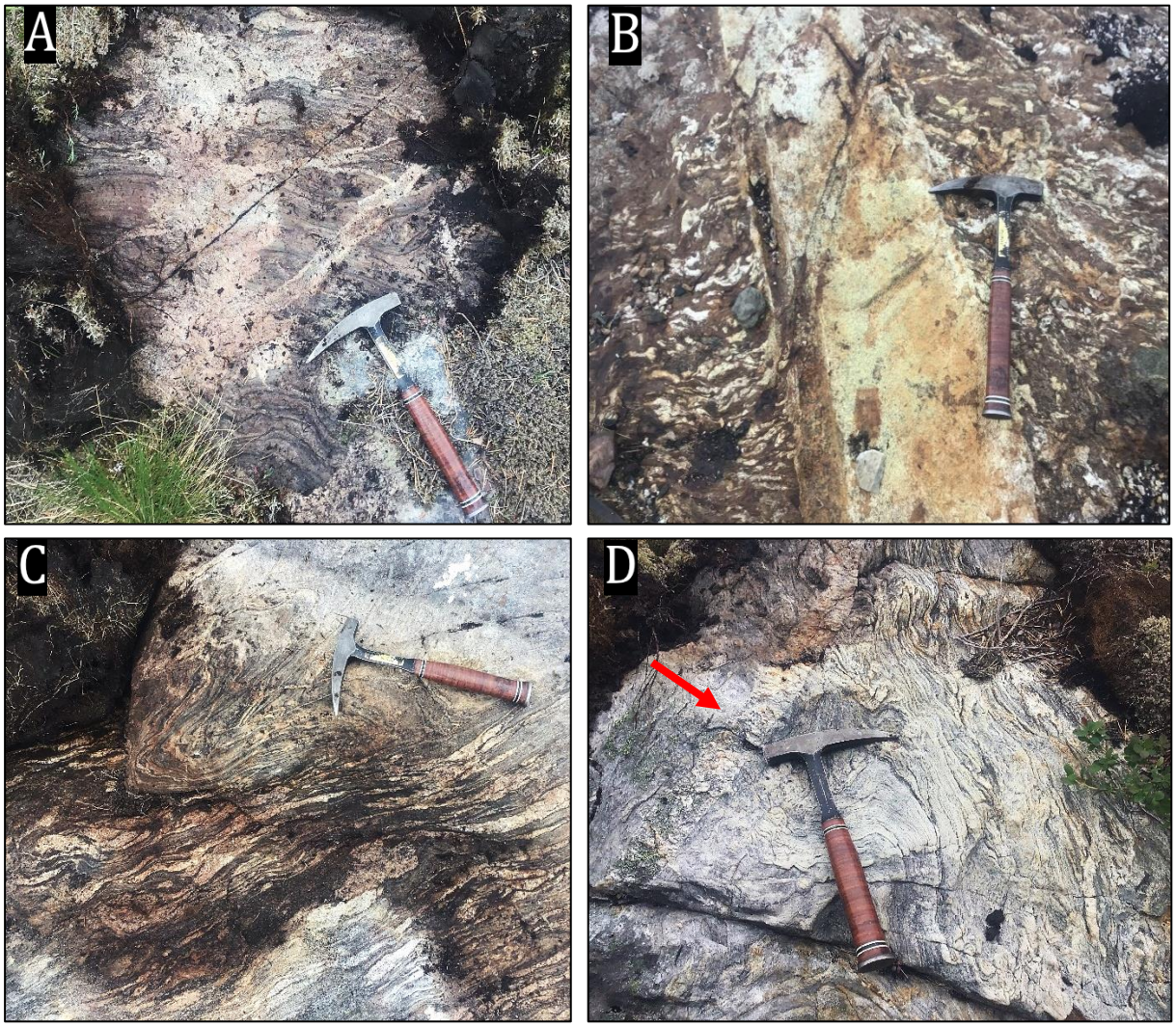

Figure 3.9: Migmatization of the metaarkose rocks. **A**) Leucosomes cut the laminated bands of biotite. **B**) Granitic intrusion and migmatization of the host rock. **C**) Foliation-parallel, mingled leucosomes. **D**) Migmatized metaarkose, which is later cut by a granitic dyke (red arrow).

3.2.2.1 Metaarkose

The metaarkose is a light grey to grey, fine- to medium-grained, equigranular, foliated rock (fig. 3.10 A), consisting of quartz, feldspar, biotite, and minor muscovite (fig. 3.10 B). Garnet may rarely occur as single ruby-red crystals or in more massive clusters. Although similar to the metagreywacke, the typical quartzofeldspathic mineral assemblage of the metaarkose was easily differentiated from the mica-rich composition of the metagreywacke. The metaarkose often occurs as small sections within the metagreywacke. However, some more extensive bodies of metaarkose are observed along the northeastern side of the Stormarka ridge and most of the Svealia ridge (fig. 3.3). It is also common on the southern shores of Storvatnet.

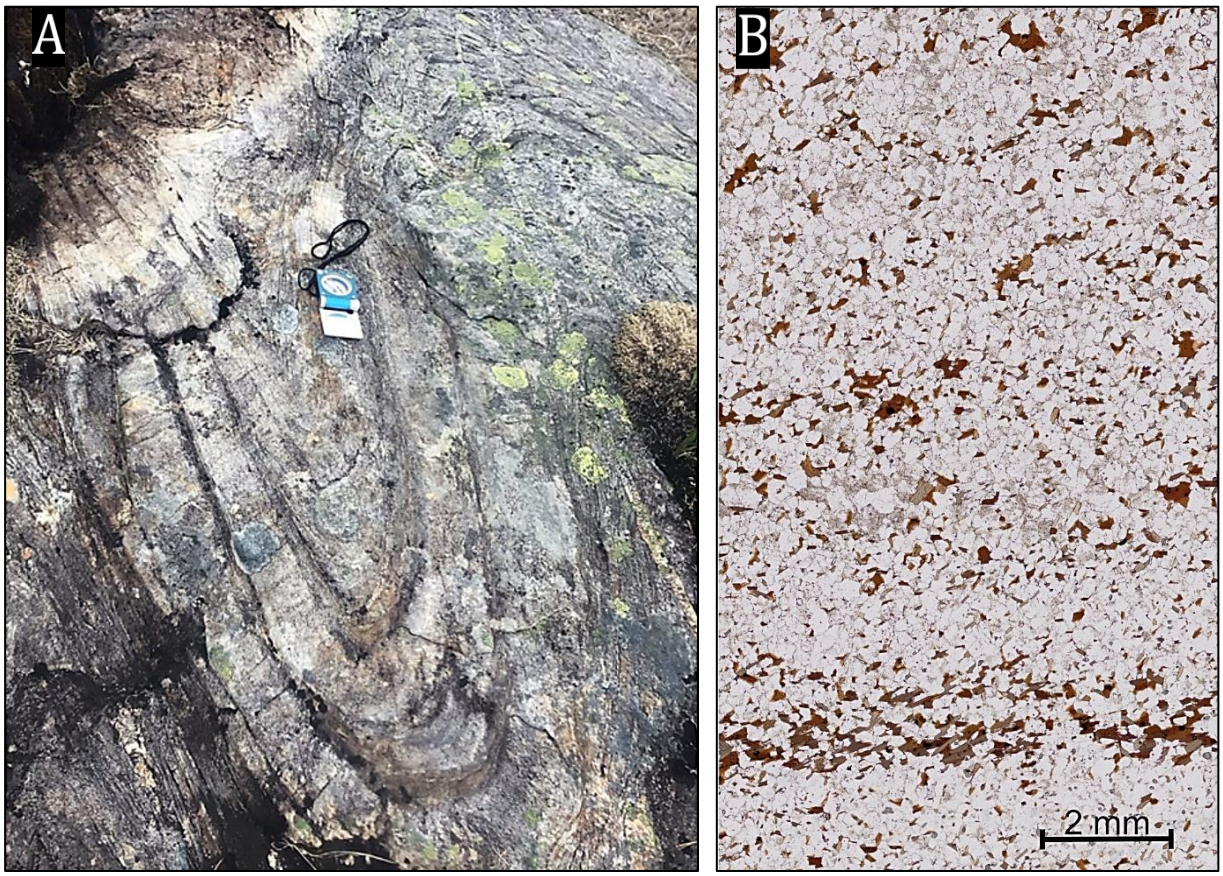

Figure 3.10: Macro- and microscopic image of the metaarkose. **A**) Typical field appearance of the metaarkose with a characteristic isoclinal fold. **B**) Ppl micrograph of the metaarkose (BC-02). Bands of the dominant minerals (quartz, feldspar and biotite) form the observed foliation.

3.2.2.2 Metagreywacke

The metagreywacke is often melanocratic to mesocratic, grey to light grey, fine- to medium-grained, inequigranular with foliation of biotite, muscovite, and sillimanite (fig. 3.12 A). The foliation planes are separated by 0.2 – 0.5 cm zones of quartz and feldspar. The largest quartz grains show extensive sub-grain formation, with surrounding smaller recrystallized grains.

Two generations of muscovite crystals are observed: A euhedral muscovite phase has overgrown anhedral muscovite crystals. The euhedral phase is commonly also overgrowing biotite crystals (fig. 3.12 B & C). The anhedral muscovite includes fibrolite needles within the core of the mineral. These needles are not found within the euhedral muscovite. Fibrolite is also found within garnets together with small biotite laths. It seems that the garnet, the anhedral muscovite, biotite, and sillimanite are in equilibrium based on the mineral textures and that the euhedral muscovite represents a later mineralogical assemblage. This is further elaborated in chapters 3.6.1 and 4.3.1.

The metagreywacke is the most dominant siliciclastic metasedimentary rock of the field area. The field appearance of the metagreywacke is characterized by a dark brown to grey weathering surface (fig. 3.11 A) and clearly developed foliation (fig. 3.11 B). The foliation is generally more developed than the foliation of the metaarkose, likely related to the higher mica content of the metagreywacke. The rock is often gneissic with abundant isoclinal folds and often occurs with thin lamina of metaarkose (fig. 3.11 B). The rock is often aphanitic with only some visible biotite grains. It can, therefore, be challenging to distinguish it from the metaarkose. Brownish red to dark pink garnets (~0.3cm) frequently occur (fig. 3.12 B), with a "warty" appearance on some surfaces. The metagreywacke frequently transitions into a mica-schist, typically in the southwestern field area. The mica-schist type also occurs periodically in proximity to more massive magmatic intrusions, especially the leucocratic intrusion at Dengelhalsen (fig. 3.3).

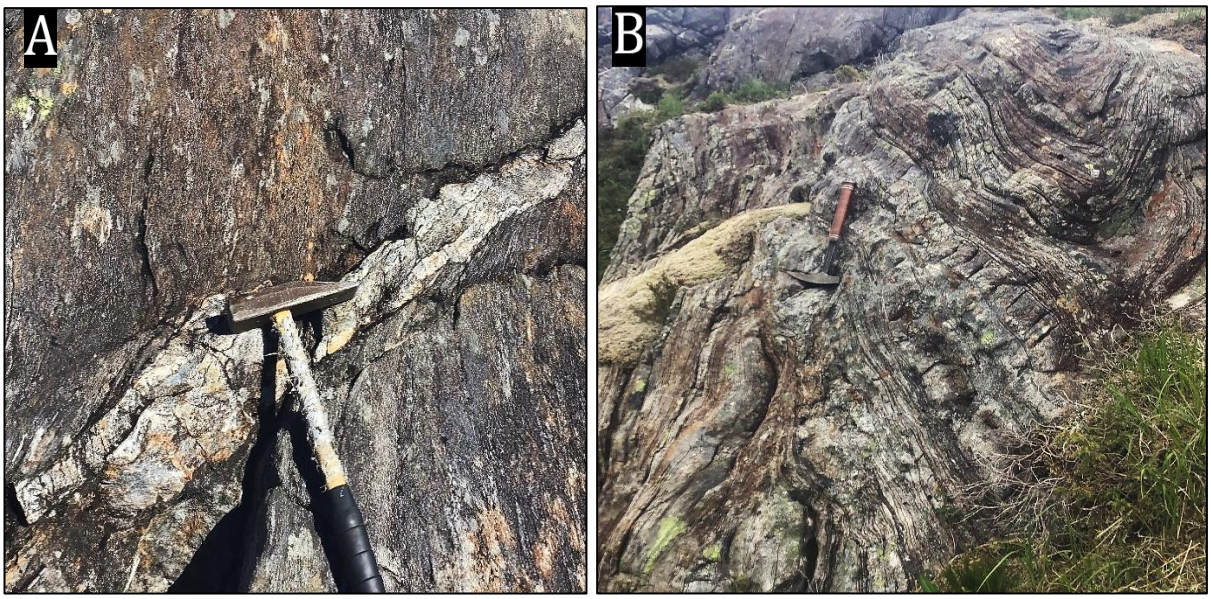

Figure 3.11: Pictures of metagreywacke. **A**) Characteristic brown to grey field appearance of metagreywacke. A small dioritic dyke cuts the foliation of the metagreywacke. **B**) Strongly foliated and isoclinal folded layers of metagreywacke (brown) and metaarkose (light grey).

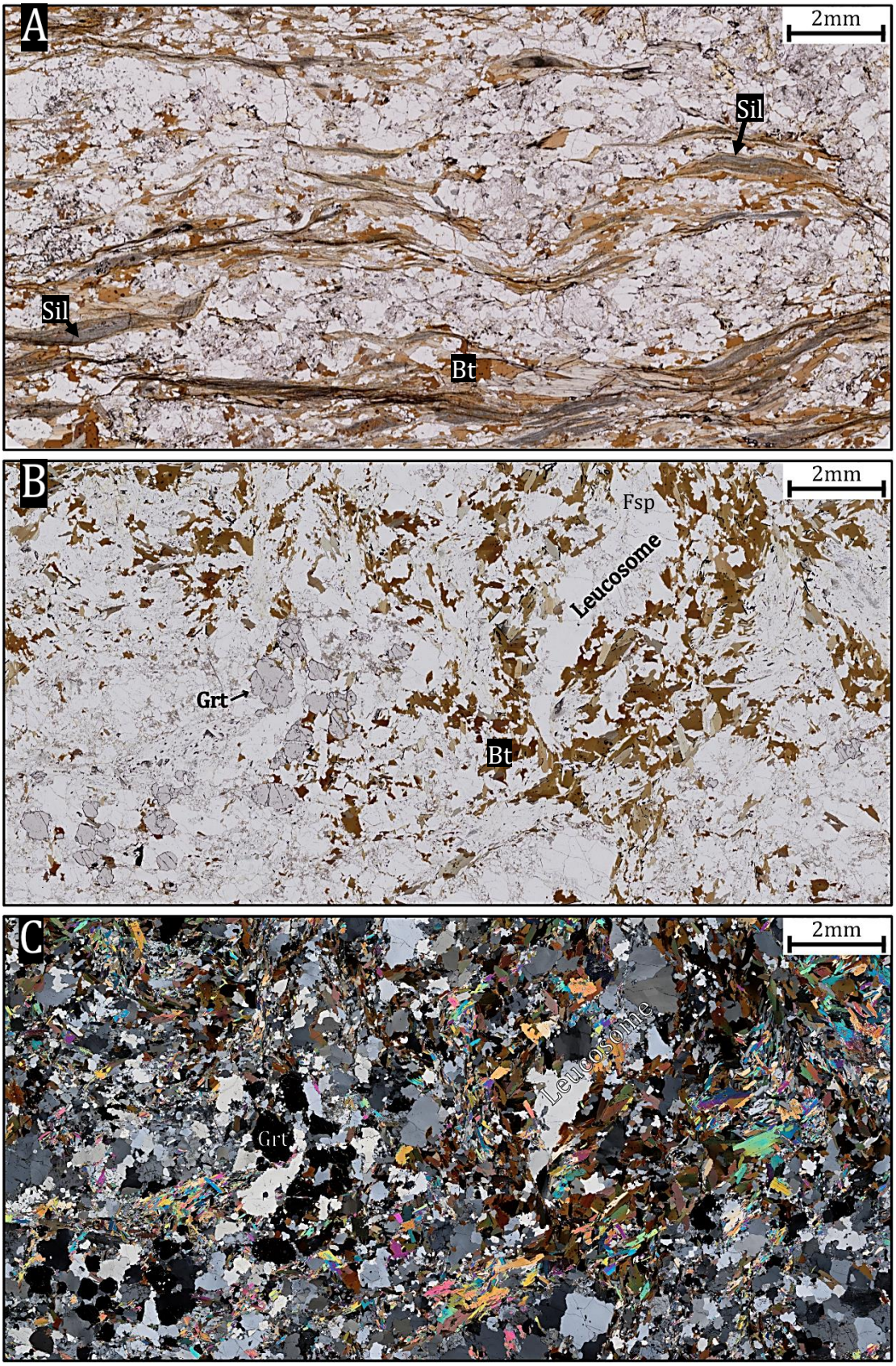

Figure 3.12: Ppl micrographs of the metagreywacke. **A**) The most common type of metagreywacke (BC-03). The rock consists of laminated biotite, muscovite and sillimanite (fibrolite), with quartz, biotite, and feldspar being the main elements, with minor titanite. **B**) PPL micrograph of a garnet-bearing foliated (mica-schist) metagreywacke (BC-16). Leucosomes is seen on the microscopical level, as indicated in the picture. **C**) XPL micrograph of the same section shown in picture B.

3.2.2.3 Mica-Schist (Mica-Gneiss)

The mica-schist/mica-gneiss occurs on the southern part of Storvatnet and southern and western Fjellvatnet. It is the dominant rock type of Stortuva and Hardangsfjellet (fig. 1.3). The rock is dark grey to grey, fine to medium-grained, inequigranular, and consists mainly of quartz, feldspar, and mica, with minor garnet, (cm-scale) calcite lenses, and leucosomes (fig. 3.13 A). A prominent foliation is characteristic, and a clear gneissic texture is often observed. Extensive migmatization of the mica-schist occurs on the eastern side of Storvatnet. Several generations of granitic dykes cut the foliation. These dykes are later deformed (fig. 3.13 B).

Although this rock shows similarities with the mica-schist variant of the metaarkose, this rock was separated due to the clear gneissic texture and larger mica grains. It was also evident that this rock is the dominant type found within the steep mountains surrounding Vassbygda to the south and west, indicating different lithological properties and thickness than the relatively flat and narrow ridges of metagreywacke and metaarkose within Vassbygda. No sample was collected from the rock type, which means no microscopical analysis exists to clarify the mica-schist and the metagreywacke differences.

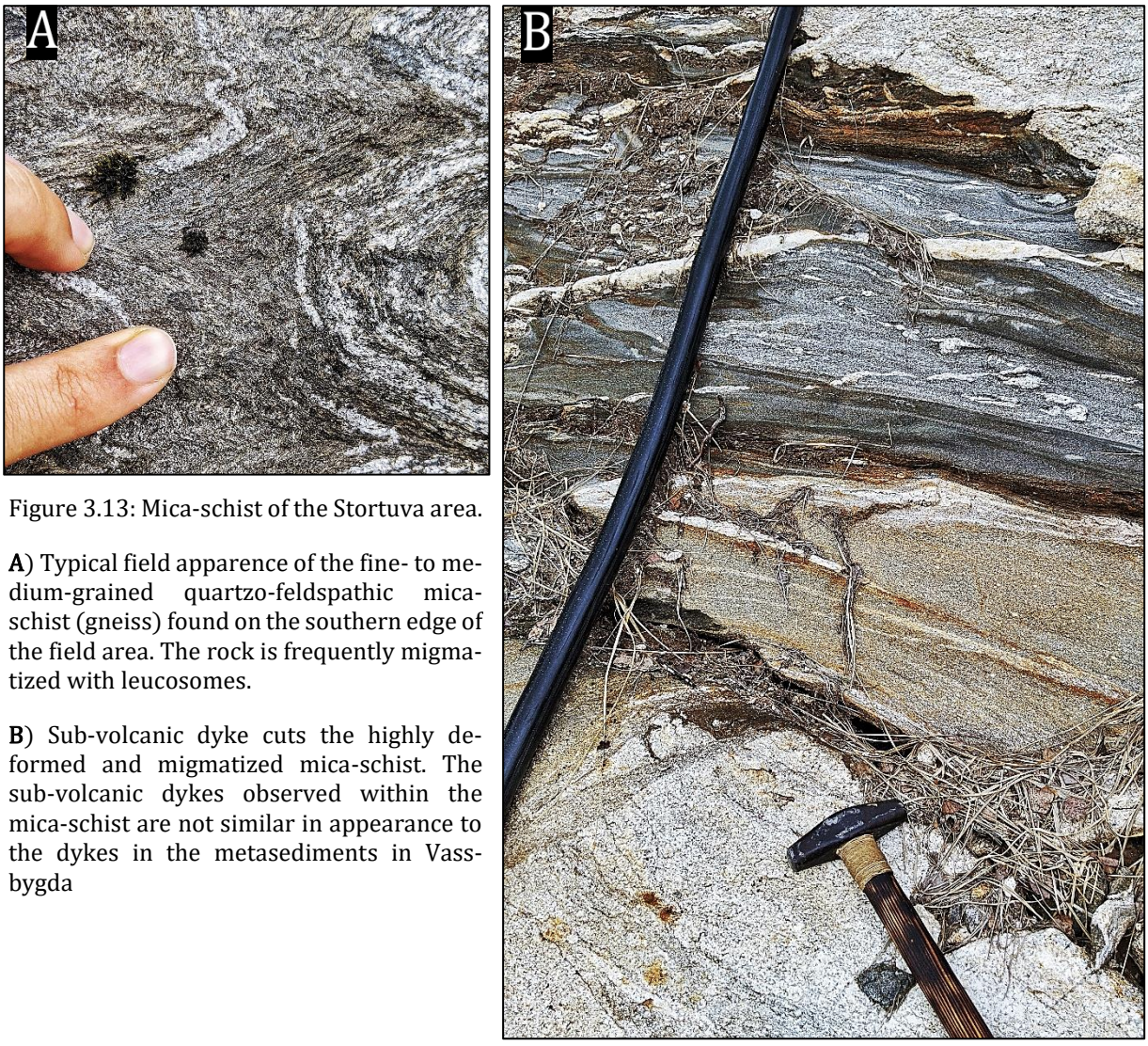

Figure 3.13: Mica-schist of the Stortuva area.

A) Typical field apparence of the fine- to medium-grained quartzo-feldspathic mica-schist (gneiss) found on the southern edge of the field area. The rock is frequently migmatized with leucosomes.

B) Sub-volcanic dyke cuts the highly deformed and migmatized mica-schist. The sub-volcanic dykes observed within the mica-schist are not similar in appearance to the dykes in the metasediments in Vassbygda

3.2.3 Igneous Rocks

Igneous rocks occur as dykes or sheets/sills throughout the field area. There are three main types of intrusive rocks characterized by their field appearance: 1) Dark grey to black mafic dykes, 2) dioritic dykes and 3) sills or sheets of leucogranittic composition, most commonly found on the eastern and northeastern side of Storvatnet (fig. 3.3).

In addition to the mentioned igneous rocks, several other generations and types of dykes were observed. The most interesting of these is a syn-deformational quartz-poor dyke observed within the calc-mylonite zone close to the nappe boundary. A sample of this dyke was taken (BC-06) to be used for structural analysis.

Compared to the marbles, the weathering resistance of the igneous rocks has made the outcrops protrude as "fences" in the terrain, similar to the calc-silicate layers (see chapter 3.2.4). However, the igneous rocks cut the foliation and are easily seen on DEM/hillshade maps of the topography (3.16 B). The cross-cutting relationship observed was the mafic dyke being cut by the quartz dioritic dykes, which also cuts the migmatized leucosomes and leucogranitic sills (3.9 D). The relationship between the mafic dykes and the leucogranite was not directly observed.

3.2.3.1 Mafic Dykes

The mafic intrusions are uncommon in the area. They are dark grey to greenish-black, fine to medium-grained, and are commonly observed alongside calc-silicate rocks. The mafic dykes usually show a white to pale brown alteration rim to the host rocks (3.14 B). Quartz dioritic dykes (see chapter 3.2.3.2) cut the mafic intrusions, as seen in 3.14 A. The mafic dykes consist of zoned hornblende crystals, plagioclase, and biotite, with minor titanite, microcline, and sulphides (fig. 3.14 C & D).

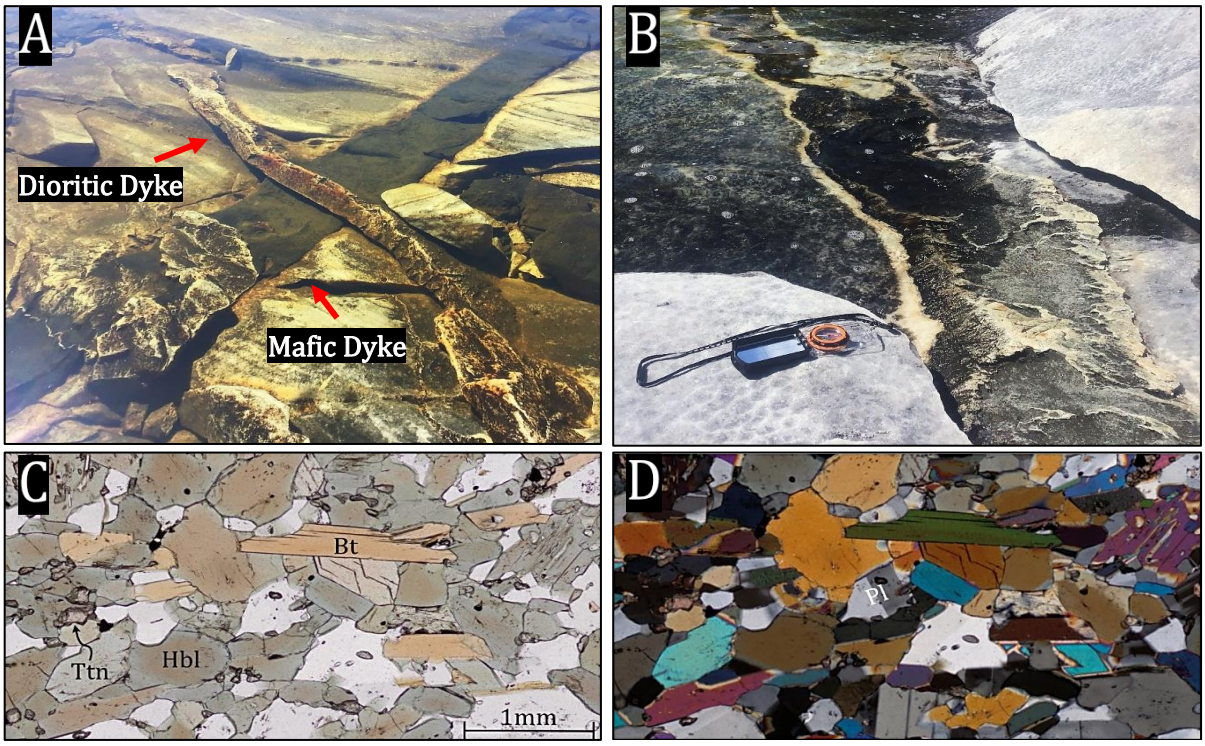

Figure 3.14: Mafic dykes. **A**) Mafic, hornblende-rich dyke (~40cm wide) is cut by a later dioritic intrusion. **B**) Diabasic dyke cuts through a marble unit. A white to pale brown alteration rim is characteristic of these intrusions. **C**) Micrograph (ppl) showing the mineralogic composition of the mafic dykes. Zoned hornblende crystals occur throughout the section. **D**) XPL micrograph of the same area as in C.

The mafic dykes are often highly deformed and are the most evidently deformed rock out of the igneous intrusions. The mafic dykes are commonly folded by at least one fold phase, with typical intermediate to tight folds (fig. 3.15 A). The dykes may also appear as boudinaged layers or completely dismembered segments (fig. 3.15 B). The mafic dykes are clearly observed in the marbles, where the host rock is often void of any deformation indication and only shows an infill texture surrounding boudinaged dykes (fig. 3.15 B).

Figure 3.15: Typical deformation observed in the mafic dykes.

A) Picture of a large (1,5m wide) mafic dyke. The dyke is located in the wall of an old marble quarry in the central part of Vassbygda. One or more apparent fold phases has deformed the dyke. The mafic dyke is later cut by small, less deformed, leucokratic dykes.

B) A typical size mafic dyke within the banded marbles on the shore of Fjellvatnet. The dyke is deformed into detached, asymmetric budins. The banded marble shows little deformation compared to the dyke, with only a infill texture in between the segments, emphasising the rheological contrast between the rocks.

3.2.3.2 Quartz Dioritic Dykes

The quartz dioritic dykes are consistently medium-grained, mesocratic grey to light grey inequigranular. The dykes are characteristic with a field appearance of visible biotite, amphibole, and muscovite grains(fig. 3.16 C), although the muscovite may not be visible in fine-grained variants. The overall mesocratic appearance and the characteristic protruding surface expression were used for classification when the muscovite was not visible.

The quartz dioritic dykes are the most common igneous rock in the field area and occurs as steeply dipping to sub-vertical dykes that often protrude 1-2m from the surrounding marble (fig. 3.16 A). The dykes occur most frequently north and northeast of Fjellvatnet, around Godvatnet, and throughout Stormarka. The dykes are usually on a meter-scale, with the largest observed at 5m thickness. However, they may be as narrow as 5-10cm. Since the quartz dioritic dykes usually protrude out of the marble surface, they are easy to spot on a hillshade map of the DEM (fig. 3.16 B). The width of the quartz dioritic dykes was too narrow to be represented on the geological map, although their location was marked and traced on the field map (3.1) using outcrop location and hillshade images. An experiment using automated lineation mapping was also done, and although promising, the methodology needed more adjustments to accurately reflect the dykes. A proof of concept for the automated lineament mapping is included in digital Appendix 1 and should be considered for further work on the area (see chapter 6.3).

The mineralogical assemblages of the dykes are biotite, amphibole (hornblende), plagioclase, and quartz with minor muscovite, pyrite, hematite, allanite, and titanite. The allanite is commonly surrounded or wholly replaced by an alteration zone of (clino)zoisite (fig. 3.16 D). The AMS results gave a specific mineralogic composition of 6% quartz, 1% alkali feldspar, and 50% plagioclase (Table 3.6), reflecting the quartz dioritic composition normalized and plotted in the QAPF-diagram (Streckeisen, 1974).

The quartz dioritic dykes show less interaction with the host rock. No alteration rim in the host marbles is visible, which is common surrounding the mafic dykes. Although inconsistent, there seems to be a trend of a more coarse-grained, good quality graphite-spotted marble close to dioritic dykes, especially in areas with a high density of dykes.

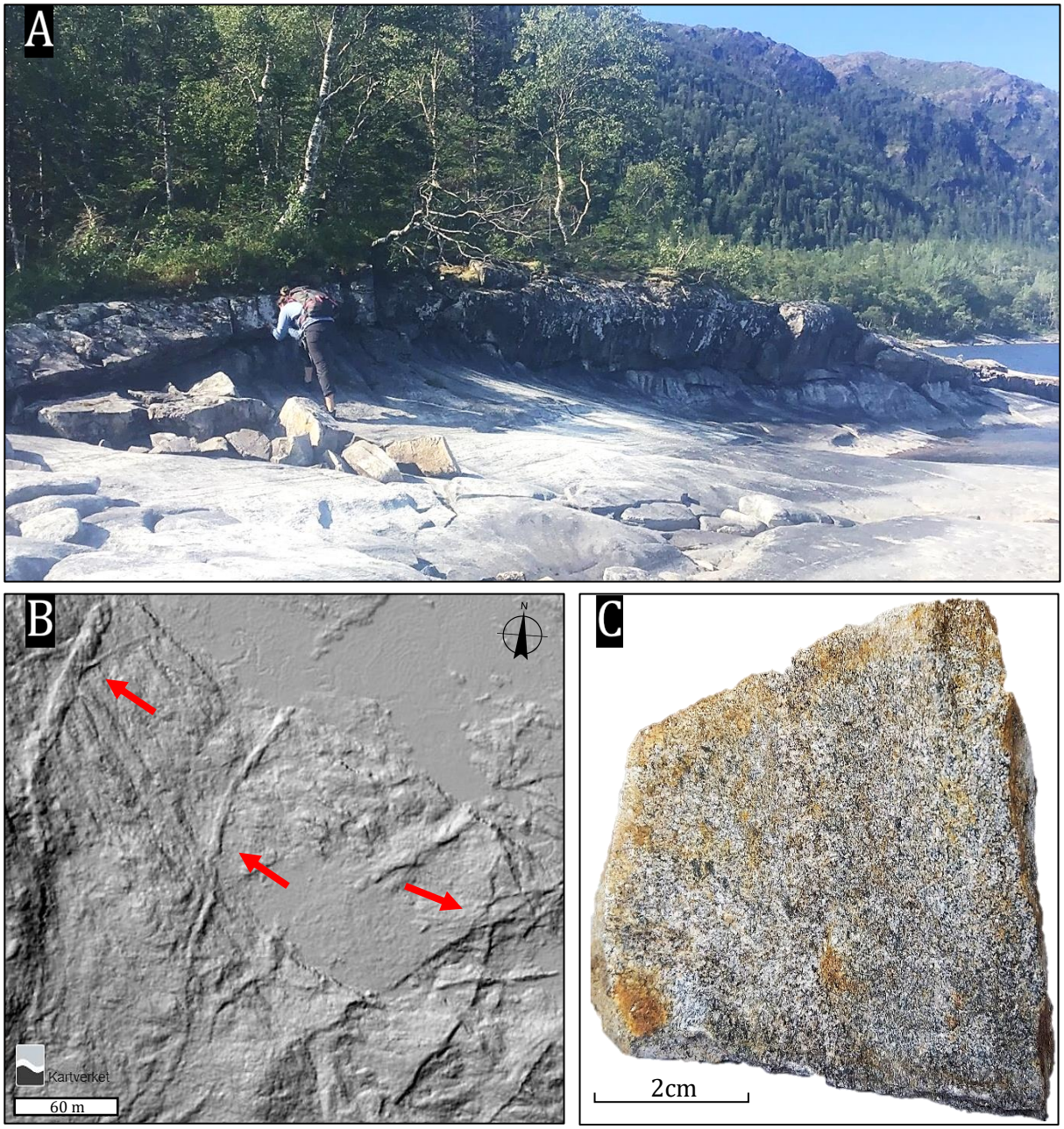

Figure 3.16: Field appearance of the quartz dioritic dykes. **A**) Typical protruding expression of the dioritic dykes found throughout Vassbygda. The dykes are often sub-vertical to steeply dipping and usually om meter-scale in width. **B**) Hillshade image of the eastern part of Fjellvatnet. The dioritic dykes (red arrows) are easily visible due to their erosional contrast to the host marbles. These dykes can be followed for several 100 meters. Source: hoydedata.no. **C**) Handsample of a dioritic dyke. The rock is characterized by equigranular quartz, feldspar, biotite ± muscovite. **D**) Micrograph of the same rock as shown in picture C. Allanite (Aln) is commonly altered to (clino)zoisite (Zo). Large titanite (Ttn) crystals are common, together with amphiboles, quartz (qz), plagioclase (Pl) and biotite (Bt).

3.2.3.3 (Porphyric) Leucogranitic Rocks

The leucogranites are associated with the migmatization of the siliciclastic metasedimentary rocks of the field area (fig. 3.17 C). On a small scale, the rock occurs as leuco- and melanosomes (often garnet-bearing) in the metasedimentary rocks (fig. 3.17 A). The leucogranite is a phaneritic, inequigranular/porphyritic, fine- to medium-grained feldspar-rich sub-volcanic intrusion.

The most common appearance of the leucogranite is white to light grey dykes or sub-horizontal sills. The leucogranite also occurs as larger intrusions commonly containing 1-3cm sub- to anhedral feldspar phenocrysts (fig. 3.17 B) and garnets (fig. 3.17 D).

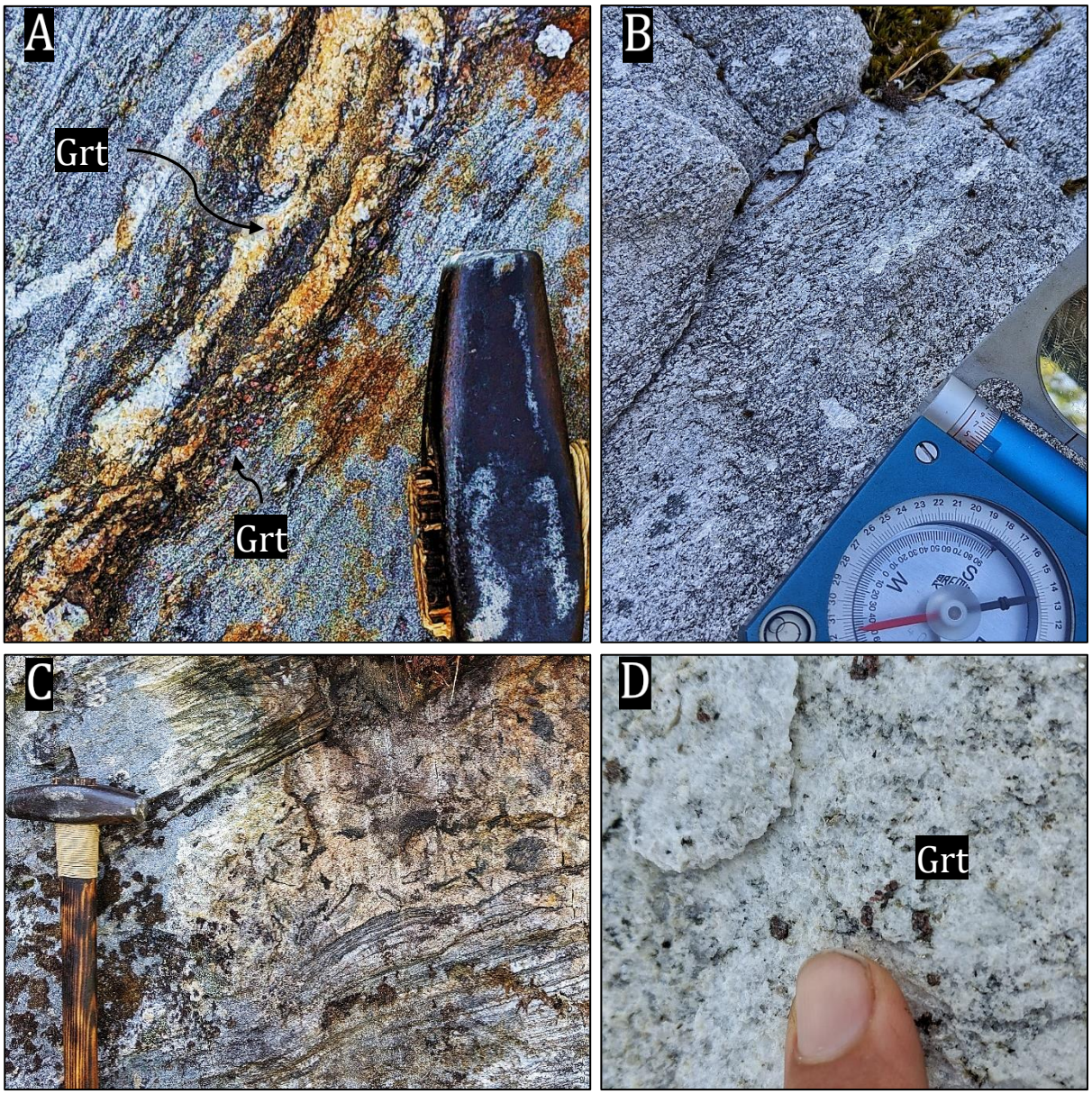

Figure 3.17: Leucogranittic intrusions. **A**) Garnet-bearing leucosomes and melanosome in a migmatized garnet metaarkose close to a larger leucogranite body (Picture edited with 150% saturation to enhance the garnets). **B**) Sub- to anhedral feldspar phenocrysts are often seen on the larger granite intrusions. **C**) Meta-arkose (bottom) cut by a leucogranite sheet (top). The intrusion cuts the foliation and assimilates parts of the host rock. **D**) Foto of a characteristic garnet leucogranite.

The large intrusions are often marked by a transition of steadily more migmatized siliciclastic metasedimentary rocks until the host rock is no longer visible or appears as xenoliths within the leucogranite (fig. 3.18 B). The strongly migmatized host rocks show garnet-bearing leuco- and melanosomes (fig. 3.17 A), which are both foliation-parallel and -cutting (fig. 3.18 A).

The leucogranite occurs as sills on the eastern side of the field area, which is not observed in any other places within Vassbygda, although some small leucogranitic outcrops are seen at Godvassli. However, one large leucogranitic intrusion is observed close to Mellomenget, east of Stormarka (fig. 3.3).

The largest porphyric leucogranite is found on Dengelhalsen, on the northeastern shore of Storvatnet (fig. 3.3). The Dengelhalsen intrusion and a smaller leucogranitic intrusion close to Mellomenget in eastern Vassbygda are the only igneous rock body massive enough to be included on the geological map.

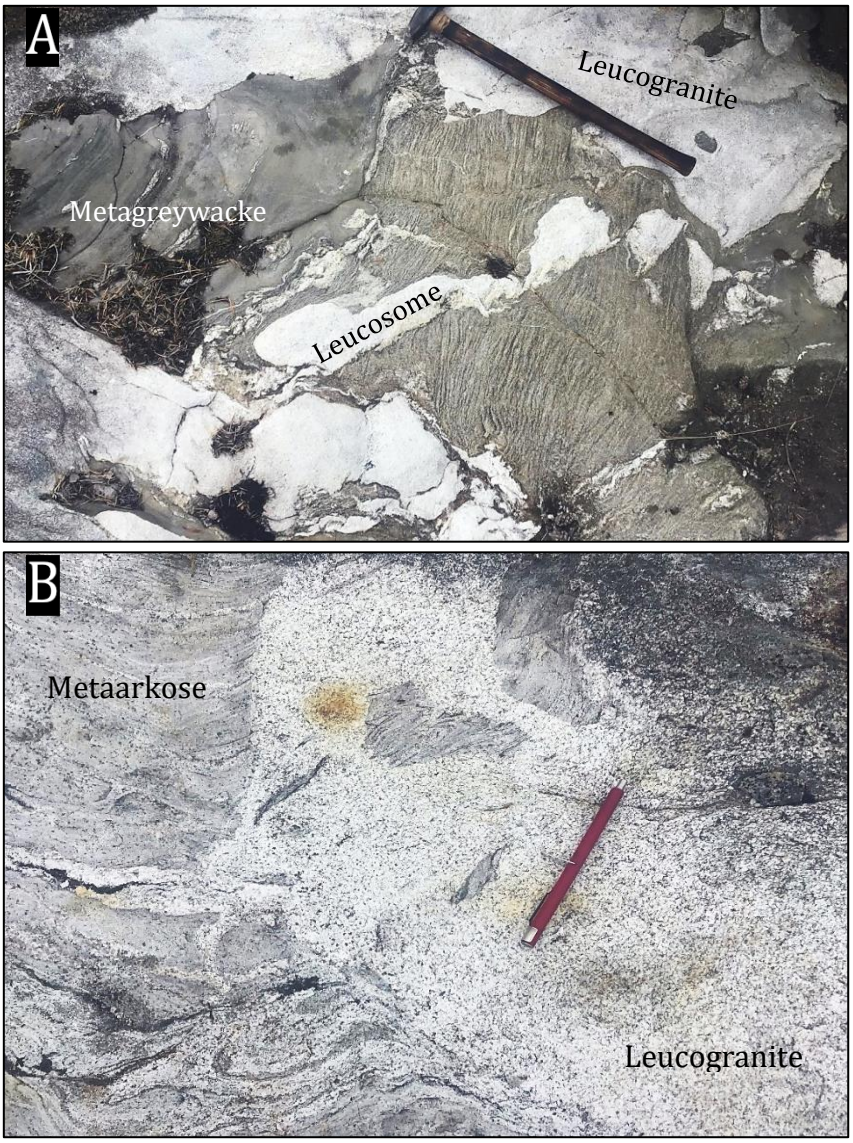

Figure 3.18: Partial melting of the siliciclastic metasedimentary rocks. **A**) A xenolith of siliciclastic metasedimentary rock in a magmatic sill. The remaining xenolith is partially melted with large foliation-cutting leucosomes. **B**) Melted section of the metaarkose. A xenolith of the folded host rock is visible in the melted zone.

3.2.4 Calc-Silicates and Skarn

Calc-silicate rocks occur throughout the marbles of Vassbygda. The rock also occurs in calc-rich zones in the siliciclastic metasediments. They are rarely more massive than a few meters, but one region in the centre of Stormakra (along the road to Godvassli) contains a sizeable calc-silicate body. This body was the only large enough to be included on the geological map (fig. 3.3).

Two types of calc-silicate rocks were identified. The most common type of calc-silicate rock is meso- to melanocratic dark grey to greenish-black, equigranular, fine- to medium-grained, and may often be extensively oxidized on weathering surfaces. These rusted calc-silicate layers (usually 1-4m wide) are most frequently found within the banded marble. The rock contains calcic amphiboles, plagioclase, diopside, and in places up to 10% titanite with minor ilmenite, sulphides, and rutile crack sealing (fig. 3.19 and 3.20 A & C). The rusted colours are likely due to the sulphide content, sometimes observed as medium- to coarse-grained pyrite cubes within the rocks.

This rock is extremely hard and resistant to erosion such that they often form walls up to 1m above the surrounding marbles (fig. 3.20 A & C). However, the calcsilicate rocks are not as visible on the hillshade images as the granitic intrusions since the calc-silicate layers are mostly confined within the marble and usually protrude less than the quartz-dioritic dyke. However, the rusted appearance can be seen on aerial photographs of the shorelines of Stor- and Fjellvatnet since it contrasts easily with the white marble.

The second variant of calc-silicates occur in areas of extensive magmatic intrusions, frequently observed on the southeastern side of Storvatnet and sandwiched between leucogranitic dykes on the islands of Storvatnet.

This variant is schistose, fine- to medium-grained, and appears dark grey to black with elongated amphibole crystals (fig. 3.20 B). The schistose calc-silicate rocks do not show the characteristic rusted weathering surface as the first type, often appearing similar to the biotite-rich metasedimentary rocks. The rock consists of hornblende, diopside, plagioclase, and biotite, with minor titanite, allanite, (clino)zoisite, rutile, pyrite, and chalcopyrite.

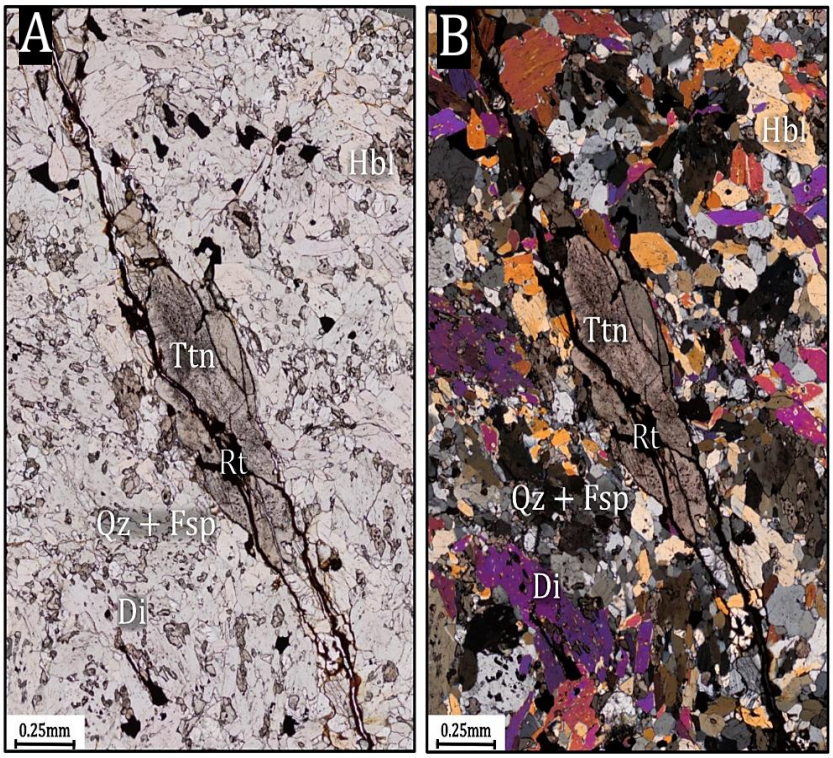

Figure 3.19: Migrocraphs of a titanite-bearing calc-silicate layer. **A**) PPL micrograph (BC-10) of a rutile(Rt)-filled crack with large titanite (Ttn) crystals. Opaques (mainly sulphides) are also common, **B**) XPL micrograph of the same area. The groundmass is dominated by quartz (Qz) and feldspar (Fsp) with larger diopside (Di) crystals.

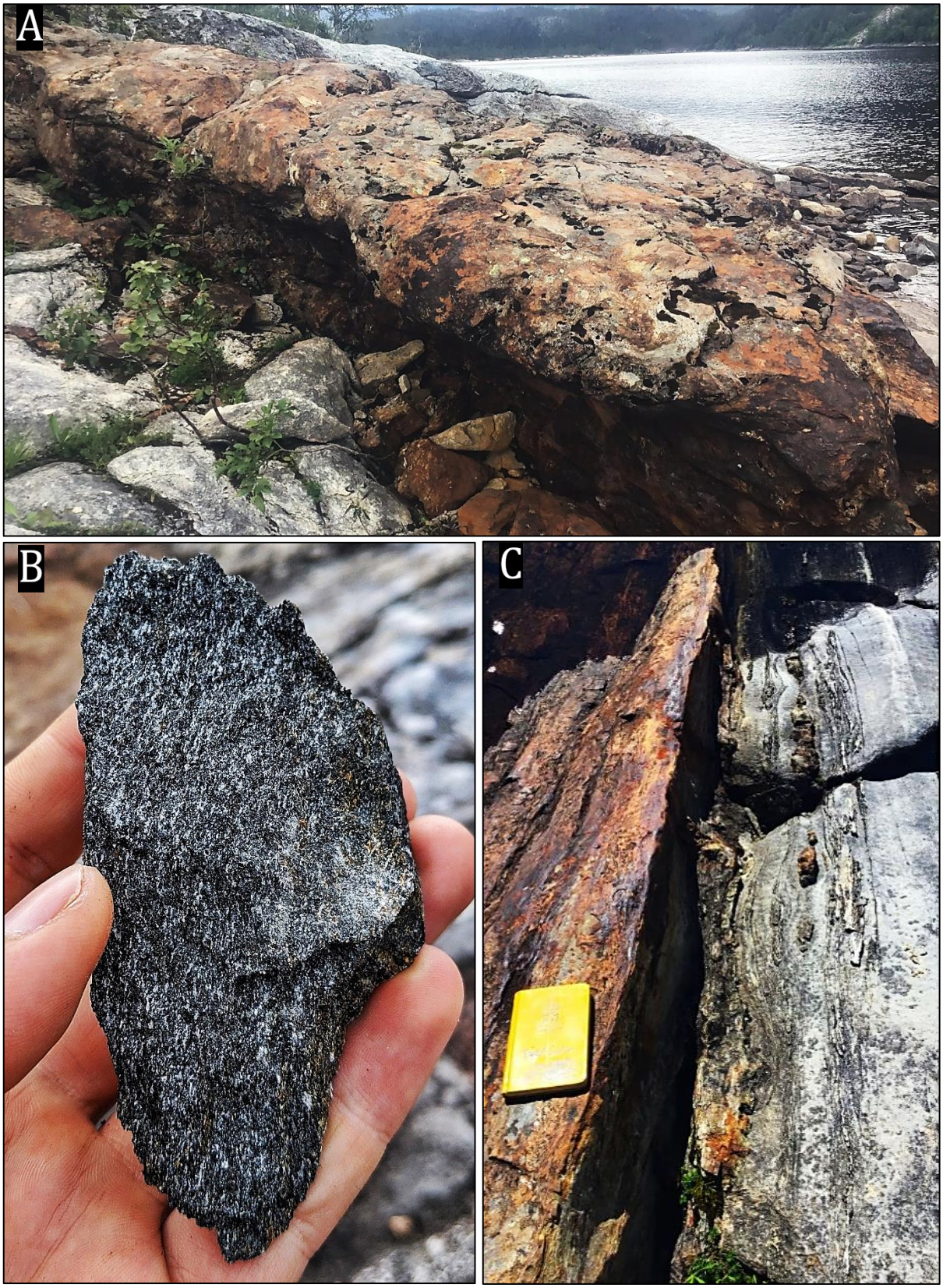

Figure 3.20: Typical field appearance of calc-silicate layers within the banded marble. **A**) Typical (1m high) "fence"-like surface expression of the calc-silicate layers. The rusted appearance corresponds to high sulphide content usually observed as pyrite crystals on fresh surfaces. **B**) Amphibole-rich calcsilicate typically found close to large intrusions or areas with dyke swarms. This appearance is often challenging to differentiate from fine-grained metagreywacke. **C**) Semi-gradual transition from the banded marble to a rusted calc-silicate layer. The layer extrudes ~0.5m from the surrounding marbles.

Small inequigranular skarn bodies (0.5-5m) infrequently occur throughout the marbles, always surrounded by amphibolitic calc-silicate rocks. The skarn usually appears with a medium- to coarse-grained green or blackish green groundmass and frequent diopside and calcite crystal growth in pockets and fractures. These large, elongated crystals are often green to dark green and up to 10 centimetres long.

The skarns consist of altered amphiboles and diopside crystals, feldspars (microcline+plagioclase) and minor chlorite, pyrite, chalcopyrite, titanite, and rutile. The microscopic texture of the skarn is dominated by zones of altered pyroxene crystals and sericitized feldspars in between areas with relatively unaltered crystals (fig. 3.21). The alteration zone consists of heavily altered elongated crystals, most likely amphiboles. Chlorite shows abnormal Berlin/Prussian-blue interference colours. The dominant pyroxene is diopside, which corresponds well to the green colour of the skarn groundmass. Augite with exsolution lamella of orthopyroxenes is also common.

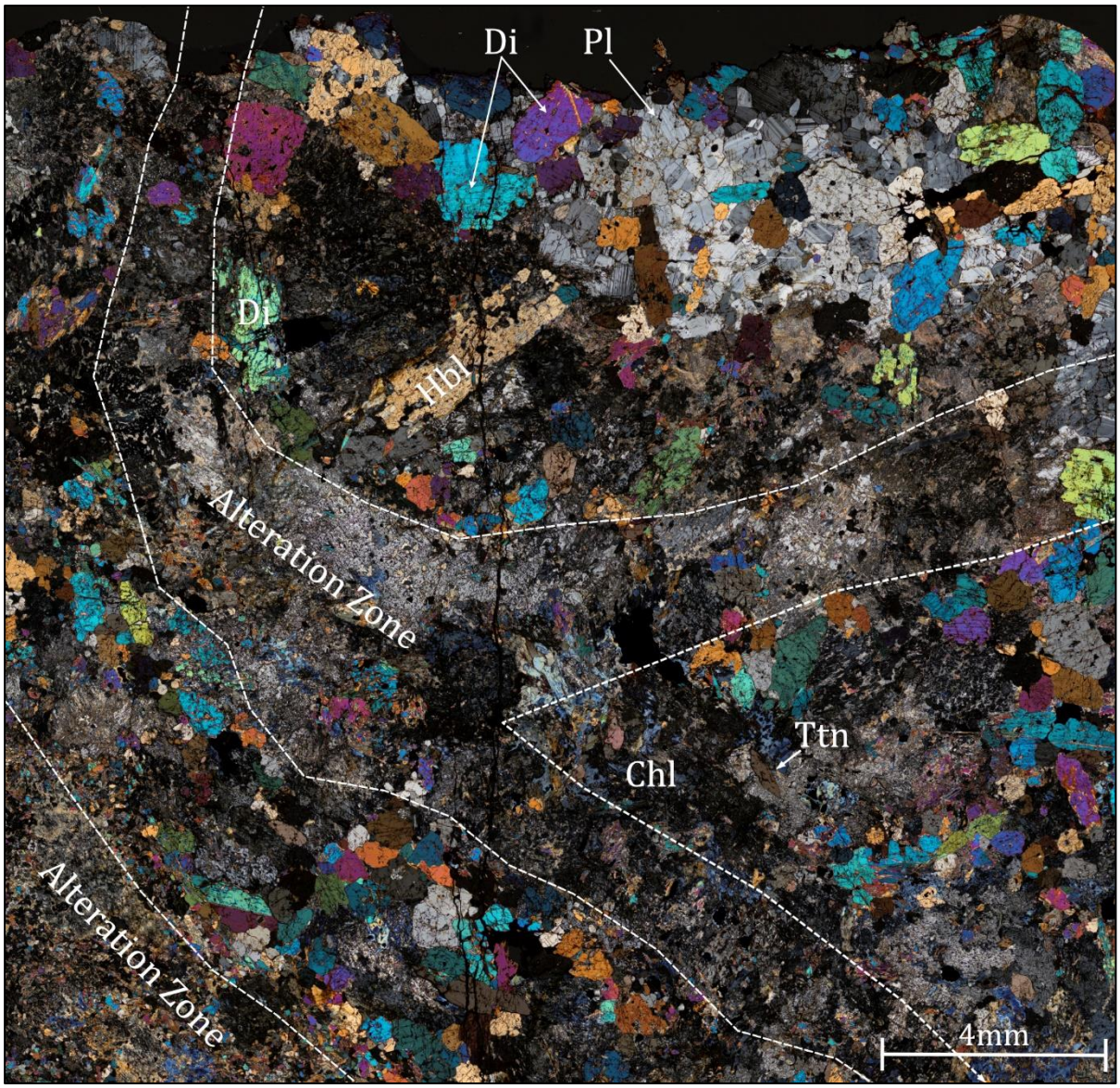

Figure 3.21: XPL micrograph of a skarn rock (BC-09). Sericitized plagioclase (Pl) crystals, clino- and orthopyroxene (Cpx/Opx) and chlorite form distinct alteration zones between less altered, coarser-grained crystals. Minor titanite (Ttn) is also common.

3.2.5 Mantle-Derived Rocks

Several lenses of mantle-derived, ultramafic rocks occur as beads-on-a-string along the structural contact between the Lower and Middle nappe on the eastern side of the field area (fig. 3.3). These ultramafic bodies consist mainly of rocks varying from dunitic to harzburgitic compositions, with lightly serpentinized zones. The unaltered mantle-derived rocks consist of fine-grained black to greenish-black mafic minerals, distinct weathering surfaces, and characteristic talc veins (fig. 3.22 B). Some sections of the dunitic rocks are chromite- bearing with rounded chromite crystal aggregates up to 5cm (fig. 3.22 A).

One such lens of mantle-derived rocks is located along the road to Nordfjellmark (fig. 3.3). Here, the ultramafic rocks are overlain by a laminated garnet-bearing tuff-like metamorphic rock (fig. 3.22 C), which in turn is overlain by a section of metagabbro and a polymict basal conglomerate consisting of a mafic groundmass and clasts of mantle-derived sources (Åsnes conglomerate (Thorsnes & Løseth, 1991), fig. 3.22 D). The ultramafic bodies are interpreted to be the first tectonostratigraphic unit of the Middle nappe, with several similar ultramafic bodies located along the bottom of the Middle nappe (Thorsnes & Løseth, 1991).

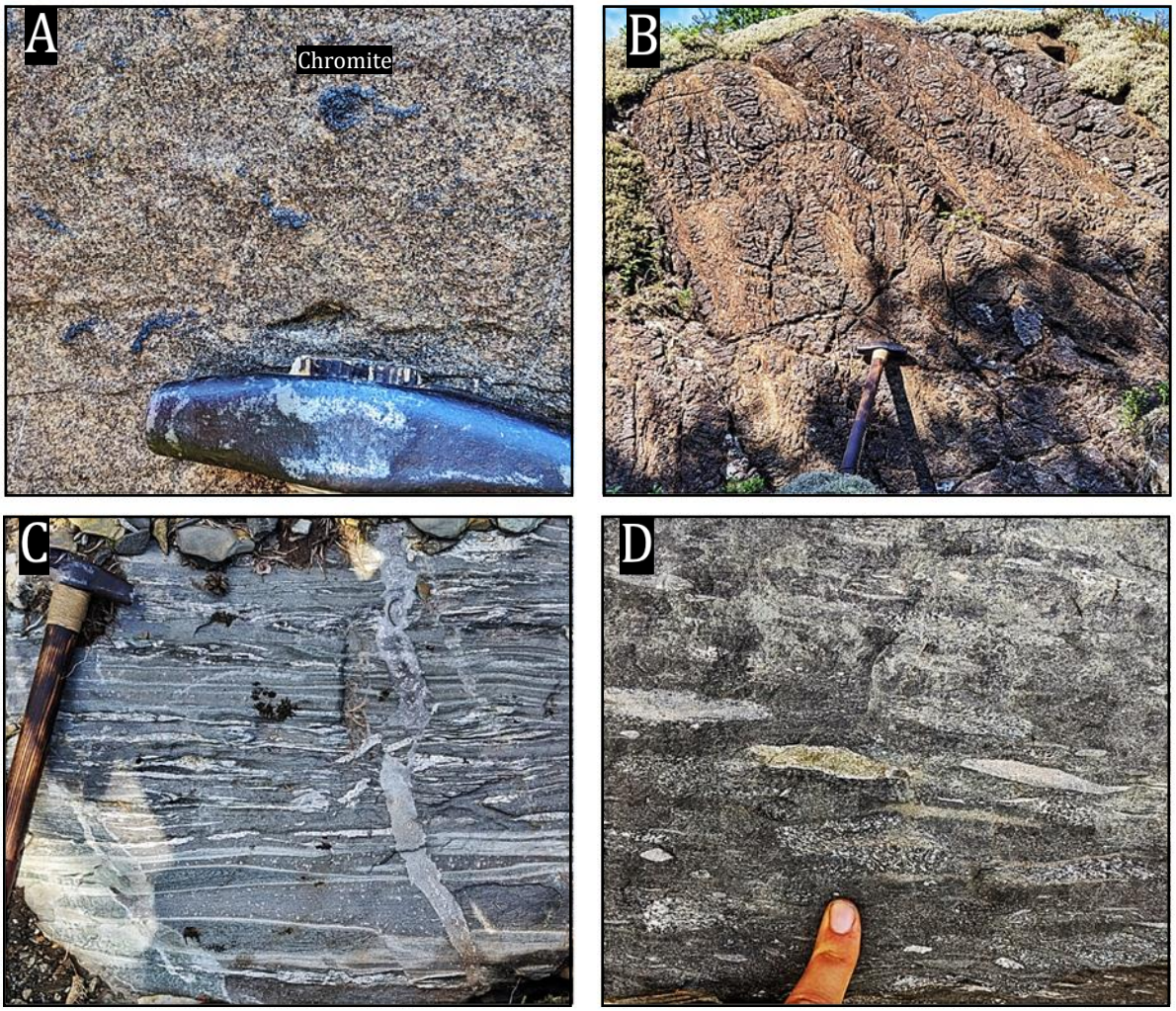

Figure 3.22: Ultramafic rocks of the field area. **A**) Chromite-bearing lightly serpentinized dunite. **B**) Typical textures found within the dunite zones. **C**) Garnet-bearing metatuff? **D**) Åsnes conglomerate, a polymict conglomerate consisting of a mafic groundmass with deformed greenstone and gabbro clasts.

3.3 Petrophysical Analysis

The geophysical analyses were run as a standard procedure by NGU, and the majority of the results were originally beyond the scope of this thesis. However, some of the results indicate interesting parameters regarding rock descriptions and possible future studies. Only the relevant results are included in this chapter. The full list of results is found in Appendix D: Petrophysical Analysis.

The most interesting results concern the density, susceptibility, and NRM of the samples, as seen in Table 3.1. The rock densities range from 2.53 to 3.13 g/cm^3. When plotted against susceptibility (fig. 3.23), both the marbles and the calc-silicates (except sample BC-13) form distinct groups. The marbles have an average density of 2.73 g/cm^3 (corresponding to the expected value of calcite at approximately 2.71 g/cm^3 (Ellis & Singer, 2007)) and an average susceptibility of -19.3 µSI. The calc-silicate rocks show the highest measured density and susceptibility, with an average density and susceptibility of 3.04 g/cm^3 and 683.3 µSI, respectively. The siliciclastic metasedimentary rocks have a broader density (2.63–2.87 g/cm^3) and susceptibility range (74–663 µSI).

When comparing the metaarkose to the metagreywacke and the related mylonitic mica-schist, it is evident that the metaarkose is the less dense siliciclastic rock type. Even though the siliciclastic metasedimentary rocks have overlapping density values with the marbles, they can be differentiated by their elevated susceptibility values. The siliciclastic metasedimentary rocks are also separated from the calc-silicates by having a lower density. Finally, the igneous rocks plot with the largest density (2.53 to 3.06 g/cm^3) and a susceptibility range (16 to 684 µSI). This range was expected since the samples come from three vastly different igneous rock types.

Table 3.1: Results of the geomagnetic and density measurements of the 13 samples. NRM: Natural Remnant Magnetization, IM: Induced magnetization, calculated using the measured regional field of 52384.07 nT.

Sample	Density [g/cm^3]	Susceptibility [10^{-6} SI]	NRM [mA/M]	IM [mA/m]
(Quartz Diorite Dyke) ***BC-01***	2.80	477	12	2.00
(Migmatitic Metaarkose) ***BC-02***	2.63	74	9	0.31
(Metagraywacke) ***BC-03***	2.71	289	7	1.21
(Graphite-spotted Marble) ***BC-04***	2.68	-80	2	-0.34
(Banded Calc-mylonite) ***BC-05***	2.83	63	10	0.26
(Granitic Dyke) ***BC-06***	2.53	16	9	0.07
(Mylonitic Mica-schist) ***BC-07***	2.81	663	43	2.78
(Skarn / Calc-silicate) ***BC-08***	3.13	614	548	2.58
(Calc-silicate) ***BC-09***	3.00	713	410	2.99
(Calc-silicate) ***BC-10***	2.99	723	1554	3.04
(Impure Banded Marble) ***BC-11***	2.67	-41	9	-0.17
(Mafic Dyke) ***BC-12***	3.06	684	11	2.87
(Amphibolite Calc-silicate) ***BC-13***	2.87	299	7	1.26

The average susceptibility of the marble units is -11 µSI, with a natural remnant magnetization of 7 mA/M. The Ca-silicate rocks carry the most remnant magnetization with a maximum value of 1554 mA/M and an average of 631 mA/M. The Ca-silicate rocks also have the highest average susceptibility of 683 SI. A wide span, similar to the density, can also be observed in the intrusions, where the common quartz dioritic intrusion has a susceptibility of 477 µSI, whereas the tonalite only shows 16 µSI.

Sample BC-06 is both the least magnetic and the least dense of all the samples. This result corresponds well with the thin section optical microscopy where no magnetite or hematite was found,

together with the abundance of feldspar, which has a density as low as 2.55 g/cm^3 (Orthoclase) (Nesse, 2011).

The geomagnetic field was measured to 52384.07 nT during the sampling, equivalent to 42 A/m. fig. 3.24 shows the calculated induced magnetization plotted against the natural remnant magnetization. All the rock samples are dominated by remnant magnetization, especially the calc-silicates, since all plot with a Q-value above 1 (Clark, 1997). The calc-silicates have an average NRM-value of 630 mA/m, while the other samples show NRM-values below 13mA/m, except sample BC-07 with an NRM-value of 43mA/m.

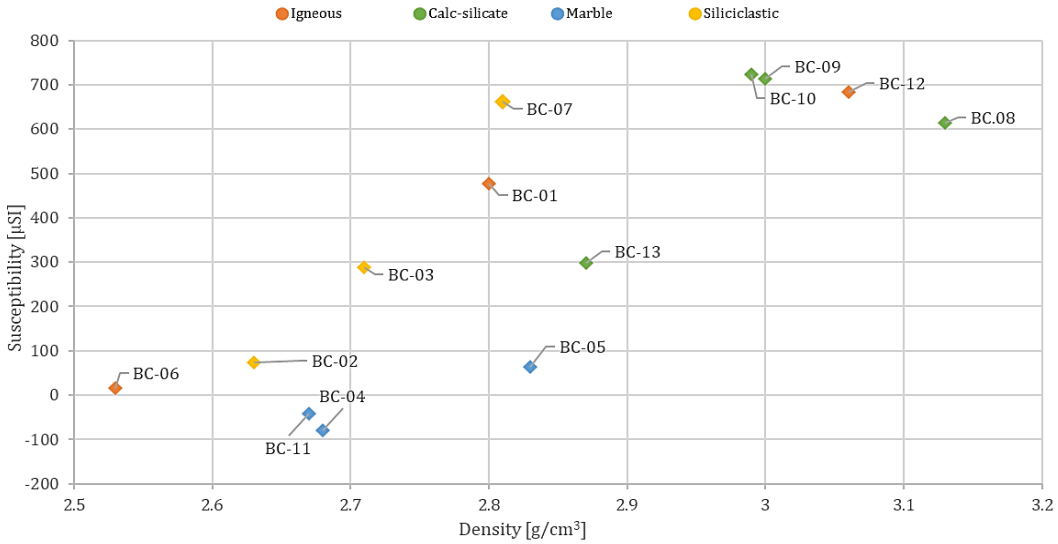

Figure 3.23: Plot of sample densities vs. susceptibility.

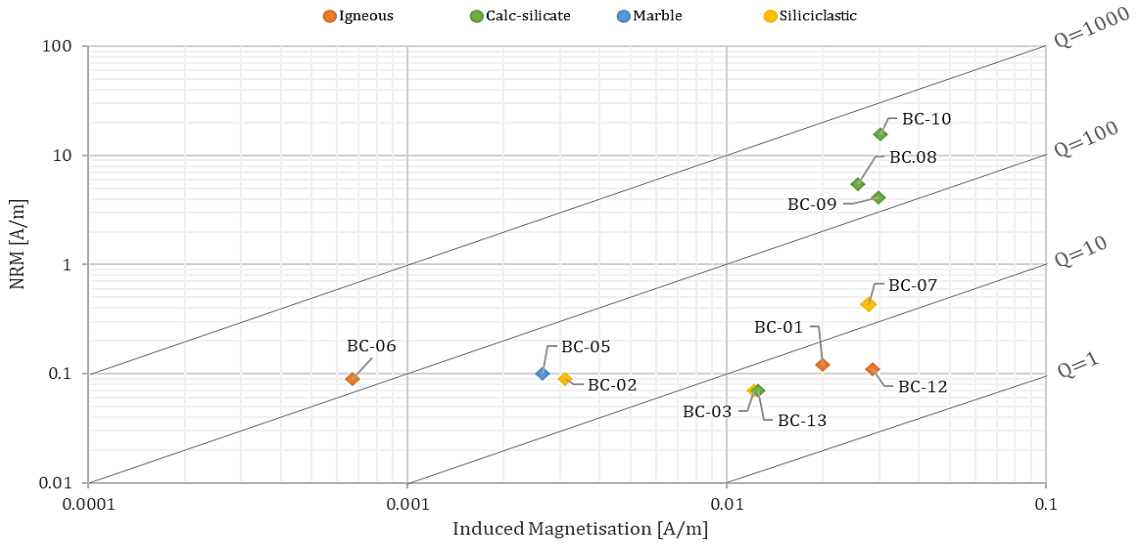

Figure 3.24: A log-log plot of the natural remnant magnetization (NRM) and induced magnetization. All samples are NRM-dominated. BC-04 and BC-11, both marbles, were not plotted due to negative susceptibility values.

Although the results are interesting, the analysis is based on only a few samples. Besides, a full geophysical interpretation is beyond the scope of this thesis. The results form the geophysical analyses and the potential for geophysical exploration of the field area is discussed in further work (chapter 6.1).

3.4 Chemical Analysis

This chapter summarizes some of the results of the chemical analysis. Only the relevant results are presented; however, a full table of chemical results is found in Appendix E: Chemical Analysis – Results.

3.4.1 XRF: Main Element Analysis

3.4.1.1 Marbles

The marbles are all high in calcite, with the graphite-spotted marble and the banded marble containing about the same amount of calcium (~50 wt.%, Table 3.2). On the other hand, the calc-mylonite contains only 31 wt% CaO and 20 MgO wt%, indicating a more dolomitic composition. It also comprises silicate minerals, similar to the banded marble. In contrast, the graphite-spotted marble has a low concentration of silicate minerals with 0.73 wt% SiO_2.

Table 3.2: Main-element analysis of all three marble samples. The high loss on ignition (LoI) is probably the burn-off of carbon and oxygen from the calcite and graphite as CO_2. Elements are noted as wt%.

	BC-04 (Graphite-Spotted Marble)	**BC-05** (Calc-Mylonite)	**BC-11** (Banded Marble)
SiO_2 [%]	0.73	2.05	3.43
Al_2O_3 [%]	0.182	0.683	0.638
Fe_2O_3 [%]	0.183	0.421	0.251
TiO_2 [%]	0.016	0.050	0.041
MgO [%]	0.21	20.4	0.30
CaO [%]	55.0	31.4	53.3
Na_2O [%]	<0.1	<0.1	<0.1
K_2O [%]	0.027	0.274	0.156
MnO [%]	0.015	0.015	<0.01
P_2O_5 [%]	0.013	0.088	<0.01
LoI [%]	43.1	44.9	41.7
Total [%]	99.5	100	99.9

3.4.1.2 Siliciclastic Metasedimentary Rocks

The main-element XRF analysis of the siliciclastic metasedimentary rocks shows a clear chemical distinction between the two types. The metaarkose is quartz dominated and hence contains significantly more SiO_2 than the mica- and aluminosilicate-dominated metagreywacke (Table 3.3). The presence of fibrolite and muscovite in the metagreywacke is also seen in the high aluminium, potassium, and iron concentration.

Table 3.3: Main-element analysis of the siliciclastic metasedimentary rocks. Elements are noted as wt%.

	BC-02 (Metaarkose)	**BC-07** (Metagreywacke)
SiO_2 [%]	74.3	55.1
Al_2O_3 [%]	12.7	21.8
Fe_2O_3 [%]	3.43	8.39
TiO_2 [%]	0.483	1.07
MgO [%]	0.79	2.26
CaO [%]	1.27	0.735
Na_2O [%]	4.23	2.14
K_2O [%]	1.57	5.43
MnO [%]	0.027	0.097
P_2O_5 [%]	0.087	0.086
LoI [%]	0.51	2.61
Total [%]	99.4	99.7

3.4.1.3 Magmatic Intrusions

The various magmatic intrusions are of distinct chemical composition (Table 3.4). The granitic dyke is dominated by quartz and feldspar, corresponding well with the high silica and aluminium content. The silica content of the dykes varies a lot, where the mafic dyke contains the least amount (44.8 wt% SiO_2). The quartz diorite is relatively silica-poor (51.2 wt% SiO_2) compared to the granitic dyke (75.6 wt% SiO_2) found within the HTSZ.

Table 3.4: Main-element analysis of the magmatic intrusions. Elements are noted as wt%.

	BC-01 (Quartz Diorite)	**BC-06** (Granitic Dyke)	**BC-12** (Mafic Dyke)
SiO_2 [%]	51.20	75.60	44.80
Al_2O_3 [%]	19.500	13.400	15.200
Fe_2O_3 [%]	8.140	0.205	11.700
TiO_2 [%]	1.370	0.041	1.670
MgO [%]	4.49	<0.1	9.22
CaO [%]	7.28	1.01	11.5
Na_2O [%]	3.82	3.06	2.46
K_2O [%]	2.320	5.400	1.530
MnO [%]	0.113	<0.01	0.178
P_2O_5 [%]	0.340	0.114	0.279
LoI [%]	0.895	0.429	0.473
Total [%]	99.4	99.2	99.1

3.4.1.4 Calc-Silicates and Skarn

The four calc-silicate rocks show similar chemical compositions with high silica, aluminium, iron, magnesium, and calcium content (Table 3.5). The titanium amount varies from 0.95 to 4.7 wt%, with the highest concentration from the rutile- and titanite-rich rusted calc-silicate layer in the banded marble (BC-10).

Table 3.5: Main-element analysis of the calc-silicate rocks. Elements are noted as wt%.

	BC-08 (Skarn/ Calc-silicate)	**BC-09** (Calc-silicate)	**BC-10** (Calc-silicate)	**BC-13** (Schistose Calc-silicate)
SiO_2 [%]	44.9	47.70	38.40	56.4
Al_2O_3 [%]	13.9	15.1	16.5	13.1
Fe_2O_3 [%]	9.420	9.81	7.82	5.15
TiO_2 [%]	0.953	1.18	4.83	0.666
MgO [%]	9.25	8.83	11.0	8.96
CaO [%]	17.4	11.3	14.3	10.3
Na_2O [%]	1.00	1.94	1.76	1.36
K_2O [%]	0.519	2.120	0.647	2.74
MnO [%]	0.104	0.171	0.123	0.151
P_2O_5 [%]	0.085	0.385	0.630	0.150
LoI [%]	2.00	0.843	2.83	0.815
Total [%]	99.5	99.4	98.7	99.8

3.4.2 LA-ICP-MS: REE

The results of the LA-ICP-MS analysis are represented as REE/Chondrite-plots in fig. 3.25. The plot shows that all the samples follow a gently decreasing trend towards heavy-REE, where they flatten. The plot also shows two distinct groups of samples: The majority of the samples consistently have 10-100 times higher REE concentrations than samples BC-04, BC-05, BC-06, and BC-11. Three of these samples (BC-04, BC-05, and BC-11) are marbles, whereas BC-06 is a deformed granitic dyke that cuts a mylonitic zone in the marble close to the boundary between the Middle and Lower nappe. Interestingly, BC-06 is chemically different from the more common dykes in the area (BC-01). BC-06 also shows a positive Eu anomaly.

The results may not convey the whole truth since several rocks from Vassbygda contain varying amounts of allanite, apatite, and zircon – minerals with very high REE distribution coefficients and may give rise to problems due to disproportionate REE patterns (Winter, 2001).

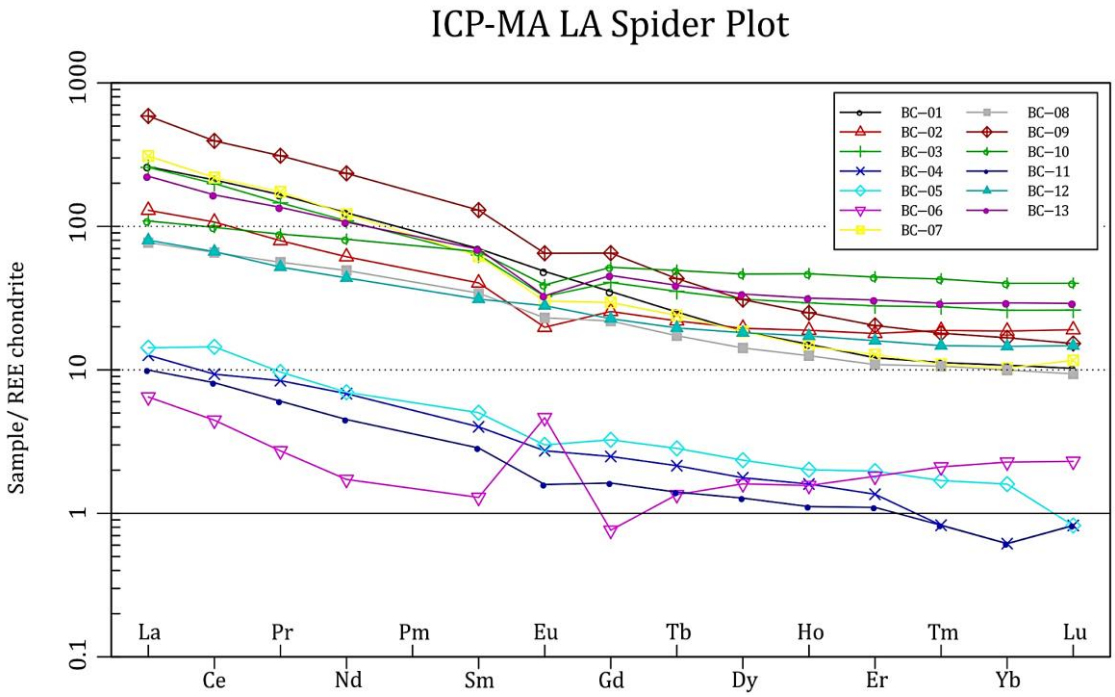

Figure 3.25: ICP-MS plot of the chondrite-normalized REE of the samples. A notable positive Eu- anomaly is observed in sample BC-06. Chondrite normalization values from Anders and Grevesse (1989).

3.5 Automated Mineralogy (AMS)

The results from the AMS analysis are summarized in Table 3.6. The complete dataset from the AMS analysis, including mineral and element associations and montage images from the classification, is found in Appendix B: AMS.

The AMS results give the amount of minerals present and can, in comparison to the XRF, give a spatially-resolved, mineralogical quantification. Sample BC-04 is a characteristic graphite-spotted marble found within Stormarka (Table 3.6). The sample consists of 98.2 wt% calcite with minor impurities of graphite and quartz. Only trace amounts of sulphides and oxides are present. The element distribution from sample BC-04 indicates that 99.98% of the Ca comes from Calcite, with apatite and titanite containing the rest. The XRF results also showed 0.21 wt% MgO, which has a 99.25% element association to calcite, most likely related to dolomite inclusions.

The element association of the calcite in the graphite-spotted marble (Appendix B: AMS) is abnormally high for all elements, which most likely results from an incorrect spatial resolution of the analysis, indicating the presence of smaller inclusions than the selected step-size.

Table 3.6: Extract from the results of automated mineralogy. Mineral classification and additional information are found in Appendix B: AMS . ***** The graphite and resins quantification was attempted outside the standard procedures for the apparatus and may only be used as an indication.

Sample	Mineral	Area %	Weight %	Grain Size (µm)	Grain Size Std Dev (µm)
BC-01	Albite	52.74	50.93	64.62	204.21
Quartz Diorite	Epidote	<0.01	<0.01	10.00	0.00
	Hematite	0.17	0.33	33.89	51.13
	Zircon	<0.01	0.01	11.98	4.78
	Microcline	<0.01	<0.01	10.00	0.00
	Pyrrhotite	<0.01	<0.01	12.18	5.31
	Rutile	<0.01	<0.01	38.29	0.00
	Allanite	0.03	0.04	18.32	13.50
	Muscovite	0.18	0.20	13.78	11.56
	(clino)Zoisite	2.54	3.17	67.45	154.63
	Biotite	18.46	21.25	70.96	130.09
	Quartz	8.20	8.22	55.24	106.42
	Magnesio-Hornblende	11.89	14.13	98.38	161.99
	Titanite	0.97	1.27	51.06	66.04
	Apatite	0.39	0.45	22.82	23.86
	Pyrite	0.01	<0.01	57.77	48.53
	Unclassified	4.4		18.0	22.6
BC-02	Quartz	41.60	42.23	162.63	211.47
Metaarkose	Zircon	<0.01	<0.01	10.00	0.00
	Apatite	0.01	0.01	14.00	9.63
	Hematite	0.02	0.03	21.80	33.10
	Albite	41.59	42.21	171.34	247.20
	Biotite	11.31	13.18	80.46	92.61
	Muscovite	0.79	0.92	24.59	40.41
	Rutile	<0.01	<0.01	13.45	6.01
	Unclassified	3.20		13.31	7.67

Continued on next page

Table 4.6 continued	*Mineral*	*Area%*	*Wt%*	*Grain Size (µm)*	*Grain Size Std Dev (µm)*
BC-04	Calcite	93.42	98.19	645.49	754.89
Graphite-spotted	Pyrite	<0.01	0.01	100.52	58.88
marble	Apatite	0.02	0.01	80.06	64.33
	Quartz	0.44	0.46	243.21	257.79
	Magnetite/siderite	<0.01	<0.01	15.30	10.88
	Hematite	0.08	0.17	42.69	69.84
	Albite	0.06	0.02	28.30	0.06
	Graphite*	0.35	0.29	18.88	24.73
	Titanite	0.03	0.03	82.55	73.63
	Pyrrhotite	<0.01	<0.01	10.00	0.00
	Resin	2.10	0.82	34.18	65.59
	Unclassified	3.38		17.93	19.20
BC-12	Magnesio-Hornblende	62.75	68.26	318.39	508.34
Mafic dyke	Epidote	<0.01	<0.01	10.00	0.00
(amphibolite)	Hematite	0.08	0.14	15.61	11.57
	Zircon	<0.01	<0.01	10.00	0.00
	Pyrite	0.01	<0.01	14.43	10.72
	Microcline	<0.01	<0.01	10.00	0.00
	Pentlandite	<0.01	<0.01	11.83	6.44
	Pyrrhotite	0.52	0.18	50.81	65.57
	(clino)Zoisite	0.23	0.26	29.29	46.48
	Rutile	<0.01	<0.01	10.00	0.00
	Titanite	2.95	3.50	67.15	64.10
	Albite	24.83	21.95	29.59	98.60
	Muscovite	0.01	0.01	12.05	8.50
	Biotite	4.98	5.24	92.11	163.62
	Allanite	0.04	0.06	10.04	0.67
	Apatite	0.37	0.39	27.95	25.39
	Quartz	<0.01	<0.01	12.00	4.47
	Unclassified	3.12		14.56	14.01

The metaarkose is dominated by quartz and feldspar, which confirms the quartzofeldspathic field appearance of the rock. The feldspars were classified as albite (determined by the set ratio of $X_{Or}<0.2$, $X_{An}<0.3$), although it was not determined if the albite is detrital or authigenic. Biotite is the only other significant mineral within the rock.

The mafic dyke (BC-12) is dominated by amphiboles (magnesio-hornblende (see chapter 3.6.2)) and albite at 63.65 and 24.33 area%, respectively. The mafic dykes are also rich in titanite (3.50 wt%), whereas quartz diorite contains 1.24 wt% in comparison. This trend is not equally visible in the main-element XRF results (Table 4.4), where the mafic dykes contain 1.67 wt% TiO_2, and the quartz diorite contains 1.37 wt% TiO_2. This discrepancy may be due to the relatively small section of the sample used for AMS. The Ti in BC-01 is associated with biotite (22.25%) and titanite (74.27%), whereas the titanite of BC-12 contains 98.6% of the Ti (Appendix E: Chemical Analysis – Results). The dominant feldspar for both igneous rocks is the albite class.

The AMS also provides data on mineral associations, which can be used to analyse the impurities within the marble. Table 3.7 shows the mineral associations of the graphite-spotted marble. The data shows that titanite, graphite, and apatite are the most common inclusions within the calcite. Quartz occurs as separate crystals and is therefore not observed as inclusions within the calcite. This observation can be seen in the montage images seen in Appendix B: AMS. The oxide and sulphide impurities are correlated with a strong association between hematite, magnetite, pyrite, and pyrrhotite.

Table 3.7: Mineral associations from sample BC-04 (Graphite-spotted marble). The table shows which mineral (left list) occurs in another (top list). The background represents the resin used for the thin section. Values are given as percentages.

Inclusion Mineral \ Host Mineral	Apatite	Calcite	Graphite	Hematite	K-Feldspar	Magnetite/ siderite	Na-Feldspar	Pyrite	Pyrrhotite	Quartz	Titanite	Background	Unclassified
Apatite	-	45.73	0.12	0.00	0.00	0.00	0.00	0.00	0.00	0.00	0.61	4.88	46.95
Calcite	0.08	-	1.03	0.02	0.04	0.00	0.02	0.00	0.00	0.12	0.12	25.25	63.17
Graphite	0.00	13.55	-	0.40	0.04	0.01	0.00	0.00	0.00	0.00	0.02	1.21	22.32
Hematite	0.00	4.13	5.23	-	0.28	2.13	0.00	2.79	0.03	0.00	0.00	3.89	61.46
K-Feldspar	0.00	8.65	0.56	0.32	-	0.00	6.04	0.00	0.00	0.08	0.00	2.36	80.34
Magnetite/ siderite	0.00	7.91	1.44	22.30	0.00	-	0.00	0.36	0.00	0.00	0.00	1.44	56.47
Na-Feldspar	0.00	5.46	0.05	0.00	7.78	0.00	-	0.00	0.00	0.00	0.00	2.99	83.30
Pyrite	0.00	3.28	0.00	66.39	0.00	0.82	0.00	-	4.92	0.00	0.00	0.00	24.59
Pyrrhotite	0.00	0.00	0.00	12.50	0.00	0.00	0.00	75.00	-	0.00	0.00	0.00	12.50
Quartz	0.00	5.89	0.01	0.00	0.02	0.00	0.00	0.00	0.00	-	0.00	6.59	86.35
Titanite	0.52	60.23	0.73	0.00	0.00	0.00	0.00	0.00	0.00	0.00	-	2.09	32.88

3.6 Electron Probe Micro Analysis (EPMA)

EPMA was carried out on samples BC-01 and BC-16 for geothermobarometric estimations of the metamorphic conditions experienced by the rocks. The full list of results from the EPMA is found in Appendix E: Chemical Analysis – Results. The results have been filtered by removing outliers in the dataset. These outliers were misidentified mineral phases, analysis of cracks or edges of mineral grains, or otherwise poor data results. The results for the amphibole analyses were particularly bad, with 65% of all point analyses being discarded due to too low oxide totals. Averages were recalculated based on the remaining point analyses and used for P-T estimations. The outliers are marked in red, and calculations of averages and standard deviations with and without the discarded data points are shown (Appendix E: Chemical Analysis – Results.).

3.6.1 Garnet Geothermobarometry (BC-16)

The analyses of garnets had reasonable standard deviations for the analysed elements. Three garnets were tested for zonation by isolating datapoints that formed traces across single garnet crystals. Two of the garnets show a clear zonation pattern of Mn-rich, Fe-poor cores, and Fe-rich, Mn-poor rims (fig. 3.26). Fig. 3.27 shows bivariate plots of the garnets' core and rim compositions, where the two data clusters are clearly defined. In addition to high Fe rims and high Mn core, a trend of more Ca-rich cores is also shown. The chemical zoning in the garnets is not visible on SEM backscatter or optical microscopy.

The plagioclase crystals of BC-16 show a linear trend in compositions, unrelated to the core or rim position of the point analysis. This trend is shown in the bivariate diagrams shown in fig. 3.28. The zonation may represent primary chemical variation in the plagioclase grain since no microtextures of the zonation are seen by an optical microscope or on backscatter images. The zonation may also represent a transition in feldspar composition between the leucosomes and the primary feldspars. A conclusion of what causes the zonation was not obtained from the results of this thesis.

By separating the linear plagioclase variation into two “endmember” populations based on the Ca content, a plagioclase-dependent P-T estimate representing the outer limits of the plagioclase composition was created to study the relationship between pressure-temperature and plagioclase composition. Two populations of data points were selected to represent the endmembers of the analyses, one to represent a high Ca-feldspar with 5 ± 0.2 wt% CaO and one to represent a low Ca-feldspar with 3.5 ± 0.2 wt% CaO.

The calculated P-T estimates utilized combinations of the core and rim compositions of both the garnets and the high and low CaO content of the plagioclase. The results of the estimates are summarized in Table 3.8 and plotted in fig. 3.29.

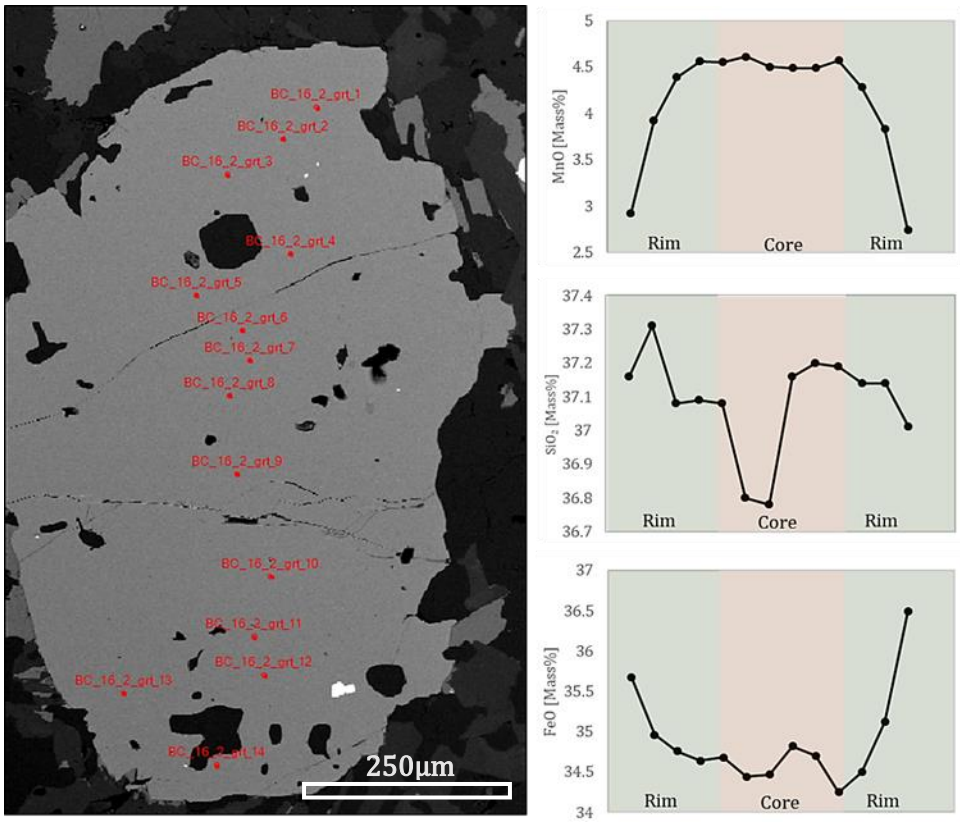

Figure 3.26: Point analyses of a garnet in sample BC-16. An image of the location of each data point is shown, together with the change in chemical composition between the core and rim.

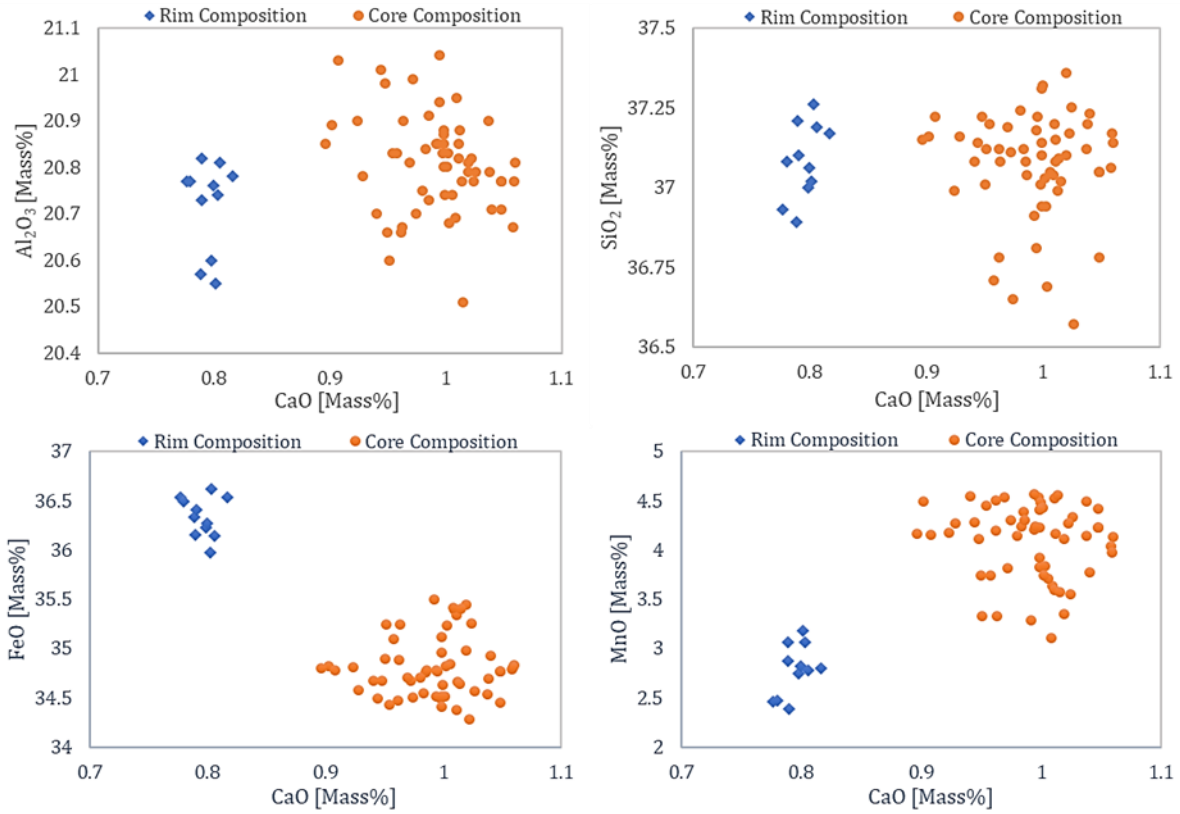

Figure 3.27: Bivariate plots of all garnet compositions of BC-16. The data used have been corrected for outliers, for full dataset see appendix C. The oxides are plotted against CaO for reference. A bimodal division of the data points can be seen in all diagrams.

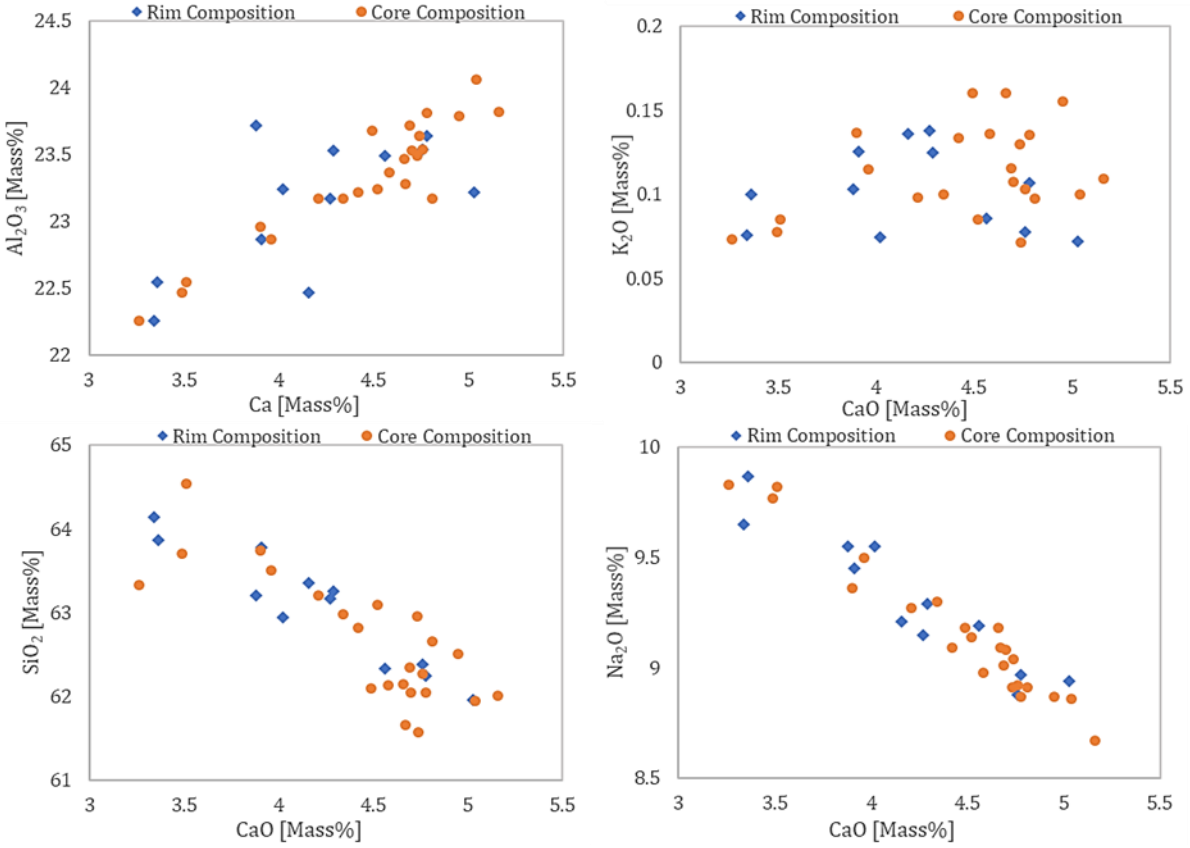

Figure 3.28: Bivariate plots of the plagioclase composition. The data used have been corrected for outliers, for full dataset see appendix C. The oxides are plotted against CaO for reference.

Only the GASP geobarometer utilized the plagioclase compositions; hence four lines representing the pressure estimate from the garnet zonation and the endmember plagioclase composition are shown in Table 3.8. The GASP estimate with the Ca-rich plagioclase corresponds well with the results from the GB+GBAQ and GBMAQ, whereas the Ca-poor plagioclase corresponds with the GM-GMAQ estimates.

Table 3.8: Results from the calculated P-T estimates using garnet geothermobarometry. The estimates are listed together with the uncertainty of the estimates if stated in the publication.

Garnet Geothermobarometry

	Garnet Rim		Garnet Core		Uncertainties	
Type	**T** [°C]	**P** [Bar]	**T** [°C]	**P** [Bar]	$\mathbf{T_{Error}}$ [°C]	$\mathbf{P_{Error}}$ [Bar]
GB+GBAQ	631	4222	647	4519		± 1800
GM+GMAQ	535	3367	545	3518	± 60	± 1400
GBMAQ	633	4976	648	5057		± 800
GASP High Ca Pl		2797	4726	3653		± 800
GASP Low Ca Pl		4292		5180		± 800

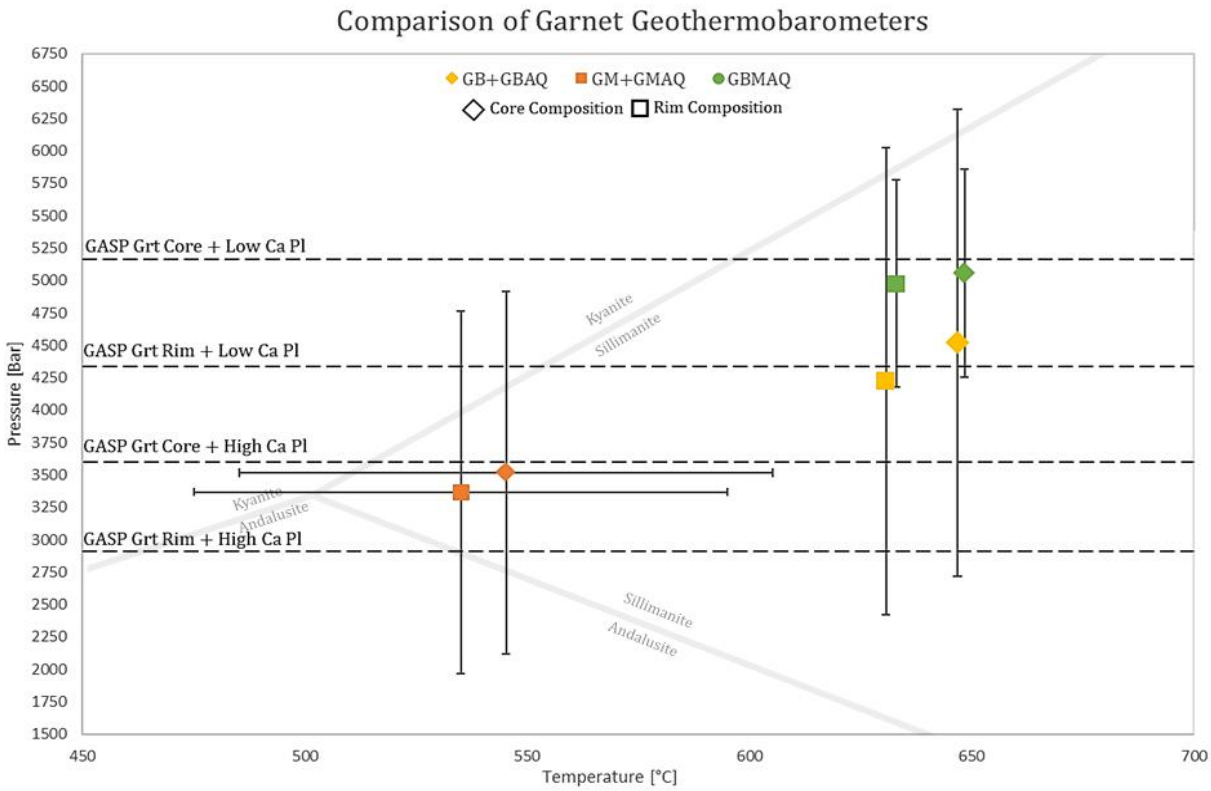

Figure 3.29: Diagram showing the comparison between the garnet geothermobarometers used and the estimate uncertainties. Dashed lines represent the GASP geobarometer (Holdaway, 2001) with the corresponding composition of garnet and plagioclase used for the estimate (±800bar).

The muscovite-derived GM geothermometer estimates lower temperatures than the biotite-derived GB, which indicates that the biotite and muscovite within the sample are not in equilibrium. Optical microscopy of the sample revealed that there are seemingly two generations of muscovite, one anhedral phase with fibrolite needles within the core of the muscovite grains, and one euhedral muscovite with no visible alteration. The easily visible euhedral muscovite is likely overrepresented in the EPMA dataset due to the difficulty of distinguishing the anhedral muscovite within surrounding quartz and feldspar grains on the backscatter image.

Interestingly the GBMAQ geothermobarometer, which also utilizes the muscovite composition, similar to the biotite-derived GB+GBAQ. It is not clear why this is the case, although it may result from the calibrations used when creating the geothermobarometers.

3.6.2 Calcic Amphibole Geothermobarometry

The amphiboles in sample BC-01 were classified using the EPMA results, which plotted within the magnesio–hornblende field of the Ca-amphibole subgroup (Hawthorne *et al.*, 2012; Li *et al.*, 2020).

The filtered data from the amphibole analyses is seen in fig. 3.30. No indication of a zonation or notable compositional variation within the dataset is observed. The average of the data was therefore used for further P-T calculations.

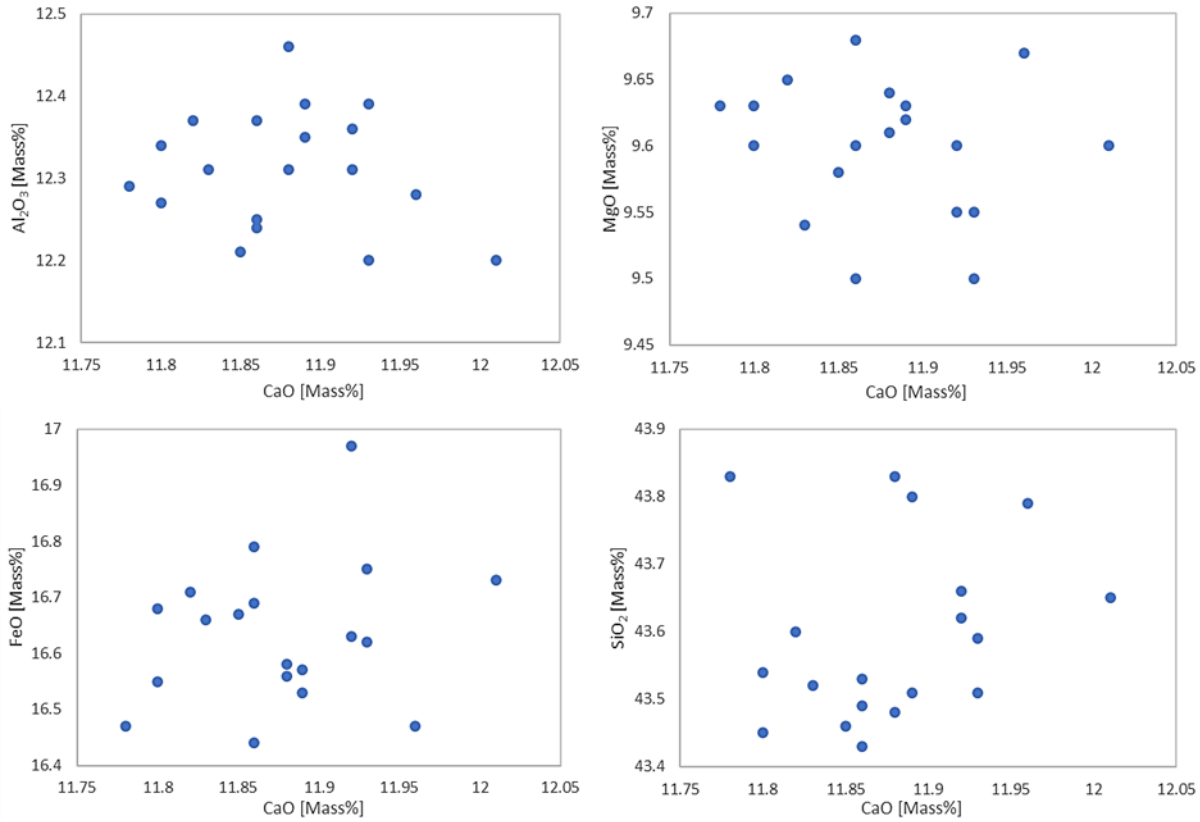

Figure 3.30: Bivariate plots of the amphibole compositions. The data shown is without outliers.

A zonation in the plagioclase of sample BC-01 can be seen with optical microscopy and SEM backscatter images. The zonation is observed as a core with, or surrounded by, a mantle of sericitisation or minor inclusions and an unaltered rim. The alteration can often be seen as a ring separating the rim and core of the plagioclase (fig. 3.31). The zonation was studied by selecting an array of data points that formed a trace through a plagioclase grain. The results showed that the rim and core compositions were similar. However, the alteration zone was characterized by a higher content of Al_2O_3 and CaO and a lower SiO_2 and Na_2O. The bivariate plots in fig. 3.31 show the same trends in a separate feldspar grain.

The alteration zone is also commonly dominated by sericite. Analyses of the very fine-grained sericite are likely the origin of many of the outliers in the plagioclase dataset since these outliers usually contain a high K content. The rim of the plagioclase grains is in equilibrium with the amphiboles in the sample. The P-T estimate shows that the alteration zone is consistently lower than the core/rim compositions.

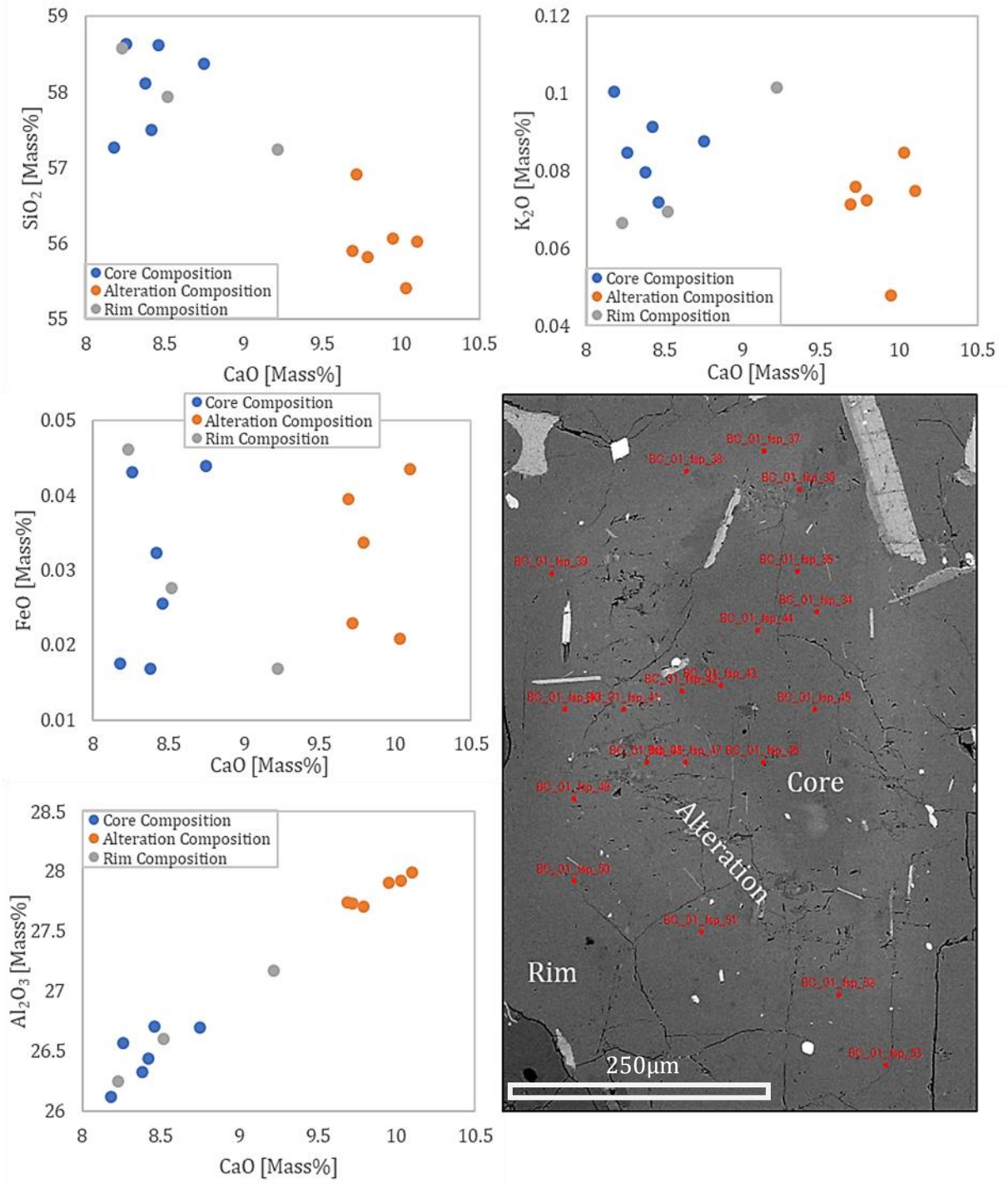

Figure 3.31: Bivariate plots showing the chemical zonation within the BC-01 plagioclase. The backscatter image shows a zoned feldspar grain with an alteration zone between the core and the rim. Datapoints used in the diagram are marked in red on the picture.

The rim and core compositions were combined into one class, separated from the alteration composition, and used for P-T estimate calculations. The altered plagioclase yields a pressure of 6156±600 bar and a temperature of 740±75°C, whereas the rim/core composition yields 6755±600 bar and 709±75°C. The P–T estimations from the quartz dioritic dyke (BC-01) are considerably higher than the host rock (BC-16), indicating either errors in calculations or a geological explanation. This is further discussed in chapter 4.3.

3.7 Structural Geology

The structural observations and measurements in the field are, along with the post-field structural analysis, crucial for understanding the complex geometry of the marble occurrence in Vassbygda. The following subchapters present the structural observations from the area together with calculations and plots used for further interpretations. The Vassbygda area is the main focus of this thesis; however, other structurally important observations outside the area are also presented and used for the discussion in chapter 3.7.2. The structural framework and geometry of the Vassbygda area are further discussed in chapter 4.2. A proposed chronological evolution of the structural and magmatic events can be found in chapter 4.4.

3.7.1 Structural Observations of the Vassbygda Area

As previously mentioned (chapter 3.2.2), the siliciclastic metasedimentary rocks form sequences with a gradual transition into marbles (fig. 3.32). The layers range in width from a few centimetres to several hundred meters. No undisturbed bedding (S_0) or primary sedimentary structures were observed during the fieldwork. It is unclear how many repeating sequences of siliciclastic metasedimentary rocks and marbles there are in Vassbygda due to the later folding of the original sedimentary character.

Figure 3.32: Transition between the siliciclastic metasedimentary rocks and the banded marble. The transition is characterized by a gradual influx of increasingly wider bands of impure calcite marble.

The overall trend of the rocks is north-south striking. However, one or more large-scale folding events have altered the geometry of the siliciclastic ridges. This folding is particularly visible by the Liaheia and Stormarkheia ridges, which deviates from the overall north-south trend of the area. They are deformed into open folds with thick hinge zones and thin limbs, which results in the characteristic geometry of central Vassbygda (fig. 3.3). The pattern of the metasedimentary units resembles a surface pattern of a type 2 fold interference (Ramsay & Huber, 1987).

The dominant planar structure of the area is a strong foliation (S_1) of the siliciclastic metasedimentary rocks and the banding of graphite and clastic fragments in the marble units. It is not evident that the foliation evolved along bedding planes due to the lack of visible primary sedimentary structures. However, the transition between the marble units and the siliciclastic metasedimentary rocks are parallel with the foliation (fig. 3.32). Indicating that the foliation may be in places regarded as a transposed bedding (i.e., S_{0+1}). Foliation planes are usually on cm-scale but may be challenging to observe in the marbles due to the lack of siliciclastic components. The

graphite-spotted marble units show only a weak foliation compared to the finer-grained banded marble. Microscopically, the foliation seen within the siliciclastic metasedimentary rocks is defined by recrystallized biotite and muscovite crystals (fig. 3.12 A) or shape-preferred orientation of calcite, feldspar, or calcite grains (fig. 3.8 A).

All measurements of the dominant foliation in the field area are shown in fig. 3.34. The stereonet shows a wide scatter in orientations: One cluster of poles occurs in the south-western quadrant (east-northeast-dip); however, this is likely an overrepresentation of the easily accessible parallel metasedimentary layers of eastern Vassbygda (fig. 3.3). The overall scatter illustrates that the measured foliation is either folded or composed of several generations of foliation, or both. Although a best-fit plane and corresponding L-pole can be constrained (fig. 3.35), the scatter is much too big to be explained by one simple folding phase. This data is further explored in chapter 3.7.4.

The S_{0+1} foliation is frequently folded into tight to isoclinal F_1 folds with typical sub-horizontal to shallowly plunging fold axes (fig 3.35 and 3.33) and west to northwest subhorizontal to shallowly dipping axial planes. A weak crenulation cleavage (S_2) is observed throughout the siliciclastic metasedimentary rocks where the isoclinal folding is dominant. Frequent mineral crenulation lineation (CL_1) occurs parallel to the isoclinal fold axes. Some tight to isoclinal folds are also defined by a vertical to sub-vertical axial plane, although these are rare.

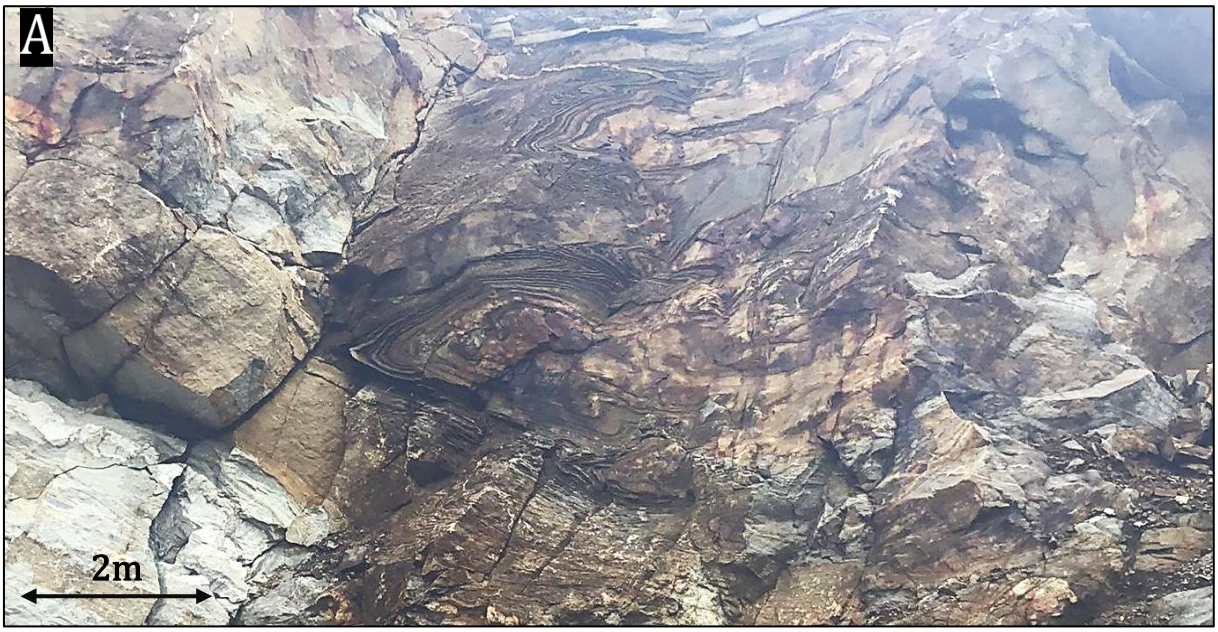

Figure 3.33: Isoclinal folding in the marbles and siliciclastic metasediments. **A**) Tight to isoclinal folding in a calc-silicate layer in the wall of an abandoned marble quarry. The fold is defined by a shallow north-northwest plunging fold axis (29→151) and a sub-horizontal to gently southwest dipping axial plane (233/20). **B**) Typical isoclinal folding of siliciclastic layers in the banded marble. The isoclinal folding of the siliciclastic metasedimentary layers in the marble is characterized by subhorizontal to shallowly dipping fold axes with gently dipping axial planes. The folds in the marbles differentiate from the siliciclastic rocks by a longer amplitude and wavelength.

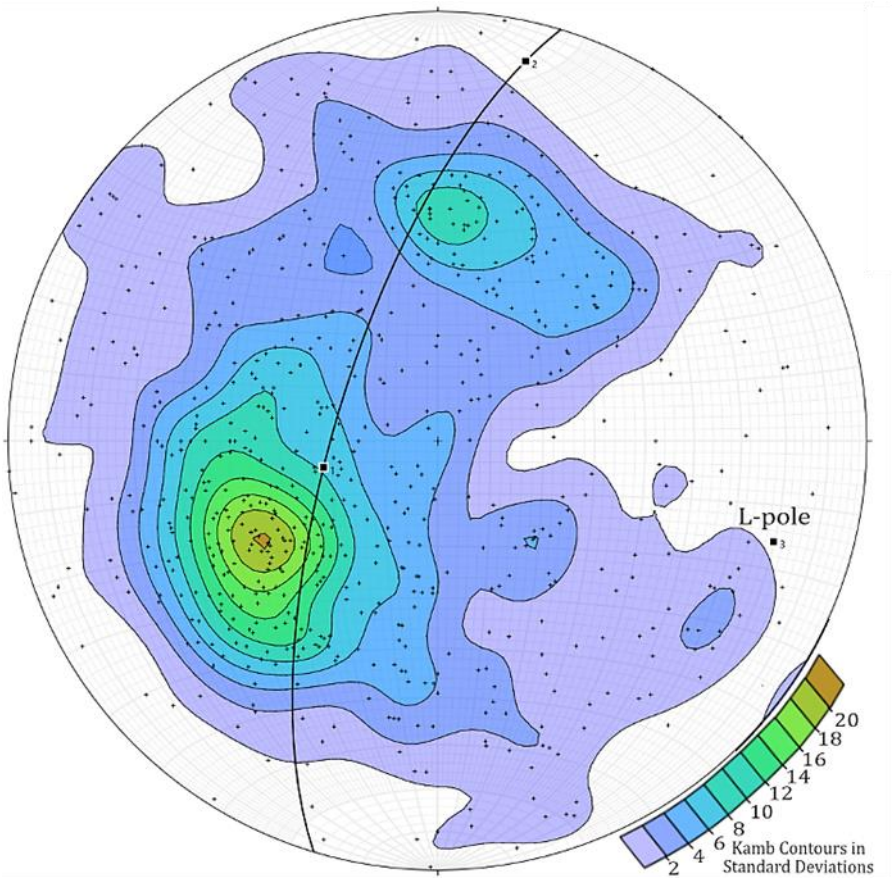

Figure 3.34: Plot of all 679 poles to foliation from the Vassbygda area. Included in the plot is the best-fit plane for all the measurements, the L-pole (20→107) for all measurements. Two clusters within the data set can be seen. See text for further description.

The isoclinal fold axes of the Vassbygda (fig. 3.35) area are typically sub-horizontal to shallowly plunging. However, an important observation is that the orientation of F_1 fold axes differs substantially throughout the field area (fig. 3.35). This implies either that a) the F_1 folding has been strongly disharmonic, or b) that the F_1 folds have themselves been refolded. Although the former may be viable to some extent in light of the high competence contrast between marbles and siliciclastic metasedimentary rocks, it cannot explain all variation as different orientations are also present within homogeneous banded marble layers. Three pronounced clusters forms from the data: The fold axes divide into the southwestern and northeastern quadrant, with a third large cluster in the southwestern quadrant. These clusters are further analysed in chapter 3.7.4.

Measurements of the axial plane cleavages (S_2) are shown in fig. 3.36. A cluster of shallowly dipping northwest striking axial planes is seen. However, not enough observations of the axial plane cleavages were made to determine if they are related to F_1 or F_2.

Four observations of a clearly symmetrical, upright open fold yielded fold axes of 25→115, 10→130, 14→057, and 41→041. These upright folds are rarely found in pristine form and are often visible refolded. A sense of an upright fold phase can be interpreted from several outcrops. However, it is rarely directly measurable.

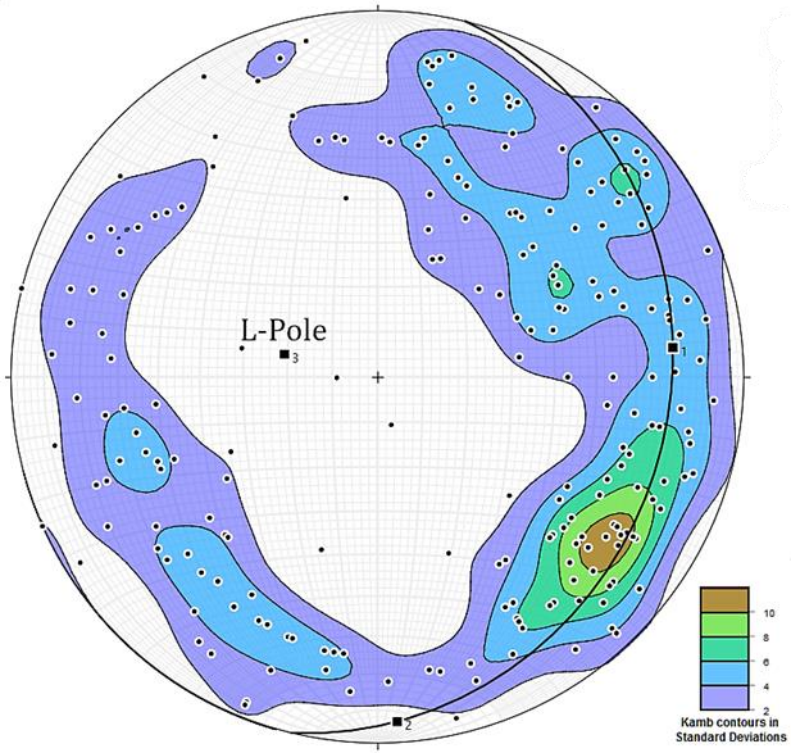

Figure 3.35: Stereonet plot of all isoclinal fold axes. The fold axes are sub-horizontal to shallowly plunging with a large cluster of the overrepresented observations from the parallel layers of the HTSZ. A best-fit plane and corresponding L-pole is shown. The L-pole indicates a hypothetical steeply northeast-plunging (64→284) fold axis.

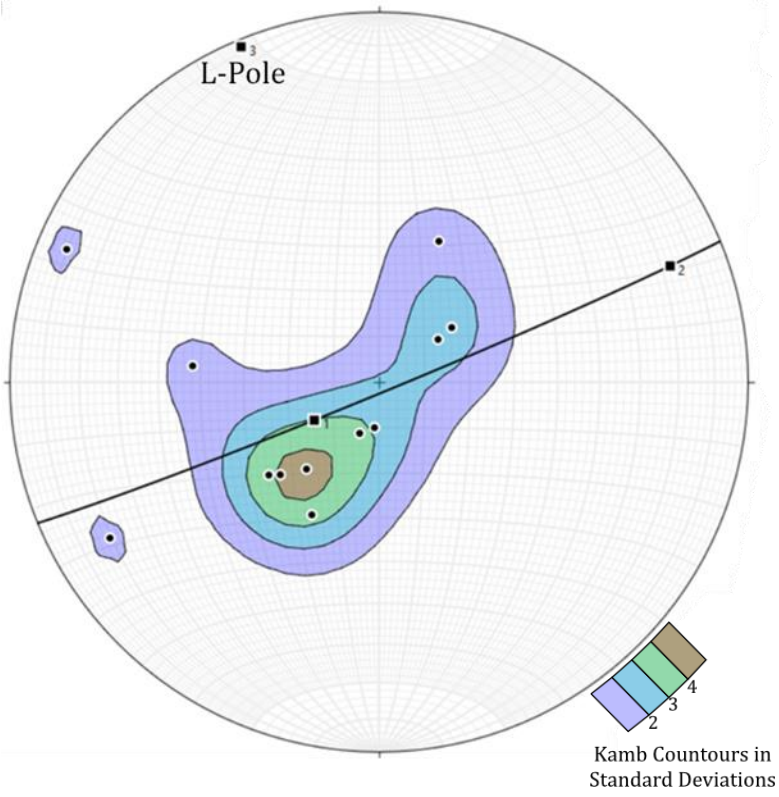

Figure 3.36: Stereonet plot of poles to measurements of axial plane cleavage. A best-fit plane and L-pole marks a hypothetical fold axis of 02→338.

The quartz diorite dykes are the most common within Vassbygda, and due to their protruding character in the topography, were often measured for dip-dip azimuth. The measurements show that the majority of the dykes are sub-vertical to steeply dipping (fig. 3.37 A).

The leucogranitic sills found on the shores of Storvatnet are usually gently to moderately dipping. The stereonet plot (fig. 3.37 B) shows two clusters of measurements of the leucogranitic sills, indicating a possible folding of the rock. A best-fit plane and L-pole (20→232) are included in the figure and described further in chapter 4.4.

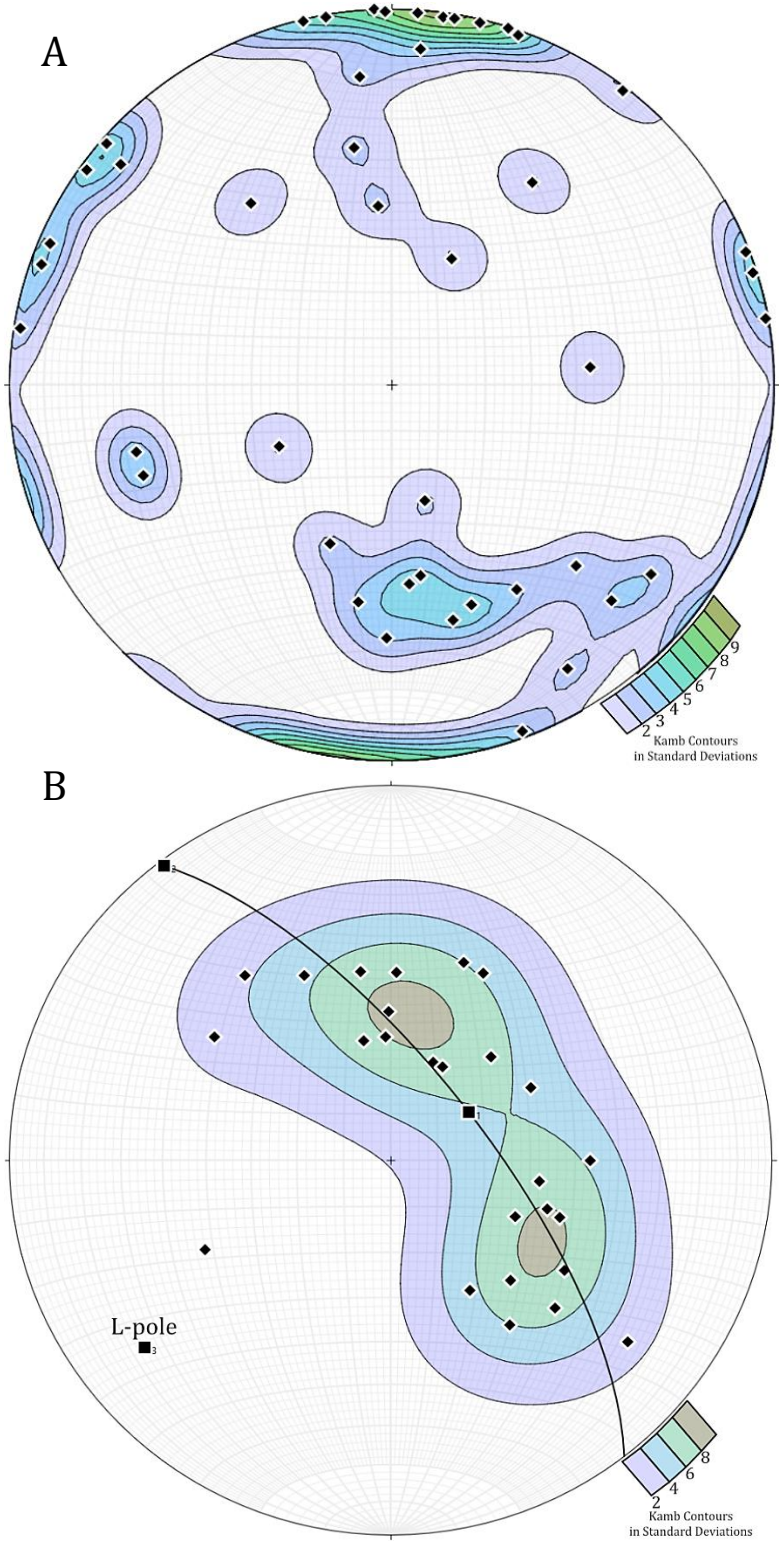

The quartz diorite is not commonly deformed, whereas the mafic dykes are typically boudinaged or folded into tight overfolded to recumbent folds. The mafic dykes appear to be deformed alongside the isoclinal folding observed through the field area. No apparent deformation of the large leucogranite sills is observed, although a vague trend of foliation-sub-parallel sills is seen. This trend is discussed in 4.4.2.

Figure 3.37: Stereonet plot of all measurements of igneous dykes and sills.

A) Stereonet plot of all quartz diorite dykes (black diamonds). The dykes are consistently horizontal to steeply dipping.

B) Plot of the shallowly dipping to sub-horizontal leucogranitic sills. A best-fit plane and L-pole (20→232) mark a possible fold axis.

3.7.2 Structural Relationship Between the Lower and Middle Nappe

A key locality in understanding the regional deformation and effect of nappe juxtaposition is the contact between the Lower and Middle nappe of the HNC. As previously mentioned, the contact is characterized by a transition from marbles and siliciclastic metasediments of the Lower nappe to mantle-derived rocks and mafic polymict conglomerates of the Middle nappe (Thorsnes & Løseth, 1991). All measurements of the foliation and mineral lineations on the boundary or proximal rocks are presented in fig. 3.43.

Overall, there is a notable change in the variability in foliation orientation from the general Vassbygda area, where orientation varies a lot, to the 500-1000m closest to the contact, where the foliation is very consistently ENE-dipping, parallel to the contact, and similar to the orientation of the Middle nappe rocks (fig. 3.35 and 3.43). The deformation along the nappe boundary, named the Heggfjord–Tosen shear zone (HTSZ), is also seen as the development of a strong mylonitic foliation (fig. 3.43) and isoclinal folding of the metasedimentary rocks. Kinematic indicators show both a top-to-the northwest reverse shear, in the form of overturned folds (fig. 3.38 1B & 1A), and as top-to-the-southeast normal displacement observed as asymmetrical (sigmoidal) clast (fig. 3.8 C).

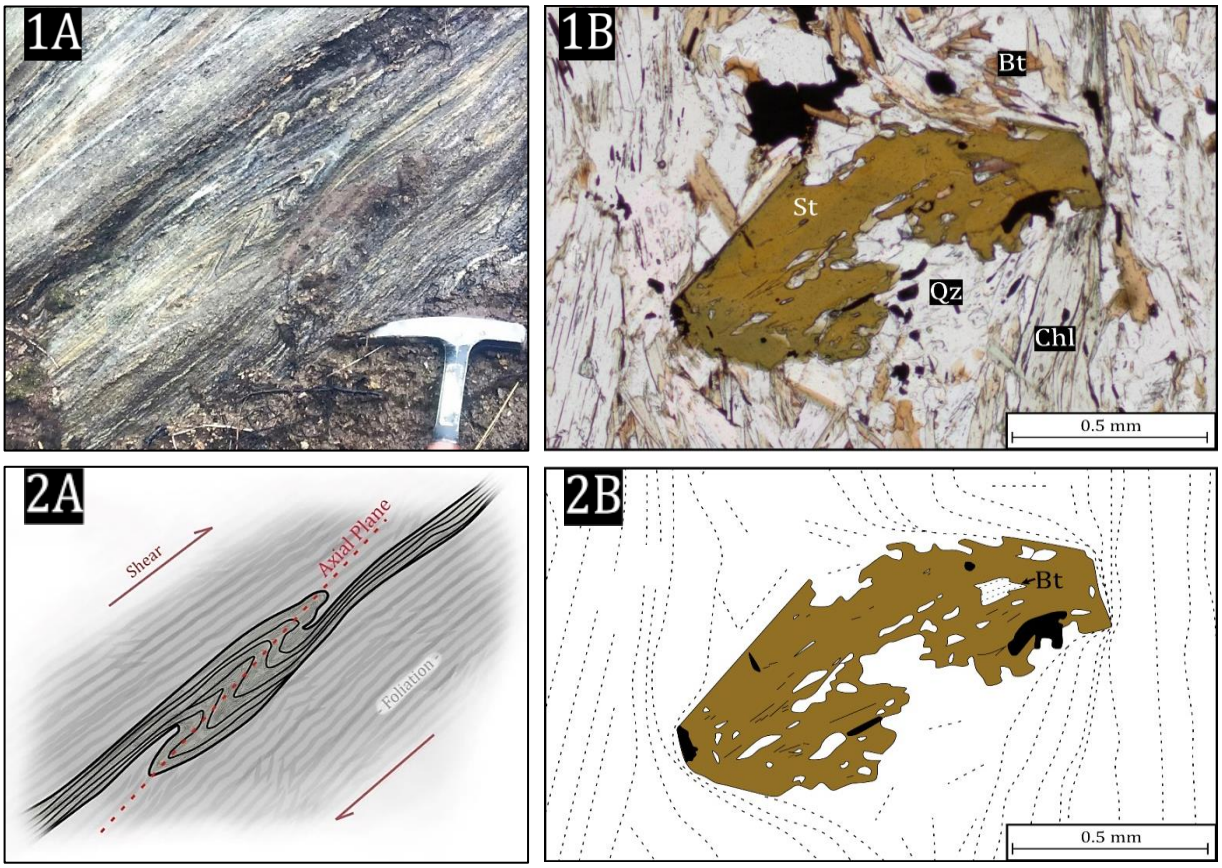

Figure 3.38:. Deformation of the Heggfjord–Tosen shear zone (HTSZ). **1A**) Calc-mylonite close to the Middle-Lower nappe boundary. The dolomitic calc-mylonite is only found close to the boundary to the Middle nappe. The picture shows an asymmetrical isoclinal intrafolial fold. The picture was taken towards the southwest. **1B**) Illustration of the fold sown in picture 1A. The axial plane indicates top-to-the-northwest shear direction. **2A+B**) PPl micrograph and illustration of a pre- to syn-tectonic staurolite porphyroblast found within the rocks close to the nappe boundary. The foliation of the trapped biotite, alongside the orientation of quartz inclusions, are close to perpendicular to the dominant foliation of the rock. St=staurolite, Bt=biotite, Qz=quartz, Chl=chlorite.

A staurolite porphyroblast found within the HTSZ shows a weak foliation of quartz and biotite inclusions (fig. 3.38 2A & 2B). The orientation of the quartz inclusions and the foliation of the trapped biotite crystals is close to perpendicular to the dominant foliation of the rock. The dominant foliation of the rocks diverts around the staurolite with vague pressure shadows on each side indicated by the infill of quartz and the lack of a clear orientation of the mica grains. This structure of the staurolite indicates pre- or syntectonic growth.

The large-scale shear deformation of the Lower nappe rocks due to the HTSZ and the development of a mylonitic foliation trend may represent a re-orientation of the S_{0+1+2} fabric into a new S_3 foliation. This shear deformation is discussed further in chapter 4.4.2.

Although the nappe contact is present within the field area (fig. 3.3), it is not directly observable due to few outcrops exactly at the contact. However, two lenses of ultramafic rocks mark the first appearance of the Middle nappe on the eastern side of the field area (fig. 1.7). The best locality is found close to the road to Nordfjellmark. Here, the marbles of Vassbygda are highly deformed and transitions into a dolomitic calc-mylonite c. 20m from the presumed nappe contact.

A section of a highly foliated chlorite-rich metagreywacke (mica schist) is found close to the calc-mylonite together with a granitic dyke (BC-06). The granitic dyke cuts the mylonite and is relatively undeformed compared to the host rock. Only a weak mineral lineation can be observed in the dyke. Microtextural analysis of the granitic dykes shows extensive myrmekite formation in feldspar grains.

About 100 meters up the road from the calc-mylonite is the first appearance of the ultramafic mantle-derived rocks of the Middle nappe (fig. 3.39 A). The body shows an apparent dunitic appearance in the bottom and gradually chances to more harzburgitic further up. The mantle-derived body shows little signs of deformation compared to the highly deformed marbles below. The deformation observed within the ultramafic rocks are small, tightly folded bands (fig. 3.39 B), and zones of isoclinal to tightly folded schistose ultramafic rocks are found on top of the large dunitic/harzburgitic body (fig. 3.39 D). A highly deformed mylonitic metagabbro can be observed further up the road to Nordfjellmark (fig. 3.39 C). This deformed rock is defined by a localized shear zone with isoclinal folds and deformed clasts. The protolith of this deformed rock may be the Åsnes conglomerate (Thorsnes & Løseth, 1991) due to similarities between the ultramafic clasts.

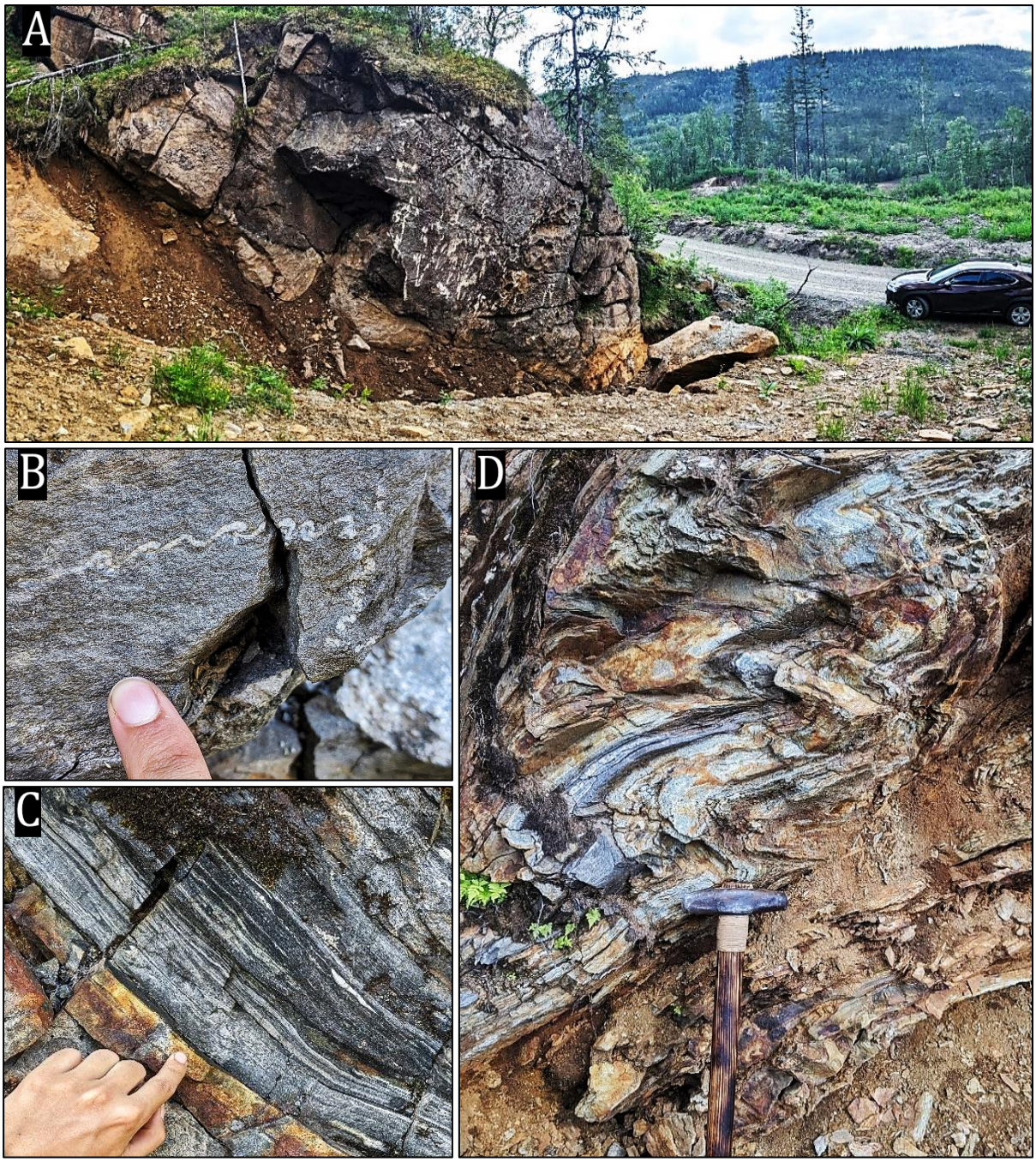

Figure 3.39: Appearance and structures of the mantle-derived rocks along the road to Nordfjellmark. **A**) The main dunitic to harzburgitic body along the road. The appearance changes from dunitic at the bottom to more harzburgitic towards the top. **B**) Localized deformation observed in the mantle-derive rocks. A small leucocratic layer has been extensively folded whereas the surrounding rocks are seemingly unaffected. **C**) Localized shear with asymmetrical folds in a mylonitic zone within a metagabbro structurally overlaying the mantle-derived body. **D**) Tight to isoclinal folds in a small, deformed zone at the top of the mantle-derived body seen in picture A.

The best location to directly observe the contact between the Lower and Middle nappe is at the shoreline close to Granneset within Heggfjorden (fig. 1.9) – a location mentioned by Thorsnes and Løseth (1991). Like the Nordfjellmarka locality, the Lower nappe directly under the contact is characterized by highly deformed marbles. The marbles are here so strongly deformed that they are often void of any clear structures. Bands of siliciclastic sedimentary rocks in the marble occur as discontinuous bands, rootless folds, or boudinaged completely into separated sections or fold hinges (fig. 3.40).

Figure 3.40: Highly deformed marble with siliciclastic bands close to the contact between the Middle and Lower nappe

A discrete transition zone defines the contact between the Lower nappe marbles and the ultramafic rocks of the Middle nappe (fig. 3.41 A). The contact plane dips steeply to the north-northeast and contains a moderately east-plunging mineral lineation (fig. 3.43). The contact is characterized by a ~30cm transition zone (fig. 3.41 D), with a cm-scale contact plane of altered rocks infrequently occurring (fig. 3.41 C). This alteration zone is often very fine-grained, white, and may stretch into both the mantle-derived rocks and the marbles. This zone likely comprises talc and serpentine, but this has not been confirmed by microscopical analysis.

A weak crenulation (likely fold axis crenulation) is observed plunging 26° towards the west in the deformed marble along with a mineral lineation of 10→135 close to the contact plane. Isoclinal folds in the deformed marble are defined by moderately dipping north-northeast plunging fold axes. The structurally overlying ultramafic rocks are relatively undeformed compared to the marbles. However, brittle deformation is observed as small faults and fractures. A clear fault event is observed within an alteration fabric close to the nappe contact (fig. 3.41 A). A set of small faults cuts the alteration fabric with a large sinistral shear component (fig. 3.41 B).

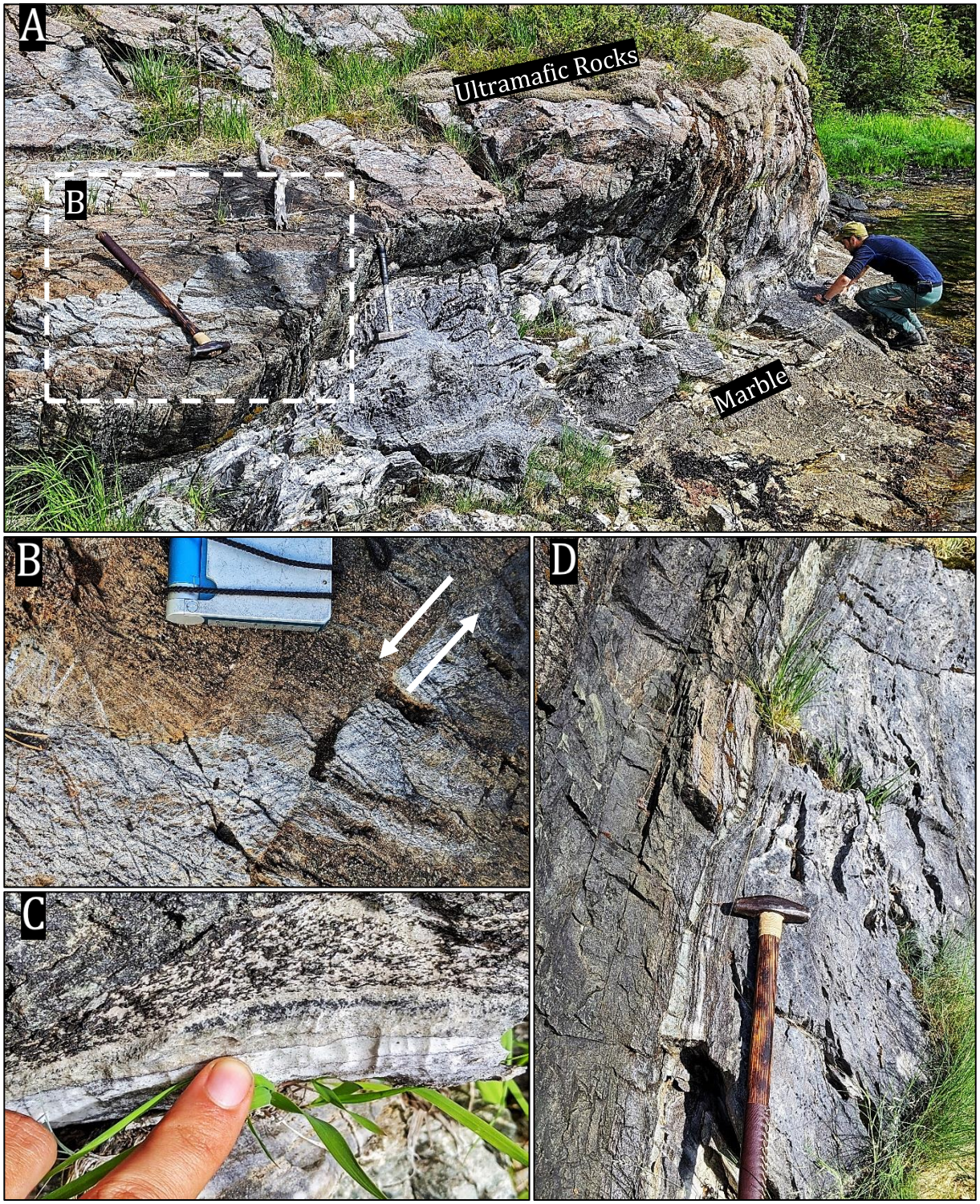

Figure 3.41: Pictures of the contact between the Lower and Middle nappe. **A**) Overview of the contact. The grey marbles of the Lower nappe are overlaid by the brown ultramafic rocks of the Middle nappe. A white alteration fabric in the mantle-derived rocks is cut by the contact. The stippled box marks the location of picture B. **B**) Close up of the alteration fabric. The fabric is cut by pairs of small faults with sinistral displacement. **C**) A cm-scale alteration zone defines the contact plane. **D**) The contact is a sharp transition between the deformed marbles to the relatively pristine ultramafites.

The ultramafic rocks contain small, localized shear zones located about 50m north of the Middle–Lower nappe boundary. This zone consists of a ~20-30 mm wide sub-horizontal main shear plane (002/48) and two wider inclined ramps (072/46) (fig. 3.42 A). The shear zone is well foliated with thin, very fine-grained laminas interpreted as talc, serpentine, and chlorite. A talc rich mineralization zone also surrounds the core of the shear zone. Lineations in talc on the main shear plane measure 24→066, with 43→099 observed on the ramp plane. The foliation in the ramps clearly bends into the flat-lying shear zone, indicating a sinistral-reverse sense of movement (fig. 3.42 B). The ramp-plane structures resemble a large-scale S-C shear fabric.

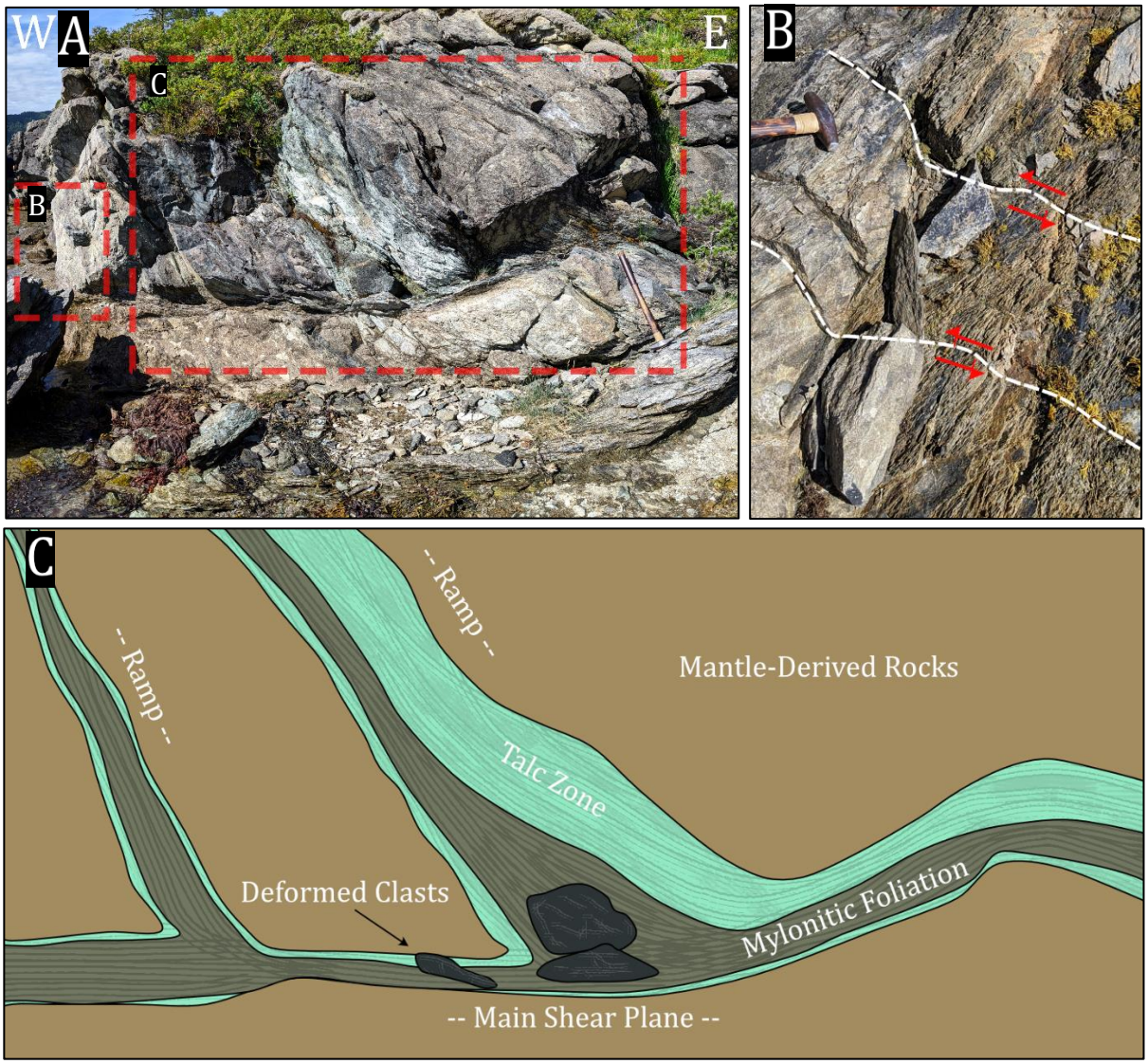

Figure 3.42: Shear zone in the mantle-derived rocks at the bottom of the Middle nappe. **A**) Overview picture of a shear plane with two corresponding ramps. Marked on the picture is the location of picture B and illustration C. **B**) Brittle deformation observed in the bottom of the shear zone with A "staircase"-pattern of sinistral faults in the mylonitic foliation. **C**) The shear zone is localized along a small (~20 – 30 cm wide) sub-horizontal main shear plane, defined by a fine-grained mylonitic foliation and two corresponding inclined ramps. A zone of talc with varying thickness surrounds the shear planes. The main shear plane and ramp texture are reminiscent of an S-C fabric. See text for further descriptions.

This kinematic interpretation is supported by elongated deformed asymmetric clasts within the shear plane. The main shear plane is deformed by later small brittle faults (fig. 3.42 C). These faults cuts and displaces the highly foliated shear zone and form repeated faults in a “staircase”-pattern. The faults are sub-vertical to steeply dipping with sinistral displacement.

A top-to-the northwest vergence is observed on the Heggfjorden localities, whereas the Nordfjellmark area contains both top-to-the southeast and northwest.

The summarized results from all foliation and mineral lineation measurements on the contact plane or in proximal rocks are seen in fig. 3.43. The principal mean plane indicates an overall north-east gently dipping contact, although the boundary is commonly alternating a fair bit along the contact trace. The mineral lineations plots along the principal mean plane and are generally west to west-northwest plunging. The interpretation of these results is further discussed in chapter 4.4.2.

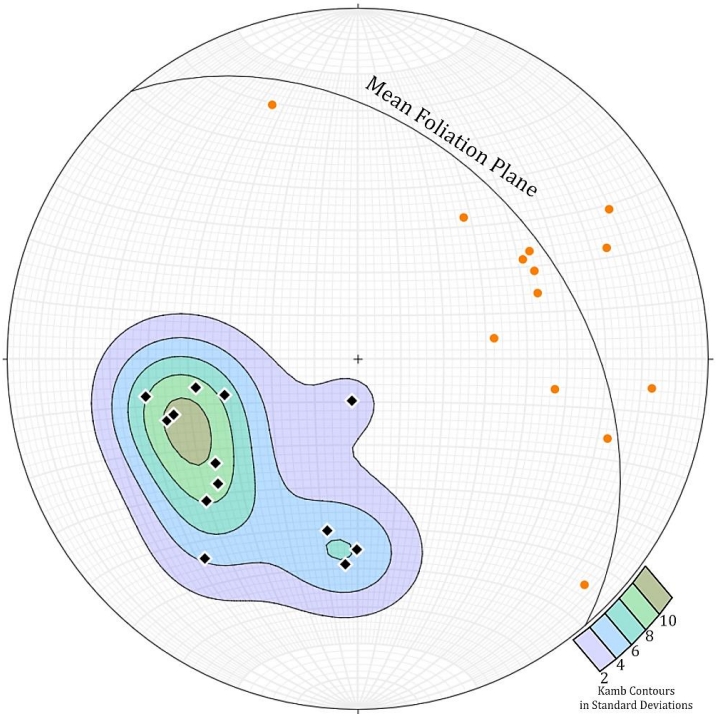

Figure 3.43: Stereonet showing the foliation (black) and mineral lineations (orange) measured on, or close by, the contact between the Lower and Middle nappe. Included is the mean principal plane for all foliation measurements.

3.7.3 Large-Scale Lineaments

Two large-scale lineaments can be seen on the topographical map of Vassbygda and can be followed clearly with the hillshade image from the DEM dataset (fig. 3.44). The smallest of these lineaments is observed in the hillside on the southern part of Hardangsfjellet. It can be traced from Brenneset in the Vågan fjord, over Hardangsfjellet, and northeastwards, following Fiskbekken upstream. The trace continues through Stormaka, cutting the Stormarkheia and Svealia ridge and fading out north of Høgåsen on the eastern side of the field area. It is unclear from the DEM if the lineament continues into the Middle nappe. The observable length of this lineament is close to 12km. Observations and structural measurements within and close by this lineament do not indicate any visible displacement of the adjacent rocks.

The largest lineament can be traced from Vågan and along the southern hillside of Hardangsfjellet. Here it deviates from the Fiskbekken lineament and strikes east through Fjellvatnet and Storvatnet and follows Auneelva up towards Barstad before fading out north of Lande. A subsidiary of this lineament can be followed across Landseterfjellet and northeast through Landkskåkdalen before entering Tosenfjorden south of Kråkhaugen. The observable length of this lineament is ~22km. There is no direct evidence for displacement along this lineament; however, it is evident from the trace that it cuts the Lower–Middle and Middle–Upper nappe boundary. The lineament also seems to define the rock boundary between the banded marbles and the mica schists at Langdalsstranda, south of Fjellvatnet. This transition is relatively sharp compared to other marble-siliciclastic metasedimentary rock transitions of the field area.

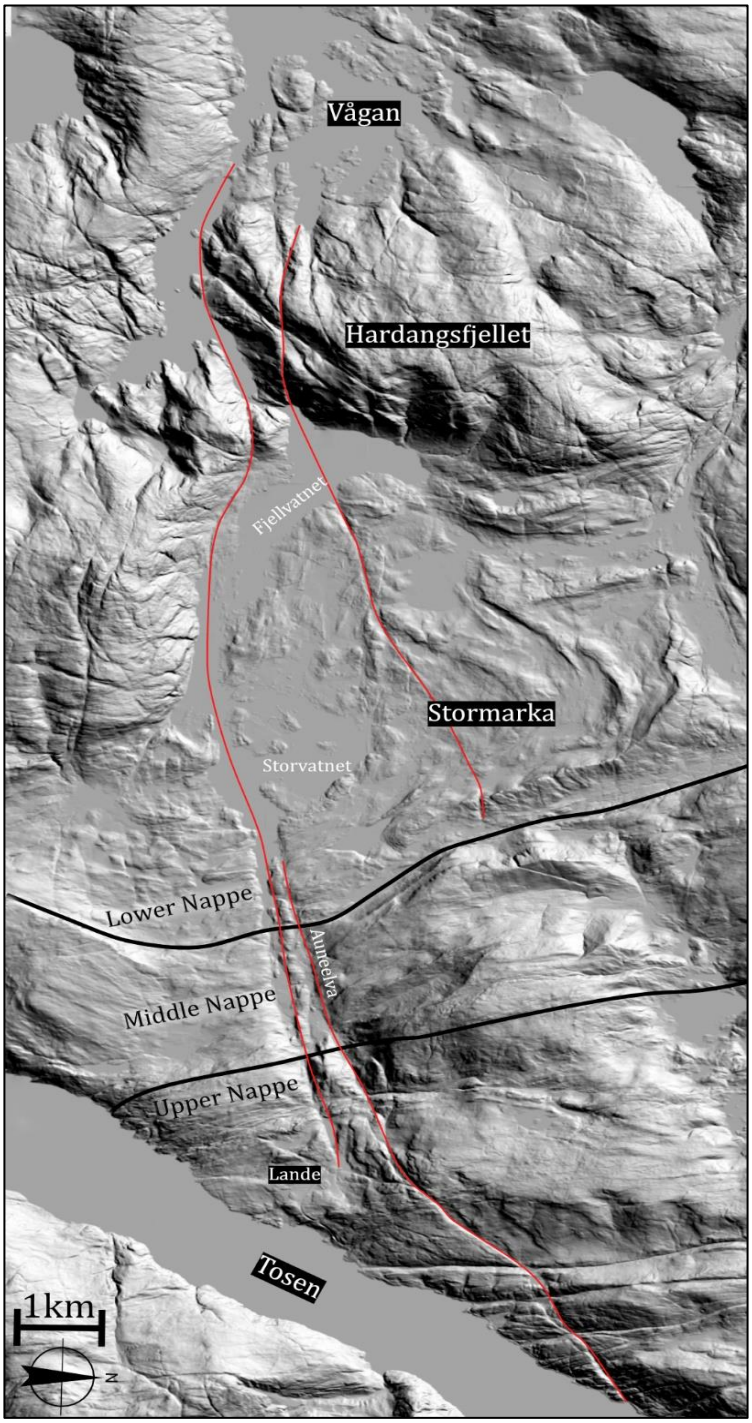

Figure 3.44: Hillshade image of the large-scale lineaments in Vassbygda. The red lines represent the trance. Only the longest lineament appears to cut the Lower–Middle nappe boundary. Hillshade image form hoydedata.no. Approximated Middle–Upper nappe boundary from Barnes and Prestvik (2000).

3.7.4 Folding Analysis Based on Structural Data

The large scatter of structural data may be due to the refolding of the isoclinal folding observed in the field. This chapter utilizes data analyses and calculations to explore the presence and character of multiple possible folding phases.

As indicated in fig. 3.34 and 3.35, the foliation and isoclinal fold measurements from Vassbygda are likely refolded by a second fold phase (F_2), which was not directly observed during fieldwork. Although some indications of an open upright fold were occasionally seen as interference in some isoclinal folds of the siliciclastic metasediments, few direct measurements could be made. The presence of a larger fold structure is primarily inferred from the topography and geometry of the siliciclastic metasediments surrounding Stormarka (fig. 3.3).

This will be analyzed from different perspectives. First, a folding analysis of the two most structurally relatable areas. These areas show a relatively consistent structural trend compared to the more complicated Stormarka area and can be analysed to establish folding relatively unaffected by interferences. Secondly, the complex Stormarka area can be dissected into the large-scale folds seen within the siliciclastic metasedimentary ridges. Analysis of these folds can help to unravel the complicated fold pattern.

3.7.4.1 Fold Analyse of the Southwestern and Northeastern Field Area

Structural measurements form the shorelines fo Fjellvatnet and the northeastern areas of the field area (fig. 3.45 A) is considerably less chaotic than the Stormarka area. These areas show clear structural trends where the foliation measurements exhibit little variation and where the fold axes plot along the mean foliation plane (fig. 3.45 B & C). An analysis of whether these areas represent different fold limbs to F_2 was therefore performed.

The northeastern area (fig. 3.45 B) is characterized by an intermediate northwest dipping foliation (328/36), and shallowly southeast to northeast plunging fold axes. The fold axes plot along the mean foliation plane, which indicates that the fold axes have been folded alongside the foliation. Interestingly, the fold axes form two distinct clusters: one moderately northeast-plunging and one shallowly south-southeast-plunging. The area is significantly deformed by the HTSZ, which may indicate that the observed mylonitic foliation has overprinted the S_{0+1} foliation, although the measurements for this analysis was chosen such that the distance from the HTSZ would reduce this uncertainty.

In the southern area (fig. 3.45 C), foliation dips shallowly to intermediate to the southwest (198/35), and fold axes plunge shallowly southeast to southwest. The fold axes follow the mean foliation plane, similarly to the northeastern area. The two clusters of fold axis measurements seen in the northeastern data are not evident in the southwestern area.

The combined data of the two areas are shown in fig. 3.45 D. The plot shows that the two areas can be combined in F_2 fold structures characterized by a shallowly southeast-plunging fold axis (16→122), a sub-vertical axial plane (034/87) and an interlimb angle of 102°. The axial plane of this folding is sub-parallel to HTSZ and most likely related to the shear deformation. The connection between the F_2 folding and the shear deformation along the nappe boundary is discussed in chapter 4.4.2. The calculated axial plane of the refolding is also similar to the L-pole calculation of the axial plane cleavages (fig. 3.36).

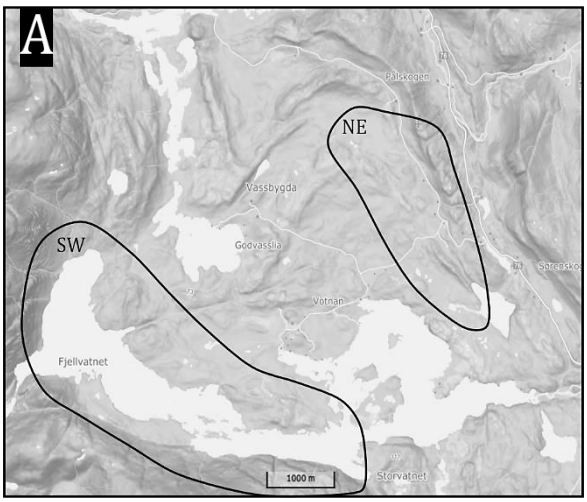

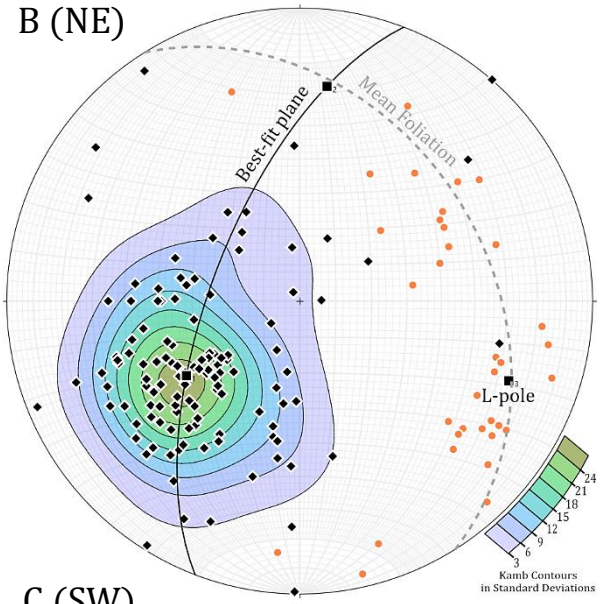

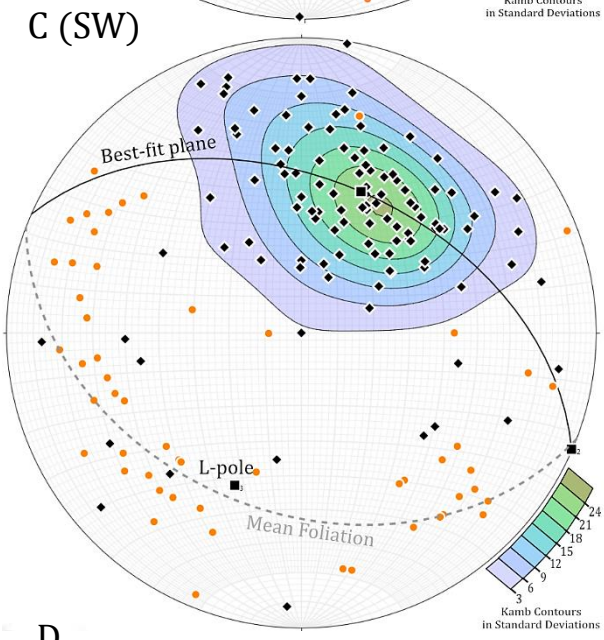

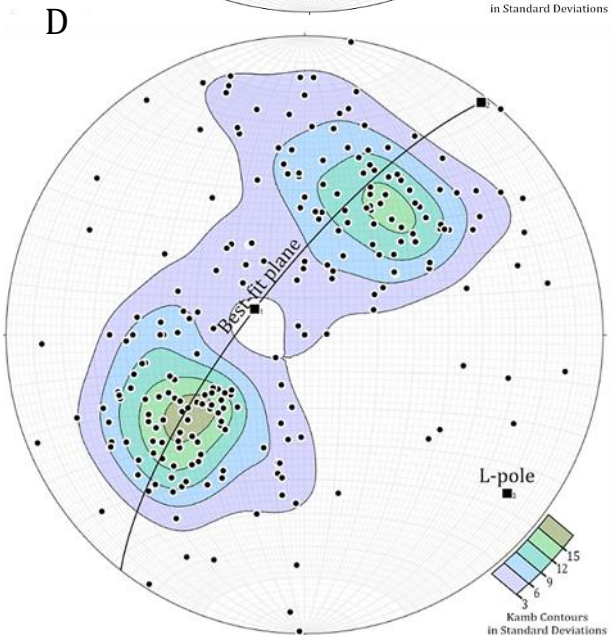

Figure 3.45: Plots of the isoclinal fold axes and poles to the foliation of the structurally distinct areas.

A) Map of separated structural observations. The circles show two areas, a southwestern (C) and a northeaster (B), with clearly defined foliation trends. Background map from norgeskart.no

B) Foliation and fold axes of the northeastern part of the field area, affected by the HTSZ. The poles to the foliation plots in a single cluster, with a mean principal plane of 062/40. Fold axes forms a scatter line along the principal mean plane of the foliation.

C) Foliation and fold axes of the southwestern area. The mean principal plane defines an average foliation of 198/35, with the F_1 fold axes plotting along the mean principal plane.

D) Combined foliation of the southwestern and northeastern area. A best-fit plane marks a possible fold axis (L-pole) of 16→122 and, which is an open upright fold with an interlimb angle of 102° and an axial plane of 034/87.

3.7.4.2 Unravelling the Stormarka Geometry

The F_2 fold phase that refolds F_1 isoclinal folds has created an intricate fold interference pattern, clearly shown by the clastic metasedimentary ridges surrounding Stormarka. Here, large scale folding deforms the ridges with several perceived fold axes resulting from the fold interference (fig. 3.46). To study the F_1 fold phase, the large-scale folds were analysed separately to analyse the geometries of the fold phases that cause in the interference.

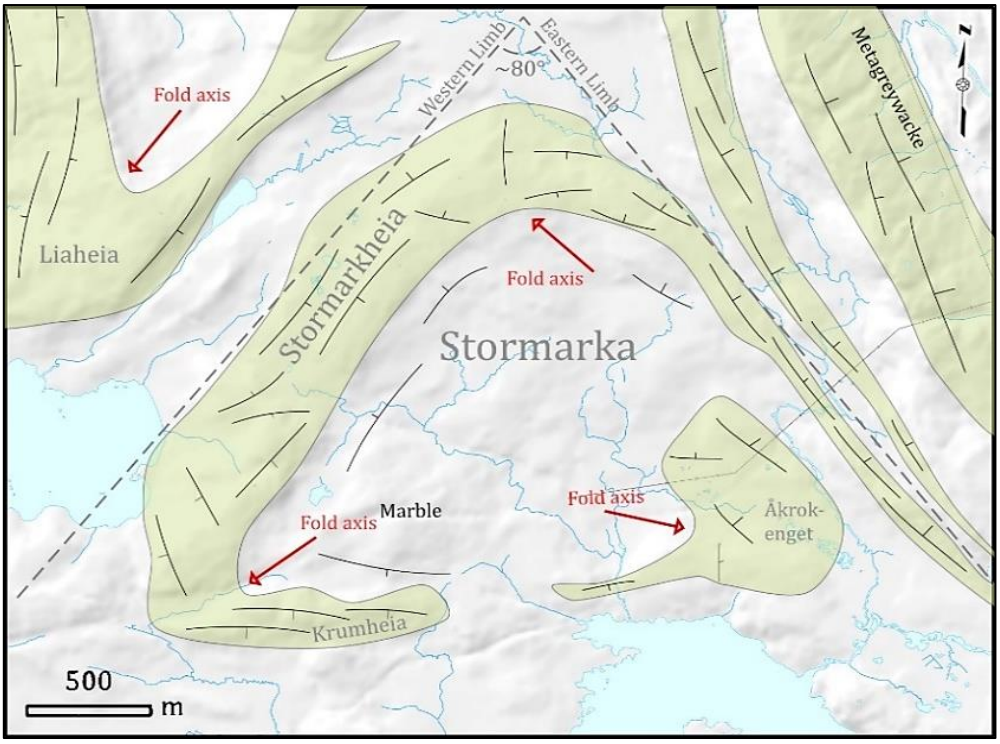

Figure 3.46: Simplified geological map of Stormarka with indicated large-scale fold axes.

The appearance and structural measurements of the large-scale Liaheia and Krumheia folds were interpreted to represent the F_1 isoclinal folding. The Liaheia and Krumheia foliation and isoclinal fold axes measurements are shown in fig. 3.47 and 3.48, respectively, and are characterized by moderately plunging fold axes. The best-fit plane and corresponding L-pole to the foliation measurements of the Liaheia fold coincide with the measured fold axes, which indicates that the deviation observed within the foliation results from the F_1 isoclinal folding. On the other hand, the Krumheia fold axes are more scattered and may indicate some interference by later fold phases. These large-scale folds, especially Liaheia, are not significantly affected by F_2 folding and should represent the F_1 folding.

The Åkrokenget fold measurements (fig. 3.49) show shallowly south-southwest-plunging fold axes. This fold axis differs from the aforementioned Liaheia and Krumheia fold axes, in that the measured Åkrokenget fold axes, and calculated L-pole, seem to coincide between the perceived F_2 fold axis, derived from the connection between the southwestern and northeastern sections (chapter 3.7.4.1, fig. 3.45 D), and the strike of the F_1 axial plane, interpreted from the Liaheia fold (fig. 3.47). This combination indicates that the Åkrokenget fold axis results from the F_{1+2} interference.

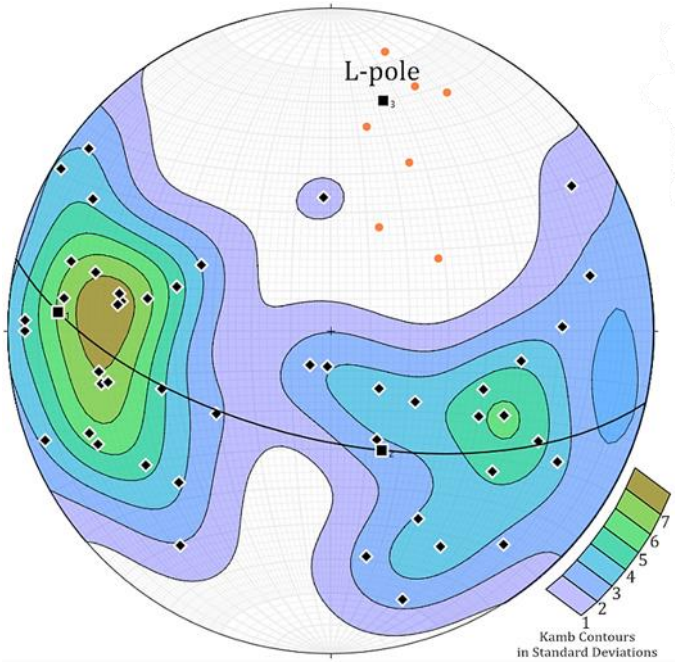

Figure 3.47: Stereonet sowing the poles to the foliation (black) and fold axes (orange) of the **Liaheia** fold. The best-fit plane and corresponding L-pole marks a shallowly north-northeast-dipping fold axis.

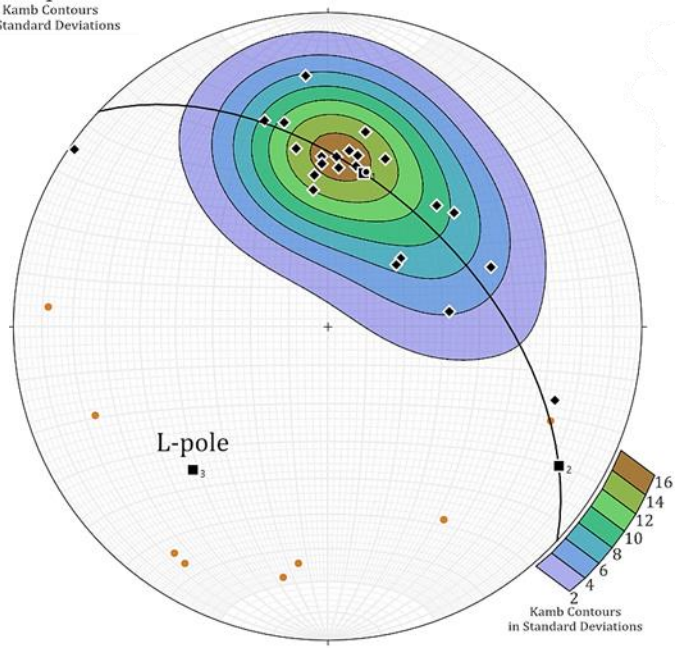

Figure 3.48: Stereonet plot of foliation (black) and fold axes (orange) surrounding the **Krumheia** fold. The best-fit plane marks a fold axis (L-pole) of 34→220.

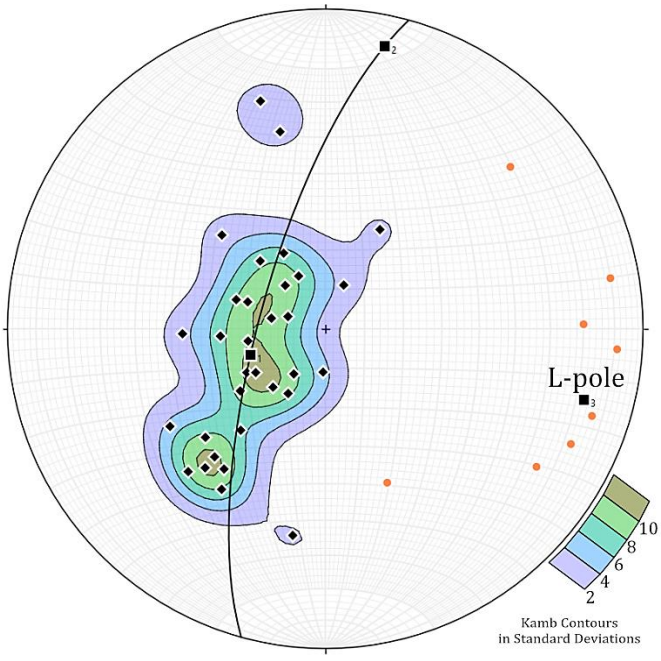

Figure 3.49: Stereonet plot of foliation (black) and fold axes (orange) measured on **Åkrokenget**. The best-fit plane marks a fold axis (L-pole) of 19→101.

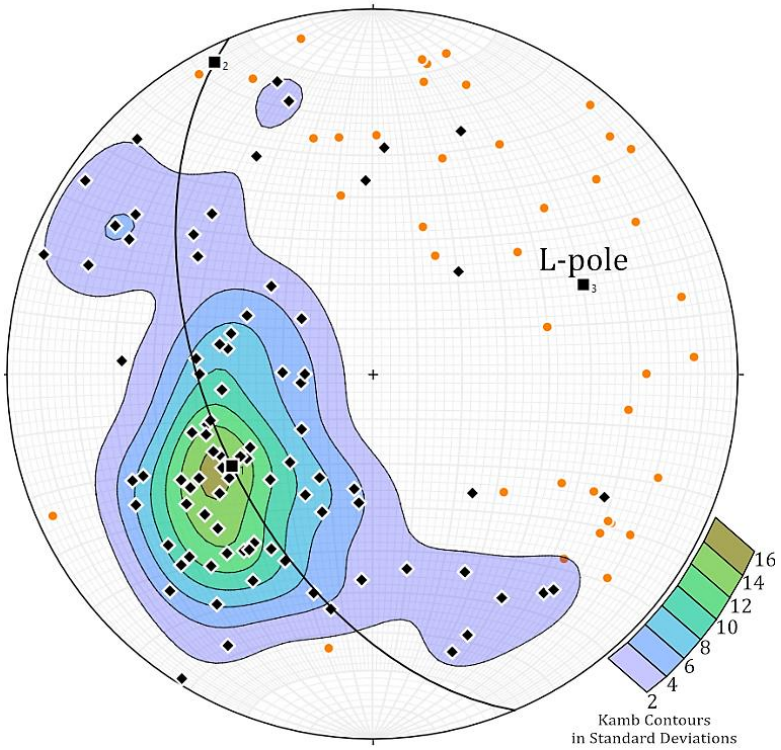

Figure 3.50: Stereonet plot of foliation (black) and fold axes (orange) measurements of the Stormarkheia fold.

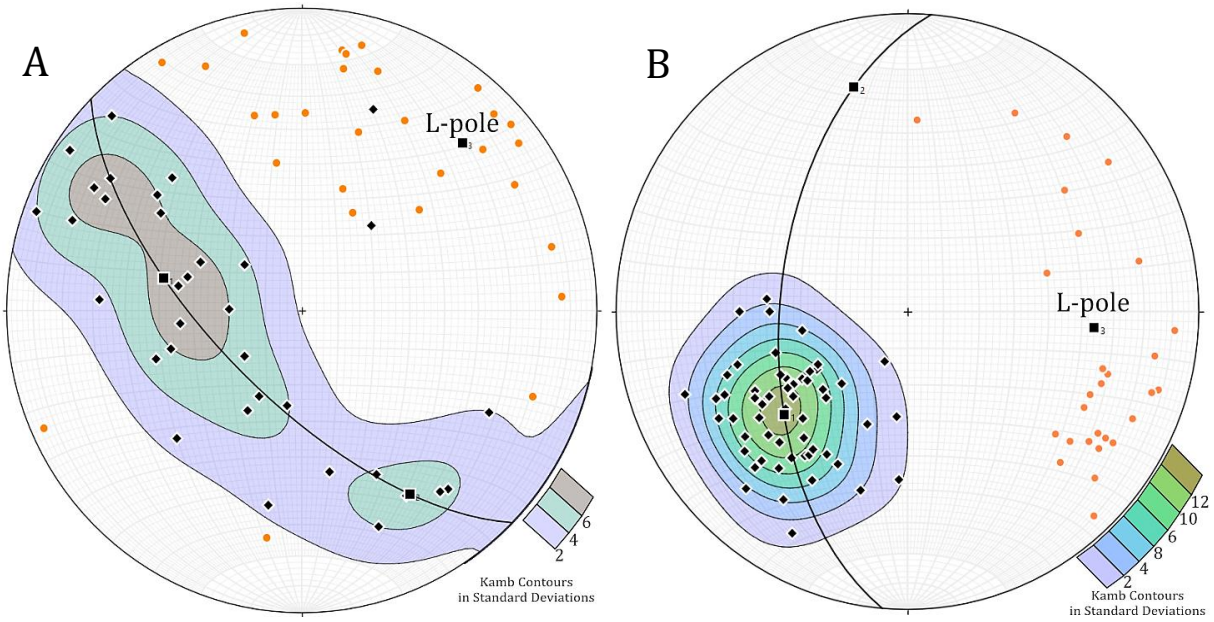

Figure 3.51: Stereonet plots of foliation (black) and fold axes (orange) from the western (**A**) and eastern (**B**) limbs of the Stormarkheia fold. Western L-pole=22→046, eastern L-pole = 36→095.

Finally, the Stormarkheia fold (fig. 3.46) is the most chaotic of the large-scale folds. Stereonet plots of the foliation and fold axis measurements (fig. 3.50) could not determine the fold axis of the Stormarkheia fold. The variation within the dataset indicates that the ridge is clearly affected by at least two non-parallel folding phases. To further analyse the Stormarka fold, the dataset was divided into western (fig. 3.51 A) and eastern limbs (fig. 3.51 B). The interlimb angle of these libs is approximately 80° (fig. 3.46).

The foliation measurements on the eastern limb deviate significantly. A best-fit plane marks a shallowly northeast-plunging L-pole, which describes the possible fold axis. However, the measured fold axes of the western limb show a significant scatter and do, therefore, not clearly support this L-pole. The large scatter of the fold axis measurements indicate that the western limb is significantly affected by the F_2 refolding. The eastern limb is dominated by southeast-plunging fold axes, whereas the western libs consist of more scattered northeast-plunging fold axes.

When removing outliers to visualize the cluster better, the situation in fig. 3.52 is seen. The L-pole marks a potential fold axis (56→240) between the two limbs, defined by an east-northeast-striking sub-vertical axial plane (240/85). Such folding is not observed during fieldwork or supported by other analyses, indicating that the deformation of the Stormarkheia might not be related to the refolding of the isoclinal F_1 folds. This is further discussed in chapter 4.2.2.

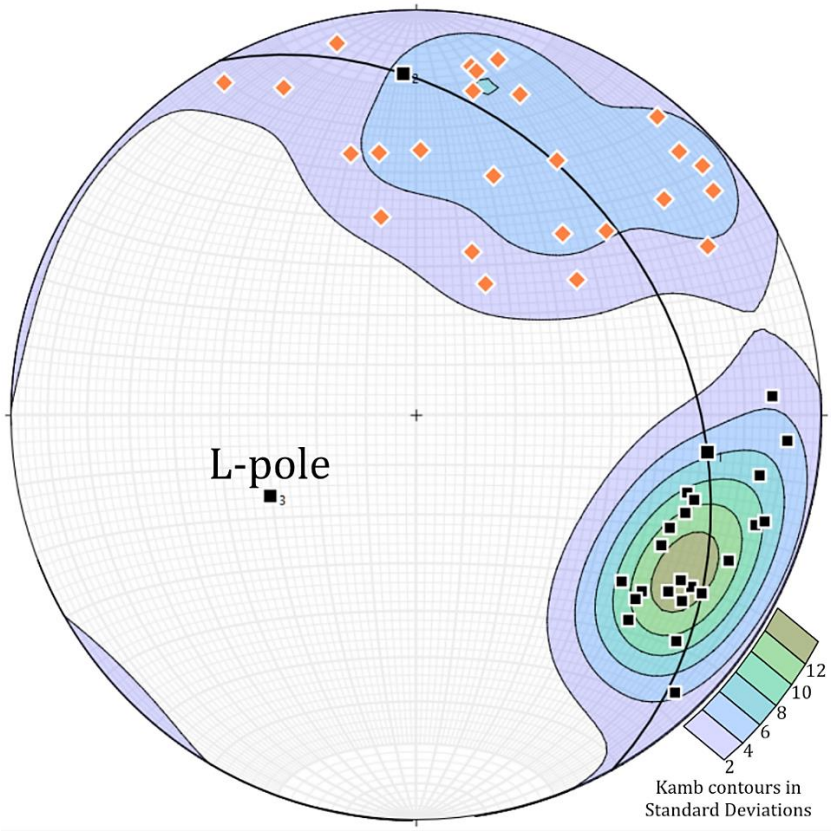

Figure 3.52: Contour plot of the fold axes from the eastern (black) and western (orange) limb of the Stormarkheia fold. The L-pole marks a potential fold axis (56→240) and an upright (240/85) axial plane.

Besides, by isolating the fold axes observations of HTSZ (fig. 3.53), two clusters can be seen similar to the Stormarkheia ridge (fig. 3.52), and the data from the northeastern field area (fig. 3.45 B). One cluster has an average fold axis plunge and trend of 22→122, with the other averaging 31→048. Since both these clusters are of isoclinal folds with similar appearance, it is not evident if the one cluster represents the original F_1 fold axis and the second represents the refolded F_1, or if one cluster represents F_1 and the other an F_2 or a possible later event (see chapter 4.2.2.for further discussion).

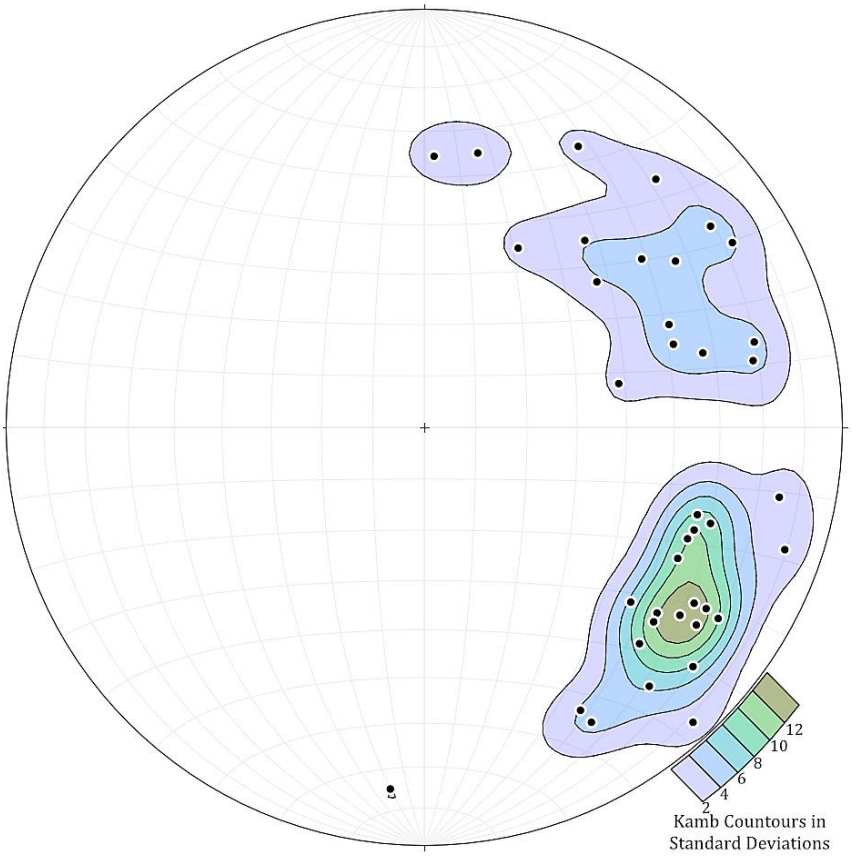

Figure 3.53: Stereonet plot of fold axes within the HTSZ. Two clusters of axes are seen with an average plunge and trend of 22→122 and 31→048.

4 Discussion

The Vassbygda area consists of geometry-defining siliciclastic metasedimentary ridges, igneous intrusions, and highly deformed marbles of varying quality. This chapter will discuss the results from fieldwork and acquired data to suggest the quality of the marble, the geometry of the rocks, and the geological evolution regarding metamorphic events and deformation of the area.

As one of the main goals of this thesis, a region-wide 3D geological model and volumetric properties of the Stormarka deposit are also presented based on the interpretations mentioned above.

4.1 Marble Deposits of the Vassbygda Area

The chemical and physical properties of the Vassbygda marbles are essential for the evaluation of the suitability of mining in the Vassbygda area after the end of the open-pit mining at Akselberg. This chapter discusses the quality and appearance of the Vassbygda marble and compares the rocks to the marbles currently mined at Akselberg.

4.1.1 Marble Appearance, Mineralogy, and Quality

The Vassbygda marbles are heterogeneous in appearance, mineralogy, and external factors such as dykes and sills and are therefore challenging to classify based on the quality of the final product (mix of unavoidable intrusions and marble). However, it is possible to describe the marble quality based on microscopical and macroscopical analysis.

The AMS results show that the graphite-spotted marble, although finer-grained than its equivalent at Akselberg, is still a good quality marble with graphite, mica, and sulphides grains occurring along calcite grain boundaries (fig. 3.4 B). Therefore, these impurities are likely removed during crushing and flotation (Sandvik *et al.*, 1999), which has been confirmed by analyses of the processing and flotation of drill-core samples from Vassbygda (Storruste, personal communication, 2020).

The banded marble is considerably more fine-grained than the graphite-spotted marble and consists of more silicate, sulphide, and graphite minerals. The bands of silicate minerals or sulphides are not ideal for pigment production, although as stated above, it may be possible to remove these with crushing and floatation if the impurities occur along calcite grain boundaries. The layers between bands of silicate minerals (fig. 4.1) often consist of relatively pure calcite. The distance between bands varies significantly, form only a few cm to several meters. The considerable variation in both appearance and mineralogic composition of the banded marble makes the determination of the quality difficult. Further work on detail-mapping of the banded marble is needed to establish the quality variations fully.

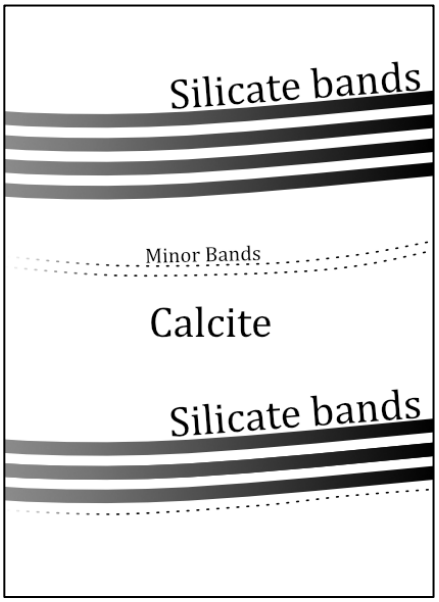

Figure 4.1: Illustration of a silicate-banded marble. Areas between the bands are often pure calcite with few impurities.

Although the mineralogical properties of the marbles are promising, a question arises when looking at the macroscopic characteristics of the Vassbygda deposit. The area is often densely populated by dykes and sills that cut the marble. Besides, large zones of calc-silicate layers often occur as sequences throughout the marbles. It may prove difficult to avoid these if a quarry is opened in an area with a high density of intrusions and silicate-rich sequences. The eastern field area (on the shores of Storvatnet and surrounding Svartvatnet) is particularly challenging due to a large amount of sub-horizontal leucogranitic sills and abundant amphibolitic calc-silicate layers, which seems to be related to highly migmatized areas.

The massive leucogranitic Dengelhalsen intrusion on the northeastern shore of Storvatnet (fig. 3.3) and related sills should be avoided since the marbles in these locations is often trapped between sills and dykes of different orientations. The marbles surrounding Storvatnet is also often banded with tight silicate bands. Stormarka and Stormyra mainly contain sub-vertical dykes and are easier to avoid if further mapped, although good-quality graphite-spotted marble occurs proximal to more extensive magmatic intrusions. Stormarka does not contain the sub-horizontal leucogranitic sills, although the area is the host to a high population of sub-vertical quartz dioritic dykes. Although the population of quartz dioritic dykes is significant within the Stormarka marbles, the sub-vertical nature makes the dykes more avoidable than the sub-horizontal leucogranitic sills. Besides, the powerful DEM-datasets are exceptionally useful for mapping the protruding dykes in these areas and should be used as a crucial tool for the eventual planning of further exploration.

A challenge with the Stormarka marbles is the occurrence of a sizeable calc-silicate body along the road to Godvassli (fig. 3.3). This geometry of the body is only based on a few measurements and maybe oversized on the geological map. However, presences of calc-silicate sequences are common in the Stormarka marbles and may be challenging for mining due to their extreme hardness, although these layers are rarely any more than 3-4m.

The best quality marble, both microscopically and macroscopically, is found on the south-western shore of Fjellvatnet (Langdalsstranda) and Stormarka (fig. 3.3). The Langdalsstranda deposit consists of primary “white” calcite marble without any visible graphite. The deposit has the best mineralogical quality of the Vassbygda area. However, the Langdalsstranda deposit is relatively inaccessible and a part of the Eidvatnet nature reserve, meaning it is likely not of any value regarding mining. Therefore, the most promising high-quality marble deposit is the Stormarka locality which contains high-quality marbles, although there is a significant quality variation and a large number of quartz dioritic dykes.

4.1.2 Comparison with the Northern Saus Carbonates

It is useful for easier cross-referencing to compare the Vassbygda marbles with the currently mined marbles north of the Sausfjellet pluton. Sandøy (2003) described marbles of the Saus carbonates based on colour and visible minerals, and although he utilized a more detailed classification of the marble than this thesis, a viable comparison between the Saus marbles and the Vassbygda marbles can be made.

Sandøy (2003) describes a "graphite-bearing speckled white" marble that comprises white calcite with graphite grain aggregates disseminated evenly throughout the rock. He describes this marble as being of medium to coarse grain-size and a white mesoscopic appearance. Sandøy (2003) does not observe any shape preferred orientation of the graphite aggregates, although a lineation could occasionally occur. This description fits with the graphite-spotted marble observed in the Vassbygda area, although the Vassbygda variants frequently show a preferred orientation of the graphite aggregates when transitioning into the banded marble.

Sandøy (2003) also describes a silicate-banded marble as the most common marble type of the Saus carbonates. The silicate-banded marble is characterized as fine- to medium-grained, heterogeneous with varying thickness of silicate mineral bands and a dark grey to black weathering surface with protruding silicate minerals. This description is similar to the banded marble, which is the dominant marble of the Vassbygda area (3.2.1.2).

Therefore, it is highly likely that the Saus carbonates are a lateral continuation of the Vassbygda marbles, only disrupted by emplacement of the Sausfjellet pluton. This connection indicates that previous studies and experience with the current Akselberg marbles can be utilized if future mining of the Vassbygda deposits commences.

4.2 Deformation and Geometry of the Vassbygda Units

To fully describe the Vassbygda marble deposit, the complex geometry and deformational history need to be unravelled. Due to the high rheological contrast, the marbles are more intensively deformed than the siliciclastic metasedimentary rocks. Therefore, the characteristic siliciclastic metasedimentary ridges, which enclose the marble deposits, was studied to explore the geometry.

This chapter discusses the dominant shear deformation related to the HTSZ, folding of the Vassbygda units and the large-scale deformation patterns interpreted from the geological map. Fig. 4.2 shows a simplified map of the Vassbygda area with all the names of localities discussed in the following sub-chapters.

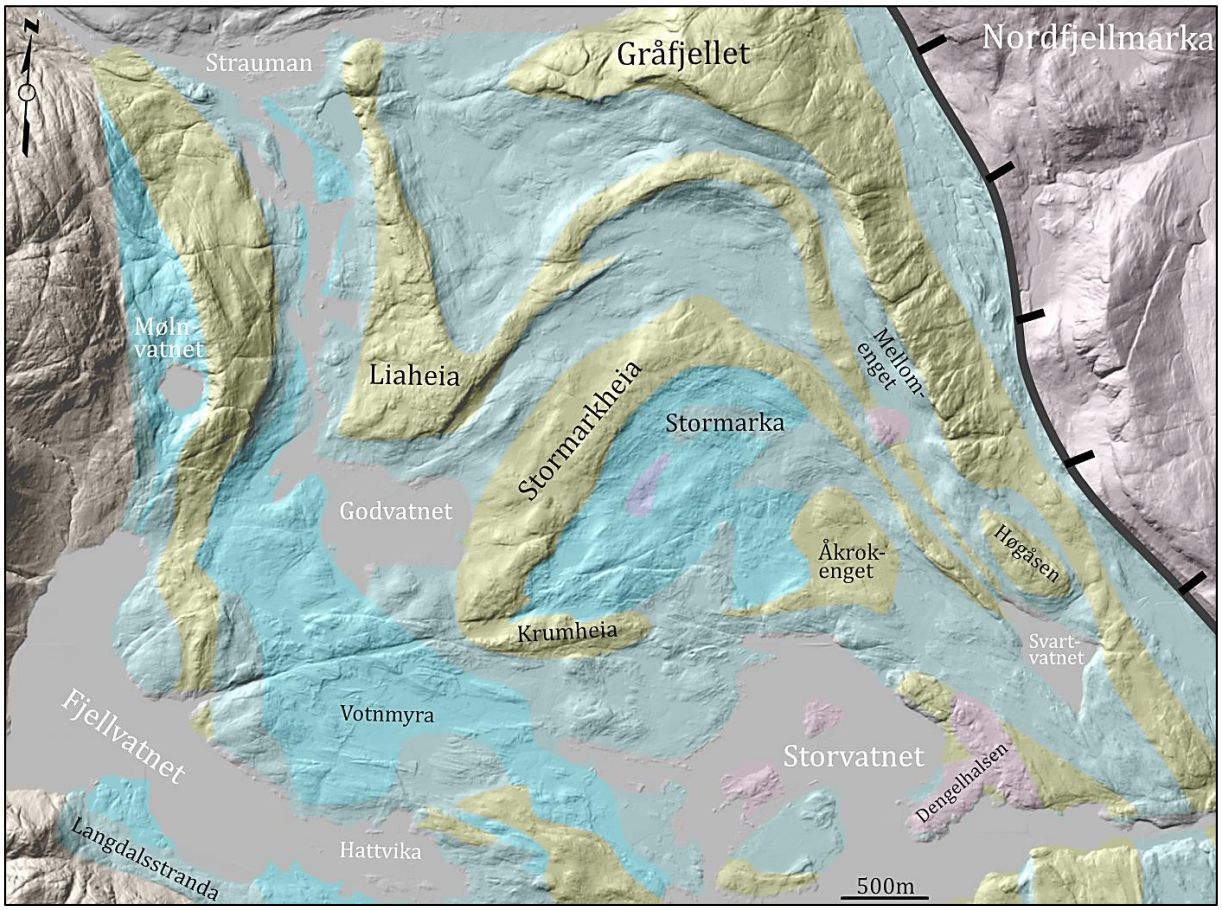

Figure 4.2: Simplified geological map of Vassbygda overlaid a hillshade image to enhance the topographical features. See the geological map (fig. 3.3) for more details on rock types. Hillshade from hoydedata.no

4.2.1 Shear Deformation along the Lower–Middle Nappe Boundary

The intense shear deformation observed along the Lower–Middle nappe was named the Heggfjord-Tosen shear zone (HTSZ). The HTSZ is seemingly most evident within the uppermost part of the Lower nappe, where the shear zone consists of highly deformed marbles, calc-mylonites, and mylonitic schists. The amount of deformation observed within these marbles are not seen elsewhere in the field area. The strain is apparently localized within the uppermost marbles of the Lower nappe since the siliciclastic metasedimentary rocks are relatively undeformed. The mantle-derived rocks in contact with the deformed marbles at Heggfjorden show the same pattern. Here the mantle-derived rocks are only locally deformed with small shear zones and brittle faults.

The strongly developed northeast-dipping (fig. 3.43) mylonitic foliation (S_3) is interpreted to overprint the S_{0+1} foliation and S_2 axial plane cleavage seen throughout Vassbygda, based on the presence of a preliminary foliation within the staurolite porphyroblast found within the mylonitic rocks (fig. 3.38). The structural measurements of the mylonitic foliation (fig. 3.43) show an average northeast dip direction with mineral lineations indicating a dip-slip to oblique displacement. However, it was not evident if the mineral lineations result from the primary thrusting or the reactivated normal displacement. The faulted shear zone and alteration fabric within the mantle-derived rocks at Heggfjorden indicate a dominant reverse-sinistral displacement.

The parallel layers of metasedimentary rocks proximal to the nappe boundary (fig. 4.2) have the same dip and dip direction as the mylonitic foliation, which is interpreted as a large-scale deformation of the HTSZ. The foliation of the bottom of the Middle nappe rocks is similar to the mylonitic foliation of the Lower nappe rocks, indicating that the shear deformation occurred in both nappes. However, it is uncertain how far the HTSZ reaches into the Middle nappe since the high competence contrast between the lower Nappe marbles and the ultramafic rocks of the Middle nappe has localized the deformation within the malleable marbles. The observed shear zone in the ultramafic rocks indicates similar displacement as the rest of the contact zone and was likely deformed simultaneously with the marbles. It is clear that the mantle-derived rocks were deformed in the ductile-brittle transition since the localized shear zone is cut by brittle faults (fig. 3.42). The contrast in deformation style is consistent with the expected rheological behaviour of mantle-derived rocks and marble.

The parallel layers of siliciclastic metasedimentary rocks affected by shear deformation seem to be thinned and eventually pinched out on the southeastern side of Svartvatnet (fig. 4.2), which is likely a large-scale deformation similar to the thinning and boudinage of siliciclastic layers within the deformed marbles (fig. 3.40). It is reasonable that the mesoscopic deformation is present at a macroscopic scale. Therefore, the siliciclastic metasedimentary rocks that form Høgåsen (fig. 4.2) are likely a large-scale boudinaged fragment of one of the layers.

Sandøy (2003) also mentioned the parallel nature of the metasedimentary rocks; However, he observed an isoclinal antiform that connects the seemingly parallel layers and indicates that the layers are connected with syn- and anticlinal fold pairs. No observations of this were seen in Vassbygda during fieldwork for this thesis, although this is likely due to the extensive folding seen elsewhere.

4.2.2 Folding

As presented in chapter 3.7.1, fold axes and foliation measurements throughout Vassbygda cannot be described with one singular fold phase. The scatter of the F_1 fold axes along the mean principal foliation indicate at least one more folding phase. Structural analysis (Chapter 3.7.4) indicates that this scatter is caused by refolding about an upright F_2 fold that intersects the F_1 axial plane with an angle between 90° and 0°.

The stereonet plots of the foliation of the southwestern and northeastern sections of the field area (fig. 3.45) show a possible open, sub-horizontal southeast–northwest-trending fold axis, with a northwest-southeast striking upright axial plane. The spread of isoclinal fold axes along the mean principal plane of the foliation for the two sections of the area indicates that the isoclinal fold axes are folded about the same northwest-southeast-trending axis. Therefore, the isoclinal folds must be older than the northeast-southwest folding, clarifying the recumbent isoclinal folding as F_1 and the open upright folding as F_2.

The dominant Stormarkheia ridge does not clearly show an evident folding from stereonet plots of the foliation and isoclinal fold axes. However, the F_1 folding can be interpreted by the Krumheia, and Liaheia folds based on isolated measurement of isoclinal fold axes and foliations within the hinge zones (fig. 3.48 and 3.49). Therefore, the subsequent northeast-southwest striking recumbent axial plane of these folds is interpreted as F_1.

The fold axes measured within the mylonitic foliation of the HTSZ and the Stormarkheia ridge shows two clear clusters (fig. 3.53). The measured fold axes within the HTSZ are of isoclinal folds, indistinguishable from the rest of the isoclinal folds in the field area, which leaves two scenarios for these clusters:

1) These clusters of fold axes are of the same F_1 isoclinal folds, which means that they must have been refolded by a fold phase with a 240/84 axial plane (fig. 3.52). This interpretation indicates that the area is affected by three fold phases: F_1 northeast-southwest recumbent isoclinal, F_2 northwest-southeast open upright (fig. 3.45 D), and F_3 east-northeast–west-southwest open upright (fig. 3.52). This third phase is not seen, nor supported by other analysis, and is therefore unlikely.

2) The two clusters represent two different isoclinal folds. The northeastern cluster is similar to the Liaheia, and Krumheia fold axes, and is likely of the F_1 phase, whereas the southeastern cluster is similar to the calculated open upright F_2 folding between the southwestern and northeastern field area. This would indicate that the F_2 isoclinal folds are related to the large-scale upright F_2 folding. This may result from extensive localized deformation within the HTSZ, which created isoclinal folds, whereas the remaining area was deformed to a lesser extent (fig. 4.3). The high rheological contrast within the marble and siliciclastic metasediments may have further dispursed the strain form the HTSZ.

Therefore, scenario number two is most likely, and since the axial plane of F_2 is parallel to the mylonitic foliation of the HTSZ, it is interpreted that the folding occurred due to the over-thrusting of the Middle nappe.

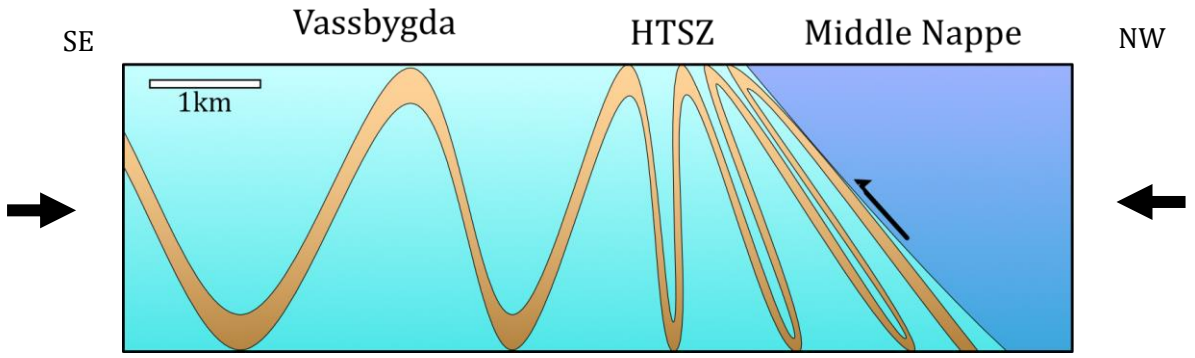

Figure 4.3: Localization of deformation during F_2 folding. The Vassbygda area is deformed by open, upright folds, whereas the HTSZ are extensively deformed with isoclinal folds.

In summary, the geometry and variation of the foliation and fold axis measurements in Vassbygda can be described by an F_1 isoclinal phase with a recumbent northeast-southwest-striking axial plane, followed by an F_2 phase of an open upright northwest-southeast-striking axial plane. The introduction of the F_2 phase created a type 2 fold interference pattern (Ramsay & Huber, 1987), as visualized in fig. 4.4.

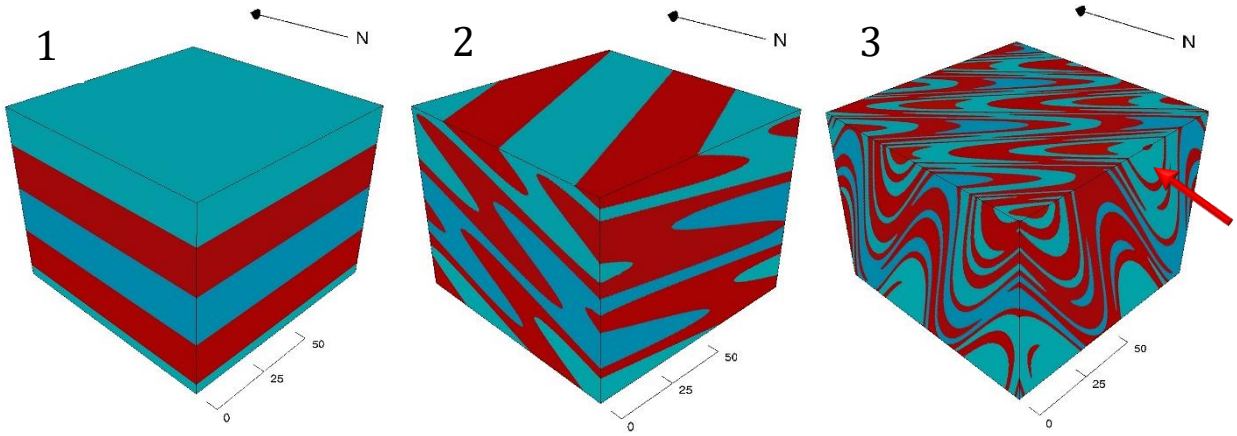

Figure 4.4: Visualization of the fold interference. **1**) Initial model with horizontal layers representing the metasedimentary rocks of the area. **2**) F_1 isoclinal folding with a northwest-southeast-striking recumbent axial plane. **3**) Interference pattern upon introducing the F_2 upright folding with a northwest-southeast-striking axial plane. The red arrow marks a possible geometry of the Stormarka marbles. Figures created from visiblegeology.com (not to scale)

4.2.3 Present-Day Geometry

The dominant structures of the area are the two protruding siliciclastic metasedimentary ridges (Stormarkheia and Liaheia), which surrounds the Vassbygda marble deposits. These ridges thin out towards the southeast, where they almost disappear south of Mellomenget. The ridges thicken southwest of the road before pinching out to a thin sliver and submerging under Svartvatnet. No connection between the Stormarkheia and the Liaheia ridge is observed, although the section under and south-west of Svartvatnet was not explored. There are two scenarios for the two ridges: 1) They are connected as a fold hinge under, or southeast of, Svartvatnet, or 2) the ridges are not connected and follow the overall southeast trend of the HTSZ. Scenario one indicates that the layers are tightly folded into the geometry observed today. No evidence of such folding is observed, and no surface expression of this fold hinge or hinge zone is observed on orthophoto or DEM southeast of Svartvatnet. The presence of a hinge zone would likely have created a ridge in the terrain, similar to that of the Stormarkheia fold hinge, not the depression seen as Svartvatnet. Therefore, theory number two is more likely, which means that the Stormarkheia and Liaheia ridges are two separate siliciclastic metasedimentary sequences with a marble unit in between.

The pinch-out and parallel geometry of the eastern field area is likely a large-scale deformation related to the HTSZ, similar to that of the strongly boudinaged and stretched silicate bands found within the marbles.

The Stormarkheia ridge turns east in the central part of the field area, which is today seen as the Krumheia ridge, enclosing the Stormarka marbles. The ridge then disappears before an area of a flat-lying siliciclastic metasedimentary rock occurs at Åkrokenget. This is interpreted as a result of the fold interference pattern (see chapter 5.2.2), indicating that the Stormarkheia, Krumheia and Åkrokenget siliciclastic metasedimentary rocks are connected beneath the Stormarka marbles, forming a cradle-like structure (fig. 4.4). However, since there is no surface connection between Stormarkheia–Åkrokenget, or Krumheia–Åkrokenget, it may be speculated that the cradle-structure has been further deformed, and perhaps boudinaged by deformation similar to the one observed within the HTSZ (fig. 3.40).

It may also be speculated that the Åkrokenget and the host rock of the Dengelhalsen intrusion were connected. The marbles between these two ridges show a large-scale infill-pattern observed between boudinaged segments on a smaller scale, where the strike of the banding changes as seen in fig. 3.15 B.

The Liaheia ridge curves north in central Vassbygda and continues straight until its cut by the Sausfjellet shear zone and pluton (Dumond, 2002). This observation further strengthens the scenario that the Stormarkheia rocks are not connected to the Liaheia rocks by an anti- or synform fold at Svartvatnet (fig. 4.2), since the present-day geometry would not be possible in such a scenario. It is likely that the Liaheia ridge also forms a cradle-like structure with the Gråfjellet metagreywackes, although this area is extensively deformed by the HTSZ and do likely not represent the expected “undisturbed” fold interference geometry.

Dumond (2002) interpreted a shear connection between the Stormarkheia and Liaheia rocks close to Mellomenget. However, this connection was not observed during fieldwork for this thesis. Outcrops along the creek between the two ridges indicate that the marble unit continues south and could be followed to Svartvatnet. Dumond (2002) also interpreted a shear zone in the Liaheia ridge, although this was also not observed during field mapping. If the Liaheia and Stormarkheia

are connected, a type 3 surface fold interference pattern (Ramsay & Huber, 1987) is expected, which is not supported by the interpreted fold phases (chapter 4.2.2).

The siliciclastic metasedimentary ridge that encloses the Mølnvatnet marble deposit can be followed south, where it pinches out near Fiskbekken. The siliciclastic rocks found southwest of Votnmyra (fig. 3.1) may be a pre-deformational continuation of the Mølnvatnet ridge. However, this connection is unclear due to the extensive migmatization of the area east of Hattvika and the small lens of graphite-spotted marble seemingly cutting through the siliciclastic sequence. The area may represent a leucogranitic intrusion, although this was not established due to few observations. The lack of outcrops within Votnmyra wetlands did also not reveal any connection between the two siliciclastic metasedimentary units. However, a few outcrops of metagreywacke on the hill between Votnmyra and Fjellvantet (fig. 3.1) may be a boudinaged fragment of the once connected siliciclastic layer. It is not clear why the Mølnvatnet ridge does not form the same pattern as Liaheia and Stormarkheia, although the distance from the HTSZ may have resulted in less shear deformation.

The large-scale lineaments that cut through the area were likely formed by brittle deformation in later stages of either the HNC nappe stacking, the Scandian deformation during the Caledonian orogeny or, most likely, during post-Caledonian extensional deformation. No evidence of displacement along these lineaments was found, indicating little effect on the subterranean geometry of the metasedimentary rocks of the area. The lineaments are parallel to the glacial flow pattern in the area (Kleman *et al.*, 1997), which may have led to extensive erosion, resulting in the distinct present-day topography.

The amount of, if any, tilting of the rocks before, under, or after folding will drastically change the expected surface geometry of the area. Since it is not possible to observe the amount of tilting until present-day, it cannot be used to accurately determine the theoretical surface pattern created by the fold interference.

4.2.4 Geometrical Uncertainties

The previous mapping done by Brønnøy Kalk utilized the industrial classification (Table 2.4), which primarily focuses on the detailed classification of marble types. However, the classification creates a problem for both the geological mapping, and core logs used for 3D modelling, since rocks are usually classified under broad definitions such as “Gneiss” and “Peg” for siliciclastic metasediments granitic intrusions. Since the classification used did not separate between the same rock types used in this thesis, approximations had to be used to interpret the rock boundaries. This was primarily a problem for the class “DOL” (dolerite), which usually incorporates any green to greenish-black rock due to the similarities and difficulty to distinguish calc-silicate rocks and mafic intrusions in core logs. From personal experience working with some of the Vassbygda cores, many rocks given the “DOL” classification is calc-silicate rocks. Since the most massive mafic dyke (dolerite) observed in the field area was about 3m wide, it is unlikely that the several 10s of meters of dolerite logged in some of the wells are correct.

The problem with this classification was also pointed out by Sandøy (2003). The classification “GNEISS” has been used to map the metasedimentary rocks, indicative of which type of meta-sediments present. When using data of “GNEISS”-locations, meta-greywacke was assumed based on the dominance of this rock type. This assumption significantly reduces the certainty of the meta-arkose dominant areas shown on the geological map (fig. 3.3) and excludes other metaarkose areas not mapped during this thesis.

4.2.5 3D-Models of the Vassbygda Region and Marble Deposits

Based on the structural observations and interpretations discussed in the prior sub-chapters, a region-wide 3D-model of the area was created. Also, an in-depth model of the Stormarka marble deposit was created to explore the complicated geometry and volumetric properties of the marble.

4.2.5.1 Region-wide Model

The created region-wide model (fig. 4.5) shows the distribution of rock units of the Vassbygda area and shows the geometrical properties of the major structures of the area. The model was created to a depth of 500m below sea level to show the geometry clearly. The region-wide model is available as a 3D-PDF in the digital Appendix 2. The model is divided into separate rock units, shown in fig 4.8 and fig. 4.9. Two cross-sections (fig. 4.7) were created from the 3D-model to help visualize the complex geometry of the central Vassbygda rocks.

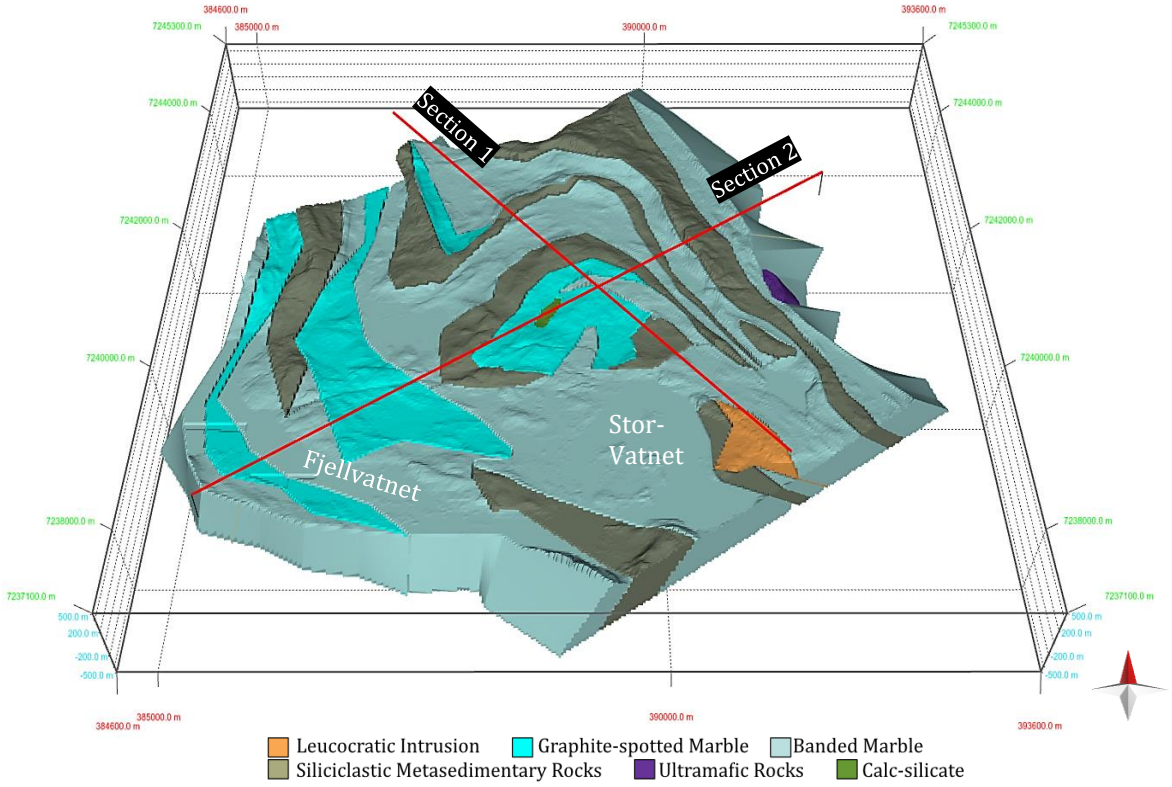

Figure 4.5: Region-wide 3D model of the Vassbygda marble deposits, modelled to a depth extent of 500m below sea level. The colours represent the same rocks as seen on the geological map (fig. 3.3). Red lines mark the cross-section shown in fig. 4.7.

The complex geometry of the area created problems for the modelling software, which often misrepresented rock bodies when the rock boundaries were overturned or folded. Several steps were taken to reduce the complex modelling errors, although some sections were especially problematic. These areas include the overturned folding of the Stormarka ridge. The software often modelled a seam between the top and bottom of the fold (fig. 4.6), which added extra volume to the rock body. A correction of this artefact was attempted for volume estimates.

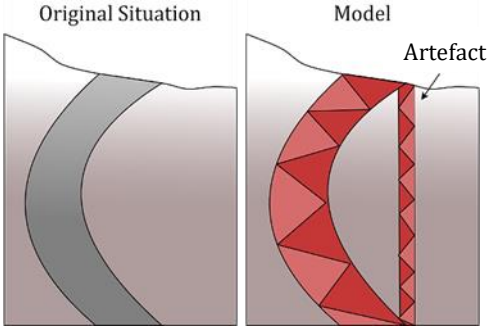

Figure 4.6: Artefacts created when modelling overturned layers.

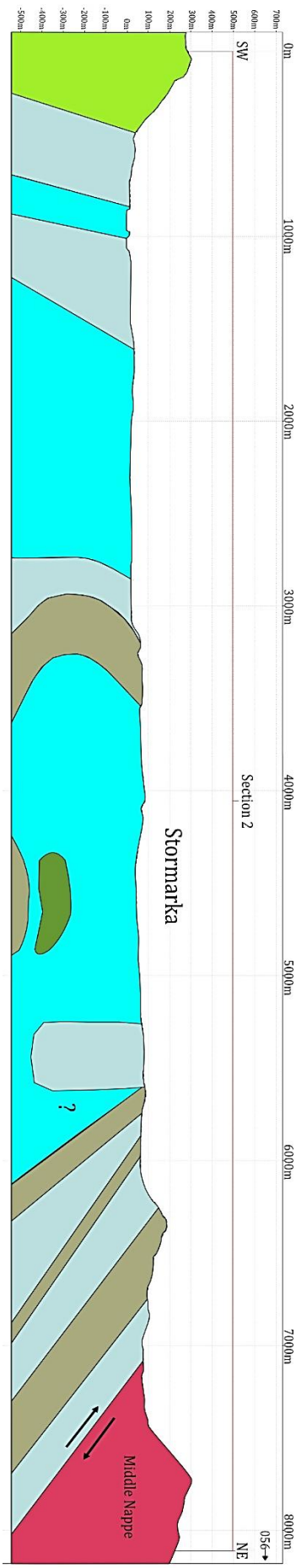

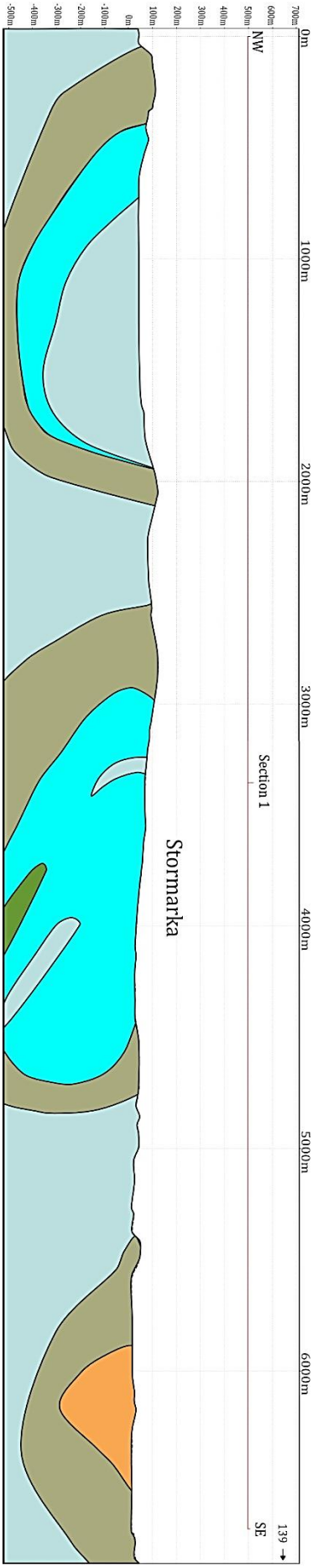

Figure 4.7: Cross-sections created from the regional 3D model (fig. 4.5).

Section 1 indicates the complicated geometry of Stormarka and the cradle-structure formed by the fold interference. The cradle must be deeper than 265m (see text for details)

Section 2 shows the parallel layers deformed by the HTSZ.

- Leucocratic Intrusion
- Graphite-spotted Marble
- Banded Marble
- Mica-gneiss
- Siliciclastic Metasedimentary Rocks
- Calc-silicate

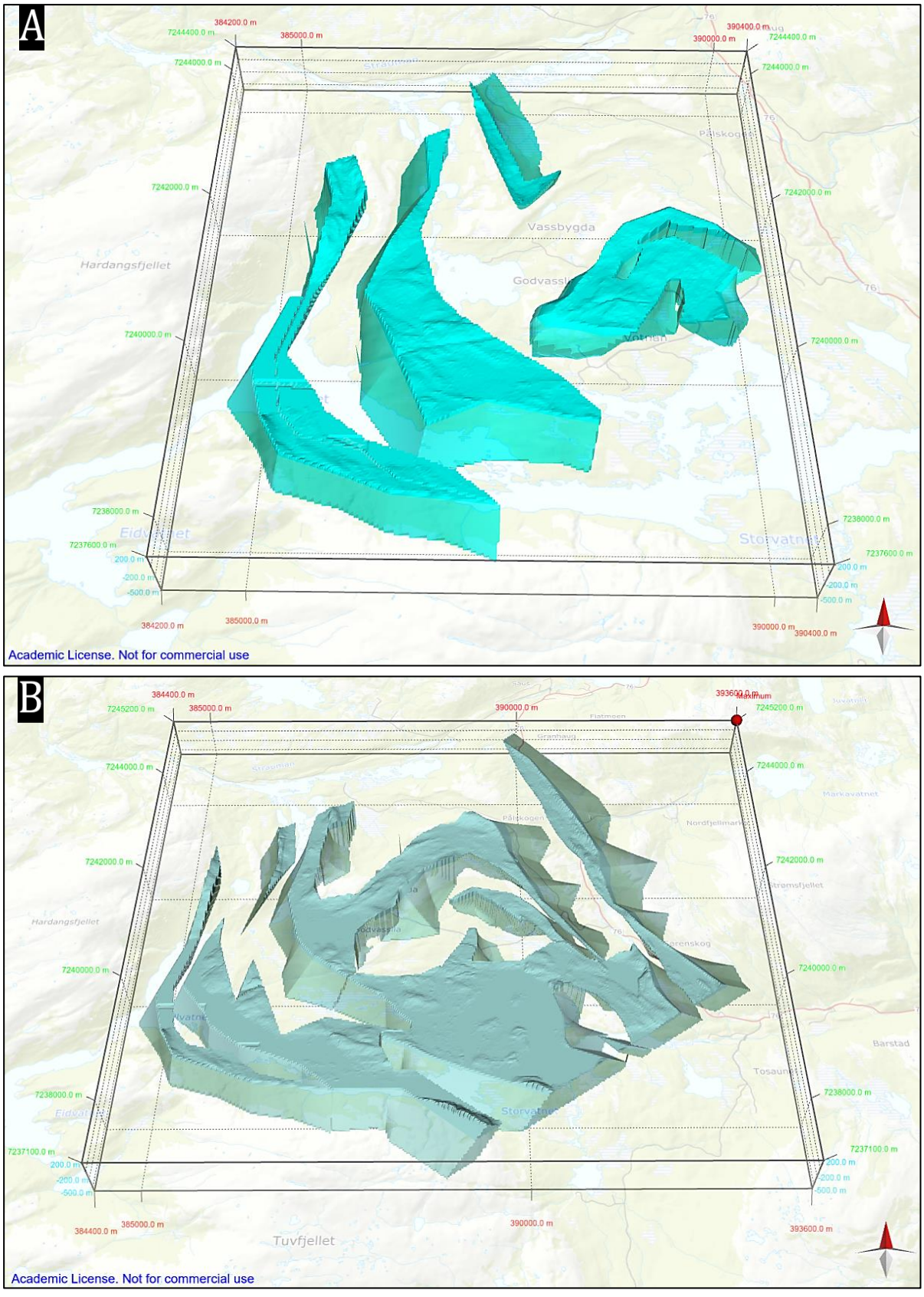

Figure 4.8: 3D-model of the Vassbygda marbles. **A**) Graphite-spotted and white marble **B**) Banded marble or similar quality. Background map from norgeskart.no.

Figure 4.9: 3D-model of the siliciclastic metasedimentary rocks (brown), the Stormarka calc-silicate (green) and the Dengelhalsen leucogranite (orange). **A**) View from the south, including the small ultramafic lense (purple) of the bottom of the Middle nappe **B**) view from the southwest. Background map from norgeskart.no.

4.2.5.2 In-depth Analysis of the Stormarka Marble Deposit

The complex geometry of the Stormarka deposit can be seen when isolating the siliciclastic metasedimentary ridges, as seen in fig. 4.10 A. The Stormarkheia and Åkrokenget ridges form a cradle-like structure due to type 2 refolding (Ramsay & Huber, 1987), although this is not fully visible in the model due to uncertainties with the depth of the connection. However, the cross-sections (fig. 4.7) indicate the curvature of the siliciclastic ridges at depths. Therefore, the marble is likely lying on top of the connection between the Stormarkheia and Åkrokenget ridges (fig. 4.10 B).

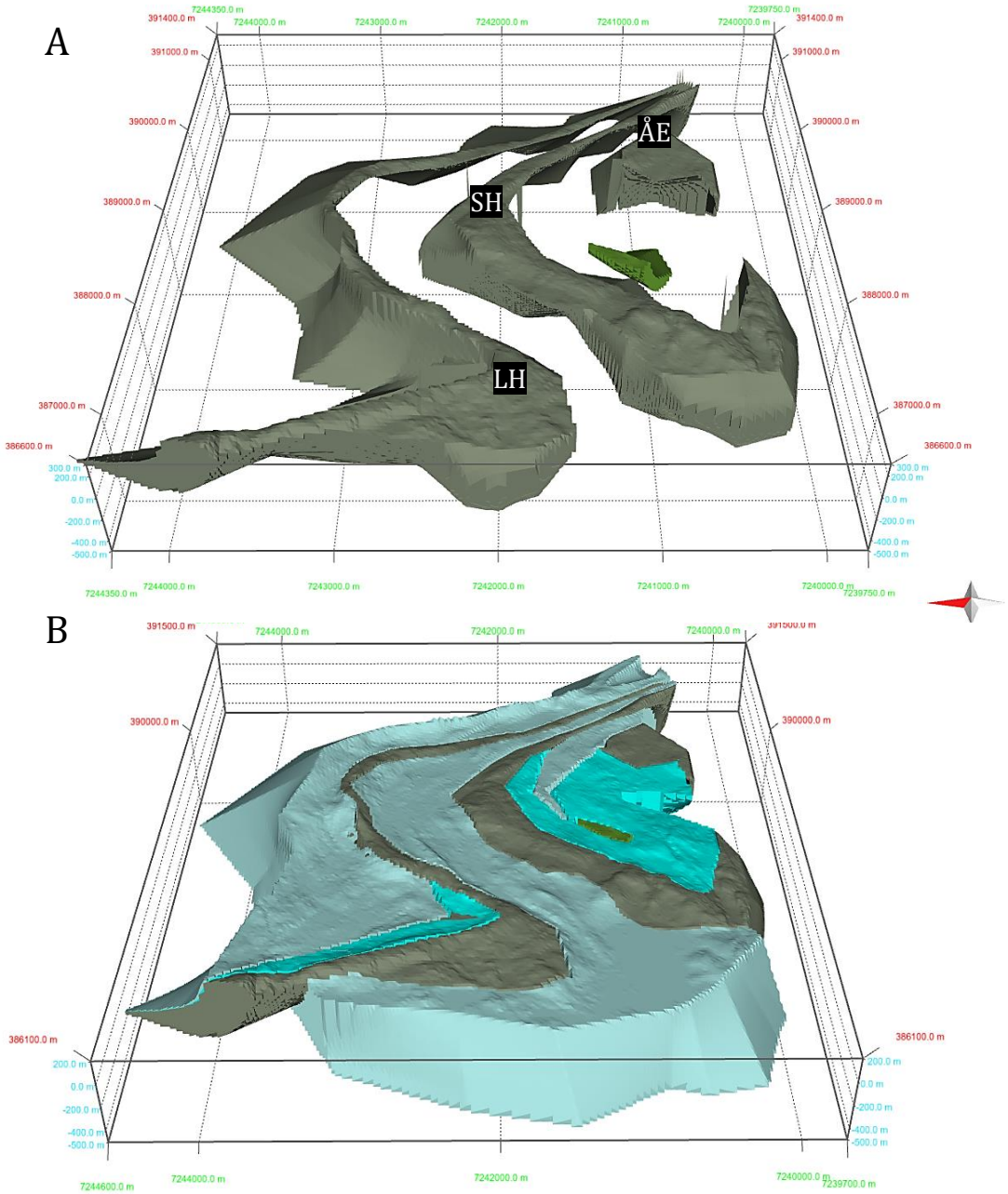

Figure 4.10: 3D-model of the Stormarka area. View from the west. **A**) Siliciclastic metasedimentary rocks of the Liaheia (LH), Stormarkheia (SH) and Åkrokenget (ÅE) ridges. The Stormarka calc-silicate (green) is also included. **B**) Marbles, calc-silicate and siliciclastic metasedimentary rocks of the area.

It is challenging to establish the depth of this connection due to the high competence contrast between the marble and metasandstones, which complicates the estimation of amplitude or wavelength of these large-scale folds. Core logs of the Stormarka area give the only indication of depth since the deepest (265m) of the cores does not enter the siliciclastic ridge, indicating that the connection has to be below this depth.

It is also challenging to establish the deformation created by the HTSZ, which may have altered the expected cradle structure. It was therefore decided to create the model without the connection between the ridges.

The Stormarka deposit consists of a large body of graphite-spotted marble, enclosed by the Stormarkheia, Krumheia, and Åkrokheia ridges (fig. 4.10). Two zones of predominantly banded marble are located to the south and east of the graphite-spotted marble (fig. 4.5) and are likely marbles that may have been folded into the fragmented/boduinaged siliciclastic metasedimentary rocks, and are likely not as dominant as the graphite-spotted marble. They were, therefore modelled as thin zones that pinch out instead of a continuous layer (fig. 4.11 A).

The graphite-spotted marble of Stormarka was isolated to enhance the geometry of this body (fig. 4.11 A & B). The two indentations seen in the model are the position of the banded marble bodies (fig. 4.5 and 4.10). The calc-silicate body is situated in the hole in the western part of the area. Graphite-spotted marble follows the cradle-structure previously described and is therefore likely most extensive in the centre of the surrounding ridges.

The Stormarka deposit has been divided into smaller sections to represent better the volumetric distribution of marbles with different lithological and structural complexities (fig. 4.12). Volume estimations are limited to a maximum depth of 200m (below sea level) to better represent a reasonable depth of an open-pit mine. To reduce the errors of artefacts created during the modelling process (fig. 4.6), sections of the volumes were removed where the artificial volumes were too severe. The filtered volume of the Stormarka deposit reduced the total volume by 18%. This reduction helped produce a more realistic volume estimate, although the very complex geometry of the area greatly limits the calculated volume accuracy.

The volumes for each zone are listed in Table 4.1 and indicate that the largest undisturbed graphite-spotted marble section occurs between the western limb of Stormarkheia and Krumheia (zone 3, fig. 4.12). However, this area is less mapped than the northern Stormarka area and is therefore of more significant uncertainty regarding marble quality. The transition between the siliciclastic metasedimentary rocks of Stormarkheia and the graphite-spotted marble of northern Stormarka (zone 1 in fig. 4.12) is well-mapped of excellent quality. This estimate of 100 million m^3 (corresponding to 268 million tonnes) is likely rather accurate, although the uncertain geometry of the Stormarkheia ridge creates some uncertainty of continuation at depths. Zone 2 (fig. 4.12) is also of good-quality graphite-spotted marble, although the sizeable calc-silicate body should be further explored to enhance the accuracy of this estimate.

In total, the Stormarka marble deposit is estimated to contain 1 772 million tonnes of high-quality graphite-spotted marble and 305 million tonnes of medium-quality banded marble, where the most promising zone is the northernmost area of Stormarka, which is estimated to contain 268 million tonnes of excellent quality graphite-spotted marble.

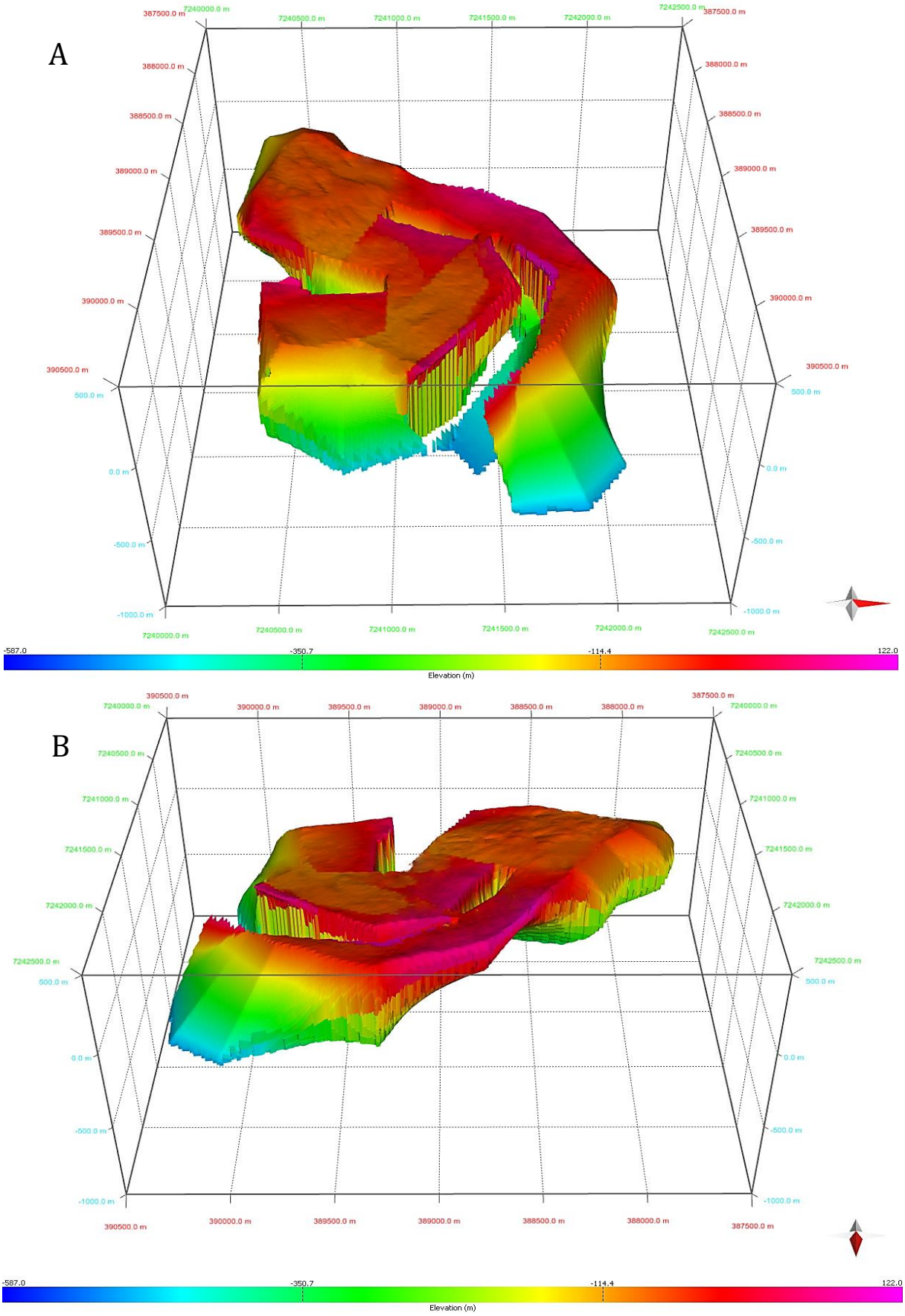

Figure 4.11: 3D-model of the Stormarka graphite-spotted marble. Colour range represents elevation (above sea level) **A**) View from the east. **B**) View from the south.

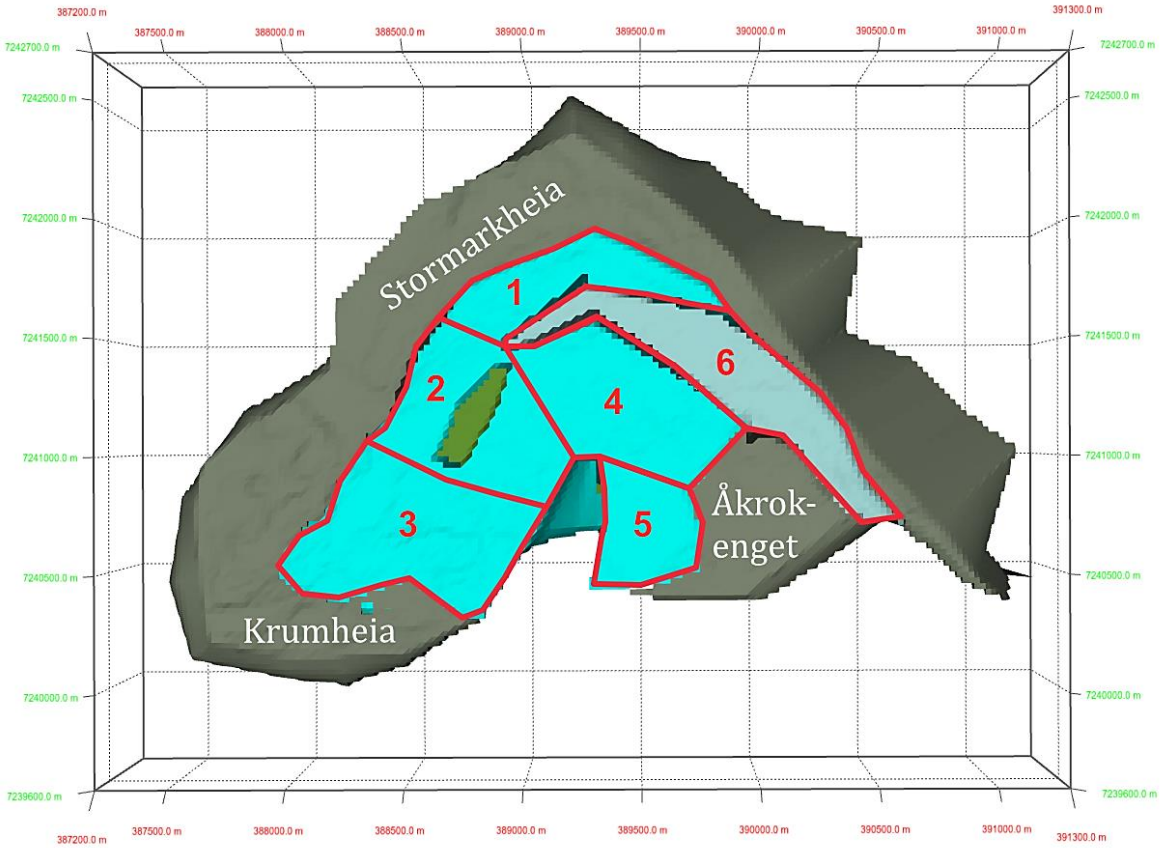

Figure 4.12: Top-down view of the Stormarka marble deposit. The red boxes mark the division used for the volume calculations shown in table 4.1.

Table 4.1: Volume calculations of the Stormarka deposit. The table is divided into six zones, shown in fig. 4.11. The tonnage was calculated with the corresponding rock densities for banded marble and graphite-spotted marble given in table 3.1.

Zone	Rock Type	Volume [m³]	Tonnage [t]
1	Graphite-spotted Marble	100 141 094	268 378 132
2		126 265 408	338 391 293
3		284 074 237	761 318 955
4		76 865 185	205 998 696
5		73 955 957	198 201 965
6	Banded Marble	113 626 960	304 520 253
Total	Graphite-spotted Marble	661 301 881	1 772 289 041
Grand Total	Combined	774 928 841	2 076 809 294

4.3 P-T Estimates

4.3.1 Garnet Geothermobarometry

The results from the garnet geothermobarometry (fig. 3.29) indicated two P-T estimates, one at 4.5-5.2kbar and 630-650°C and a second at 3.4-3.5kbar and 535-545°C. These estimates may represent two different metamorphic events experienced by the Vassbygda rocks. However, it is not clear what the second estimate represents or if it is entirely valid. This is further discussed below.

The first estimate (4.5-5.2 kbar and 630-650°C) is supported by the GB+GBAQ, GBMAQ, and the Ca-poor plagioclase GASP estimate. This event is interpreted to represent dehydration melting of muscovite and formation of peritectic sillimanite and k-feldspar, which occurs at 600-750°C (Thompson, 1982). Spear *et al.* (1999) describe the partial melting of pelites containing garnet + muscovite + sillimanite + plagioclase + biotite + quartz to occur between ~525-725°C at ~5 kbar (assuming the only fluid present is H_2O released form the dehydration reaction). The result of this melting would give pelites with extensively resorbed garnets, little k-feldspar, fabric-cutting late muscovite, and dispersed leucosomes with rims containing biotite+sillimanite and cores that contain late muscovite grains (Spear *et al.*, 1999). The description by Spear *et al.* (1999) fits well with the observed mineralogical textures of BC-16 (Appendix A: Petrographical Description) and the garnet zonation (fig. 3.27). The presence of primary muscovite suggests that the dehydration melting reaction did not proceed to completion, which is also supported by the P-T estimate of 4.5-5.2 kbar and 630-650°C.

GM+GMAQ and the Ca-rich plagioclase GASP support the second estimate (3.4-3.5kbar and 535-545°C). This estimate is somewhat unclear since some of the same mineral compositions used for the other P-T estimate have also been applied here. The GM+GMAQ estimate may reflect the conditions of which a secondary euhedral muscovite formed, as observed in the thin section (fig. 3.12 B & C. It is speculated that this may be related to either a cooling event following the first dehydration melting of muscovite or related to a separate deformation event – perhaps the secondary fold phase (see chapter 4.4.2). It may also be speculated if any calculated estimates accurately represent the P-T conditions if the euhedral muscovite and the garnet are not in equilibria. Therefore, further analysis of the minerals should be undertaken to support the estimates (see chapter 6.5).

Interestingly, the Ca composition of the feldspar seems to relate to the two P-T estimates for the other geothermobarometers. The GASP estimate Ca-poor composition is similar to the 4.45-5.2kbar estimate of the GB+GBAQ and GBMAQ geothermobarometers, whereas the Ca-rich plagioclase composition corresponds with the GM+GMAQ geothermobarometer.

All analysed minerals fall within the compositional limits of the geothermobarometers used. However, certain geothermobarometers perform better for certain mineral assemblages: Wu and Cheng (2006) suggest that the naturally and experimentally calibrated GB thermometer (Holdaway, 2000) and the GASP barometer (Holdaway, 2001) are preferable over other similar geothermobarometers when the sample contains biotite and aluminosilicates. This is the situation for sample BC-16, which contains both of these minerals. Therefore, it is concluded that the 4.5-5.2 kbar and 630-650°C estimate is the most accurate for the peak metamorphic conditions experienced by the Vassbygda metasedimentary rocks.

4.3.2 Amphibole Geotermobarometry

The Hbl-Pl geothermometer gives a combined P-T estimate of 6.2-6.8kbar and 710-740°C for the quartz dioritic dyke.

The P-T estimate for the quartz diorite is problematic due to the relative age of the intrusions as seen during fieldwork. The dykes are seen cutting the leucosomes of the migmatized siliciclastic metasedimentary rocks, indicating that the dykes intruded after the partial melting, which occurred at 4.5-5.2 kbar and 630-650°C (chapter 4.3.1). Therefore, it is believed that the amphiboles present in the quartz dioritic dykes are of primary magmatic composition and that the P-T estimate indicates the emplacement conditions of the rock. This interpretation explains the higher temperature. However, the higher pressure is not fully understood since increased pressure is not recorded within the host rock. Also, Barnes and Prestvik (2000); Yoshinobu *et al.* (2002) indicate a clockwise P-T-t path and would not fit with the higher temperature and pressure post-migmatization of the siliciclastic metasedimentary rock.

It was not established if the amphiboles were primary magmatic or grew during a metamorphic event. The higher pressure and temperature may indicate that the amphiboles are primary.

4.3.3 Calcite Twinning Geothermometry

The calcite twinning geothermometer (Ferrill *et al.*, 2004) estimates temperatures of $<170°$ for the graphite-spotted marble and $>200°C$ for the calc-mylonite. However, this estimate is below the garnet geothermometry for the siliciclastic metasedimentary rocks and is likely unable to be used in marbles deformed to the extent experienced by the Vassbygda units. Since it is proposed by this thesis that the siliciclastic metasedimentary rocks and the marbles are sedimentarily related, they would have experienced the same metamorphic conditions. Therefore, the twinning observed within the calcite is likely created during a later deformation phase, or as a result of deformation after recrystallisation of the calcite grains (Bestmann & Prior, 2003).

4.3.4 Regional Comparisons

Little work has been done on geothermobarometry of the metasedimentary rocks of the HNC. The focus of earlier studies has been on P-T conditions of magmatic rocks during pluton emplacements.

Barnes *et al.* (2011) calculate a P-T estimate for the migmatized rocks of the Upper nappe by using the GASP geobarometer and the Ti-in-zircon geothermometer, which gave a pressure range of 500-700MPa and temperatures of c. 800°C. These P-T conditions are interpreted to coincide with biotite dehydration melting and migmatization of the Upper nappe (Barnes *et al.*, 2011). The P-T estimates for the migmatized metasedimentary rocks of Vassbygda are considerably lower in both temperature and pressure, which indicates that the migmatization of the Upper nappe was a separate event from the Lower, further establishing the presence of two distinct nappes with differing metamorphic evolution.

The host rocks of the Vega pluton have been studied by Oalmann *et al.* (2011), which estimates that the metasedimentary rocks were metamorphosed to ~550°C at ~6.8-8 kbar and with a clockwise P-T path. The temperature estimate for these rocks is similar to the estimate of the Vassbygda units; however, the pressure estimate is considerably higher, indicating different metamorphic conditions for the rocks of the Horta nappe and the metasedimentary rocks of the Lower nappe.

Barnes and Prestvik (2000) estimate the pressures of the Velfjord plutons to 600-800 MPa based on Al-in hornblende geobarometry. GASP results indicated initial melting of pelites in the wall rocks of the Velfjord plutons at 7-8 kbar and 750-800°C, and that the temperature from the plutons likely affected rocks up to 1km from the pluton contact (Barnes & Prestvik, 2000; Barnes *et al.*, 2002). Central Vassbygda is about 3.5km from the Sausfjellet pluton and should not be directly influenced by the heat emitted during pluton emplacement. However, the Hbl-Pl geothermobarometry indicated similar pressure (6-7kbar) for the quartz dioritic dykes in Vassbygda, although the temperature estimates of these intrusions are somewhat lower (710-740°C) than the results from Barnes and Prestvik (2000). The lower temperature could be a result of the distance to the Sausfjellet pluton.

Barnes and Prestvik (2000) also recognize a close to isothermal decompression (exhumation (Yoshinobu *et al.*, 2002)) event in the wall rock of the Velfjord plutons, decreasing the pressure from 7-8kbar to ~4-5kbar, which coincide with the pressure (4.5-5.0kbar) and estimates derived from the garnet geothermobarometry done during this thesis. The 630-650°C estimated from the garnet geothermobarometery may reflect the distance of the Vassbygda from the Sausfjellet pluton. However, field observations suggest that the migmatization of the siliciclastic metasedimentary rocks occurred prior to the emplacement of the Sausfjellet pluton (chapter 4.4).

In summary, the scarcity of previous publications of P-T estimates of the metasedimentary rocks of the Lower nappe makes a direct comparison challenging. The geographically closest estimate comes from the host rocks of the Velfjord pluton (Barnes & Prestvik, 2000; Barnes *et al.*, 2002). However, their metamorphic imprint is dominated by contact metamorphic conditions and therefore not directly relatable to the regional metamorphic conditions of the Vassbygda metasediments. The migmatitic siliciclastic metasedimentary rocks of Vassbygda likely represent region-wide migmatization with dehydration melting of muscovite and did not reach the temperatures of the Velfjord plutons proximal host rocks. However, the quartz dioritic dyke analysis interpretation is unclear, since it yields higher P-T conditions than the migmatized host rock. This is further discussed in chapter 4.4.3.

4.4 Geological Evolution

The geological evolution of the Vassbygda units within the Lower nappe is interpreted in the following subchapters. The deformation, metamorphism, and migmatization of the Vassbygda rocks are interpreted based on the observations made during the two field seasons and the available regional geology from the HNC. A proposed depositional environment is also presented based on lithological observations.

Following are four subchapters discussing the geological evolution of the Vassbygda area. Each chapter corresponds to a step in fig. 4.13, which summarizes the discussed topics. The last step (the present-day geometry) has been described in chapter 4.2.3.

4.4.1 Sedimentation and Depositional Environment (Step 1)

Although beyond the scope of this thesis, an estimation of the depositional environment can be made from the observations made during fieldwork. The sedimentary transition between the siliciclastic metasedimentary rocks and the marble units indicates that they formed in a periodically energetically changing depositional environment. Conditions for the deposition of calcareous sediments were likely dominant, judging by the relative size of the marble units compared to the siliciclastic metasedimentary rocks of the area. However, the rheological contrast and the different physical properties between the two rocks and may have led to unequal compaction and deformation. Calcareous sediments were likely deposited in a low-energy setting with sequences of arkose to greywacke depositions occurring as bands within the marbles and more massive deposits (siliciclastic metasedimentary ridges). The depositional environment had to be above the carbonate compensation depth at c. 3km depth (Nichols, 2009) in order for the deposition of calcareous sediments.

The sequential transition between the large-scale metasedimentary ridges and the marbles indicates periods of gradual environmental change, whereas a rapid change in a deposition may produce the relative sharp contact between many small siliciclastic layers in the marbles. The graphite within the marbles is likely a result of graphitization of detritus matter in the sediments (Landis, 1971; Weis *et al.*, 1981) – a process proposed to occur above 400°C (Landis, 1971).

The Neoproterozoic age (Barnes *et al.*, 2007) of the sedimentary rocks is also challenging since no exact sedimentary provenance has been established. McArthur *et al.* (2014) proposed that the Lower nappe may be a rifted fragment of southeastern Greenland or Labrador based on the similarity of zircon spectra. However, Slagstad and Kirkland (2017) show that detrital zircon U-Pb analysis of Laurentian and Baltican rocks yields nonunique results and cannot be used to determine the sedimentary provenance.

The depositional environments of the Vassbygda units are difficult to establish since no primary sedimentary structures are observed, and the extensive tectono-metamorphic events that followed have severely altered and deformed the rocks. An estimate would be a foreland basin, where calcareous sedimentation graded into siliciclastic sediments during prolonged tectonic activity. Turbidite activity within the basin created a sharp transition to fine-grained sediments within the marble deposits.

The sedimentary depositions are illustrated in fig. 4.13 -1.

4.4.2 Isoclinal F_1 Folding and Migmatization (Step 2)

The first recorded deformation event in Vassbygda caused the development of the clear tectonic foliation (S_1). This foliation is in places sub-parallel to S_0 (the sedimentary contacts; fig 4.13 -1). No direct evidence from the original bedding is observed, although the parallel nature of the foliation likely represents the transposed bedding.

The foliation formed before or, most likely, during the development of the dominant F_1 folding (fig. 4.13 -2). F_1 folding is defined by northwest-vergent overfolded to recumbent, tight to isoclinal folds with subhorizontal northeast-plunging fold axes. A weak axial plane cleavage (S_2) was developed alongside F_1 folding. F_1 are associated with the migmatization of the Lower nappe and likely developed syn-magmatic based on the observed foliation-parallel leucosomes often being folded and later cut by later stage leucosomes. The age of F_1 folding and migmatization coincides with the migmatization of the Lower nappe, which was interpreted by Yoshinobu *et al.* (2002) to occur at ~480Ma.

The results from the garnet geothermobarometry indicate that the migmatization and folding of the siliciclastic metasediments in Vassbygda occurred at 630-650°C and 4.5-5.0kbar – initiating muscovite dehydration melting. The generated magmas are seen cutting older mafic dykes, which must have intruded the siliciclastic metasediments before migmatization. The timing of the mafic dykes is confirmed by the extensive deformation of these mafic dykes, often as boudinage or as folds with the same overfolded to recumbent axial planes as F_1.

4.4.3 Nappe Juxtaposition and F_2 Folding (Step 3)

The juxtaposition of nappes in the HNC was completed before 475 Ma, according to Barnes *et al.* (2007), and is seen as the mylonitic HTSZ between the Lower and Middle nappe. The shear zone was interpreted by (Nordgulen *et al.*, 2011) to be ~1km wide, which matches well with the approximately 1.2km of rocks seemingly directly affected by the shear zone on the eastern side of Vassbygda. The affected rocks form parallel layers of deformed and boudinaged metasedimentary rocks with a strong mylonitic foliation proximal to the Lower–Middle nappe transition. The mylonitic foliation (S_3) overprints the original foliation (S_{0+1}), as seen in the pre- to syntectonic staurolite porphyroblast (fig. 3.38 -2).

The HTSZ is believed to have formed during juxtaposition of the Middle nappe on top of the Lower nappe. The trusting is observed in the field area as isoclinal asymmetrical folds with top-to-the-west reverse shear (fig. 3.38 A). This top-to-the-west shear is also supported by the Heggfjorden outcrop observations (fig. 3.41 and 3.42), where the observed mineral lineations and s-c fabric indicated the same vergence. Thorsnes and Løseth (1991) also reached the same conclusion when studying the same area. The presence of the sigmoidal clast within the mylonitic foliation indicated a top-to-the-east shear, which is believed to result from a normal reactivation of the shear zone (Nordgulen *et al.*, 2011; Yoshinobu *et al.*, 2002). The mineral lineation within the HTSZ (fig. 3.43) indicates northeast down-dip to oblique east movements, although it is not clear if these lineations represent the primary thrusting or the normal reactivation.

An F_2 fold phase characterized by open upright to shallowly southeast-plunging folds, with northwest-southeast striking axial planes (fig. 4.13 -3) is interpreted to have formed contemporaneously with the over-thrusting of the Middle nappe. The F_2 folds refolded the isoclinal F_1 folds, which created a type 2 (Ramsay & Huber, 1987) interference pattern.

The stereonet plot of the quartz dioritic intrusions (fig. 3.37 A) shows sub-vertical dykes, which indicates that no apparent significant folding of these dykes has occurred. This is also confirmed by the undeformed nature of the quartz dioritic dykes, which is seen cutting the highly deformed and migmatized metasedimentary rocks (fig. 3.9 D). The fact that the quartz-dioritic dykes cut the leucosomes, and related leucogranitic intrusions, indicate that the quartz-dioritic magmas intruded after the migmatization of the Lower nappe. The quartz dioritic dykes are heavily deformed within the HTSZ and are not observed within the mantle-derived rocks of the Middle nappe. This observation is also described by Thorsnes and Løseth (1991) and indicates that the quartz dioritic dykes were emplaced before nappe juxtapositioning.

The quartz dioritic dykes were initially believed to be related to the Sausfjellet pluton based on the mineralogical comparison to the two-mica granite described by Dumond (2002). Further, the similar Al-in-hornblende pressure estimate for the quartz diorite and the Velfjord plutons indicates that the magmatism was related to the same event. However, since the dykes are deformed by the HTSZ, it must have occurred before nappe juxtaposition at c. 478 Ma (Barnes *et al.*, 2007) and long before pluton emplacement at 445 Ma (Yoshinobu *et al.*, 2002). Therefore, the timing of the quartz dioritic dykes is constrained between the F_2 folding and the juxtaposition of the Middle and Lower nappes. The quartz-diorites may be related to the similar dykes observed within the migmatites of the Horta nappe (Barnes *et al.*, 2007). However, the pressure estimate of these rocks (Oalmann *et al.*, 2011) are not consistent with the estimate for the Vassbygda dykes.

4.4.4 Pluton Emplacement (Step 4)

The suite of Velfjord plutons intruded into the Lower (and Middle) nappe at 448-445 Ma (Yoshinobu *et al.*, 2002), at pressures of 7-8 kbar and temperatures of 750-800°C (Barnes & Prestvik, 2000). The wall rocks of the pluton indicate a decompression event linked to a rapid exhumation of the HNC (Barnes & Prestvik, 2000; Yoshinobu *et al.*, 2002). This event likely marks the normal reactivation of HTSZ described in chapter 4.4.2. The Andalshatten pluton (442 Ma) cuts the Lower–Middle nappe boundary and sets the minimum age for shear deformation along this structure (Barnes *et al.*, 2007; McArthur *et al.*, 2014).

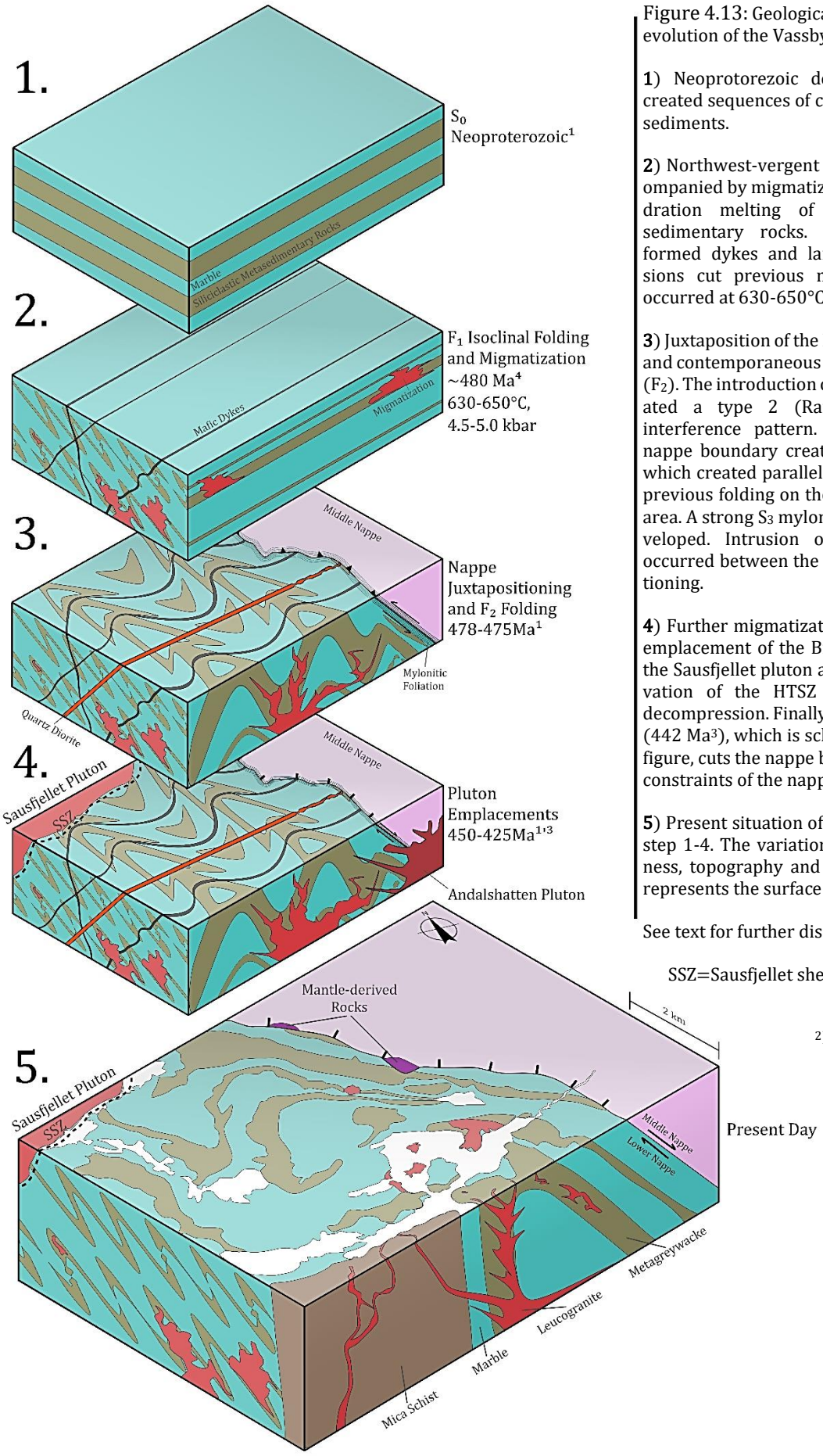

Figure 4.13: Geological model summarizing the evolution of the Vassbygda area.

1) Neoprotorezoic depositional environment created sequences of calcareous and siliciclastic sediments.

2) Northwest-vergent isoclinal folding (F_1) accompanied by migmatization by muscovite dehydration melting of the siliciclastic metasedimentary rocks. The generated magma formed dykes and larger leuocgranitic intrusions cut previous mafic dykes. This event occurred at 630-650°C and 4.5-5.0kbar.

3) Juxtaposition of the Middle and Lower nappes and contemporaneous open symmetrical folding (F_2). The introduction of a second fold phase created a type 2 (Ramsay & Huber, 1987) interference pattern. Deformation along the nappe boundary created a shear zone (HTSZ) which created parallel layers that overprint the previous folding on the eastern side of the field area. A strong S_3 mylonitic foliation was also developed. Intrusion of quartz diorite dykes occurred between the F_2 folding and juxta-positioning.

4) Further migmatization of the HNC led to the emplacement of the Bindal batholith, including the Sausfjellet pluton at 445Ma[4]. Normal reactivation of the HTSZ is simultaneously with decompression. Finally, the Andalshatten pluton (442 Ma[3]), which is schematically shown on the figure, cuts the nappe boundary and sets the age constraints of the nappe amalgamation.

5) Present situation of Vassbygda, derived from step 1-4. The variation of rock sequence thickness, topography and intricate folding pattern represents the surface geometry of the rocks.

See text for further discussion

SSZ=Sausfjellet shear zone (Dumond (2002)

[1]Barnes *et al.* (2007)
[2]Barnes & Prestvik (2000)
[3]Anderson *et al.* (2013)
[4]Yoshinobu et al. (2002)

5 Conclusion

The Vassbygda area is defined by a lowland of marble, calc-silicate rocks and igneous dykes, enclosed by siliciclastic metasedimentary ridges of predominantly metagreywacke and metaarkose. The marble deposits are characterized by two dominant types of marbles: 1) A high-quality graphite-spotted marble and 2) a banded marble with varying quality.

The graphite-spotted marble is a medium- to coarse-grained calcite marble with graphite laths or aggregates located along the calcite grain boundaries. It also holds minor impurities such as quartz and sulphides along the grain boundaries. These minerals are likely easily removed during processes and gives the graphite-spotted marble the best quality found within the area. The banded marble contains varying amounts of silicate minerals and sulphides, which form bands of varying thickness and spacing. Due to the considerable compositional variation, it is challenging to determine an overall quality for the banded marble.

Understanding the deformational history of the Vassbygda units is crucial to interpret the geometry of the marble deposits. The area likely started out as horizontal layers of siliciclastic metasedimentary rocks and marbles, first deformed by isoclinal folding with a northeast-southwest recumbent axial plane (F_1). The isoclinal folding was accompanied by migmatization of the siliciclastic metasedimentary rocks, which occurred at 4.5-5.0kbar and a temperature of 630-650°C, based on garnet geothermobarometry. Migmatization of the siliciclastic metasediments created leucogranitic magmas that are interpreted as the source for the Dengelhalsen intrusion.

The juxtaposition of the Middle nappe along the Heggfjord-Tosen shear zone caused large-scale shear deformation in the uppermost part of the Lower nappe. This deformation led to the straight, parallel geometry and large-scale boudinage of the eastern metasedimentary rocks of Vassbygda. The compression also refolded the Vassbygda units with an upright northwest-southeast axial plane (F_2), creating a type 2 interference pattern with the F_1 isoclinal folds. Quartz dioritic dykes intruded the deformed Vassbygda units and was later followed by emplacement of the Velfjord plutons.

The multi-phase deformation history has resulted in the present-day complex geometry of the Vassbygda units, which is challenging for the exploration of marble deposits. The Stormarka marble deposits are the most promising occurrences within Vassbygda since the area mostly consists of high-quality graphite-spotted marble with only minor bodies of medium-quality banded marble and quartz dioritic dykes. The Stormarka deposit has a cradle-like structure formed by the fold-interference with a depth of more than 256m. However, when modelling the deposit to a reasonable quarry depth of 200m, the 3D model of the deposit gives a volume estimate of c. 1.8 billion tonnes high-quality graphite-spotted marble and c. 305 million tonnes of medium-quality banded marble. A particularly promising zone in the northeastern section of Stormarka is interpreted to contain c. 268 million tonnes of excellent quality graphite-spotted marble.

6 Further Work

6.1 Geophysical Properties and Potential Uses

The marbles are the least magnetical susceptible due to the paramagnetic properties of calcite (Schmidt *et al.*, 2006). The Ca-silicate rocks consist of several magnetic minerals such as magnetite, hematite, and ilmenite (Rosenblum & Brownfield, 1999) and are therefore logically the most magnetic rock in the area. A geophysical exploration can help distinguish rocks in inaccessible or completely overgrown terrain. It can also help to determine the depth extent of rocks and other structural properties not seen during the field mapping. Two types of geophysical exploration may be of value: 1) A gravimetric survey utilizing the contrast in densities and 2) a magnetic survey using the broad span of susceptibility values of the rocks.

A gravimetric survey may help detect ambiguous rock boundaries on the surface and delimit deposits underground. However, some contrast between the densities of the bodies is needed when using gravimetrical methods (Reynolds, 2011). The calc-silicates (except BC-13) have an overall elevated density. If mapped, the calc-silicates would probably give a gravimetric anomaly. Both the marbles, the siliciclastic- and the igneous rocks overlap in density and would therefore be hard to distinguish from each other.

A ground or airborne magnetic survey can also be a useful method for investigating the field area. As the siliciclastic metasedimentary rocks have an overall higher susceptibility than the marbles, one would assume it would be able to differentiate between them, especially since the majority of the marbles show a negative susceptibility. However, as the samples have a Q-value above 1, the samples are remanent-dominated, the difference in susceptibility may be neglectable compared to the remanent magnetization. On the other hand, as their remanent magnetization values are quite similar, it may be possible to detect a slight variation between them. The calc-silicate rocks have elevated NRM- and susceptibility values and would most likely be differentiated on a total magnetic intensity map.

In a best-case scenario, the negative susceptibility value of the high-grade graphite-spotted and banded marble can be used to define the contact between the marbles and siliciclastic metasedimentary rocks and their depth extent. Such data can be used to either confirm or reinterpret the geometry proposed in this thesis. It may also be possible to distinguish the metaarkose from the metagreywacke if the spatial resolution of the geophysical mapping is sufficient to cover the rapid transition observed in the field between these two rocks. The different susceptibility of the banded marble and the graphite-spotted marble may also be further studied to explore the possibility of differentiating the quality of the marble with geophysical measurements. If this is the case, a detailed map of the deposits could be made with ground magnetic surveys.

Geophysical explorations of ornament marbles have also been tested in previous experiments (Martínez *et al.*, 2017; Ojo *et al.*, 2003) and show that methods such as ground-penetrating radar, electric resistivity, and electro-magnetics are useful tools for determining the quality and geometry of the marble deposits.

6.2 Further Mapping and Core Drilling

This thesis provides a general map of the marbles within vassbygda and the enclosing siliciclastic metasedimentary rocks. The classification based on quality used by Brønnøy Kalk was simplified in order to prioritize the geological understanding of the area. This mapping still leaves more work in the detailed mapping of the marbles based on quality, impurities, and structures further to enhance the data on the marble deposits at Vassbygda.

The Stormarka deposit shows a good marble quality at the surface, although further detailed mapping should be undertaken to better map the quality variation. The granitic intrusions, which often occur as swarms throughout Stormarka, should also be mapped for their influence regarding mining. GIS-software utilizing automated lineament mapping (Torgersen *et al.*, 2020) could be an effective method for mapping the dykes based on their protruding surface expression.

Additional core drilling could help determine the depth-extent and quality of the marbles of Stormarka. The core drilling should target the transition between the marbles and the siliciclastic metasediments to constrain the high uncertainty of the depth extent and geometry of the folded ridges. The uncertainty of the amplitude and period of the folded Stormarkheia ridge is essential to investigate in order for a more certain volume estimate and geometry of the Stormarka marble deposit.

6.3 AMS

The AMS is a powerful tool for the classification of rocks and the quantification of minerals and geometric properties. By continuous use of AMS, Brønnøy Kalk may increase the knowledge of the mineralogical properties of the Vassbygda marbles and the processes required for more efficient production. The amount of crushing needed to liberate graphite grains or other impurities can be analysed using AMS' mineral association tools. A better understanding of the geometrical and mineralogical properties of the marble may lead to more cost-efficient crushing and flotation during the mechanical and chemical separation processes of Hustadmarmor. It may be achievable to analyse the marbles for the geometrical properties and to map the area based on the ease-of-separation properties of the various marble types.

6.4 U-Pb Dating

The results from the optical microscopy and AMS confirms the presence of zircons within the siliciclastic metasediments, which can be used for U-Pb age estimates (Winter, 2001). Besides, the siliciclastic metasedimentary rocks and calc-silicate rocks contain abundant titanite, which can be used to date the peak metamorphic event (Romer & Rötzler, 2003; Sun *et al.*, 2012). An age estimate for the metasedimentary rocks of Vassbygda could further explore the affinity to the Lower nappe. A Neoproterozoic age of the siliciclastic metasediments would verify that the Vassbygda units are part of the Lower nappe.

The intrusions found throughout the field area should be dated using Pb-U in zircons to estimate the intrusive age. This age could be used to compare established deformational events, pluton emplacements, and migmatization to see if the Vassbygda intrusions can be seen on a regional scale and setting. The granitic dyke, which cuts the mylonitic shear zone at the top of the Lower nappe (discussed in chapter 3.2.3), can be ideal for estimating a minimum age of the deformation due to its relatively undeformed nature compared to the host rock. Based on the REE composition of the dyke it can also be speculated that the dyke intruded late in the deformational history of the

nappe based on the depleted REE pattern observed. These two observations could be linked to establish an age of the end of the deformation based on U-Pb analyses of zircons.

6.5 Geothermobarimetry

A new study with a larger sample population should be undertaken to confirm the geothermobarometry results in this thesis. The two samples used for this thesis indicated the P-T conditions experienced by the rocks. However, with only two samples, this indication may not accurately represent the P-T condition and should therefore be verified. Especially the results form the calcic amphibole should be revisited based on the large scatter of P-T estimates and uncertainty of the zonation, and low quality of the data points.

The mineral assemblage of graphite and calcite found within the graphite-spotted marble is a prime candidate for further analysis using the calcite-graphite geothermometer (Dunn, 2005; Dunn & Valley, 1992). The dolomite-rich calc mylonite may also yield valuable results if analysed by the Calcite-Dolomite geothermometer (Rathmell *et al.*, 1999). Calcite – graphite or calcite – dolomite thermobarometry can give a vital confirmation for the results from the garnet geothermobarometry. Besides, adding more samples to undertake a quantifiable analysis of calcite twinning (Burkhard, 1993; Ferrill, 1991; Ferrill *et al.*, 2004; Turner, 1953; Weiss, 1954) may yield further confirmation of temperature constraints in the deformational history of the marbles and calc-mylonite of the region.

7 References

Allmendinger, R. W., Cardozo, N., & Fisher, D. M. (2011). *Structural geology algorithms: Vectors and tensors*: Cambridge University Press.

Anders, E., & Grevesse, N. (1989). Abundances of the elements: Meteoritic and solar. *Geochimica et Cosmochimica acta, 53*(1), 197-214.

Anderson, H. S., Yoshinobu, A. S., Nordgulen, Ø., & Chamberlain, K. (2013). Batholith tectonics: Formation and deformation of ghost stratigraphy during assembly of the mid-crustal Andalshatten batholith, central Norway. *Geosphere, 9*(3), 667-690. doi:10.1130/ges00824.1

Anderson, J. L., & Smith, D. R. (1995). The effects of temperature and fO2 on the Al-in-hornblende barometer. *American mineralogist, 80*(5-6), 549-559. doi:10.2138/am-1995-5-614

Andréasson, P. G. (1994). The Baltoscandian margin in neoproterozoic-early palaeozoic times. Some constraints on terrane derivation and accretion in the Arctic Scandinavian Caledonides. *Tectonophysics, 231*(1), 1-32. doi: 10.1016/0040-1951(94)90118-X

Barnes, C. G., Barnes, M. A., Nordgulen, Ø., & Prestvik, T. (1992). Geology of three dioritic plutons in Velfjord, Nordland.

Barnes, C. G., Frost, C. D., Yoshinobu, A. S., McArthur, K., Barnes, M. A., Allen, C. M., . . . Prestvik, T. (2007). Timing of sedimentation, metamorphism, and plutonism in the Helgeland Nappe Complex, north-central Norwegian Caledonides. *Geosphere, 3*(6), 683-703. doi:10.1130/ges00138.1

Barnes, C. G., & Prestvik, T. (2000). Conditions of pluton emplacement and anatexis in the Caledonian Bindal Batholith, north-central Norway. *Norsk Geologisk Tidsskrift, 80*(4), 259-274. doi:10.1080/00291960051030581

Barnes, C. G., Reid, K., Frost, C. D., Barnes, M. A., Allen, C. M., & Yoshinobu, A. S. (2011). Ordovician and Silurian magmatism in the Upper Nappe, Uppermost Allochthon, Helgeland Nappe Complex, north-central Norway. *Norwegian Journal of Geology, 91*(3), 121-136.

Barnes, C. G., Yoshinobu, A. S., Prestvik, T., Nordgulen, Ø., Karlsson, H. R., & Sundvoll, B. (2002). Mafic magma intraplating: anatexis and hybridization in arc crust, Bindal Batholith, Norway. *Journal of Petrology, 43*(12), 2171-2190.

Baudino, M. R., Gardini, C. E., & Rossi, M. (2010). Using Geologic Models to Support Resource and Reserve Estimation of Marble Deposits in Complex Settings.

Bestmann, M., & Prior, D. J. (2003). Intragranular dynamic recrystallization in naturally deformed calcite marble: diffusion accommodated grain boundary sliding as a result of subgrain rotation recrystallization. *Journal of structural Geology, 25*(10), 1597-1613. doi:https://doi.org/10.1016/S0191-8141(03)00006-3

Blundy, J. D., & Holland, T. J. B. (1990). Calcic amphibole equilibria and a new amphibole-plagioclase geothermometer. *Contributions to Mineralogy and Petrology, 104*(2), 208-224. doi:10.1007/BF00306444

Braathen, A., Nordgulen, Ø., Osmundsen, P.-T., Andersen, T., & Roberts, D. (2000). Devonian, orogen-parallel opposed extension in the Central Norwegian Caledonides: Reply. *Geology, 28*, 615-618. doi:10.1130/0091-7613(2000)28<615:DOOEIT>2.0.CO;2

Braathen, A., Osmundsen, P. T., Nordgulen, Ø., Roberts, D., & Meyer, G. (2002). Orogen-parallel extension of the Caledonides in northern Central Norway: An overview. *Norsk Geologisk Tidsskrift, 82*, 225-241.

Bucher, K., & Grapes, R. (2011). *Petrogenesis of Metamorphic Rocks* (8 ed.). Berlin, Heidelberg: Berlin, Heidelberg: Springer Berlin Heidelberg.

Burkhard, M. (1993). Calcite twins, their geometry, appearance and significance as stress-strain markers and indicators of tectonic regime: a review. *Journal of structural Geology, 15*(3), 351-368. doi:https://doi.org/10.1016/0191-8141(93)90132-T

Cardozo, N., & Allmendinger, R. W. (2013). Spherical projections with OSXStereonet. *Computers & Geosciences, 51*, 193-205.

Clark, D. (1997). Magnetic petrophysics and magnetic petrology: Aids to geological interpretation of magnetic surveys. *AGSO journal of Australian geology & geophysics, 17*, 83-104.

Cocks, L., & Torsvik, T. H. (2002). Earth geography from 500 to 400million years ago: a faunal and paleomagnetic review. *Journal of The Geological Society - J GEOL SOC, 159*, 631-644. doi:10.1144/0016-764901-118

Corfu, F., Gasser, D., & Chew, D. M. (2014). New perspectives on the Caledonides of Scandinavia and related areas: introduction. *Geological Society, London, Special Publications, 390*(1), 1-8. doi:10.1144/sp390.28

Deer, W. A., Howie, R. A., & Zussman, J. (1992). *An Introduction to the Rock-forming Minerals* (2 ed.): Longman Scientific & Technical.

Dumond, G. (2002). *Magma chamber construction in the middle crust: insights from the Sausfjellet pluton, Bindal batholith, Norway.* (Master). Texas Tech University,

Dumond, G., Yoshinobu, A. S., & Barnes, C. G. (2005). Midcrustal emplacement of the Sausfjellet pluton, central Norway: Ductile flow, stoping, and in situ assimilation. *GSA Bulletin, 117*(3-4), 383-395. doi:10.1130/b25464.1

Dunn, S. R. (2005). Calcite–graphite isotope thermometry in amphibolite facies marble, Bancroft, Ontario. *Journal of Metamorphic Geology, 23*(9), 813-827. doi:10.1111/j.1525-1314.2005.00611.x

Dunn, S. R., & Valley, J. W. (1992). Calcite–graphite isotope thermometry: a test for polymetamorphism in marble, Tudor gabbro aureole, Ontario, Canada. *Journal of Metamorphic Geology, 10*(4), 487-501. doi:10.1111/j.1525-1314.1992.tb00100.x

Eide, E., Osmundsen, P. T., Meyer, G., Kendrick, M., & Corfu, F. (2002). The Nesna Shear Zone, north-central Norway: An 40Ar/ 39Ar record of Early Devonian -Early Carboniferous ductile extension and unroofing. *Norsk Geologisk Tidsskrift, 82*, 317-339.

Eide, E. A., & Lardeaux, J. M. (2002). A relict blueschist in meta-ophiolite from the central Norwegian Caledonides—discovery and consequences. *Lithos, 60*(1), 1-19. doi:https://doi.org/10.1016/S0024-4937(01)00074-3

Ellis, D. V., & Singer, J. M. (2007). *Well logging for earth scientists* (Vol. 692): Springer.

Essex, R. M., Gromet, L. P., Andréasson, P.-G., & Albrecht, L. (1997). Early Ordovician U-Pb metamorphic ages of the eclogite-bearing Seve Nappes, Northern Scandinavian Caledonides. *Journal of Metamorphic Geology, 15*(5), 665-676. doi:10.1111/j.1525-1314.1997.tb00642.x

Ferrill, D. A. (1991). Calcite twin widths and intensities as metamorphic indicators in natural low-temperature deformation of limestone. *Journal of structural Geology, 13*(6), 667-675. doi:https://doi.org/10.1016/0191-8141(91)90029-I

Ferrill, D. A., Morris, A. P., Evans, M. A., Burkhard, M., Groshong Jr, R. H., & Onasch, C. M. (2004). Calcite twin morphology: a low-temperature deformation geothermometer. *Journal of structural Geology, 26*(8), 1521-1529.

Fossen, H., Pedersen, R.-B., Bergh, S., & Andresen, A. (2008). En fjellkjede blir til. In *The Making of a land: geology of Norway* (2 ed., pp. 180-233). Trondheim: The Norwegian Geological Association.

Gee, D. G. (1975). A tectonic model for the central part of the Scandinavian Caledonides. *American Journal of Science, 275(A), 468-515.*

Gee, D. G., Fossen, H., Henriksen, N., & Higgins, A. (2008). From the Early Paleozoic Platforms of Baltica and Laurentia to the Caledonide Orogen of Scandinavia and Greenland. *Episodes, 31*, 44-51.

Gee, D. G., & Sturt, B. A. (1985). *The Caledonide orogen : Scandinavia and related areas*. Chichester; New York: Wiley.

Gustavson, M. (1973). *Børgefjell: beskrivelse til det berggrunnsgeologiske gradteigskart J. 19-1:100 000*: Universitetsforlaget.

Gustavson, M. (1975). The Low-grade Rocks of the Skålvær Area, S. Helgeland, and Their Relationship to High grade Rocks of the Helgeland Nappe Complex. *NGU Bull., 322*.

Gustavson, M. (Cartographer). (1981). Berggrunnskart Mosjøen M 1:250 000 [Bedrock Map, NGU Skrifter 87]

Hawthorne, F. C., Oberti, R., Harlow, G. E., Maresch, W. V., Martin, R. F., Schumacher, J. C., & Welch, M. D. (2012). Nomenclature of the amphibole supergroup. *American mineralogist, 97*(11-12), 2031-2048. doi:10.2138/am.2012.4276

Heldal, T. (2001). Ordovician stratigraphy in the western Helgeland Nappe Complex in the Bronnoysund area, north-central Norway. *NGU Bulletin, 438*, 47-62.

Henderson, I., Korneliussen, A., & Raaness, A. (2019). 3D-modellering og visualisering av Nestbylia karbonatforekomst, Saltdal kommune.

Holdaway, M. J. (2000). Application of new experimental and garnet Margules data to the garnet-biotite geothermometer. *American mineralogist, 85*, 881-892. doi:10.2138/am-2000-0701

Holdaway, M. J. (2001). Recalibration of the GASP geobarometer in light of recent garnet and plagioclase activity models and versions of the garnet-biotite geothermometer. *American mineralogist, 86*(10), 1117-1129. doi:10.2138/am-2001-1001

Holland, T., & Blundy, J. (1994). Non-ideal interactions in calcic amphiboles and their bearing on amphibole-plagioclase thermometry. *Contributions to Mineralogy and Petrology, 116*(4), 433-447. doi:10.1007/BF00310910

James, D. W., Mitchell, J. G., Ineson, R., & Nordgulen, Ø. (1993). Geology and K/Ar chronology of the Målvika scheelite skarns, Central Norwegian Caledonides. *NGU Bulletin, 424,* 65-74.

Janoušek, V., Farrow, C. M., & Erban, V. (2006). Interpretation of Whole-rock Geochemical Data in Igneous Geochemistry: Introducing Geochemical Data Toolkit (GCDkit). *Journal of Petrology, 47*(6), 1255-1259. doi:10.1093/petrology/egl013

Kleman, J., Hättestrand, C., Borgström, I., & Stroeven, A. (1997). Fennoscandian palaeoglaciology reconstructed using a glacial geological inversion model. *Journal of Glaciology, 43*(144), 283-299. doi:10.3189/S0022143000003233

Kollung, S. (1967). Geologiske undersøkelser i sørlige Helgeland og nordlige Namdal. *Norges Geologiske Undersøkelse*(254).

Krill, A. G., & Zwaan, K. (1987). Reinterpretation of Finnmarkian deformation on western Sørøy, northern Norway. *Norsk Geologisk Tidsskrift, 67*(1), 15-24.

Kruhl, J. H. (1984). Deformation and metamorphism at the base of the Helgeland nappe complex, northwest of Grong (northern Norway). *Geologische Rundschau, 73*(2), 735-751.

Landis, C. A. (1971). Graphitization of dispersed carbonaceous material in metamorphic rocks. *Contributions to Mineralogy and Petrology, 30*(1), 34-45. doi:10.1007/BF00373366

Li, X., Zhang, C., Behrens, H., & Holtz, F. (2020). Calculating amphibole formula from electron microprobe analysis data using a machine learning method based on principal components regression. *Lithos, 362-363*, 105469. doi:10.1016/j.lithos.2020.105469

Martínez, J., Montiel, V., Rey, J., Cañadas, F., & Vera, P. (2017). Utilization of integrated geophysical techniques to delineate the extraction of mining bench of ornamental rocks (marble). *Remote Sensing, 9*(12), 1322.

McArthur, K., Frost, C., Barnes, C., Prestvik, T., & Nordgulen, O. (2014). Tectonic reconstruction and sediment provenance of a far-travelled oceanic nappe, Helgeland Nappe Complex, west-central Norway. *Geological Society Special Publication, 390*. doi:10.1144/SP390.3

Molina, J. F., Moreno, J. A., Castro, A., Rodríguez, C., & Fershtater, G. B. (2015). Calcic amphibole thermobarometry in metamorphic and igneous rocks: New calibrations based on plagioclase/ amphibole Al-Si partitioning and amphibole/ liquid Mg partitioning. *Lithos, 232*, 286-305. doi: 10.1016/j.lithos.2015.06.027

Mørk, M. B. E., Kullerud, K., & Stabel, A. (1988). Sm-Nd dating of Seve eclogites, Norrbotten, Sweden — Evidence for early Caledonian (505 Ma) subduction. *Contributions to Mineralogy and Petrology, 99*(3), 344-351. doi:10.1007/BF00375366

Nesse, W. D. (2011). *Introduction to mineralogy* (2 ed.): Oxford University Press.

NIBIO. (2020). Kilden (Web Map). Retrieved from https://nibio.no/tjenester/kilden. Available from The Norwegian Institute of Bio-Economy Retrieved 30.06.2020 https://nibio.no/tjenester/kilden

Nichols, G. (2009). *Sedimentology and stratigraphy*: John Wiley & Sons.

Nordgulen, Ø., Barnes, C. G., Yoshinobu, A. S., Frost, C., Prestvik, T., Austrheim, H., . . . McArthur, K. (2011). Magmatism & Tectonics in the Uppermost Allochthon, Central Norway *Eurogranites*.

Nordgulen, Ø., Bickford, M. E., Nissen, A. L., & Wortman, G. L. (1993). U-Pb zircon ages from the Bindal Batholith, and the tectonic history of the Helgeland Nappe Complex, Scandinavian Caledonides. *Journal of the Geological Society, 150*(4), 771-783. doi:10.1144/gsjgs.150.4.0771

Nordgulen, Ø., Braathen, A., Corfu, F., Osmundsen, P. T., & Husmo, T. (2002). Polyphase kinematics and geochronology of the late-Caledonian Kollstraumen detachment, north-central Norway. *Norsk Geologisk Tidsskrift, 82*, 299-316.

Nordgulen, Ø., Solli, A., & Thorsnes, T. (Cartographer). (1990). Majafjellet. Berggrunnskart; Majafjellet; 18252; 1:50 000; sort/hvitt;

Nordgulen, Ø., Thorsnes, & T. Husmo, T. (1989). Terråk. Berggrunnskart; Terråk; 18253; 1:50 000; sort/hvitt;.

Oalmann, J. A., Barnes, C. G., & Hetherington, C. J. (2011). Geology of the island of Ylvingen, Nordland, Norway: Evidence for pre-Scandian (~ 475 Ma) exhumation in the Helgeland Nappe Complex. *Norwegian Journal of Geology/Norsk Geologisk Forening, 91*.

Ojo, J., Olorunfemi, M., Folami, S., Omosuyi, G., Abiola, F., & Enikanselu, P. (2003). Geophysical investigation of marble occurrence in Takalafia area, around Abuja, Central Nigeria. *Global Journal of Geological Sciences, 1*(1), 51-62.

Osmundsen, P., Braathen, A., Nordgulen, O., Roberts, D., Meyer, G., & Eide, E. (2003). The Devonian Nesna shear zone and adjacent gneiss-cored culminations, North-Central Norwegian Caledonides. *Journal of The Geological Society - J GEOL SOC, 160*, 137-150. doi:10.1144/0016-764901-173

Osmundsen, P. T., Eide, E., Haabesland, N., Roberts, D., Andersen, T., Kendrick, M., . . . Redfield, T. (2006). Kinematics of the Høybakken detachment zone and the Møre–Trøndelag Fault Complex, central Norway. *Journal of the Geological Society, 163*(2), 303-318.

Passchier, C. W., & Trouw, R. A. (2005). *Microtectonics*: Springer Science & Business Media.

Pedersen, R. B., & Furnes, H. (1991). Geology, magmatic affinity and geotectonic environment of some Caledonian ophiolites in Norway. *Journal of Geodynamics - J GEODYNAMICS, 13*, 183-203. doi:10.1016/0264-3707(91)90038-G

Pirrie, D., & Rollinson, G. K. (2011). Unlocking the applications of automated mineral analysis. *Geology Today, 27*(6), 226-235. doi:10.1111/j.1365-2451.2011.00818.x

Powell, R., & Holland, T. J. B. (2008). On thermobarometry. *Journal of Metamorphic Geology, 26*(2), 155-179. doi:10.1111/j.1525-1314.2007.00756.x

Ramberg, I. B. (1967). *Kongsfjell-områdets geologi, en petrografisk og strukturell undersoekelse i Helgeland, Nord-Norge*: Univ. Forl.

Ramsay, J. G., & Huber, M. I. (1987). Modern structural geology. *Folds and Fractures, 2*, 309-700.

Rathmell, M. A., Streepey, M. M., Essene, E. J., & Van der Pluijm, B. A. (1999). Comparison of garnet-biotite, calcite-graphite, and calcite-dolomite thermometry in the Grenville Orogen; Ontario Canada. *Contributions to Mineralogy and Petrology, 134*(2-3), 217-231.

Reed, S. J. B. (2005). *Electron microprobe analysis and scanning electron microscopy in geology*: Cambridge university press.

Reid, K. (2004). *Magmatic processes in the tosenfjord region, north-central norway: implications for the evolution of the helgeland nappe complex.* (Master). Texas Tech University

Reynolds, J. M. (2011). *An introduction to applied and environmental geophysics*: John Wiley & Sons.

Ridolfi, F., Renzulli, A., & Puerini, M. (2010). Stability and chemical equilibrium of amphibole in calc-alkaline magmas: an overview, new thermobarometric formulations and application to subduction-related volcanoes. *Contributions to Mineralogy and Petrology, 160*(1), 45-66.

Roberts, D. (2003). The Scandinavian Caledonides: Event chronology, palaeogeographic settings and likely modern analogues. *Tectonophysics, 365*, 283-299. doi:10.1016/S0040-1951(03)00026-X

Roberts, D., Melezhik, V., & Heldal, T. (2002). Carbonate formations and early NW-directed thrusting in the highest allochthons of the Norwegian Caledonides: evidence of a Laurentian ancestry. *Journal of the Geological Society, 159*(2), 117-120.

Roberts, D., & Nissen, A. L. (2006). Geochemical changes accompanying mylonitisation of granite at the base of the Helgeland Nappe Complex, Nord-Trøndelag, central Norway. *NGU Bulletin, 446*.

Roberts, D., Nissen, A. L., & Renisbakken, A. (1983). Progressive mylonitization along the western margin of the Bindal massif: a preliminary note. *389*, 27-36.

Romer, R. L., & Rötzler, J. (2003). Effect of metamorphic reaction history on the U-Pb dating of titanite. *Geological Society, London, Special Publications, 220*(1), 147-158.

Rosenblum, S., & Brownfield, I. K. (1999). *Magnetic susceptibilities of minerals*: Citeseer.

Sandvik, K. L., Digre, M., & Malvik, T. (1999). *Oppredning av primære og sekundære råstoffer*. Trondheim: Tapir.

Sandøy, R. (2003). *Geological variations in marble deposits: The geometry, internal structure and geochemical variations of the industrial mineral marble deposits in the Velfjord area (Norway).* (PhD). Norwegian University of Science and Technology, Trondheim.

Schmidt, M. W. (1992). Amphibole composition in tonalite as a function of pressure: an experimental calibration of the Al-in-hornblende barometer. *Contributions to Mineralogy and Petrology, 110*(2), 304-310. doi:10.1007/BF00310745

Schmidt, V., Günther, D., & Hirt, A. (2006). Magnetic anisotropy of calcite at room-temperature. *Tectonophysics, 418*, 63-73. doi:10.1016/j.tecto.2005.12.019

Séguret, M., Séranne, M., Chauvet, A., & Brunel, A. (1989). Collapse basin: A new type of extensional sedimentary basin from the Devonian of Norway. *Geology, 17*(2), 127-130. doi:10.1130/0091-7613(1989)017

Sindre, A. (1980). Tyngdemålinger ved Nævernes-Strøm, Velfjord. *NGU Bull., 1742*, p.7.

Sinergise. (2020). Sentinel Hub: EO Browser (Web Map). Retrieved from https://www.sentinel-hub.com/explore/eobrowser/. Available from Sinergise Retrieved 30.06.2020 https://www.sentinel-hub.com/explore/eobrowser/

Skilbrei, J. R., & Olesen, O. (2005). Deep structure of the Mid-Norwegian shelf and onshore-offshore correlations: Insight from potential field data. In B. T. G. Wandås, J. P. Nystuen, E. Eide, & F. Gradstein (Eds.), *Norwegian Petroleum Society Special Publications* (Vol. 12, pp. 43-68): Elsevier.

Skår, Ø. (2002). U–Pb geochronology and geochemistry of early Proterozoic rocks of the tectonic basement windows in central Nordland, Caledonides of north-central Norway. *Precambrian Research, 116*(3), 265-283. doi:10.1016/S0301-9268(02)00026-8

Slagstad, T., & Kirkland, C. L. (2017). The use of detrital zircon data in terrane analysis: A nonunique answer to provenance and tectonostratigraphic position in the Scandinavian Caledonides. *Lithosphere, 9*(6), 1002-1011. doi:10.1130/l663.1

Spear, F. S., Kohn, M. J., & Cheney, J. T. (1999). P-T paths from anatectic pelites. *Contributions to Mineralogy and Petrology, 134*(1), 17-32. doi:10.1007/s004100050466

Storruste, B. K. (2020). [Personal Communication on the topic of marble quality and flotation results of the Vassbygda marbles].

Streckeisen, A. (1974). Classification and nomenclature of plutonic rocks recommendations of the IUGS subcommission on the systematics of igneous rocks. *Geologische Rundschau, 63*(2), 773-786.

Sturt, B. A., & Gee, D. G. (1986). *The Caledonide orogen: Scandinavia and related areas*. Chichester ; New York: Wiley.

Sturt, B. A., & Ramsay, D. M. (1994). The structure and regional setting of the Skei Group, Leka, north-central Norway. *NGU Bulletin(426),* 31-46.

Sun, J., Yang, J., Wu, F., Xie, L., Yang, Y., Liu, Z., & Li, X. (2012). In situ U-Pb dating of titanite by LA-ICPMS. *Chinese Science Bulletin, 57*(20), 2506-2516.

Terry, M. P., Robinson, P., Hamilton, M. A., & Jercinovic, M. J. (2000). Monazite geochronology of UHP and HP metamorphism, deformation, and exhumation, Nordøyane, Western Gneiss Region, Norway. *American mineralogist, 85*(11-12), 1651-1664.

Thompson, A. B. (1982). Dehydration melting of pelitic rocks and the generation of H 2 O-undersaturated granitic liquids. *American Journal of Science, 282*(10), 1567-1595.

Thorsnes, T., & Løseth, H. (1991). Tectonostratigraphy in the Velfjord-Tosen region, southwestern part of the Helgeland Nappe Complex, Central Norwegian Caledonides. *NGU Bulletin, 421,* 1-18.

Torgersen, E., Redfield, T. F., Svendby, K., & Fabian, K. (2020). *What to do with a Lineament Map?* Paper presented at the 34th Nordic Geological Winter Meeting Oslo, Norway. Abstract retrieved from https://www.geologi.no/images/NGWM20/Abstractvolume_NGWM20.pdf

Turner, F. J. (1953). Nature and dynamic interpretation of deformation lamellae in calcite of three marbles. *American Journal of Science, 251*(4), 276-298.

Weis, P. L., Friedman, I., & Gleason, J. P. (1981). The origin of epigenetic graphite: evidence from isotopes. *Geochimica et Cosmochimica acta, 45*(12), 2325-2332. doi:https://doi.org/10.1016/0016-7037(81)90086-7

Weiss, L. E. (1954). *A study of tectonic style; structural investigation of a marble-quartzite complex in southern California*. Berkeley: University of California Press.

Whitney, D. L., & Evans, B. W. (2010). Abbreviations for names of rock-forming minerals. *American mineralogist, 95*(1), 185-187.

Winter, J. (2001). An Introduction to Igneous and Metamorphic Petrology. *SERBIULA (sistema Librum 2.0)*.

Wu, C.-M., & Cheng, B.-H. (2006). Valid garnet–biotite (GB) geothermometry and garnet–aluminum silicate–plagioclase–quartz (GASP) geobarometry in metapelitic rocks. *Lithos, 89*(1), 1-23. doi:https://doi.org/10.1016/j.lithos.2005.09.002

Wu, C.-M., & Zhao, G. C. (2007). The metapelitic garnet–biotite–muscovite–aluminosilicate–quartz (GBMAQ) geobarometer. *Lithos, 97*(3), 365-372. doi:https://doi.org/10.1016/j.lithos.2007.01.003

Wu, C. M. (2015). Revised empirical garnet–biotite–muscovite–plagioclase geobarometer in metapelites. *Journal of Metamorphic Geology, 33*(2), 167-176. doi:10.1111/jmg.12115

Wu, C. M. (2017). Calibration of the garnet–biotite–Al2SiO5–quartz geobarometer for metapelites. *Journal of Metamorphic Geology, 35*(9), 983-998. doi:10.1111/jmg.12264

Wu, C. M. (2018). Metapelitic Garnet-Muscovite-Al2SiO5-Quartz (GMAQ) Geothermobarometry. *Journal of Earth Science, 29*(5), 977-988. doi:10.1007/s12583-018-0851-z

Wu, C. M., & Zhao, G. (2006). Recalibration of the Garnet–Muscovite (GM) Geothermometer and the Garnet–Muscovite–Plagioclase–Quartz (GMPQ) Geobarometer for Metapelitic Assemblages. *Journal of Petrology, 47*(12), 2357-2368. doi:10.1093/petrology/egl047

Yoshinobu, A., Barnes, C., Nordgulen, Ø., Prestvik, T., Fanning, C., & Pedersen, R. (2002). Ordovician magmatism, deformation, and exhumation in the Caledonides of central Norway: An orphan of the Taconic orogeny? *Geology, 30*. doi:10.1130/0091

8 Appendices

Appendix A - Petrographical Descriptions

Appendix B - AMS

Appendix C - Chemical Analysis - Methods

Appendix D - Petrophysical Analysis

Appendix E - Chemical Analysis - Results

Appendix A: Petrographical Description

Sample: **BC-01**	Rock Name: Biotite hornblende quartz-diorite
Field description:	Fine-grained grey to white magmatic dyke cutting through marble. Consists of dark elongated minerals along grains of white minerals with some visible biotite. Dark grey to grey weathering surface.
Major phases	Biotite (30%), Hornblende (30%), Plagioclase (60%), Quartz (10%)
Minor phases and accessory minerals	Pyrite, Hematite, Epidote/zoisite/chlorite, Allanite, Zircon, Titanite
Overall shape of grain aggregates	Allotriomorphic
Microstructures and textures	Long lathes of hornblende (0.25-2.4 mm) and biotite (2mm) are intergrown and show a shape preferred orientation—strong green pleochroism of hornblende grains. Plagioclase appears as equant to rounded (0.2-2.5 mm) with some showing undulose extinction, deformation and zonation. Biotite contains radioactive elements due to several halos. Titanite appears as skeletal crystals or aggregates (up to 2.4 mm). Altered Allanite crystals (up to 1.5 mm) appears as prismatic crystals with extensive alteration to clino(zoisite). There are places where the allanite is wholly altered to zoisite aggregates. Zoisite show undulose interference clours from yellow to blue on full rotation. Quartz grains show subgrain formation. Elongated grains of biotite are parallel oriented (SPO). Pyrite is commonly altered to an oxide (magnetite?)

Sample: **BC-02**	Rock Name: Migmatitic Meta-Sandstone
Field description	Dark grey to grey, melanocratic, fine-grained rock. Partly melted with visible grains of quartz and biotite. Foliation is visible as zones of biotite. Some zones show salmon-pink to light brown minerals. These mineral zones look like small intrusions, although the zones are parallel to the foliation. The small scale makes it difficult to determine the origin of these zone in hand sample.
Major phases	Biotie (20%), Quartz & Feldspar (80%)
Minor phases and accessory minerals	Zircon, Rutile, Muscovite
Overall shape of grain aggregates	Xenoblastic
Microstructures and textures	Small equigranular laths of biotite (~0.3mm) and equant, equigranular quartz and plagioclase grains (~0.3mm) show sign of a weak foliation with some zones of parallel biotite grains (SPO).

Sample: **BC-03**	Rock Name: Foliated Sillimanite-bearing Biotite Meta-Arkose
Field description:	Gray to light grey / light brown strongly foliated fine-grained rock with larger grains of quartz oriented parallel to the schistosity. Some biotite grains are visible on fresh surfaces; however, most of the grains are not visible to the naked eye. Biotite crystals are larger than the rest of the minerals. Lenses or zones (1-2cm) of white to light brown minerals occurs throughout the rock.
Major phases	Biotite (30%), Muscovite (15-20%), Quartz (45-50%)
Minor phases and accessory minerals	Sillimanite (5%), Plagioclase
Overall shape of grain aggregates	Hypidioblastic, inequigranular - polygonal
Microstructures and textures	Large prismatic biotite crystals (up to 2.5mm) occur together with staurolite (fibrolite) in locally strongly foliated zones. A possible aluminium silicate mineral occurs throughout the section and is extensively altered or replaced by quartz. Quartz and skeletal biotite occupy the area between the deformation zones and seem unaffected by the strain. The muscovite is locally replaced by quartz. The largest quartz grains show extensive subgrain formation, whereas the smaller does not.

Sample: **BC-04**	Rock Name: Graphite-bearing Calcite Marble
Field description	Coarse-grained leucocratic marble with graphite inclusions. The rock is brittle and emits a characteristic smell when broken. Field appearance corresponds to the industrial "Spotted marble" classification. It was collected from the contact between marble and meta-sediments.
Major phases	Calcite (99%)
Minor phases and accessory minerals	Graphite (1%), Pyrite, Hematite
Overall shape of grain aggregates	Equant, Xenoblastic
Microstructures and textures	Large grains of calcite (~4mm) dominate the rock with minor graphite laths (0.5 mm) in clusters spotted throughout the section with small (1mm) grains of sulphides. The pyrites are commonly surrounded by a rim of an oxide (magnetite). The overall shape of the sulphate minerals is equant/rounded, to somewhat elongate with the sulphide core averaging around (150μm) and the rim reaching 70μm in thickness. The calcite show extensive deformation twinning.

Sample: **BC-05**	Rock Name: Calc-Mylonite
Field description	Oriented sample of a fine-grained light grey to white marble. The rock is locally seemingly unaffected by tectonics. However, darker bands show a distinct foliation. The rock was folded with small, open fold indicating reverse movement.
Major phases	Calcite (99%)
Minor phases and accessory minerals	Muscovite, Pyrite
Overall shape of grain aggregates	Xenoblastic
Microstructures and textures	Somewhat lepidoblastic texture with inequigranular calcite and muscovite parallel oriented (S on thin-section). Deformation twins in the calcite have two main directions (SE and SW on the thin-section), with many of the calcite crystals having both deformation twins. The calcite occurs as anhedral, equant grains (1.5mm), whereas the muscovite forms prismatic needles (0.5mm) in between the calcite grains. Trace amounts of pyrite (~50μm) occur scattered around the section.

Sample: **BC-06**	Rock Name: Myrmekitic Granitc Dyke
Field description	Tonalitic dyke which cuts the mylonitic shear zone (sample BC-05). It consists of fine- to medium-grained grey to dark minerals in a fine-grained leucocratic matrix. Larger minerals are seemingly parallel (SPO).
Major phases	Feldspar (Microcline+orthoclase?) (80%), Quartz (20 %)
Minor phases and accessory minerals	Biotite, Muscovite, Titanite
Overall shape of grain aggregates	Xenoblastic, Seriate - interlobate
Microstructures and textures	Felspars occurs as both plagioclase and microcline, although microcline seems to be the dominant variant. Myrmekilitic texture: Large microcline crystals (up to 6mm), with smaller quartz grains (0.1-1mm) within. Seemingly two different types of feldspar occur: the tartar patterned microcline and a textureless type (orthoclase?). The feldspar shows varying degrees of sericitisation, where some grains are unaffected and some wholly altered.

Sample: **BC-07**	Rock Name: Sulphide-bearing Mica-Schist
Field description	Oriented sample of fine-grained mica rich, grey to light grey melanocratic, foliated rock. Visible biotite and muscovite grains form parallel layers with some smaller quartz grains. The rock is locally aphanitic.
Major phases	Biotite (30%) Muscovite (30 %) Quartz (35%)
Minor phases and accessory minerals	Pyrite (5%), Chlorite, Chalcopyrite, Zircon
Overall shape of grain aggregates	Xenoblastic
Microstructures and textures	Lepidoblastic, inequigranular micas (~350μm) occur in a groundmass of quartz. All elongated grains follow the foliation throughout the section. Some larger grain aggregates of muscovite. Sulphides form inequigranular (50-500μm) parallel laths and follow the overall foliation.

Sample: **BC-08**	Rock Name: Chlorite-bearing Diopside Skarn
Field description	Dark grey to green, fine- to medium-grained, dense rock with extensive surface oxidation (dark brown, rust). Fresh surfaces show zones of yellow to creamy white aphanitic crystals. It is extremely hard and resistant to breaking. It occurs locally in small bodies (up to 5x5m) often surrounded by the rock in sample BC-09. May contain large crystals (up to 3-4 cm) of diopside/ hedenbergite?
Major phases	Orto- and clinopyroxene, Plagioclase, Chlorite
Minor phases and accessory minerals	Amphibole, Titanite, Rutile, Pyrite, Chalcopyrite.

Overall shape of grain aggregates	Xenoblastic
Microstructures and textures	Large amphiboles are heavily altered or replaced by sericite or pyroxene. Zoned chlorite with anonrmal Prussian-blue interference colours appears throughout the section. The rim of these chlorites is dark brown, with a sharp transition into blue closer to the centre. Titanites occur as (200-1300 μm) sub- to anhedral crystals.

Sample: **BC-09**	Rock Name: Schistose Biotite Amphibolite
Field description	Dark grey to blackish-grey/green, melanocratic, fine- to medium-grained somewhat foliated rock consisting mainly of dark elongated minerals with spots of smaller white minerals. Ranges from extremely hard to brittle. May sometimes flake or break during handling. Contains locally secondary quartz-veins that cuts through foliation.
Major phases	Hornblende (25%), Diopside (25%) Plagioclase (30%) Bioite (20%)
Minor phases and accessory minerals	Titanite, Allanite, Epidote, Rutile?, Pyrite, Chalcopyrite
Overall shape of grain aggregates	Hypidioblastic/Hypidiomorphic
Microstructures and textures	Amphiboles occur as sub- to anhedral hornblende crystals (~0.7mm) or aggregated masses. The amphiboles show medium to week green pleochroism and parallel extinction (Hornblende). Sections with euhedral grans and two distinct cleavages show a darker green parallel to elongation. The amphiboles have a broad range in interference colours from dark brown/orange to light blue/green. However, all show the same pleochroism and is therefore believed to be the same type. The euhedral sections have the lowest interference clour. Biotite laths of ~0.5mm occur throughout the section and are seemingly intergrown with the amphiboles. Slight foliation, mostly visible in thin section scan. Pyrite is the dominant sulphide and occurs as anhedral, equant to skeletal grains (200μm) and is commonly intergrown with smaller (70μm) chalcopyrite grains. Allanite occurs as rounded to elongated crystals (~120μm) and shows alteration to epidote. The epidote appears as a skeletal ring around the allanite crystals and seems to occupy grain boundaries around the altered allanite and surrounding crystals. Titanite occurs as smaller (70μm) anhedral crystals and aggregates, although some show sub- to euhedral grain form and can reach 530μm in the elongated direction.

Sample: **BC-10**	Rock Name: Titanite Amphibolite (Skarn?)
Field description	Light grey to grey aphanitic rock with extensive surface oxidisation. Cuts seemingly through surrounding marbles with no apparent sedimentary transition. Fresh surfaces show some larger sulphides and extensive fracturing with dark red to brown infill. The rock is extremely hard, and it was a challenge to break off samples.
Major phases	Actinolite and Diopside (40%) Plagioclase (40%) Pyrite (5-10%) Titanite (5-10%)
Minor phases and accessory minerals	Rutile, Ilmenite
Overall shape of grain aggregates	Xenoblastic
Microstructures and textures	Colourless to weak green diopside? With inclined extinction and first- to lower second-order interference colours (0.3-0.8mm) occur together with smaller feldspar grains (0.1mm). Sulphides show alteration rims. Cracks split mineral grains and are sealed with larger titanite grains (up to 1.6 mm) and. Amphiboles / Pyroxenes show sign of alteration/ replacement to rutile (rutilization). Sulphides (150µm) often occur together with larger titanite aggregates and consist entirely of pyrite. Oxides (Ilmenite?) (100µm) occur in clusters of titanite grains.

Sample: **BC-11**	Rock Name: Banded Calcite Marble
Field description	Heavily weathered marble with medium to coarse-grained calcite crystals. May resemble a sandstone on some weathered surfaces. The rock shows parallel banding of darker sections and is devoid visible of graphite inclusions. This marble type occurs in seemingly random positions, but are concentrated close to meta-sedimentary contacts.

Sample: **BC-12**	Rock Name: Biotite Titanite-bearing Amphibolite
Field description	Dark grey to greenish-black, fine-grained rock often found round larger skarn bodies. It consists mainly of dark green to black minerals with minor extent white minerals. The rock is slightly foliated with elongated minerals in SPO. Often extremely hard and is similar in appearance to some of the darker calc-silicates in the area. The sample is from a dyke in short proximity to a skarn-quarry.
Major phases	Hornblende (60%) Biotite (10%) Plagioclase (40%)
Minor phases and accessory minerals	Titanite (3-5%), pyrite. Chalcopyrite, Pentlandite Microcline
Overall shape of grain aggregates	Xenoblastic to hypidiomorphic
Microstructures and textures	Zoned, equant and anhedral amphiboles (~0.6mm) with a brown-green centre and green rim. Biotite occurs as long needles (0.1-2.5mm). Somewhat lepidoblastic texture. Feldspar crystals (~0.3mm) show plagioclase lamella with some showing microcline tartar textures. Sulphides consist mainly of pyrite/ pyrrhotite with smaller inclusions/alterations to chalcopyrite and pentlandite with characteristic flame texture.

Sample: **BC-13**	Rock Name: Schistose Biotite-bearing Amphibolite
Field description	Gray to light-grey foliated fine-grained rock consisting of a mix of dark and light minerals. Some larger quartz veins appear along foliation planes.
Major phases	Hornblende (25%), Diopside (25%), Microcline (50%)
Minor phases and accessory minerals	Titanite, Biotite, Allanite, Epidote, Chlorite, Plagioclase
Overall shape of grain aggregates	Xenoblastic
Microstructures and textures	Sub- to euhedral hornblende crystals (~5mm) appear as laths intergrown with quartz or smaller, almost euhedral crystals. Quartz and feldspar (~0.3mm), biotite (~0.4mm) and hornblende are foliated with shape preferred orientation of the elongated hornblende and biotite grains. Altered diopside occurs throughout the section. The feldspars are difficult to distinguish due to the lack of lamella, although some show the characteristic microcline tartar pattern. Allanite, epidote and the amphiboles occur as described in sample BC-09 although this sample shows more extensive alteration of amphibole grain boundaries. As well as as the replacement of clino-amphiboles (no pleochroism) which is almost wholly altered into either anomalous berlin blue chlorite or epidote (unsure).

Sample: **BC-16**	Rock Name: Garnet Mica-schist
Field description	Similar to BC-07 with the addition of small 2-3mm reddish-brown garnets.
Major phases	Quartz, Plagioclase, Biotite (25%), Muskovite, Garnet
Minor phases and accessory minerals	Microcline, Chlorite, Titanite, Rutile, Sillimanite (Fibrolite)
Overall shape of grain aggregates	Hypidiomorphic
Microstructures and textures	Large leucosomes of plagioclase and quartz dominates the thin sections. These leucosomes cut the through the primary fabric. Some of the grains in the leucosomes show subgrain formation, with the feldspar and is relatively pristine compared to the cracked and sericite-altered primary feldspar. The primary feldspars are microclinic occurs as sericitized and fractured grains of about the same size as the larger quartz grains. Characteristic tartar-pattern is observed on several microcline grains. The primary feldspars commonly contain muscovite or fibrolite needles. The primary quartz occurs as small (0.04 mm) rounded grains surrounding large (up to 2mm) grains. These larger grains show extensive sub-grain formation and irregular grain boundaries. The smaller quartz grains are likely the result of sub-grain rotation within the larger quartz grains. Biotite and muscovite occur as elongated laths (0.06 – 1.4 mm) or rounded, skeletal crystals in semi-foliated zones. Although elongated minerals show a shape preferred orientation to the surrounding grains, no overall foliation is observed throughout the thin section. Euhedral muscovite crystals commonly overgrow the biotite. These muscovite crystals are not similar in appearance as other, anhedral, muscovite grains found within the rock, indicating two generations of muscovite growth. The anhedral muscovite also includes fibrolite needles within the core of the mineral. These needles are not found within the euhedral muscovite. Needles are also found within garnets – the same is small biotite laths. It seems that the garnet, the anhedral muscovite, biotite and sillimanite are in equilibrium based on the mineral textures. Garnets occur as an- to subhedral, minutely altered crystals (0.2 – 1.5 mm).

Appendix B: AMS

BC-01 - Quartz Diorite

Mineral Distribution

Mineral	Number	Area %	Weight %	Grain Size (µm)	Grain Size Std Dev (µm)	Average Composition
Albite	6532	52.74	50.93	64.62	204.21	O 44,93; Si 35,53; Al 19,54;
Epidote	26	0.00	0.00	10.00	0.00	O 38,61; Fe 25,46; Si 18,26; Ca 13,79; Al 3,88;
Hematite	234	0.17	0.33	33.89	51.13	Fe 70,29; O 29,71;
Zircon	57	0.00	0.01	11.98	4.78	Zr 49,47; O 31,08; Si 19,45;
Microcline	15	0.00	0.00	10.00	0.00	Si 41,61; O 40,78; Al 17,31; Fe 0,3;
Pyrrhotite	13	0.00	0.00	12.18	5.31	Fe 59,13; S 40,87;
Rutile	2	0.00	0.00	38.29	0.00	Ti 73,78; O 25,76; Fe 0,46;
Allanite	247	0.03	0.04	18.32	13.50	O 33,85; Si 19,52; Al 14,75; Fe 11,53; Ca 11,51; Ce 8,82; Nd 0,03;
Muscovite	1850	0.18	0.20	13.78	11.56	O 41,59; Si 28,75; Al 20,25; K 9,38; Fe 0,02; Mg 0,01;
(clino)Zoisite	637	2.54	3.17	67.45	154.63	O 35,51; Ca 20,57; Si 18,51; Al 16,88; Fe 8,52;
Biotite	6135	18.46	21.25	70.96	130.09	O 34,33; Si 18,96; Fe 16,76; Al 11,07; K 9,99; Mg 8,45; Ti 0,44;
Quartz	3436	8.20	8.22	55.24	106.42	Si 58,82; O 41,06; K 0,09; Na 0,01; Ca 0,01; Al 0,01;
Magnesio-Hornblende	2277	11.89	14.13	98.38	161.99	O 35,29; Si 22,22; Fe 16,03; Ca 11,9; Mg 7,48; Al 7,07; Na 0,02;
Titanite	822	0.97	1.27	51.06	66.04	O 34,39; Ca 26,15; Ti 24,72; Si 14,46; Al 0,27; Fe 0;
Apatite	1695	0.39	0.45	22.82	23.86	Ca 47,58; O 34,33; P 18,09;
Pyrite	7	0.01	0.00	57.77	48.53	S 51,91; Fe 48,09;
Unclassified	30395	4.4	0.0	18.0	22.6	O 36,7; Si 21,9; Fe 13,41; Al 11,07; Ca 8,49; Mg 4,85; K 0,82; P 0,77; Zr 0,63; Na 0,61; Ti 0,54; As 0,06; Cl 0,04; Ce 0,04; Au 0,04; S 0,01; Nd 0,01; Ag 0,01; Mn 0,01;

Element distribution (normalized)

Mineral	Al %	Ca %	Ce %	Fe %	K %	La %	Mg %	Na %	Nd %	Ni %	O %	P %	Pr %	S %	Si %	Ti %	Zr %
Albite	68.42	57.14	46.07	2.22	8.36	33.33	1.19	99.67	77.26	77.97	52.81	0.10	76.42	18.66	54.73	1.88	6.64
Zircon	0.00	0.00	0.00	0.01	0.00	0.00	0.00	0.00	0.00	0.00	0.01	0.00	0.00	0.00	0.00	0.00	60.32
Epidote	0.00	0.00	0.00	0.01	0.00	0.00	0.00	0.00	0.00	0.00	0.00	0.00	0.00	0.00	0.00	0.00	0.00
Microcline	0.00	0.00	0.19	0.00	0.00	0.00	0.00	0.00	0.00	0.00	0.00	0.00	0.00	0.00	0.00	0.00	0.00
Rutile	0.00	0.00	0.00	0.00	0.00	0.00	0.00	0.00	0.00	0.00	0.00	0.00	0.00	0.00	0.00	0.17	0.00
Pyrite	0.00	0.00	0.00	0.02	0.00	0.62	0.00	0.00	0.00	0.00	0.00	0.00	0.00	29.99	0.00	0.00	0.00
Pyrrhotite	0.00	0.00	0.00	0.00	0.00	0.00	0.00	0.00	0.00	0.00	0.00	0.00	0.00	3.59	0.00	0.00	0.00
Hematite	0.07	0.01	1.12	3.29	0.01	0.00	0.00	0.00	0.00	0.69	0.24	0.00	0.00	19.79	0.05	0.00	0.00
Allanite	0.05	0.07	34.10	0.07	0.00	0.00	0.00	0.00	0.20	0.00	0.04	0.00	0.00	0.11	0.03	0.00	0.00
Muscovite	0.32	0.08	0.26	0.00	0.76	0.54	0.00	0.12	0.14	0.32	0.22	0.00	0.74	0.07	0.20	0.03	0.00
(clino)Zoisite	4.29	9.60	6.08	4.18	0.02	0.30	0.00	0.04	9.50	0.44	3.03	0.22	2.66	0.55	2.07	0.05	0.33
Biotite	18.85	0.37	1.19	55.10	87.85	0.85	62.27	0.06	0.33	4.29	19.63	0.75	3.64	6.31	14.21	22.25	4.17
Quartz	0.00	0.01	10.18	0.16	0.32	63.47	0.03	0.03	11.79	11.72	9.07	0.12	14.43	17.51	17.03	0.10	22.55
Magnesio-Hornblende	7.97	24.71	0.62	34.93	2.66	0.88	36.50	0.07	0.37	2.78	13.37	0.16	1.66	3.31	11.03	1.23	0.65
Titanite	0.03	4.89	0.03	0.00	0.01	0.00	0.01	0.01	0.00	0.92	1.17	0.16	0.29	0.12	0.65	74.27	0.30
Apatite	0.00	3.13	0.17	0.01	0.00	0.00	0.00	0.00	0.39	0.86	0.41	98.48	0.15	0.00	0.01	0.02	5.04

BC-02 - Metaarkose

Mineral Distribution

Mineral	Number	Area %	Weight %	Grain Size (µm)	Grain Size Std Dev (µm)	Average Composition
Quartz	2369	41.60	42.23	162.63	211.47	Si 57,8; O 42,08; K 0,09; Na 0,02; Ca 0; Al 0;
Zircon	7	0.00	0.00	10.00	0.00	Zr 45,91; O 34,88; Si 19,22;
Apatite	57	0.01	0.01	14.00	9.63	Ca 46,1; O 36,35; P 17,55;
Hematite	26	0.02	0.03	21.80	33.10	Fe 69,29; O 30,71;
Albite	4555	43.04	43.63	98.47	145.39	O 39,32; Si 33,75; Al 15,06; Na 8,46; Ca 3,35; K 0,04; Fe 0,02;
Biotite	3609	11.31	13.18	80.46	92.61	O 33,62; Fe 19,74; Si 17,99; Al 11,77; K 9,69; Mg 4,57; Ti 2,63;
Muscovite	1285	0.79	0.92	24.59	40.41	O 40,07; Si 24,71; Al 23,32; K 11,38; Fe 0,52; Mg 0,01;
Rutile	7	0.00	0.00	13.45	6.01	Ti 66,62; O 32,64; Fe 0,74;
Unclassified	25959	3.20	0.00	13.31	7.67	Si 45,26; O 33,53; Al 8,91; Fe 5,2; Na 2,06; K 1,99; Ca 1,12; Ti 0,56; Zr 0,54; Mg 0,33; Cl 0,19; P 0,17; As 0,06; Au 0,04; Ag 0,01; S 0,01; Mn 0,01;

BC-04 - Graphite-Spotted Marble

Mineral Distribution

Mineral	Number	Area %	Weight %	Grain Size (µm)	Grain Size Std Dev (µm)	Average Composition
Calcite	779	93.42	98.19	645.49	754.89	Ca 53,61; O 46,37; Mg 0,01; Fe 0; Si 0; Al 0;
Pyrite	3	0.00	0.01	100.52	58.88	S 52,14; Fe 47,86;
Apatite	17	0.02	0.01	80.06	64.33	Ca 48,16; O 33; P 18,84;
Quartz	35	0.44	0.46	243.21	257.79	Si 57,77; O 42,23; K 0; Ca 0;
Magnetite/ siderite	50	0.00	0.00	15.30	10.88	Fe 60,06; O 33,53; Ca 6,41;
Hematite	149	0.08	0.17	42.69	69.84	Fe 69,23; O 30,77;
Na-Feldspar*	193	0.03	0.01	24.34	32.20	O 39,09; Si 32,48; Al 16,3; Na 7,77; Ca 4,36;
Graphite	5376	0.35	0.29	18.88	24.73	C 100;
Titanite	36	0.03	0.03	82.55	73.63	O 34,33; Ca 26,49; Ti 21,78; Si 14,65; Al 2,73; Fe 0,02;
K-Feldspar*	168	0.04	0.01	32.27	54.35	O 41,93; Si 25,59; Al 21,14; K 11,34;
Pyrrhotite	2	0.00	0.00	10.00	0.00	Fe 56,28; S 43,72;
Resin	8454	2.10	0.82	34.18	65.59	C 96,5; Cl 3,5;
Unclassified	58346	3.38	0.00	17.93	19.20	Ca 34,05; C 32,4; O 28,16; Si 2,61; Fe 0,96; Al 0,62; Cl 0,48; Na 0,22; K 0,19; Mg 0,15; Au 0,05; As 0,05; P 0,02; Ti 0,02; Ag 0,01;

*The feldspars were not reclassified as described in chapter 3.3.2, due to the low amount present.

Element distribution (normalized)

Mineral	Al %	Ca %	Cl %	K %	Fe %	Mg %	Na %	O %	P %	S %	Si %	Ti %
Calcite	17.03	99.94	2.43	0.98	2.65	99.25	89.86	99.02	27.75	1.09	0.62	19.87
Pyrite	0.00	0.00	0.00	0.00	2.64	0.00	0.00	0.00	0.00	95.78	0.00	0.40
Apatite	0.00	0.01	0.00	0.00	0.00	0.00	0.01	0.01	71.66	0.00	0.00	0.00
Quartz	0.00	0.00	0.01	0.69	0.01	0.22	0.00	0.46	0.34	0.55	94.96	0.25
Pyrrhotite	0.00	0.00	0.00	0.00	0.04	0.00	0.00	0.00	0.00	1.07	0.00	0.00
Magnetite/siderite	0.16	0.00	0.03	0.00	2.11	0.01	0.01	0.00	0.06	0.00	0.00	0.00
Hematite	1.22	0.00	0.23	0.25	91.96	0.29	0.62	0.12	0.00	1.50	0.19	0.05
Graphite	0.07	0.00	20.23	0.16	0.09	0.06	0.10	0.00	0.00	0.01	0.01	0.16
Titanite	13.02	0.02	0.00	0.02	0.00	0.00	0.04	0.03	0.08	0.00	1.69	79.08
K-Feldspar	44.07	0.00	0.00	95.12	0.09	0.09	0.15	0.01	0.00	0.00	1.29	0.03
Na-Feldspar	24.34	0.00	0.00	2.16	0.00	0.00	8.81	0.01	0.00	0.00	1.18	0.00

BC-12 - Mafic Dyke

Mineral Distribution

Mineral	Number	Area %	Weight %	Grain Size (µm)	Grain Size Std Dev (µm)	Average Composition
Magnesio-Hornblende	861	62.75	68.26	318.39	508.34	O 35,44; Si 21,95; Fe 13,87; Ca 12,28; Al 8,31; Mg 8,09; Na 0,04;
Epidote	52	0.00	0.00	10.00	0.00	O 37,71; Fe 23,6; Si 18,52; Ca 16,52; Al 3,65;
Hematite	698	0.08	0.14	15.61	11.57	Fe 80,83; O 19,17;
Zircon	19	0.00	0.00	10.00	0.00	Zr 51,14; O 28,8; Si 20,07;
Pyrite	93	0.01	0.00	14.43	10.72	Fe 51,13; S 48,87;
Microcline	6	0.00	0.00	10.00	0.00	O 42,74; Si 38,41; Al 17,27; Fe 1,58;
Pentlandite	21	0.00	0.00	11.83	6.44	S 35,49; Fe 35,29; Ni 29,22;
Pyrrhotite	388	0.52	0.18	50.81	65.57	Fe 61,46; S 38,54;
(clino)Zoisite	622	0.23	0.26	29.29	46.48	O 37,54; Ca 20,99; Si 18,73; Al 18,2; Fe 4,54;
Rutile	1	0.00	0.00	10.00	0.00	Ti 53,99; O 46,01;
Titanite	1815	2.95	3.50	67.15	64.10	O 33,92; Ca 26,42; Ti 23,38; Si 14,67; Al 1,62; Fe 0;
Albite	13328	24.83	21.95	29.59	98.60	O 45,14; Si 34,51; Al 20,35;
Muscovite	116	0.01	0.01	12.05	8.50	O 42,28; Si 28,32; Al 20,95; K 8,43; Fe 0,01; Mg 0,01;
Biotite	1196	4.98	5.24	92.11	163.62	O 34,78; Si 19,79; Fe 13,05; Mg 12,16; K 10,23; Al 9,95; Ti 0,02;
Allanite	675	0.04	0.06	10.04	0.67	O 36,93; Si 24,57; Ca 13,56; Fe 13,17; Al 9,69; Ce 2,08; Pr 0,01;
Apatite	1212	0.37	0.39	27.95	25.39	Ca 47,82; O 34,02; P 18,16;
Quartz	5	0.00	0.00	12.00	4.47	O 55,25; Si 44,75;
Unclassified	30299	3.12	0.00	14.56	14.01	O 32,97; Si 20,05; Ca 15,73; Fe 12,17; Al 10,05; Mg 4,09; P 1,18; Ti 1,18; S 1,09; Na 0,5; K 0,43; Zr 0,24; As 0,13; Cl 0,1; Au 0,04; Ni 0,02; Ag 0,01;

Element Distribution (normalized)

Mineral	Al %	Ca %	Ce %	Fe %	K %	La %	Mg %	Na %	Nd %	Ni %	O %	P %	Pr%	S %	Si %	Ti %	Zr %
Magnesio-Hornblende	56.12	72.31	3.32	90.14	38.42	28.90	88.47	2.35	21.99	17.13	67.35	0.11	36.36	0.86	64.98	0.98	11.08
Epidote	0.00	0.01	0.00	0.01	0.00	0.00	0.00	0.00	0.00	0.00	0.00	0.00	0.00	0.01	0.00	0.00	0.00
Hematite	0.01	0.01	0.00	0.80	0.01	0.00	0.00	0.02	0.00	4.56	0.06	0.00	0.00	27.13	0.02	0.01	0.00
Zircon	0.00	0.00	0.00	0.00	0.00	0.00	0.00	0.00	0.00	0.00	0.00	0.00	0.00	0.00	0.00	0.00	63.61
Pyrite	0.00	0.00	0.00	0.01	0.00	0.75	0.00	0.01	0.00	9.27	0.00	0.00	0.00	1.50	0.00	0.00	0.00
Pentlandite	0.00	0.00	0.00	0.01	0.00	0.00	0.00	0.00	0.00	27.03	0.00	0.00	0.00	0.96	0.00	0.00	0.00
Quartz	0.00	0.00	0.00	0.00	0.00	1.76	0.00	0.00	0.00	0.03	0.00	0.00	0.00	0.00	0.00	0.00	3.98
Microcline	0.00	0.00	0.00	0.00	0.00	0.00	0.00	0.00	0.00	0.00	0.00	0.00	0.00	0.00	0.00	0.00	0.00
Pyrrhotite	0.00	0.00	0.00	1.03	0.00	6.93	0.00	0.00	0.02	3.43	0.00	0.00	0.00	68.48	0.00	0.00	0.00
(clino)Zoisite	0.47	0.47	2.07	0.11	0.01	1.45	0.00	0.04	1.41	0.10	0.27	0.17	0.31	0.17	0.21	0.03	0.32
Titanite	0.56	8.02	0.13	0.00	0.00	0.00	0.01	0.04	0.05	2.02	3.33	0.18	1.12	0.08	2.24	98.60	0.29
Albite	37.58	17.44	50.55	1.28	2.25	49.77	1.19	97.52	72.87	34.85	23.47	0.04	51.04	0.62	27.95	0.23	0.66
Muscovite	0.02	0.00	0.00	0.00	0.09	0.00	0.00	0.02	0.00	0.00	0.01	0.00	0.00	0.00	0.01	0.00	0.00
Biotite	5.17	0.08	6.38	6.53	59.18	10.44	10.24	0.00	3.04	1.06	5.09	0.12	10.91	0.18	4.51	0.15	2.35
Apatite	0.00	1.59	0.12	0.00	0.00	0.00	0.00	0.01	0.62	0.52	0.37	99.38	0.12	0.00	0.01	0.01	17.71
Rutile	0.00	0.00	0.00	0.00	0.00	0.00	0.00	0.00	0.00	0.00	0.00	0.00	0.00	0.00	0.00	0.01	0.00
Allanite	0.05	0.06	37.43	0.07	0.04	0.00	0.08	0.00	0.00	0.00	0.05	0.01	0.14	0.00	0.06	0.00	0.00

AMS Montage Images

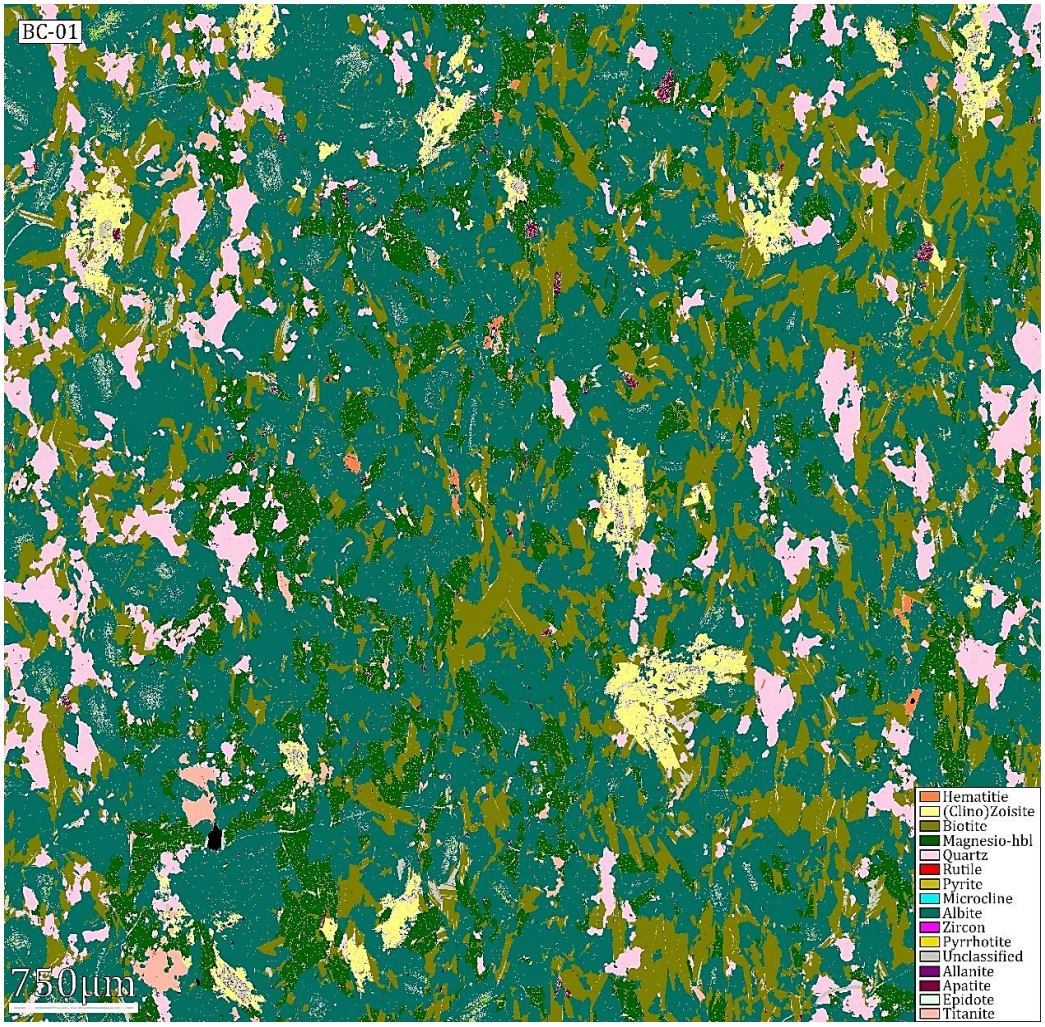

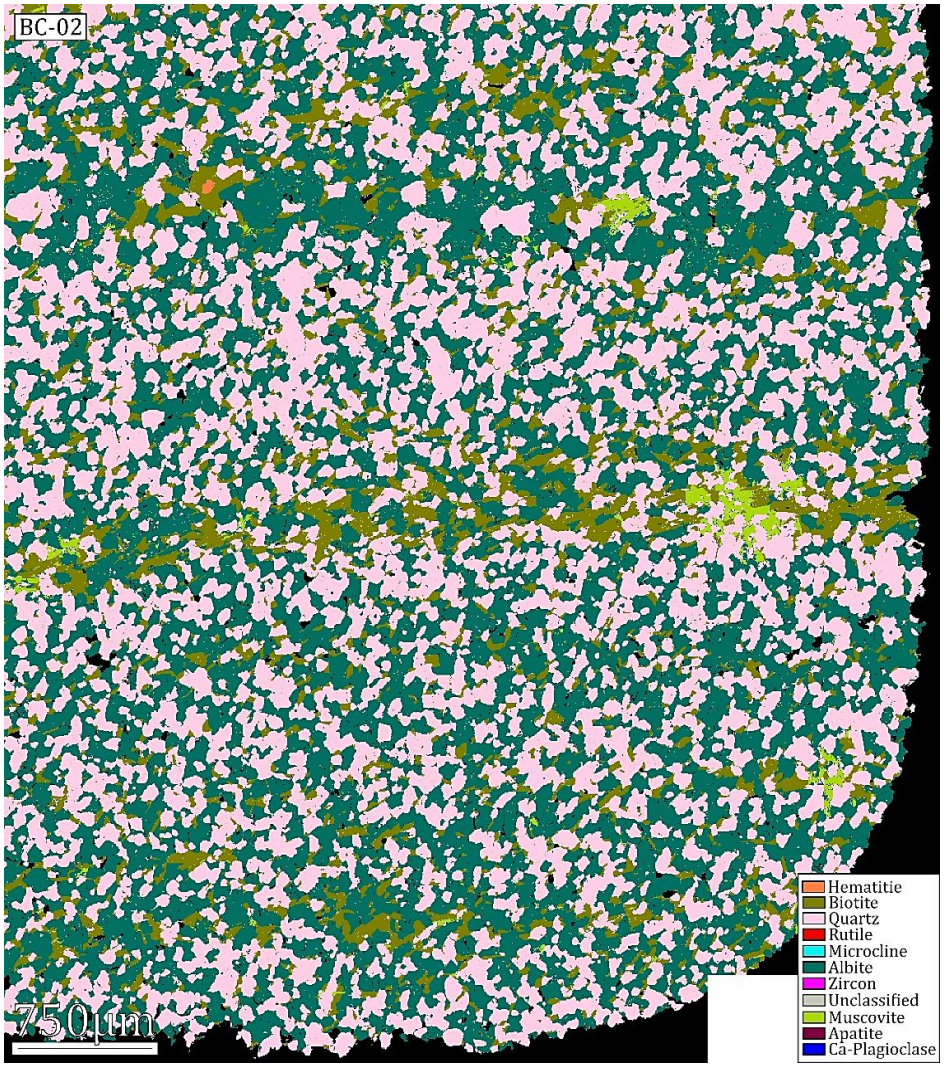

BC-04

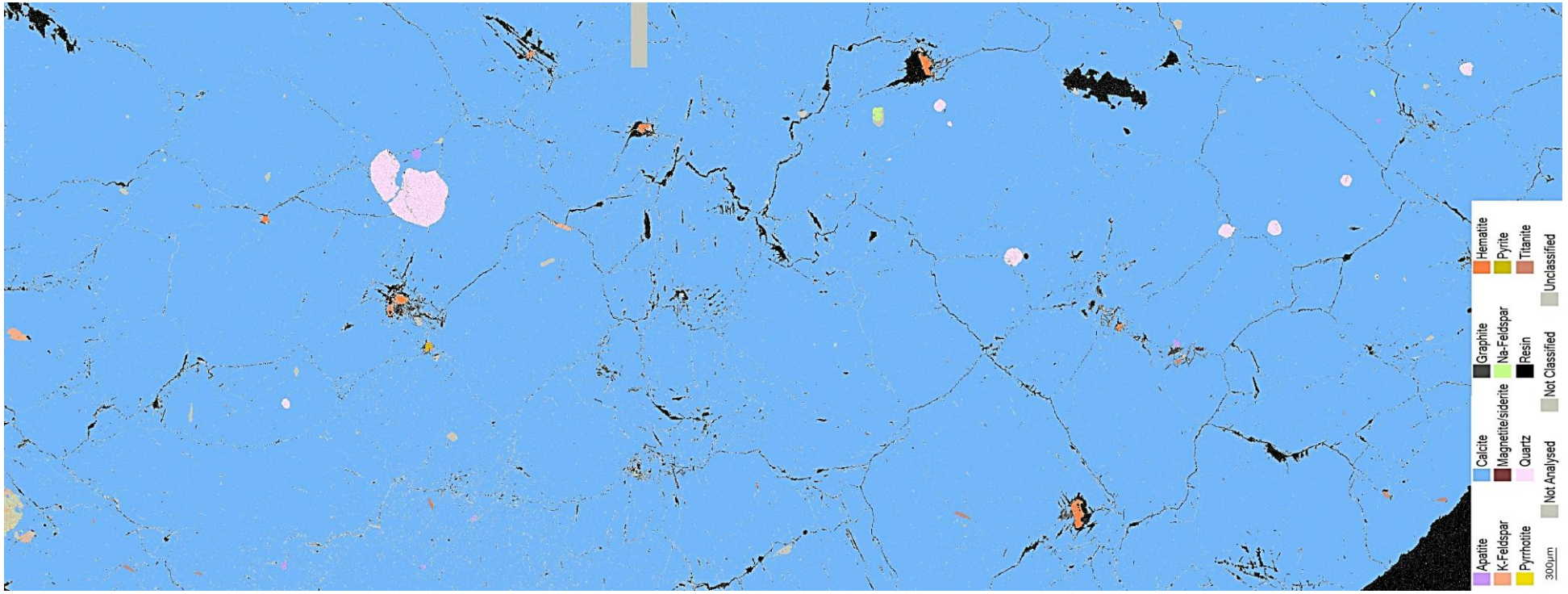
Hematite
Pyrite
Titanite
Unclassified
Graphite
Na-Feldspar
Resin
Not Classified
Calcite
Magnetite/siderite
Quartz
Not Analysed
Apatite
K-Feldspar
Pyrrhotite
300µm

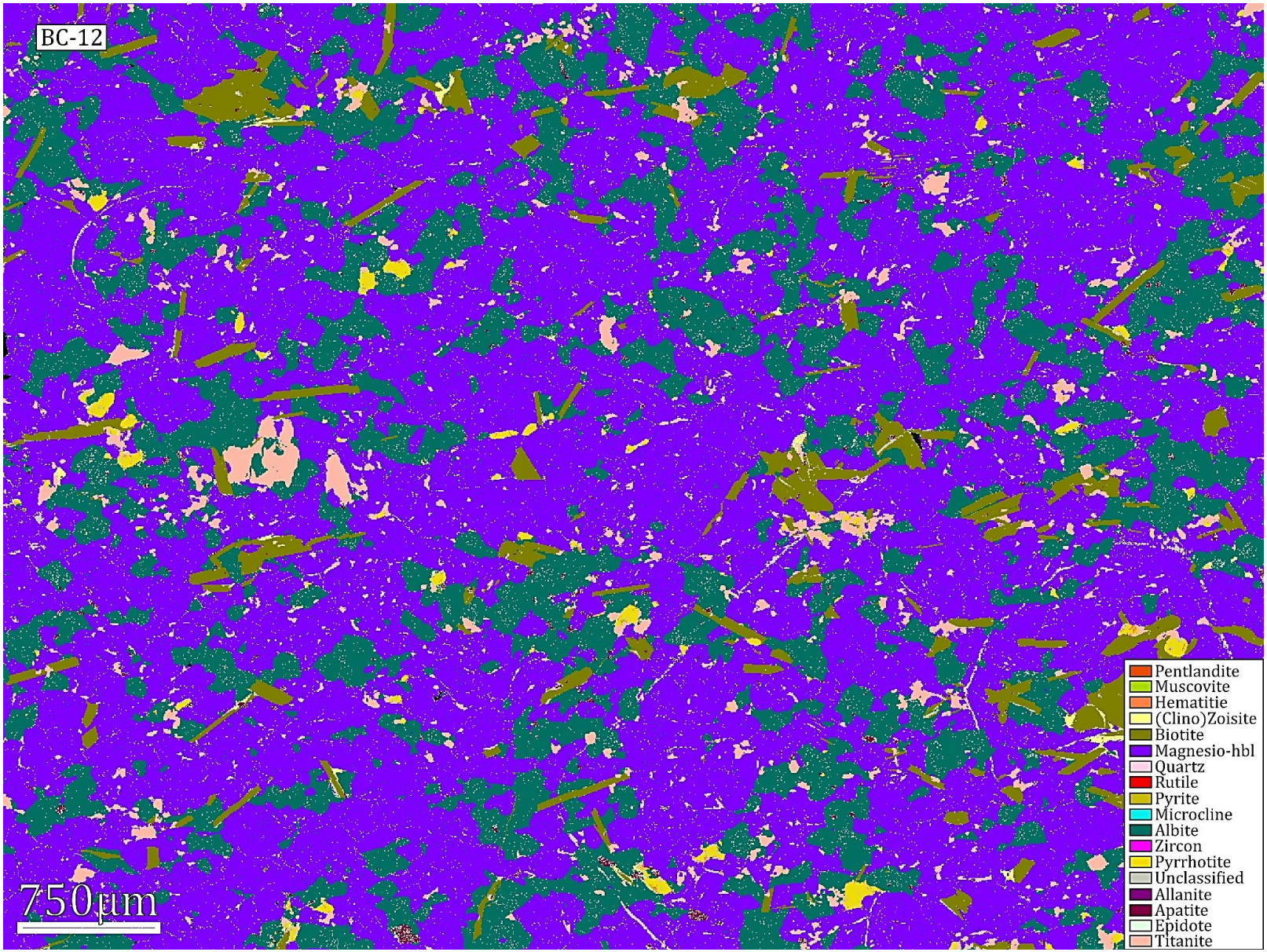
BC-12
750µm
Pentlandite
Muscovite
Hematitie
(Clino)Zoisite
Biotite
Magnesio-hbl
Quartz
Rutile
Pyrite
Microcline
Albite
Zircon
Pyrrhotite
Unclassified
Allanite
Apatite
Epidote
Titanite

Appendix C: Chemical Analysis – Methods

Main Element XRF

The method used for main element analysis is described in *NGU-SD 2.3*

Element / Compound:	SiO_2*	Al_2O_3*	Fe_2O_3*	TiO_2*	MgO*	CaO*	Na_2O*	K_2O*	MnO*	P_2O_5*	Ba	Co	Cr	Cu	Ni	Pb	Sr	V	Zn	Zr	S
LLQ:	0.5	0.02	0.01	0.01	0.1	0.03	0.1	0.01	0.01	0.01	100	30	50	50	50	50	50	50	50	50	200
Concentration	±	±	±	±	±	±	±	±	±	±	N/A										
0.01			0.005	0.005				0.005	0.005	0.005											
0.1		0.010	0.027	0.009	0.036	0.027	0.02	0.031	0.004	0.009											
0.5	0.05	0.031	0.046	0.015	0.062	0.046	0.03	0.054	0.008	0.015											
1	0.09	0.042	0.063	0.021	0.084	0.063	0.04	0.073	0.010	0.021											
5	0.20	0.090	0.135	0.050	0.181	0.135	0.09	0.158	0.050	0.050											
10	0.29	0.127	0.191	0.100	0.254	0.191	0.13	0.222	0.100	0.100											
25	0.45	0.250	0.301		0.401	0.301	0.25	0.351	0.250												
50	0.64	0.500	0.500		0.566	0.500					For orientation: highest detection limit, mg/kg										
75	0.78	0.750	0.750		0.750	0.750					Ba	Co	Cr	Cu	Ni	Pb	Sr	V	Zn	Zr	S
100	1.00					1.000					3000	200	25000	2000	5000	5000	5000	1000	5000	15000	15000

***Accredited parameters.** The given uncertainties (±) represents the coverage factor 1 (68 % confidence interval), a 95 % confidence interval is achieved by multiplying with two.

Loss on ignition (LOI): The LOI has a detection limit of 0.05% (absolute value) and uncertainty of 2.5% rel. (95% confidence interval). LOI data are reported without LLQ.

Contract no.: 2019.0177
Number of Samples: 13
Notes: The following samples were heated to 1000 °C for two hours:
197754, 197755, 197758 - 197762

Sample Material: Geological Material
Date Completed: 24.21.2020
Analysed by: Ann Elisabeth Karlsen
Reported by: Jasmin Schönenberger

Trace Element XRF

The method used for trace element analysis is described in *NGU-SD 2.4*

	Ag	As*	Ba*	Cd	Ce*	Cl	Co*	Cr*	Cu*	F	Ga*	Hf	La*	Mo*	Nb*
LLQ (mg/kg = ppm):	10	10	10	10	15	0.02	4	5	5	0.2	3	5	15	3	5
Detection limit 1 (mg/kg):	10-20	10-20	10-50	10-20	15-30	0.02-0.1	4-50	5-30	5-20	0.2-1 wt%	3-20	5-10	15-30	3-20	5-10
Uncertainty 1 (rel. %):	30	30	30	30	50	50	20	20	30	50	20	30	30	20	20
Detection limit 2 (mg/kg):	20-50	20-50	50-100	20-50	30-50	0.1-1 wt%	50-100	30-100	20-100	1-5 wt%	20-50	10-20	30-100	20-50	10-50
Uncertainty 2 (rel. %):	20	20	20	20	30	30	10	10	20	25	10	20	20	10	10
Detection limit 3 (mg/kg):	50-1000	50-1000	100-1 wt%	50-1000	50-500		100-1000	100-2.5 wt%	100-1.5 wt%		50-100	20-30	100-1000	50-250	50-1000
Uncertainty 3 (rel. %):	10	10	10	10	20		5	5	10		5	15	10	5	5

	Nd*	Ni*	Pb*	Rb*	S	Sb	Sc*	Sn*	Sr*	Th*	U*	V*	Y*	Zn*	Zr*
LLQ (mg/kg = ppm):	10	5	5	5	0.1	15	5	5	5	3	5	5	3	5	5
Detection limit 1 (mg/kg):	10-20	5-50	5-30	5-30	0.1-0.5	15-30	5-50	5-20	5-20	3-30	5-20	5-50	3-30	5-20	5-20
Uncertainty 1 (rel. %):	30	20	20	20	50	50	50	30	30	20	20	20	20	20	20
Detection limit 2 (mg/kg):	20-50	50-100	30-100	30-100	0.5-1 wt%	30-100	50-300	20-50	20-100	30-100	20-50	50-150	30-100	20-100	20-100
Uncertainty 2 (rel. %):	20	10	10	10	25	30	20	20	10	10	10	15	10	15	10
Detection limit 3 (mg/kg):	50-1000	100-4000	100-1000	100-8500		100-1000		50-2000	100-2000	100-1000	50-1000	150-1400	100-1000	100-2000	100-1500
Uncertainty 3 (rel. %):	10	5	5	5		15		10	5	5	5	10	5	10	5

***Accredited parameters.** The given uncertainties (±) represents the coverage factor 1 (68 % confidence interval), a 95 % confidence interval is achieved by multiplying with two.

Contract no.: 2019.0177

Number of Samples: 10

Notes: Samples 197754/~755/~761 were not analysed due to their carbonate matrix. The sulphide content of sample 197758/~760 is beyond detection limits.

Sample Material: Geological Material

Date Completed: 03.02.2020

Analysed by: Clea Fabian

Reported by: Jasmin Schönenberger

LA-ICP-MS

Detection limits for LA-ICP-MS are shown in the table below. The analytical uncertainty is ± 20 % rel.

Be	Rb	Sr	Y	Zr	Nb	Sn	Cs	Ba	La	Ce	Pr	Nd	Sm	Eu	Gd	Tb	Dy
mg/g	*mg/g*	*mg/g*	*mg/g*	*mg/g*	*mg/g*	*mg/g*	*mg/g*	*mg/g*	*mg/g*	*mg/g*	*mg/g*	*mg/g*	*mg/g*	*mg/g*	*mg/g*	*mg/g*	*mg/g*
1	1	1.2	0.2	1.1	0.07	2	0.4	0.9	0.1	0.07	0.03	0.21	0.13	0.03	0.3	0.04	0.16

Ho	Er	Tm	Yb	Lu	Hf	Ta	W	Pb	Bi	Th	U	V	Cr	Cu	Zn	Ga
mg/g	*mg/g*	*mg/g*	*mg/g*	*mg/g*	*mg/g*	*mg/g*	*mg/g*	*mg/g*	*mg/g*	*mg/g*	*mg/g*	*mg/g*	*mg/g*	*mg/g*	*mg/g*	*mg/g*
0.04	0.09	0.04	0.2	0.04	0.13	0.04	0.2	5	0.5	0.03	0.01	9	15	15	15	2

Contract no.: 2019.0177

Number of Samples: 13

Notes: Lithium is used as an internal standard for all samples. Some analysis is outside the detection limits. These are marked in red.
NB: Values of Cu is reported only for curiosity since the Pt-crucible were likely contaminated. Values of the XRF-P are considered most valid.

Sample Material: Geological Material

Sequence of Tablets: 200220

Date Completed: 20.02.2020

Operators: Ø. Skår
T.S. Røhr

Appendix D: Petrophysical Analysis

Unit ---------- Sample	Volume cm^3	Density $\frac{g}{cm^3}$	Pore-Volume cm^2	Open Porosity %	Suscep-tibility $10^{-6}\ SI$	NRM $\frac{mA}{M}$	Thermal Conductivity $K\left(\frac{W}{mK}\right)$	Specific heat capacity $C_p\left(\frac{J}{kgK}\right)$	Dry weight g	Weight wet in air g	Weight wet in water g	Effusivity $\frac{Ws^{\frac{1}{2}}}{m^2}k$	Δ k $\frac{W}{mK}$	Thermal Diffusivity $\frac{m^2}{s}$
BC-01	172.74	2.8	2.65	0.02	477	12	2.22	709	484.43	487.08	314.34	2101	0.2	1.12E-06
BC-02	116.33	2.63	2.24	0.02	74	9	3.55	796	306.15	308.39	192.06	2726	0.17	1.70E-06
BC-03	117.48	2.71	2.71	0.02	289	7	3.93	785	317.83	320.54	203.06	2892	0.04	1.85E-06
BC-04	239.32	2.68	1.72	<0.01	-80	2	3.36	774	641.58	643.3	403.98	2642	0.04	1.62E-06
BC-05	131.01	2.83	0.89	<0.01	63	10	4.99	786	370.67	371.56	240.55	3331	0.03	2.25E-06
BC-06	104.95	2.53	2.84	0.03	16	9	2.99	807	265.92	268.76	163.81	2470	0.02	1.46E-06
BC-07	70.17	2.81	0.73	0.01	663	43	3.36	739	197.5	198.23	128.06	2641	0.02	1.62E-06
BC-08	135.62	3.13	1.66	0.01	614	548	3.38	664	424.93	426.59	290.97	2651	0.01	1.63E-06
BC-09	107.03	3	1.03	<0.01	713	410	2.85	677	320.75	321.78	214.75	2405	0.03	1.40E-06
BC-10	143.1	2.99	2.08	0.01	723	1554	3.11	687	428.03	430.11	287.01	2528	0.01	1.52E-06
BC-11	235.33	2.67	2.59	0.01	-41	9	3.41	779	628.49	631.08	395.75	2663	0.04	1.64E-06
BC-12	198.02	3.06	2.28	0.01	684	11	2.4	652	605.02	607.3	409.28	2189	0.02	1.20E-06
BC-13	203.17	2.87	1.59	<0.01	299	7	3.28	721	583.71	585.3	382.13	2606	0.02	1.59E-06

Appendix E: Chemical Analysis – Results

Main Element XRF

Sample	SiO_2 [%]	Al_2O_3 [%]	Fe_2O_3 [%]	TiO_2 [%]	MgO [%]	CaO [%]	Na_2O [%]	K_2O [%]	MnO [%]	P_2O_5 [%]	LOI [%]	$Total$ [%]
BC-01	51.2	19.5	8.14	1.37	4.49	7.28	3.82	2.32	0.113	0.340	0.895	99.4
BC-02	74.3	12.7	3.43	0.483	0.79	1.27	4.23	1.57	0.027	0.087	0.510	99.4
BC-03	63.4	18.0	6.87	0.803	2.66	0.495	1.72	4.04	0.048	0.078	1.71	99.9
BC-04	0.73	0.182	0.183	0.016	0.21	55.0	<0.1	0.027	0.015	0.013	43.1	99.5
BC-05	2.05	0.683	0.421	0.050	20.4	31.4	<0.1	0.274	0.015	0.088	44.9	100
BC-06	75.6	13.4	0.205	0.041	<0.1	1.01	3.06	5.40	<0.01	0.114	0.429	99.2
BC-07	55.1	21.8	8.39	1.07	2.26	0.735	2.14	5.43	0.097	0.086	2.61	99.7
BC-08	44.9	13.9	9.42	0.953	9.25	17.4	1.00	0.519	0.104	0.085	2.00	99.5
BC-09	47.7	15.1	9.81	1.18	8.83	11.3	1.94	2.12	0.171	0.385	0.843	99.4
BC-10	38.4	16.5	7.82	4.83	11.0	14.3	1.76	0.647	0.123	0.630	2.83	98.7
BC-11	3.43	0.638	0.251	0.041	0.29	53.3	<0.1	0.156	<0.01	<0.01	41.7	99.9
BC-12	44.8	15.2	11.7	1.67	9.22	11.5	2.46	1.53	0.178	0.279	0.473	99.1
BC-13	56.4	13.1	5.15	0.666	8.96	10.3	1.36	2.74	0.151	0.150	0.815	99.8

Sam-ple	*Ba* [mg/kg]	*Co* [mg/kg]	*Cr* [mg/kg]	*Cu* [mg/kg]	*Ni* [mg/kg]	*Pb* [mg/kg]	*Sr* [mg/kg]	*V* [mg/kg]	*Zn* [mg/kg]	*Zr* [mg/kg]	*S* [mg/kg]
BC-01	598	37	75	71	61	<50	716	169	96	262	<200
BC-02	<100	<30	<50	<50	<50	<50	87	<50	<50	315	<200
BC-03	566	<30	95	<50	<50	<50	104	83	94	220	<200
BC-04	<100	<30	<50	<50	<50	<50	866	<50	<50	<50	536
BC-05	<100	<30	<50	<50	<50	<50	64	<50	<50	<50	504
BC-06	309	<30	<50	<50	<50	<50	85	<50	<50	<50	<200
BC-07	630	<30	122	<50	69	<50	119	137	96	266	<200
BC-08	170	65	597	298	448	<50	377	162	67	110	338
BC-09	2240	<30	354	<50	84	<50	1680	228	92	128	<200
BC-10	<100	32	<50	<50	<50	<50	697	340	88	378	351
BC-11	118	<30	<50	<50	<50	<50	1740	<50	<50	<50	1100
BC-12	351	57	303	<50	134	<50	370	253	79	110	<200
BC-13	1120	<30	<50	<50	<50	<50	172	52	84	222	<200

Trace Element XRF

Sample	*Ag* [mg/kg]	*As* [mg/kg]	*Ba* [mg/kg]	*Cd* [mg/kg]	*Ce* [mg/kg]	*Co* [mg/kg]	*Cr* [mg/kg]	*Cu* [mg/kg]	*Ga* [mg/kg]	*La* [mg/kg]	*Mo* [mg/kg]	*Nb* [mg/kg]	*Nd* [mg/kg]	*Ni* [mg/kg]
BC-01	<10	<10	631	<10	139	28.3	77.4	66.2	25.2	75	<3	13.7	54	58.6
BC-02	<10	<10	116	<10	41	5.2	49.4	<5	15.5	18	<3	11.5	15	13.5
BC-03	<10	<10	557	<10	58	8.1	93.8	9.4	23.8	33	<3	18.1	27	17.3
BC-07	<10	<10	342	<10	<15	<4	<5	<5	14.9	<15	<3	<5	<10	<5
BC-08	<10	<10	615	<10	70	18.7	125	37.2	30.9	48	<3	31.2	37	49.4
BC-09	<10	<10	149	<10	41	67.7	612	290	15.9	<15	<3	<5	20	361
BC-10	<10	<10	2320	<10	270	32.7	352	18.3	19.4	165	<3	13.8	130	77.5
BC-11	<10	<10	39	<10	69	23.2	24.5	27.5	30.2	18	<3	35.2	33	14.8
BC-12	<10	<10	312	<10	36	48.1	298	37.1	16.4	22	<3	23.0	13	113
BC-13	<10	<10	1160	<10	107	13.8	49.2	<5	18.0	69	<3	15.5	51	34.5

Sample	*Pb* [mg/kg]	*Rb* [mg/kg]	*Sb* [mg/kg]	*Sc* [mg/kg]	*Sn* [mg/kg]	*Sr* [mg/kg]	*Th* [mg/kg]	*U* [mg/kg]	*V* [mg/kg]	*Y* [mg/kg]	*Zn* [mg/kg]	*Zr* [mg/kg]	*Cl* [mg/kg]	*F* [mg/kg]	*S* [mg/kg]	*Hf* [mg/kg]
BC-01	21.1	83.8	<15	22.1	<5	713	18.4	<5	169	22.5	94.4	242	<0.02	<0.2	<0.1	5.4
BC-02	5.2	63.7	<15	11.5	<5	83.6	5.9	<5	55.2	24.4	7.5	311	<0.02	<0.2	<0.1	7.0
BC-03	19.2	147	<15	16.0	<5	99.8	13.7	<5	85.4	27.0	89.9	216	<0.02	<0.2	<0.1	6.5
BC-07	20.1	140	<15	<5	<5	79.8	<3	<5	<5	<3	<5	12.7	<0.02	<0.2	<0.1	<5
BC-08	17.2	179	<15	12.7	<5	110	14.7	5.2	134	14.4	96.4	273	<0.02	<0.2	0.59	8.2
BC-09	9.9	12.7	<15	45.2	<5	358	6.0	<5	165	17.0	70.8	88.6	<0.02	<0.2	1.16	8.5
BC-10	18.3	82.1	<15	37.3	<5	1650	89.6	n.a.	207	33.4	93.6	63.3	<0.02	<0.2	<0.1	<5
BC-11	9.4	19.1	<15	32.9	12.2	675	4.3	<5	373	59.6	93.1	377	<0.02	<0.2	1.42	7.3
BC-12	7.9	106	<15	35.8	<5	363	<3	<5	254	23.5	87.0	95.2	<0.02	0.38	<0.1	<5
BC-13	11.4	99.8	<15	15.4	<5	166	14.2	<5	44.6	41.3	86.8	229	<0.02	<0.2	<0.1	5.9

ICP-MA LA

Sample	LOI %	Be µgg-1	Rb µgg-1	Sr µgg-1	Y µgg-1	Zr µgg-1	Nb µgg-1	Sn µgg-1	Cs µgg-1	Ba µgg-1	La µgg-1	Ce µgg-1	Pr µgg-1	Nd µgg-1	Sm µgg-1	Eu µgg-1	Gd µgg-1	Tb µgg-1	Dy µgg-1
BC-01	0.895	2.0	91.2	783	21.6	266	15.0	3.3	3.64	665	61.2	127	14.8	56.3	10.3	2.72	6.91	0.919	4.49
BC-02	0.510	1.7	66.5	93.0	27.1	360	12.4	2.4	1.11	126	30.4	64.7	7.09	27.8	5.94	1.11	5.02	0.797	4.73
BC-03	1.71	2.0	153	109	43.6	255	20.6	<2	2.90	591	60.5	120	13.0	49.5	9.31	1.82	7.99	1.28	7.55
BC-04	43.1	<1	1.0	1020	2.80	2.6	0.201	<2	<0.4	18.2	2.97	5.63	0.750	3.09	0.59	0.153	0.49	0.078	0.43
BC-05	44.9	<1	5.8	78.7	2.90	10.6	0.830	<2	<0.4	61.0	3.35	8.73	0.861	3.16	0.74	0.168	0.64	0.103	0.57
BC-06	0.429	3.6	157	79.6	2.36	9.3	1.44	3.1	5.32	323	1.52	2.69	0.243	0.78	0.19	0.260	<0.3	0.049	0.39
BC-07	2.61	2.5	184	122	17.8	301	35.2	3.7	10.9	701	72.6	132	15.5	55.0	9.15	1.69	5.80	0.870	4.49
BC-08	2.00	1.1	15.3	443	16.9	115	3.49	5.1	0.74	166	18.1	39.7	5.01	22.3	5.04	1.29	4.31	0.628	3.45
BC-09	0.843	2.9	89.2	1970	34.6	142	16.8	5.7	6.97	2610	138	238	27.7	106	19.1	3.64	12.8	1.57	7.50
BC-10	2.83	1.4	21.2	780	61.0	402	40.1	15.1	2.71	35.4	25.6	59.4	7.87	36.8	9.81	2.19	10.2	1.79	11.3
BC-11	41.7	<1	5.7	2140	1.67	18.6	0.717	<2	<0.4	128	2.34	4.91	0.539	2.04	0.42	0.089	0.32	0.051	0.31
BC-12	0.473	<1	107	393	22.0	98.3	23.5	5.8	27.0	342	18.8	40.3	4.64	19.8	4.58	1.57	4.47	0.712	4.41

Sample	LOI %	Ho µgg-1	Er µgg-1	Tm µgg-1	Yb µgg-1	Lu µgg-1	Hf µgg-1	Ta µgg-1	W µgg-1	Pb µgg-1	Bi µgg-1	Th µgg-1	U µgg-1	V µgg-1	Cr µgg-1	Cu µgg-1	Zn µgg-1	Ga µgg-1
BC-01	0.895	0.838	1.93	0.272	1.75	0.249	6.57	0.497	<0.2	22.6	<0.5	16.3	3.23	165	72	78	126	26.1
BC-02	0.510	1.05	2.85	0.456	3.03	0.463	9.88	0.828	0.31	6.8	<0.5	9.67	2.32	53.6	49	<15	19	14.7
BC-03	1.71	1.63	4.44	0.667	4.23	0.634	6.79	1.41	0.41	20.1	<0.5	18.7	2.90	90.8	95	23	105	25.2
BC-04	43.1	0.089	0.216	<0.04	<0.2	<0.04	<0.13	<0.04	<0.2	<5	<0.5	0.252	0.323	<9	<15	<15	<15	<2
BC-05	44.9	0.112	0.313	0.041	0.26	<0.04	0.29	<0.04	<0.2	<5	<0.5	0.644	1.59	<9	<15	<15	<15	<2
BC-06	0.429	0.087	0.288	0.051	0.37	0.056	0.41	0.186	0.37	23.8	<0.5	0.269	1.03	<9	<15	16	24	16.8
BC-07	2.61	0.814	2.03	0.265	1.67	0.283	8.55	2.41	1.54	17.8	<0.5	20.4	2.90	143	118	53	104	35.0
BC-08	2.00	0.698	1.73	0.257	1.62	0.228	4.73	0.271	1.16	10.4	<0.5	6.73	3.30	170	616	329	80	17.9
BC-09	0.843	1.39	3.24	0.436	2.72	0.371	4.25	1.32	0.72	21.8	<0.5	98.6	20.1	242	357	21	104	20.9
BC-10	2.83	2.60	7.05	1.04	6.52	0.976	9.90	2.58	3.31	8.2	0.93	4.51	1.64	373	<15	43	88	31.5
BC-11	41.7	0.062	0.175	<0.04	<0.2	<0.04	0.52	<0.04	<0.2	<5	<0.5	0.611	0.459	<9	<15	<15	<15	<2
BC-12	0.473	0.958	2.54	0.357	2.37	0.358	2.66	1.42	1.17	8.1	<0.5	2.67	0.845	260	286	50	104	19.2
BC-13	0.815	1.76	4.88	0.704	4.76	0.707	7.51	1.31	1.06	13.3	<0.5	17.4	2.08	48.8	48	<15	95	18.5

Red values are beyond detection limits.

EPMA

Following are the results form the EPMA. The point names represent the rock sample_zone_mineral_number. All values are given in wt%. Red numbers are outliers and are excluded in the “recalculated average” and “recalculated standard deviation” rows. The outliers are discussed in chapter 3.6.

Amphibole analyses

Point	MgO	Al_2O_3	Na_2O	F	SiO_2	CaO	K_2O	Cr_2O_3	FeO	NiO	MnO	Cl	TiO_2	ZnO	H	Total
BC_01_amp	9.84	10.75	1.0192	0.0869	34.97	10.73	1.0476	0.0212	15.34	0	0.3766	0.0294	0.5296	0.0242	2	86.7647
BC_01_amp_2	9.62	11.33	1.2243	0	34.93	10.67	1.1268	0.0259	15.35	0.005	0.3473	0.034	0.5757	0.0626	2	87.3016
BC_01_amp_3	9.59	11.38	1.2844	0.0815	35.11	10.72	1.1384	0.0518	15.28	0	0.3698	0.0287	0.5678	0.0196	2	87.622
BC_01_amp_4	10.13	10.37	1.1628	0.0528	36.29	10.77	0.9729	0.1032	15.07	0.009	0.3406	0.017	0.537	0.018	2	87.8433
BC_01_amp_5	9.68	8.31	0.8073	0	13.97	7.49	0.764	0.0308	9.19	0	0.1823	0.0323	0.3965	0	2	52.8532
BC_01_amp_6	10	11.62	1.1794	0.0459	43.63	11.74	1.21	0.0087	15.92	0	0.3348	0.0235	0.6318	0.0008	2	98.3449
BC_01_amp_7	10.47	10.91	1.1955	0.0957	44.12	11.88	1.1133	0.121	15.59	0.0242	0.3637	0.027	0.7846	0	2	98.695
BC_01_amp_8	10.01	11.44	1.2281	0.1066	43.8	11.96	1.1518	0.1043	16.02	0	0.3563	0.0328	0.6838	0	2	98.8937
BC_01_amp_9	10.24	11.4	1.1886	0.0866	44.18	11.83	1.1201	0.0285	15.75	0	0.3463	0.0249	0.7273	0.022	2	98.9443
BC_01_amp_10	10.15	11.37	1.0425	0.1142	43.88	11.83	1.1464	0.0317	15.9	0.0119	0.3803	0.0284	0.7522	0.0228	2	98.6604
BC_01_amp_11	10.22	11.27	0.9679	0	43.65	11.6	1.23	0.0562	15.95	0	0.3284	0.0338	0.7825	0.0284	2	98.1172
BC_01_amp_12	10.14	11.48	1.1528	0.0883	44.19	11.94	1.1337	0.0372	16.08	0.0322	0.3534	0.0183	0.5092	0	2	99.1551
BC_01_amp_13	10.19	11.66	1.0143	0.0742	44.08	11.91	1.0432	0.0207	15.01	0	0.3054	0.0265	0.8976	0.0363	2	98.2682
BC_01_amp_14	10.35	10.82	1.1078	0.0425	44.1	11.93	1.1147	0.2156	15.64	0	0.329	0.0283	0.8598	0.029	2	98.5667
BC_01_amp_15	10.61	11.44	1.0854	0.0737	43.11	11.81	1.0433	0.2083	15.92	0	0.3418	0.031	0.8283	0.0134	2	98.5152
BC_01_amp_16	10.21	11.28	1.1821	0.1122	43.67	11.63	1.1003	0.1014	16	0.0243	0.3549	0.0244	0.7107	0.1032	2	98.5035
BC_01_amp_17	10.08	11.05	1.1147	0.1163	44.62	11.82	1.1005	0.0761	15.81	0.0198	0.3278	0.0329	0.7032	0.0054	2	98.8767
BC_01_amp_18	10.08	11.57	1.1635	0.072	43.81	11.86	1.1567	0.0508	15.86	0.0265	0.3604	0.0288	0.7715	0.0402	2	98.8504
BC_01_amp_19	10.23	10.94	1.1464	0.0222	43.77	11.82	1.1521	0.069	15.91	0.0198	0.3824	0.0276	0.8168	0.03	2	98.3363
BC_01_amp_20	10.4	11.22	1.2475	0.1068	43.97	11.8	1.1384	0.0277	16.01	0.0028	0.3326	0.0249	0.794	0	2	99.0747
BC_01_amp_21	10.42	10.75	1.2312	0.0924	44.05	11.95	1.101	0.0413	15.76	0.0073	0.3573	0.0246	0.7123	0.0386	2	98.536
BC_01_amp_22	9.81	11.71	1.1395	0.168	43.3	11.82	1.25	0.0063	15.96	0.0181	0.3518	0.0272	0.8984	0.004	2	98.4633
BC_01_amp_23	10.33	10.7	1.1634	0.1352	44.13	12.07	1.1384	0	15.52	0	0.3469	0.0525	0.7147	0.0378	2	98.3389
BC_01_amp_24	9.86	11.00	1.41	0.1277	41.91	12.19	1.1958	0.0469	15.36	0.0034	0.3107	0.0561	0.7958	0.0464	2	96.3128
BC_01_amp_25	10.41	10.68	0.9961	0.1052	43.38	11.64	1.0542	0.0635	15.81	0.0096	0.3692	0.0331	0.8196	0.0694	2	97.4399
BC_01_amp_26	10.35	10.83	1.1547	0.0997	43.3	11.53	1.1005	0.0699	15.75	0.0368	0.3397	0.025	0.916	0	2	97.5023
BC_01_amp_27	10.31	11.16	0.9936	0.0278	43.26	11.74	1.0871	0.0238	15.55	0.0255	0.3538	0.0366	0.8602	0	2	97.4284
BC_01_amp_28	10.05	11.45	1.0966	0.0756	42.62	11.72	1.1778	0.0111	16.03	0	0.3457	0.0362	0.8271	0.0458	2	97.4859
BC_01_amp_29	9.88	11.73	1.1398	0.068	41.59	11.56	1.1991	0.0087	16.28	0.0051	0.3578	0.0347	0.7765	0.0316	2	96.6613
BC_01_amp_30	10.41	11.02	1.0682	0.0864	41.73	11.51	1.0644	0	15.63	0.0255	0.352	0.0246	0.5261	0.0576	2	95.5048
BC_01_amp_31	9.58	12.43	1.2924	0.066	40.58	11.42	1.25	0.0119	16.11	0.0119	0.3329	0.0357	0.5979	0.026	2	95.7447

Point	MgO	Al_2O_3	Na_2O	F	SiO_2	CaO	K_2O	Cr_2O_3	FeO	NiO	MnO	Cl	TiO_2	ZnO	H	Total
BC_01_amp_32	9.91	11.29	1.0591	0.1326	40.29	11.38	1.1664	0.0167	15.62	0.0125	0.3301	0.0451	0.8864	0.1216	2	94.2605
BC_01_amp_33	10.53	11.03	1.1397	0.1015	41.84	11.57	1.077	0.0239	15.34	0.0198	0.3403	0.0257	0.6538	0	2	95.6917
BC_01_amp_34	10.37	10.65	1.0871	0.1782	39.25	11.14	1.0267	0.004	15.56	0	0.3833	0.0302	0.8275	0.0056	2	92.5126
BC_01_amp_35	10.33	10.78	1.0336	0.0625	39.23	11.18	1.0532	0.0214	15.64	0.0374	0.3538	0.0272	0.8583	0.1146	2	92.722
BC_01_amp_36	10.22	11.04	1.0542	0.1046	38.53	11.16	1.0472	0.0048	15.89	0.0136	0.3727	0.0224	0.5716	0	2	92.0311
BC_01_amp_37	10.15	10.81	1.0967	0.0037	39.24	11.23	1.0503	0	16.18	0	0.3684	0.0173	0.5597	0.072	2	92.7781
BC_01_amp_38	10.32	11.11	1.1027	0.0936	39.17	11.09	1.0547	0	15.93	0	0.3921	0.0355	0.5337	0.0048	2	92.8371
BC_01_amp_39	9.52	10.27	1.1289	0.1554	36.27	9.12	0.8853	0.0048	11.13	0	0.2578	0.019	0.6958	0	2	81.457
BC_01_amp_40	9.98	11.40	1.1031	0.0662	39.76	11.26	1.21	0.0223	16.31	0	0.3331	0.0281	0.8696	0	2	94.3424
BC_01_amp_41	9.94	11.58	1.1275	0.0884	40.28	11.31	1.1974	0.0103	16.02	0	0.3908	0.0414	0.5278	0.0261	2	94.5397
BC_01_amp_42	11.79	16.8	0.104	0.2493	33.55	0.0546	9.42	0.015	16.23	0.0085	0.2346	0.0287	1.77	0.0521	2	92.3068
BC_01_amp_43	9.62	12.39	1.1839	0.2029	43.51	11.89	1.3	0.0167	16.53	0.0153	0.34	0.0339	0.6788	0.0451	2	99.7566
BC_01_amp_44	9.54	12.31	1.1767	0.1088	43.52	11.83	1.32	0.027	16.66	0	0.3673	0.0254	0.6541	0.0617	2	99.601
BC_01_amp_45	9.5	12.37	1.2165	0.1017	43.43	11.86	1.28	0.0127	16.44	0.0488	0.4021	0.0341	0.6695	0.0309	2	99.3963
BC_01_amp_46	9.61	12.31	1.2019	0.109	43.48	11.88	1.31	0.0159	16.56	0.0062	0.3662	0.0376	0.676	0.0214	2	99.5842
BC_01_amp_47	9.6	12.34	1.1908	0.1642	43.54	11.8	1.34	0	16.68	0	0.3676	0.0329	0.6795	0.0261	2	99.7611
BC_01_amp_48	9.6	12.24	1.0883	0.0849	43.49	11.86	1.29	0.0199	16.79	0.0148	0.3623	0.0305	0.6979	0	2	99.5686
BC_01_amp_49	9.8	12.42	1.1825	0.0609	43.29	11.81	1.3	0	16.77	0.0068	0.3488	0.0331	0.6881	0	2	99.7102
BC_01_amp_50	9.63	12.27	1.2293	0.1403	43.45	11.8	1.31	0.0231	16.55	0.0198	0.3235	0.023	0.7039	0	2	99.4729
BC_01_amp_51	9.65	12.37	1.1477	0.0776	43.6	11.82	1.27	0.0175	16.71	0.0108	0.3626	0.03	0.6793	0	2	99.7455
BC_01_amp_52	9.5	12.39	1.1532	0.0795	43.59	11.93	1.32	0.0287	16.75	0	0.3056	0.038	0.7147	0.0421	2	99.8418
BC_01_amp_53	9.55	12.31	1.1564	0.0666	43.62	11.92	1.31	0.02	16.97	0.0097	0.3357	0.0294	0.7153	0.0151	2	100.0282
BC_01_amp_54	9.55	12.2	1.1295	0.0946	43.51	11.93	1.29	0.0104	16.62	0.0228	0.3537	0.0344	0.6824	0.0771	2	99.5049
BC_01_amp_55	9.63	12.29	1.1529	0.0817	43.83	11.78	1.28	0.0368	16.47	0.024	0.3167	0.0317	0.6841	0.0048	2	99.6127
BC_01_amp_56	9.68	12.25	1.2741	0.1094	43.53	11.86	1.29	0.036	16.69	0.0177	0.3799	0.0315	0.7027	0	2	99.8513
BC_01_amp_57	9.6	12.2	1.2492	0.0686	43.65	12.01	1.31	0.0176	16.73	0.0353	0.3614	0.0384	0.6696	0.0516	2	99.9917
BC_01_amp_58	9.58	12.21	1.1719	0.0963	43.46	11.85	1.26	0	16.67	0.0097	0.3575	0.0382	0.6603	0.0771	2	99.441
BC_01_amp_59	9.63	12.35	1.0909	0.0501	43.8	11.89	1.32	0	16.57	0.004	0.3364	0.0314	0.6961	0.0008	2	99.7697
BC_01_amp_60	9.64	12.46	1.1129	0.0372	43.83	11.88	1.28	0	16.58	0.0051	0.3272	0.0277	0.7043	0	2	99.8844
BC_01_amp_61	9.60	12.36	1.1246	0.0779	43.66	11.92	1.28	0.0272	16.63	0	0.3439	0.0338	0.6817	0	2	99.7391
BC_01_amp_62	9.67	12.28	1.1594	0.0725	43.79	11.96	1.28	0.0248	16.47	0	0.3341	0.0331	0.6929	0.0191	2	99.7859
Average	9.98	11.58	1.12	0.09	41.66	11.37	1.30	0.03	15.87	0.01	0.34	0.03	0.72	0.03		
Standard Deviation	0.40	1.01	0.16	0.05	4.51	1.62	1.05	0.04	1.17	0.01	0.03	0.01	0.18	0.03		
Recalculated Average	9.60	12.31	1.17	0.10	43.59	11.88	1.30	0.02	16.64	0.01	0.35	0.03	0.69	0.02		
Recalculated Standard Deviation	0.05	0.07	0.05	0.04	0.13	0.06	0.02	0.01	0.13	0.01	0.02	0.00	0.02	0.03		

Garnet analyses

Point	MgO	Al_2O_3	Na_2O	SiO_2	CaO	K_2O	Cr_2O_3	MnO	V_2O_3	FeO	TiO_2	Total
BC_16_grt_1	2.21	20.57	0.0155	36.89	0.7888	0	0	3.07	0	36.33	0.0302	99.9045
BC_16_grt_2	2.36	20.77	0.0471	37.08	0.7798	0	0	2.47	0.0249	36.49	0.0418	100.0636
BC_16_grt_3	2.33	20.67	0.026	37.14	0.753	0	0	3.04	0	36.04	0.0398	100.0388
BC_16_grt_4	2.29	20.73	0.0333	37.12	0.7411	0	0.0159	3.27	0.0169	35.92	0.028	100.1652
BC_16_grt_5	2.16	20.69	0.0235	37.15	0.8471	0	0	3.77	0.012	35.36	0.025	100.0376
BC_16_grt_6	2.37	20.73	0	37.21	0.7891	0	0.0071	2.88	0.0153	36.15	0.0282	100.1797
BC_16_grt_7	2.15	20.81	0	37.19	0.9693	0	0.0041	4.53	0.0088	34.71	0.0262	100.3984
BC_16_grt_8	2.14	20.73	0.0049	37.04	0.9857	0	0.019	4.3	0.008	34.78	0.0194	100.027
BC_16_grt_9	2.16	20.9	0.0243	36.99	0.9234	0.0049	0.0116	4.18	0	34.81	0.021	100.0252
BC_16_grt_10	2.24	20.77	0.0024	37.25	1.0239	0	0.0087	3.55	0	35.26	0.0217	100.1267
BC_16_grt_11	2.35	20.86	0.0167	36.86	1.0043	0	0	2.79	0.0071	36.09	0.0176	99.9957
BC_16_grt_12	2.24	20.95	0.0016	37.3	1.0263	0	0	2.85	0	35.79	0.0192	100.1771
BC_16_grt_13	2.01	20.74	0	37.26	0.803	0	0	3.07	0.0033	36.62	0.0223	100.5286
BC_16_grt_14	2.3	20.86	0.0117	36.89	1.0658	0	0.0181	2.73	0	36.07	0.0369	99.9825
BC_16_grt_15	2.24	20.85	0.0201	36.69	1.0458	0	0	3.19	0	35.93	0.0397	100.0056
BC_16_grt_16	2.24	20.69	0.03	37.04	1.0087	0	0	3.11	0	35.42	0.0407	99.5794
BC_16_grt_17	2.32	20.77	0.0106	36.93	0.7769	0	0	2.46	0	36.53	0.014	99.8115
BC_16_grt_18	2.32	20.82	0.0171	37.1	0.79	0	0.0142	2.39	0.0186	36.41	0.0346	99.9145
BC_16_grt_19	2.28	20.64	0.0146	37.29	0.8868	0	0.0045	2.43	0.0194	36.35	0.0198	99.9351
BC_16_grt_20	2.26	20.74	0.0317	37.21	0.8685	0	0.0048	2.35	0	36.36	0.0165	99.8415
BC_16_grt_21	2.11	20.78	0.0138	37.17	0.8165	0.0054	0.0031	2.8	0	36.54	0.0203	100.2591
BC_16_grt_22	2.31	20.6	0.0349	37.12	0.951	0	0	3.33	0	35.25	0.0205	99.6164
BC_16_grt_23	2.29	21.01	0.0243	37.1	1.0159	0	0.0079	4.54	0.0056	34	0.0126	100.0063
BC_16_grt_24	2.43	20.99	0.0024	37.11	0.972	0	0	3.82	0.0153	34.67	0.028	100.0377
BC_16_grt_25	2.35	20.88	0.0373	37.1	0.9982	0.0055	0.0085	4.41	0	34.41	0.0299	100.2294
BC_16_grt_26	2.31	20.67	0.0349	37.06	1.0577	0	0.003	4.04	0.0056	34.79	0.0245	99.9957
BC_16_grt_27	2.34	20.82	0.1345	37.17	1.0223	0.0712	0.0133	4.27	0.0072	34.28	0.0398	100.1683
BC_16_grt_28	2.37	20.94	0.0138	37.22	0.9946	0	0.0115	4.24	0.021	34.77	0.0206	100.6015
BC_16_grt_29	2.43	20.98	0	37.22	0.9475	0	0.0332	4.11	0.0258	34.68	0.0254	100.4519
BC_16_grt_30	2.39	20.77	0.0081	37.17	1.0586	0	0	3.97	0.0105	34.81	0.0301	100.2173
BC_16_grt_31	2.32	20.51	0.0089	37.02	1.0151	0	0.0003	3.57	0.0136	35.4	0.0098	99.8677
BC_16_grt_32	2.36	20.85	0.0194	37.17	1.0891	0	0.0095	4.41	0.0161	34.26	0.0338	100.2179
BC_16_2_grt_1	2.21	20.63	0.0089	37.16	1.1782	0	0.0004	2.92	0.0064	35.67	0.0293	99.8132
BC_16_2_grt_2	2.21	20.8	0.0357	37.31	0.9985	0	0.0199	3.92	0.0064	34.96	0.0212	100.2817
BC_16_2_grt_3	2.19	20.91	0.0276	37.08	0.985	0	0	4.39	0.0089	34.76	0.0233	100.3748
BC_16_2_grt_4	2.26	20.77	0.0373	37.09	1.0136	0	0	4.56	0	34.64	0.0308	100.4017

Point	MgO	Al_2O_3	Na_2O	SiO_2	CaO	K_2O	Cr_2O_3	MnO	V_2O_3	FeO	TiO_2	Total
BC_16_2_grt_5	2.19	20.7	0.0171	37.08	0.9407	0	0	4.55	0	34.68	0.0241	100.1819
BC_16_2_grt_6	2.22	20.56	0.0065	36.8	0.8901	0	0.0114	4.61	0.0121	34.44	0.0194	99.5695
BC_16_2_grt_7	2.21	20.66	0.0138	36.78	0.9617	0	0	4.5	0	34.47	0.0285	99.624
BC_16_2_grt_8	2.24	20.89	0.0122	37.16	0.9021	0	0	4.49	0.0138	34.82	0.0192	100.5473
BC_16_2_grt_9	2.24	20.79	0.0008	37.2	1.0378	0	0.0038	4.49	0.0121	34.7	0.0164	100.4909
BC_16_2_grt_10	2.16	20.88	0.0154	37.19	1.0713	0	0.0068	4.57	0.0266	34.25	0.0216	100.1917
BC_16_2_grt_11	2.24	21.01	0.004	37.14	0.9441	0	0	4.28	0.0161	34.5	0.0094	100.1436
BC_16_2_grt_12	2.21	20.85	0.0398	37.14	0.9987	0	0	3.83	0.0144	35.12	0.0459	100.2488
BC_16_2_grt_13	2.36	20.81	0.0325	37.19	0.8056	0	0.0026	2.78	0	36.14	0.0367	100.1574
BC_16_2_grt_14	2.16	20.71	0.0538	37.01	0.7777	0.0359	0.0077	2.74	0	36.49	0.0225	100.0076
BC_16_2_grt_15	2.24	20.79	0.0049	37.28	0.9526	0	0	3.49	0	35.4	0.0443	100.2018
BC_16_2_grt_16	2.19	20.77	0.0423	37.05	1.0477	0	0.0269	4.23	0	34.77	0.0244	100.1513
BC_16_2_grt_17	2.21	20.82	0.0073	37.08	1.0108	0	0	4.52	0	34.38	0.0155	100.0436
BC_16_2_grt_18	2.23	20.83	0.0147	37.01	0.9976	0	0.0066	4.54	0	34.5	0.024	100.1529
BC_16_2_grt_19	2.34	20.87	0	36.94	0.9985	0	0	4.23	0	34.52	0.0388	99.9373
BC_16_2_grt_20	2.2	20.95	0.0098	37.2	1.0092	0	0.0231	3.64	0.0089	35.39	0.0282	100.4592
BC_16_2_grt_21	2.26	20.85	0.0138	37.15	1.0108	0	0.0148	3.59	0	35.34	0.0339	100.2633
BC_16_2_grt_22	2.25	20.9	0.0171	37.12	1.0373	0	0.0142	4.14	0.0025	34.54	0.0224	100.0435
BC_16_2_grt_23	2.3	20.74	0.0187	37.05	1.0056	0	0	3.71	0	34.84	0.0359	99.7002
BC_16_2_grt_24	2.25	20.86	0	36.9	1.0402	0	0.0041	3.2	0	35.55	0.0154	99.8197
BC_16_2_grt_25	2.29	20.81	0.0163	37.36	1.0192	0	0.0048	3.35	0	35.45	0.021	100.3213
BC_16_2_grt_26	2.34	20.88	0.0179	36.99	1.0122	0	0.0116	4.17	0	34.66	0.0069	100.0886
BC_16_2_grt_27	2.31	20.83	0.0179	37.2	0.9542	0	0	4.45	0	34.43	0.0197	100.2118
BC_16_2_grt_28	2.24	20.74	0.0358	37.32	0.9994	0	0.0021	4.48	0	34.63	0.0285	100.4758
BC_16_2_grt_29	2.3	20.79	0.022	37.1	1.0193	0	0	4.11	0	34.98	0.0225	100.3438
BC_16_2_grt_30	2.3	20.85	0	36.91	0.9917	0	0.0208	3.29	0.0049	35.5	0.018	99.8854
BC_16_2_grt_31	2.19	20.6	0.0344	37	0.7982	0	0.0085	2.75	0.021	36.23	0.0099	99.642
BC_16_2_grt_32	2.22	20.55	0.045	37.02	0.8016	0	0.0061	3.18	0.03	35.98	0.0297	99.8624
BC_16_2_grt_33	2.18	20.68	0.0049	36.97	1.1902	0	0	3.6	0.0025	35.34	0.0278	99.9954
BC_16_2_grt_34	2.21	20.85	0.0163	37.18	0.9938	0	0.0091	4.21	0	34.78	0.0192	100.2684
BC_16_2_grt_35	2.19	21.04	0.0057	36.81	0.9943	0	0.0138	4.57	0	34.52	0.0351	100.1789
BC_16_2_grt_36	2.18	20.71	0.0229	36.78	1.0477	0	0.0058	4.42	0	34.45	0.0341	99.6505
BC_16_2_grt_37	2.14	20.83	0.0115	36.71	0.9578	0	0	3.74	0.0162	35.1	0.0363	99.5418
BC_16_2_grt_38	2.18	20.7	0.009	36.65	0.9741	0	0	4.3	0.0121	34.51	0.0413	99.3765
BC_16_2_grt_39	2.16	20.79	0.0148	36.57	1.0261	0	0.0202	4.33	0.0107	34.57	0.0176	99.5094
BC_16_2_grt_40	2.31	20.68	0.0198	36.69	1.0027	0	0.0208	3.84	0.0041	35.24	0.016	99.8234
BC_16_3_grt_1	2.27	20.71	0.065	37.23	1.04	0	0.0154	3.77	0.014	34.93	0.0196	100.064
BC_16_3_grt_2	2.28	20.84	0.0049	37.12	0.983	0	0.012	4.24	0.0131	34.55	0.0084	100.0514

Point	MgO	Al_2O_3	Na_2O	SiO_2	CaO	K_2O	Cr_2O_3	MnO	V_2O_3	FeO	TiO_2	Total
BC_16_3_grt_3	2.37	20.85	0.0313	37.15	0.8964	0.0006	0.0172	4.16	0.0074	34.8	0.0386	100.3215
BC_16_3_grt_4	2.34	21.03	0.0123	37.22	0.9075	0.0037	0	4.15	0.0189	34.78	0.0063	100.4687
BC_16_3_grt_5	2.31	20.75	0.0371	37.24	0.9799	0	0.0294	4.14	0	34.71	0.0086	100.205
BC_16_3_grt_6	2.25	20.67	0.0149	37.12	0.962	0	0	4.2	0.0107	34.89	0.0281	100.1457
BC_16_3_grt_7	2.25	20.8	0.0239	37.03	1.0012	0	0.0041	4.43	0	34.52	0.0446	100.1038
BC_16_3_grt_8	2.27	20.78	0.0132	37.16	0.9282	0	0	4.27	0	34.58	0.018	100.0194
BC_16_3_grt_9	2.25	20.81	0.0396	37.14	1.0601	0	0.0129	4.13	0	34.83	0.0164	100.289
BC_16_3_grt_10	2.36	20.76	0	37.4	0.8324	0	0.0317	3.02	0.0123	35.84	0.0411	100.2975
BC_16_3_grt_11	2.34	20.9	0.0198	37.08	0.9632	0.0074	0.013	3.33	0	35.25	0.0361	99.9395
BC_16_3_grt_12	2.34	20.83	0.0454	36.94	1.0019	0.0024	0	3.74	0.0057	34.82	0.0406	99.766
BC_16_3_grt_13	2.31	20.66	0.0355	37.01	0.95	0	0.0111	3.74	0	34.9	0.0229	99.6395
BC_16_3_grt_14	2.33	20.63	0.0456	36.85	0.7841	0	0	3.47	0.0369	35.64	0.023	99.8096
BC_16_3_grt_15	2.35	20.59	0.0298	37.08	0.8163	0	0.0173	3.16	0.0016	35.54	0.026	99.611
BC_16_3_grt_16	2.24	20.76	0.0091	37.06	0.7995	0	0	2.82	0.0139	36.27	0.0285	100.001
Average	2.263	20.786	0.021	37.073	0.956	0.002	0.007	3.743	0.007	35.175	0.026	
Standard Deviation	0.076	0.113	0.019	0.165	0.097	0.009	0.008	0.662	0.009	0.688	0.010	

Feldspar analyses

Point	Na_2O	Al_2O_3	MgO	CaO	TiO_2	SrO	BaO	FeO	K_2O	SiO_2	MnO	Total
BC_16_1_fsp_1	10.3	21.49	0	2.34	0	0.1197	0	0.0163	0.0789	65.74	0	*100.0849*
BC_16_1_fsp_2	10.25	21.73	0.0037	2.58	0	0.1052	0	0.0457	0.0494	64.27	0	*99.034*
BC_16_1_fsp_3	10.13	21.93	0.0041	2.73	0	0.1263	0	0.0577	0.0737	64.86	0	*99.9118*
BC_16_1_fsp_4	9.83	22.26	0	3.26	0.0019	0.1359	0.0232	0.108	0.0732	63.33	0.0083	*99.0305*
BC_16_1_fsp_5	9.65	22.32	0	3.34	0.0179	0.1038	0	0.0293	0.076	64.14	0.0046	*99.6816*
BC_16_1_fsp_6	9.87	22.51	0	3.36	0	0.1098	0	0.0318	0.1002	63.87	0.0288	*99.8806*
BC_16_1_fsp_7	8.94	24.03	0	5.03	0	0.0854	0.0104	0.0925	0.0721	61.96	0	*100.2204*
BC_16_1_fsp_8	9.82	22.55	0	3.51	0.0055	0.0789	0.0147	0.0482	0.0852	64.54	0.0185	*100.671*
BC_16_1_fsp_9	9.09	23.22	0	4.42	0.0167	0.0703	0.0229	0.0598	0.1334	62.82	0.0417	*99.8948*
BC_16_1_fsp_10	9.15	23.12	0	4.27	0.0028	0.0699	0	0.0724	0.1379	63.17	0.0158	*100.0088*
BC_16_1_fsp_11	9.29	23.14	0	4.29	0.0069	0.1269	0.0078	0.0763	0.1247	63.25	0.0278	*100.3404*
BC_16_1_fsp_12	9.3	23.17	0	4.34	0	0.1321	0.0298	0.0109	0.0997	62.98	0.0214	*100.0839*
BC_16_1_fsp_13	8.97	23.68	0	4.78	0	0.1676	0.0191	0.0244	0.1066	62.24	0	*99.9877*
BC_16_1_fsp_14	8.88	23.59	0.0014	4.76	0.0127	0.1046	0	0.0627	0.0777	62.38	0.0455	*99.9146*
BC_16_1_fsp_15	9.08	23.53	0	4.7	0.0127	0.1014	0	0.0033	0.1074	62.04	0.0167	*99.5915*
BC_16_1_fsp_16	9.04	23.64	0	4.74	0.0105	0.0733	0	0.0399	0.0714	61.57	0	*99.1851*
BC_16_1_fsp_17	8.92	23.54	0	4.76	0.0062	0.119	0	0.0342	0.1031	62.27	0	*99.7525*
BC_16_1_fsp_18	9.14	23.24	0.0008	4.52	0.0034	0.1458	0	0.0035	0.0852	63.09	0	*100.2287*
BC_16_1_fsp_19	9.83	22.45	0	3.34	0	0.099	0	0.0315	0.1249	63.8	0.0046	*99.68*

Point	Na_2O	Al_2O_3	MgO	CaO	TiO_2	SrO	BaO	FeO	K_2O	SiO_2	MnO	*Total*
BC_16_1_fsp_20	9.77	22.47	0.0031	3.49	0.0077	0.0763	0	0.0234	0.0776	63.7	0	*99.6181*
BC_16_2_fsp_1	9.55	22.95	0	4.02	0.0012	0.1205	0.0258	0.016	0.0747	62.94	0	*99.6982*
BC_16_2_fsp_2	9.01	23.72	0	4.69	0.004	0.0857	0	0.0141	0.1153	62.35	0	*99.9891*
BC_16_2_fsp_3	8.91	23.49	0.001	4.73	0	0.0583	0	0.0238	0.1296	62.96	0	*100.3027*
BC_16_2_fsp_4	9.5	22.87	0	3.96	0	0.1565	0.0216	0.0088	0.115	63.51	0	*100.1419*
BC_16_2_fsp_5	9.36	22.96	0	3.9	0	0.0553	0	0	0.1368	63.74	0.0176	*100.1697*
BC_16_2_fsp_6	9.09	23.28	0.0012	4.67	0	0.1377	0	0.021	0.2348	61.66	0.0167	*99.1114*
BC_16_2_fsp_7	9.18	23.47	0	4.66	0.0096	0.0961	0	0	0.1605	62.14	0	*99.7162*
BC_16_2_fsp_8	8.87	23.79	0	4.95	0	0.0891	0.0115	0.0251	0.1554	62.51	0.013	*100.4141*
BC_16_2_fsp_9	8.86	24.06	0.0051	5.04	0	0.1301	0.0167	0.0332	0.0998	61.94	0	*100.1849*
BC_16_2_fsp_10	8.67	23.82	0.0014	5.16	0	0.1435	0.0107	0.0826	0.1091	62.01	0.0102	*100.0175*
BC_16_2_fsp_11	8.98	23.37	0	4.58	0	0.1362	0	0.0206	0.1357	62.13	0.013	*99.3655*
BC_16_2_fsp_12	8.87	23.81	0.0035	4.78	0	0.0821	0.0264	0.0224	0.1355	62.04	0	*99.7699*
BC_16_2_fsp_13	9.21	23.19	0	4.16	0.0055	0.0903	0	0.0149	0.1361	63.35	0	*100.1568*
BC_16_2_fsp_14	9.55	22.89	0.0014	3.88	0	0.0709	0	0.0312	0.1032	63.21	0	*99.7367*
BC_16_2_fsp_15	9.27	23.17	0.0004	4.21	0.0124	0.1652	0	0.0299	0.098	63.21	0	*100.1659*
BC_16_2_fsp_16	8.91	23.68	0	4.81	0.0047	0.094	0	0.0037	0.0972	62.65	0	*100.2496*
BC_16_2_fsp_17	9.19	23.51	0	4.56	0	0.1016	0.0209	0.0733	0.0859	62.33	0	*99.8717*
BC_16_2_fsp_18	10.21	22.01	0	3.12	0.0009	0.0495	0.0067	0.0956	0.0333	64.38	0	*99.906*
BC_16_2_fsp_19	9.18	23.44	0	4.49	0	0.109	0.007	0.0042	0.1604	62.09	0	*99.4806*
BC_16_2_fsp_20	9.45	22.94	0	3.91	0	0.1087	0.0002	0.0609	0.1254	63.78	0	*100.3752*
BC_16_2_fsp_21	10.96	20.87	0	1.53	0	0.1001	0	0.1004	0.085	66.88	0	*100.5255*
Average	9.37	23.05	0.00	4.11	0.00	0.11	0.01	0.04	0.11	63.12	0.01	
Standard Deviation	0.50	0.72	0.00	0.82	0.01	0.03	0.01	0.03	0.04	1.12	0.01	
Recalculated Average	9.33	23.10	0.00	4.17	0.00	0.11	0.01	0.04	0.11	63.02	0.01	
Recalculated Standard Deviation	0.44	0.64	0.00	0.72	0.01	0.03	0.01	0.03	0.04	0.96	0.01	
BC_01_fsp_1	6.44	26.47	0	8.74	0	0.107	0	0.1029	0.0931	57.03	0	*98.983*
BC_01_fsp_2	7.25	25.86	0	7.81	0.0048	0.1745	0.0282	0.0391	0.0866	59.11	0.0334	*100.3966*
BC_01_fsp_3	6.16	26.89	0.0017	9.33	0	0.1934	0	0.0902	0.0934	56.66	0	*99.4187*
BC_01_fsp_4	7.83	24.58	0	6.37	0.001	0.1595	0.0524	0.0666	0.08	59.49	0.0048	*98.6343*
BC_01_fsp_5	7.23	25.83	0	7.74	0	0.2137	0	0.0459	0.0735	58.94	0.0306	*100.1037*
BC_01_fsp_6	6.69	26.23	0	8.28	0	0.1979	0.0108	0.0377	0.1235	57.56	0	*99.1299*
BC_01_fsp_7	7.19	25.33	0	7.28	0	0.2091	0.0314	0.0211	0.1437	59.17	0.001	*99.3763*
BC_01_fsp_8	6.95	26.02	0	7.9	0.0003	0.2053	0.0127	0.0378	0.119	58.34	0.0076	*99.5927*
BC_01_fsp_9	7.21	25.59	0	7.58	0.0068	0.1848	0.0297	0.0408	0.1352	59.6	0.0153	*100.3926*
BC_01_fsp_10	7.17	25.62	0.0023	7.65	0.0048	0.2216	0.0728	0.0151	0.0764	58.91	0	*99.743*
BC_01_fsp_11	7.4	25.69	0.0042	7.43	0.0178	0.1601	0.0163	0.0329	0.0727	58.14	0.0191	*98.9831*

Point	Na_2O	Al_2O_3	MgO	CaO	TiO_2	SrO	BaO	FeO	K_2O	SiO_2	MnO	*Total*
BC_01_fsp_12	6.61	26.36	0.0063	8.52	0.0073	0.2444	0.0123	0.0159	0.0387	57.85	0.001	*99.6659*
BC_01_fsp_13	7.49	25.53	0.0042	7.3	0.0144	0.1849	0.0456	0.0298	0.1334	59.19	0	*99.9223*
BC_01_fsp_14	7.46	25.28	0	7.18	0	0.1685	0.0001	0.021	0.0736	59.7	0	*99.8832*
BC_01_fsp_15	7.68	25.28	0.0008	6.98	0	0.2104	0	0.0802	0.0907	60.42	0	*100.7421*
BC_01_fsp_16	7.5	25.65	0.0031	7.46	0.0029	0.1694	0	0.0507	0.0965	59.83	0.021	*100.7836*
BC_01_fsp_17	7.15	26.04	0	7.82	0	0.2304	0.0422	0.0495	0.1865	58.59	0.0219	*100.1305*
BC_01_fsp_18	7.68	24.67	0.0048	6.51	0.0048	0.1802	0	0.0877	0.12	59.11	0	*98.3675*
BC_01_fsp_19	7.44	24.98	0	6.99	0.0003	0.2218	0	0.0215	0.1283	59.01	0.0124	*98.8043*
BC_01_fsp_20	7.34	25.86	0	7.52	0.0102	0.2104	0.0456	0.0445	0.0966	59.41	0	*100.5373*
BC_01_fsp_21	7.43	25.61	0	7.3	0.0007	0.1918	0	0.0562	0.1106	60.04	0	*100.7393*
BC_01_fsp_22	7.45	25.73	0	7.44	0	0.1784	0.0064	0.0626	0.1173	60.09	0	*101.0747*
BC_01_fsp_23	7.42	25.91	0.0013	7.71	0	0.1532	0.0095	0.0559	0.0898	59.03	0.0067	*100.3864*
BC_01_fsp_24	7.42	25.69	0.0025	7.54	0	0.1904	0.0137	0.0285	0.0923	59.95	0.0181	*100.9455*
BC_01_fsp_25	7.53	25.4	0	7.15	0.0061	0.198	0	0.0512	0.0559	60.17	0.0153	*100.5765*
BC_01_fsp_26	7.53	25.75	0.0021	7.35	0	0.1656	0.025	0.0765	0.0791	59.64	0	*100.6183*
BC_01_fsp_27	7.26	25.76	0.0054	7.41	0.0102	0.2398	0	0.053	0.115	59.93	0	*100.7834*
BC_01_fsp_28	7.19	26.06	0	7.91	0	0.2392	0.0014	0.0358	0.067	58.6	0	*100.1034*
BC_01_fsp_29	7.6	25.14	0.0019	6.93	0.0013	0.2286	0.0096	0.0551	0.1441	59.73	0.0124	*99.853*
BC_01_fsp_30	6.59	26.05	0	8.5	0	0.202	0.0117	0.0524	0.1013	57.01	0.0077	*98.5251*
BC_01_fsp_31	7.36	24.92	0.0002	7.14	0	0.2015	0.0154	0.0236	0.1554	59.04	0	*98.8561*
BC_01_fsp_32	7.34	25.02	0.0036	7.31	0	0.2226	0.0112	0.0278	0.1315	59.69	0.0038	*99.7605*
BC_01_fsp_33	7.44	24.95	0	7.21	0	0.2045	0	0.0224	0.0806	59.81	0.0067	*99.7242*
BC_01_fsp_34	6.72	26.7	0	8.75	0	0.2363	0	0.0439	0.0877	58.38	0	*100.9179*
BC_01_fsp_35	6.7	26.33	0	8.38	0	0.1688	0	0.0169	0.0797	58.11	0	*99.7854*
BC_01_fsp_36	6.09	26.56	0.015	7.87	0	0.1465	0.0355	0.0624	0.8362	57.28	0	*98.8956*
BC_01_fsp_37	5.88	27.92	0	10.03	0.0032	0.2218	0	0.0209	0.0846	55.41	0	*99.5705*
BC_01_fsp_38	5.96	27.73	0.0017	9.72	0.0022	0.2179	0.0075	0.023	0.0759	56.91	0.0086	*100.6568*
BC_01_fsp_39	6.86	26.6	0	8.52	0.0026	0.1905	0	0.0277	0.0694	57.94	0.0019	*100.2121*
BC_01_fsp_40	5.77	27.99	0	10.1	0	0.2173	0.0106	0.0436	0.0747	56.03	0.0067	*100.2429*
BC_01_fsp_41	4.27	30.5	0.0019	12.84	0.0273	0.2081	0.0233	0.0344	0.0369	52.93	0	*100.8719*
BC_01_fsp_42	6.1	27.71	0	9.79	0.0064	0.2085	0	0.0337	0.0724	55.82	0.0192	*99.7602*
BC_01_fsp_43	7	26.57	0	8.26	0.0032	0.2383	0.0264	0.0431	0.0848	58.64	0.0106	*100.8764*
BC_01_fsp_44	6.91	26.71	0.0048	8.46	0.0247	0.214	0	0.0256	0.0719	58.62	0.0164	*101.0574*
BC_01_fsp_45	6.88	26.44	0.0046	8.42	0.0125	0.2208	0.0029	0.0323	0.0914	57.5	0	*99.6045*
BC_01_fsp_46	6.74	26.12	0.0002	8.18	0	0.2068	0	0.0175	0.1003	57.27	0.0231	*98.6579*
BC_01_fsp_47	4.24	28.33	0.2168	11.72	1.74	0.1779	0	0.4884	0.7303	51.76	0.0058	*99.4092*
BC_01_fsp_48	1.51	33.8	0.2821	3.67	0	0.1043	0.0258	1.0727	6.52	49.07	0.0278	*96.0827*
BC_01_fsp_49	4.96	29.06	0	11.5	0	0.2384	0	0.0198	0.0785	53.99	0.025	*99.8717*

Point	Na_2O	Al_2O_3	MgO	CaO	TiO_2	SrO	BaO	FeO	K_2O	SiO_2	MnO	*Total*
BC_01_fsp_50	6.31	27.17	0	9.22	0.0054	0.2047	0	0.0169	0.1015	57.24	0	*100.2685*
BC_01_fsp_51	6.08	27.74	0.0143	9.69	0	0.2061	0	0.0395	0.0714	55.9	0	*99.7413*
BC_01_fsp_52	5.96	27.91	0.0002	9.95	0	0.1902	0	0	0.0477	56.07	0	*100.1281*
BC_01_fsp_53	6.83	26.25	0	8.23	0	0.1906	0	0.0461	0.0665	58.58	0.0077	*100.2009*
Average	6.74	26.41	0.01	8.16	0.04	0.20	0.01	0.07	0.24	57.97	0.01	
Standard Deviation	1.08	1.54	0.05	1.45	0.24	0.03	0.02	0.15	0.89	2.21	0.01	
Recalculated Average	6.98	26.09	0.00	8.02	0.00	0.20	0.01	0.04	0.11	58.46	0.01	
Recalculated Standard Deviation	0.56	0.87	0.00	0.94	0.01	0.03	0.02	0.02	0.11	1.32	0.01	

Biotite Analyses

Point	MgO	Al_2O_3	Na_2O	F	SiO_2	CaO	K_2O	Cr_2O_3	FeO	MnO	Cl	TiO_2	H	Total
BC_16_1_bt_1	7.06	18.22	0.0668	0.4104	35.26	0.0013	9.45	0	23.41	0.0599	0.2761	2.08	4	100.2945
BC_16_1_bt_2	7.01	18.05	0.1199	0.3492	35.17	0.0018	9.48	0.0078	23.5	0.0562	0.2317	2.19	4	100.1666
BC_16_1_bt_3	6.8	18.5	0.1017	0.353	35.35	0.017	9.37	0.0129	23.12	0.0913	0.2802	2	4	99.9961
BC_16_1_bt_4	7.03	18.11	0.1418	0.358	35.15	0.0163	9.58	0.0237	23.63	0.0659	0.1636	2.26	4	100.5293
BC_16_1_bt_5	6.8	17.75	0.1299	0.3373	35.1	0.0826	9.22	0.036	24.05	0.0913	0.2745	2.63	4	100.5016
BC_16_1_bt_6	6.72	17.67	0.1332	0.3076	35.17	0.0803	9.38	0.0227	23.74	0.0801	0.2412	2.68	4	100.2251
BC_16_1_bt_7	6.7	17.81	0.0937	0.3171	34.96	0.0421	9.22	0	23.94	0.0891	0.1795	2.74	4	100.0915
BC_16_1_bt_8	6.7	17.66	0.0727	0.3495	34.82	0.0221	9.42	0.015	24.13	0.0906	0.2642	2.71	4	100.2541
BC_16_1_bt_9	6.75	17.47	0.082	0.2595	34.87	0.0244	9.44	0.0196	23.84	0.0854	0.2688	2.76	4	99.8697
BC_16_1_bt_10	6.78	17.55	0.1154	0.3413	34.87	0.035	9.47	0.0156	24.06	0.0487	0.2294	2.79	4	100.3054
BC_16_1_bt_11	6.64	17.62	0.0803	0.2963	34.96	0.019	9.48	0.0036	24.02	0.0705	0.2453	3	4	100.435
BC_16_1_bt_12	6.68	17.84	0.0665	0.2913	34.91	0.0024	9.47	0	23.64	0.0533	0.2324	2.86	4	100.0459
BC_16_1_bt_13	6.79	17.8	0.0872	0.3476	35.2	0.0227	9.46	0.0128	23.55	0.0908	0.2209	2.63	4	100.212
BC_16_1_bt_14	6.86	18.02	0.1315	0.3344	35.02	0.0363	9.53	0	23.32	0.0848	0.205	2.57	4	100.112
BC_16_1_bt_15	6.66	17.99	0.1168	0.3223	34.97	0.0439	9.45	0.01	23.63	0.0999	0.1656	2.71	4	100.1685
BC_16_1_bt_16	0.5489	36.33	0.8295	0.1056	46.88	0.0203	9.94	0.0208	1.37	0.0186	0.0075	0.9591	4	101.0303
BC_16_1_bt_17	0.4958	36.42	0.884	0.1096	47.31	0.0149	9.97	0.0456	1.33	0.0008	0	0.9711	4	101.5518
BC_16_1_bt_18	0.4405	36.73	0.7321	0.0578	47.47	0.0229	10.13	0.022	1.1558	0.0116	0	0.8118	4	101.5845
BC_16_1_bt_19	0.5456	36.2	0.8357	0.0339	47.23	0.0113	9.95	0.0153	1.39	0.0101	0.0039	0.9598	4	101.1856
BC_16_1_bt_20	0.5143	36.56	0.8743	0.1335	47.17	0.0153	9.85	0.0121	1.2162	0.0023	0.0025	0.9454	4	101.2959
BC_16_1_bt_21	6.84	18.19	0.1291	0.336	34.71	0.0075	9.5	0.0248	23.14	0.0848	0.1918	2.52	4	99.674
BC_16_1_bt_22	6.77	17.97	0.0912	0.3307	34.86	0.0308	9.42	0.0327	23.34	0.0428	0.2221	2.6	4	99.7103
BC_16_1_bt_23	6.75	17.84	0.0675	0.276	34.76	0.0504	9.33	0.01	23.26	0.075	0.1992	2.76	4	99.3781

Point	MgO	Al_2O_3	Na_2O	F	SiO_2	CaO	K_2O	Cr_2O_3	FeO	MnO	Cl	TiO_2	H	Total
BC_16_1_bt_24	6.69	17.77	0.1007	0.2682	34.98	0.0087	9.48	0.0073	23.66	0.0959	0.2716	2.61	4	99.9424
BC_16_1_bt_25	6.86	18.13	0.0321	0.344	34.85	0.0314	9.47	0.0193	23.74	0.087	0.1755	2.69	4	100.4293
BC_16_1_bt_26	6.67	17.89	0.1063	0.3693	34.71	0.026	9.41	0.0415	23.17	0.0893	0.172	2.74	4	99.3944
BC_16_1_bt_27	6.64	17.77	0.0937	0.3742	34.87	0.0102	9.42	0.0352	23.5	0.069	0.2179	2.9	4	99.9002
BC_16_1_bt_28	6.7	17.97	0.1223	0.3569	34.86	0.0211	9.35	0	23.48	0.0697	0.2468	2.83	4	100.0068
BC_16_1_bt_29	6.57	17.67	0.0568	0.2901	34.54	0.0196	9.38	0.0287	23.47	0.0684	0.2706	2.8	4	99.1642
BC_16_1_bt_30	6.75	17.9	0.1016	0.3191	34.74	0.0303	9.39	0.0169	23.81	0.0895	0.1771	2.79	4	100.1145
BC_16_1_bt_31	6.69	17.9	0.0994	0.3719	35.06	0.0525	9.45	0	23.66	0.0663	0.1597	2.86	4	100.3698
BC_16_1_bt_32	6.68	17.83	0.1159	0.2908	34.98	0.0494	9.41	0.0175	23.72	0.0513	0.1505	2.82	4	100.1154
BC_16_1_bt_33	6.61	17.64	0.1145	0.3617	34.7	0.0449	9.27	0.0345	23.64	0.0694	0.2689	2.87	4	99.6239
BC_16_1_bt_34	6.73	17.48	0.1107	0.3784	34.72	0.0122	9.41	0.0035	24.06	0.0634	0.2422	2.83	4	100.0404
BC_16_1_bt_35	6.86	18.04	0.0958	0.4213	34.93	0.0651	9.29	0.035	23.59	0.0862	0.2367	2.24	4	99.8901
BC_16_1_bt_36	7.13	18.55	0.0889	0.2904	35.13	0.0093	9.59	0	23.25	0.0719	0.1504	1.8	4	100.0609
BC_16_1_bt_37	6.86	18.11	0.1013	0.2779	34.84	0.0456	9.39	0.0159	23.78	0.1067	0.2488	1.97	4	99.7462
BC_16_1_bt_38	6.84	18.14	0.131	0.4023	34.83	0.1012	9.04	0.0292	23.69	0.0545	0.1877	2.28	4	99.7259
BC_16_1_bt_39	7	18.03	0.0932	0.3742	35.22	0.0957	9.25	0.0024	23.42	0.0728	0.2584	2.15	4	99.9667
BC_16_1_bt_40	6.91	17.95	0.0472	0.3587	34.81	0.0771	9.35	0.0479	23.38	0.0773	0.3149	2.23	4	99.5531
BC_16_2_bt_1	6.19	17.55	0.1628	0.2947	34.85	0.1294	9.22	0.0237	23.36	0.1154	0.1238	3.91	4	99.9298
BC_16_2_bt_2	6	17.73	0.1411	0.3546	34.88	0.108	9.26	0.0233	23.28	0.1024	0.1198	4.2	4	100.1992
BC_16_2_bt_3	6.13	17.56	0.1218	0.2448	35.14	0.066	9.42	0.0187	23.62	0.1139	0.1261	3.88	4	100.4413
BC_16_2_bt_4	5.96	17.74	0.1459	0.2952	34.59	0.0314	9.48	0.0404	23.53	0.1353	0.1345	4.19	4	100.2727
BC_16_2_bt_5	6.09	17.56	0.1165	0.2623	35.12	0.0664	9.28	0.0162	23.45	0.1054	0.1721	3.77	4	100.0089
BC_16_2_bt_6	6.14	17.4	0.1632	0.3258	35.14	0.1915	9.11	0.0232	24.03	0.1063	0.1616	3.77	4	100.5616
BC_16_2_bt_7	6.01	17.44	0.2219	0.3455	35.58	0.1179	9.27	0.0161	23.91	0.111	0.1165	3.6	4	100.7389
BC_16_2_bt_8	6.08	17.31	0.1301	0.3331	34.02	0.1348	8.93	0.0163	24.11	0.1024	0.1032	3.48	4	98.7499
BC_16_2_bt_9	5.95	17.33	0.1705	0.3158	35.53	0.2298	8.91	0.0287	23.63	0.1288	0.1118	3.56	4	99.8954
BC_16_2_bt_10	6.53	18.38	0.164	0.3519	34.75	0.0797	9.13	0.0695	23.31	0.0756	0.3592	1.94	4	99.1399
BC_16_2_bt_11	6.16	18.22	0.1142	0.2759	35.02	0.0487	9.42	0.0212	23.18	0.084	0.155	3.15	4	99.849
BC_16_2_bt_12	6.13	17.52	0.1427	0.2508	34.78	0.036	9.38	0.0261	23.62	0.0631	0.29	3.48	4	99.7187
BC_16_2_bt_13	6.15	17.35	0.1023	0.2527	34.85	0.0157	9.33	0	23.49	0.0593	0.3151	3.5	4	99.4151
BC_16_2_bt_14	6.04	17.63	0.2054	0.2812	34.77	0.0784	9.21	0	23.91	0.0925	0.3068	2.9	4	99.4243
BC_16_2_bt_15	6.05	17.74	0.0697	0.2359	34.94	0.0413	9.36	0	23.81	0.0993	0.3091	3.08	4	99.7353
BC_16_2_bt_16	5.77	18.06	0.1407	0.2459	34.8	0.0818	9.33	0	23.75	0.064	0.3058	3.56	4	100.1082
BC_16_2_bt_17	5.93	16.87	0.1596	0.4028	35.12	0.1316	9.08	0.0257	24.66	0.0993	0.3071	3.39	4	100.1761
BC_16_2_bt_18	6.47	18.04	0.1936	0.2883	35.21	0.0976	9.15	0.0329	24.21	0.0677	0.2015	2.43	4	100.3916
BC_16_2_bt_19	6.54	17.98	0.1059	0.361	35.19	0.0334	9.32	0.015	23.72	0.0778	0.1988	2.23	4	99.7719
BC_16_2_bt_20	6.44	17.78	0.0961	0.2869	34.96	0.1394	8.66	0.0129	24.59	0.0824	0.2435	2.13	4	99.4212
BC_16_2_bt_21	6.64	17.95	0.1526	0.3298	35.28	0.0974	9.15	0.022	24.38	0.0956	0.319	2.11	4	100.5264

Point	MgO	Al_2O_3	Na_2O	F	SiO_2	CaO	K_2O	Cr_2O_3	FeO	MnO	Cl	TiO_2
Average	6.06	19.35	0.17	0.30	35.96	0.05	9.38	0.02	21.84	0.08	0.20	2.67
Standard Deviation	1.84	5.66	0.22	0.08	3.73	0.05	0.27	0.01	6.78	0.03	0.09	0.84
Recalculated Average	6.55	17.82	0.12	0.32	34.95	0.06	9.33	0.02	23.68	0.08	0.22	2.82
Recalculated Standard Deviation	0.35	0.31	0.04	0.05	0.25	0.05	0.17	0.01	0.34	0.02	0.06	0.59

Muscovite analyses

Point	MgO	Al_2O_3	Na_2O	F	SiO_2	CaO	K_2O	Cr_2O_3	FeO	MnO	Cl	TiO_2	H	Total
BC_16_1_ms_1	0.6126	35.72	0.8858	0.0743	46.9	0.0122	10.22	0.0025	1.5	0.0133	0.0094	0.8624	4	100.8125
BC_16_1_ms_2	0.5961	35.37	0.8738	0.1065	46.5	0.0218	10.08	0.0043	1.48	0.0211	0.0062	0.8655	4	99.9253
BC_16_1_ms_3	0.7868	34.86	0.7975	0.1123	46.79	0	10.14	0	1.68	0	0.006	0.719	4	99.8916
BC_16_1_ms_4	0.5913	35.65	0.8246	0.1187	46.78	0.0068	10.15	0.0268	1.55	0.0031	0.0011	0.9696	4	100.672
BC_16_1_ms_5	0.4973	35.78	0.9064	0.0725	46.33	0.0125	10.06	0.0179	1.36	0	0.0046	0.9523	4	99.9935
BC_16_1_ms_6	0.7411	35.07	0.8254	0.1066	46.97	0.0092	10.22	0.0399	1.59	0.0071	0.0046	0.6848	4	100.2687
BC_16_1_ms_7	0.7069	34.78	0.8151	0.1369	46.46	0	10.13	0.005	1.51	0	0	0.793	4	99.3369
BC_16_1_ms_8	0.5839	35.54	0.8794	0.131	46.34	0.021	9.85	0.0208	1.41	0.0173	0.0115	0.8598	4	99.6647
BC_16_1_ms_9	0.5923	35.34	0.8609	0.1229	46.18	0.0043	10.09	0.0034	1.42	0.0039	0.0032	0.8519	4	99.4728
BC_16_1_ms_10	0.5951	35.83	0.7831	0.0706	46.88	0.016	10.07	0	1.38	0	0.0075	0.8243	4	100.4566
BC_16_1_ms_11	0.4768	36.4	0.8407	0.101	46.7	0.0079	9.96	0	1.1482	0	0.0075	0.8496	4	100.4917
BC_16_1_ms_12	0.5617	36.29	0.8435	0.0645	46.41	0.0139	10	0.0068	1.46	0	0.0044	0.7776	4	100.4324
BC_16_1_ms_13	0.6034	35.63	0.8284	0.0343	46.3	0.0178	10.14	0	1.46	0.029	0	0.7909	4	99.8338
BC_16_1_ms_14	0.5892	36.1	0.869	0.137	46.24	0.0197	9.86	0	1.45	0	0.0094	0.8526	4	100.1269
BC_16_1_ms_15	0.4464	36.81	0.79	0.1151	46.07	0.0179	10.17	0.0105	1.1495	0	0.0023	0.6757	4	100.2574
BC_16_1_ms_16	0.4459	36.6	0.8987	0.0202	46.79	0.0108	9.96	0.0022	0.996	0	0.0034	0.7193	4	100.4465
BC_16_1_ms_17	0.5259	36.36	0.8848	0.0949	46.36	0	9.87	0.0152	1.3	0.0063	0.0068	0.8957	4	100.3196
BC_16_1_ms_18	0.4794	36.05	0.9133	0.1575	46.62	0.0143	9.88	0	1.29	0	0.0028	0.9155	4	100.3228
BC_16_1_ms_19	0.4933	36.4	0.9365	0.0868	46.31	0.0149	9.81	0.0297	1.1682	0	0.0068	0.8868	4	100.143
BC_16_1_ms_20	0.5177	36.27	0.98	0.1153	46.4	0.0137	9.85	0.011	1.2269	0.015	0.0041	0.9517	4	100.3554
BC_16_1_ms_21	0.4893	36.03	0.9131	0.0827	46.01	0.013	9.87	0.0035	1.39	0.0094	0.0057	0.905	4	99.7217
BC_16_1_ms_22	0.5511	37.19	0.5621	0.0283	46.85	0.0027	8.64	0.0353	1.4	0	0.0014	0.9182	4	100.1791
BC_16_1_ms_23	0.3595	36.76	0.8338	0.0487	46.08	0.0352	9.88	0.0003	0.9336	0.0205	0	0.7962	4	99.7478
BC_16_1_ms_24	0.3956	36.61	0.8741	0.0222	46.06	0.0094	9.92	0	1.1264	0	0.0016	0.6114	4	99.6307
BC_16_1_ms_25	0.3888	36.14	0.7885	0.0791	46.46	0.0295	9.82	0.0274	0.9202	0.0032	0.0069	0.7469	4	99.4105
BC_16_1_ms_26	0.26	1.7535	0.019	0.0789	2.0948	0.0752	0.0704	0	25.48	0.7036	0.0412	66.15	4	100.7266
BC_16_1_ms_27	0.3565	37.23	0.9535	0.0081	46.43	0.0087	10.01	0.0153	1.1473	0.0063	0.0048	0.552	4	100.7225
BC_16_1_ms_28	0.6224	35.19	0.8462	0.1372	44.89	0.0057	9.95	0.019	1.49	0.0315	0.0082	0.7502	4	97.9404
BC_16_1_ms_29	0.7656	35.25	0.7958	0.1492	46.92	0.0072	10.24	0.0018	1.66	0	0.0046	0.5934	4	100.3876

Point	MgO	Al_2O_3	Na_2O	F	SiO_2	CaO	K_2O	Cr_2O_3	FeO	MnO	Cl	TiO_2	H	Total
BC_16_1_ms_30	0.8363	34.82	0.7956	0.0806	46.52	0.0087	10.23	0.0087	1.81	0.0189	0.006	0.7749	4	99.9097
BC_16_1_ms_31	0.5829	35.82	0.8321	0.1213	46.3	0.008	10.11	0	1.41	0.0024	0.0053	0.8522	4	100.0442
BC_16_1_ms_32	0.6296	35.59	0.8673	0.0444	46.21	0.0127	10.16	0.0286	1.55	0.026	0.0032	0.8204	4	99.9422
BC_16_1_ms_33	0.5069	36.12	0.939	0.1174	46.25	0.0085	10.16	0.0271	1.37	0.0221	0.0102	0.7911	4	100.3223
BC_16_1_ms_34	0.5307	36.17	0.8974	0.0771	46.29	0.0151	10.13	0.022	1.47	0.0087	0.0016	0.8372	4	100.4498
BC_16_1_ms_35	0.555	36	0.9098	0.071	46.17	0.0099	10.16	0.0405	1.43	0.0119	0.0048	0.8148	4	100.1777
BC_16_1_ms_36	0.4798	35.93	0.8486	0.0955	46.03	0.0096	10.17	0.0299	1.51	0.0143	0	0.8161	4	99.9338
BC_16_1_ms_37	0.5766	35.74	0.8081	0.0386	46.07	0.0046	10.16	0.0034	1.56	0	0.0075	0.7239	4	99.6927
BC_16_1_ms_38	0.5299	36.01	0.8966	0.0652	47.09	0.0078	10.03	0	1.39	0	0	0.9279	4	100.9474
BC_16_1_ms_39	0.5279	35.59	0.9006	0.0775	46.71	0.0199	10.04	0	1.54	0.0159	0.0029	0.9384	4	100.3631
BC_16_1_ms_40	0.5429	36.01	0.7931	0.051	46.68	0.0082	10.32	0.012	1.47	0.0056	0.0041	0.8849	4	100.7818
BC_16_2_ms_1	0.5382	36.46	0.88	0.0449	46.77	0.0054	9.97	0	1.35	0.0279	0	0.5397	4	100.5861
BC_16_2_ms_2	0.5314	36.3	0.8935	0.0734	47.19	0.0108	9.79	0.0061	1.3	0.0151	0.0054	0.5877	4	100.7034
BC_16_2_ms_3	0.5682	35.57	0.9537	0.0899	47.5	0.0174	9.74	0	1.41	0.0056	0	0.7429	4	100.5977
BC_16_2_ms_4	0.5282	36.34	0.9412	0.1	47.04	0.0087	9.89	0.0105	1.38	0.0167	0.0079	0.5719	4	100.8351
BC_16_2_ms_5	0.5462	36.39	0.9191	0.0449	46.96	0.0044	9.98	0	1.4	0.0008	0.0009	0.5046	4	100.7509
BC_16_2_ms_6	0.5244	36.47	0.8226	0.0368	46.78	0.0098	10.23	0.0267	1.3	0	0.0068	0.6107	4	100.8178
BC_16_2_ms_7	0.2664	37.41	0.8859	0.0736	46.51	0.0136	9.93	0	0.886	0.0048	0.0038	0.4613	4	100.4454
BC_16_2_ms_8	0.4377	36.76	0.9494	0.0429	46.91	0.0191	9.8	0.0084	1.1173	0	0.0081	0.575	4	100.6279
BC_16_2_ms_9	0.4506	36.49	0.7779	0.0777	46.92	0.007	9.83	0.0157	1.1491	0	0.0013	0.6193	4	100.3386
BC_16_2_ms_10	0.5143	36.26	0.8654	0.1	46.76	0.0134	10.19	0.0159	1.38	0	0.0018	0.6175	4	100.7183
BC_16_2_ms_11	0.5584	36.33	0.8711	0.0632	46.82	0.0159	9.98	0	1.36	0.0239	0.0045	0.533	4	100.56
BC_16_2_ms_12	0.5144	36.33	0.8292	0.0816	47.15	0.0125	9.94	0.0287	1.36	0.0056	0.007	0.6511	4	100.9101
BC_16_2_ms_13	0.4943	36.24	0.8809	0.1467	47.17	0.0171	9.93	0.0056	1.32	0.0056	0.0018	0.6053	4	100.8173
BC_16_2_ms_14	0.5877	36.35	0.9313	0.1789	46.55	0.003	9.83	0.0149	1.37	0	0.0052	0.6095	4	100.4305
BC_16_2_ms_15	0.5053	35.87	0.8679	0.1164	46.32	0.0017	10.34	0.0418	1.2775	0.0087	0.0025	0.6429	4	99.9947
BC_16_2_ms_16	0.5606	36.55	0.9177	0.1222	46.5	0.0122	10.04	0.0121	1.38	0	0.0119	0.5321	4	100.6388
BC_16_2_ms_17	0.5786	36.4	0.8813	0.0795	46.48	0.0146	10.1	0.0232	1.33	0	0.0049	0.611	4	100.5031
BC_16_2_ms_18	0.5363	36.33	0.7548	0.0715	46.5	0.0232	10.07	0.0187	1.53	0	0.0081	0.711	4	100.5536
BC_16_2_ms_19	0.5123	36.12	0.6227	0.1371	46.48	0.0234	10.09	0.0289	1.52	0	0.0119	0.756	4	100.3023
BC_16_2_ms_20	0.5192	35.42	0.6034	0.0838	45.96	0.0386	10.64	0	1.96	0	0.0128	0.7335	4	99.9713
BC_16_2_ms_21	0.5457	36.08	0.662	0.1455	46.62	0.0217	10.08	0.0016	1.43	0.0136	0.0081	0.7153	4	100.3235
BC_16_2_ms_22	0.5377	36.48	0.8814	0.1473	46.23	0.0253	10.06	0.0233	1.37	0	0.0121	0.5792	4	100.3463
Average	0.54	35.51	0.84	0.09	45.82	0.01	9.86	0.01	1.77	0.02	0.01	1.80		
Standard Deviation	0.10	4.90	0.15	0.04	6.30	0.01	1.43	0.01	3.42	0.10	0.01	9.25		
Recalculated Average	0.55	36.04	0.85	0.09	46.53	0.01	10.02	0.01	1.39	0.01	0.01	0.75		
Recalculated Standard Deviation	0.09	0.54	0.08	0.04	0.41	0.01	0.24	0.01	0.19	0.01	0.00	0.13		

Al-Silicate analyses

Point	Na_2O	Al_2O_3	MgO	CaO	TiO_2	SrO	BaO	FeO	K2O	SiO_2	MnO	Total
BC_16_1_AlSi_1	0	63.03	0	0.0019	0	0.009	0.0038	0.199	0.0211	36.57	0.0221	99.8569
BC_16_1_AlSi_2	0	63.09	0	0.0083	0	0	0	0.1902	0.0274	36.62	0	99.9359
BC_16_1_AlSi_3	0	62.8	0.0076	0.0083	0.0049	0.0327	0.0016	0.1906	0.0423	35.74	0.0055	98.8335
BC_16_1_AlSi_4	0	63.17	0.0039	0.0051	0.0027	0.0377	0	0.1994	0.0372	36.67	0.0157	100.1417
BC_16_1_AlSi_5	0.0249	63.01	0.0006	0.0211	0.0175	0.0692	0	0.1989	0.0443	36.64	0	100.0265
BC_16_1_AlSi_6	0.0174	63.27	0.0033	0.0179	0.0053	0.0459	0.0182	0.2087	0.0443	36.13	0.0046	99.7656
BC_16_1_AlSi_7	0	62.91	0.0102	0.0019	0.0248	0	0	0.2249	0.0255	36.43	0.0102	99.6375
BC_16_1_AlSi_8	0	62.68	0	0.0053	0	0.0457	0	0.2228	0.0325	35.51	0	98.4963
BC_16_1_AlSi_9	0	62.96	0	0.0166	0	0.1207	0.0083	0.1741	0.0388	35.8	0	99.1185
BC_16_1_AlSi_10	0.015	63.29	0	0.0104	0.0019	0.0459	0.0115	0.1801	0.0357	36.6	0	100.1905
BC_16_2_AlSi_1	0	62.5	0	0.0078	0	0.0108	0	0.2198	0.0381	36.33	0	99.1065
BC_16_2_AlSi_2	0	62.04	0	0.0016	0.013	0.0124	0	0.2734	0.0216	36.72	0.0185	99.1005
BC_16_2_AlSi_3	0	62.36	0.0017	0	0	0.0071	0	0.2701	0.0366	36.31	0	98.9855
BC_16_2_AlSi_4	0.0637	61.31	0.0208	0.015	0.0306	0.0588	0	0.33	0.6577	36.63	0	99.1166
BC_16_2_AlSi_5	0.7438	37.41	0.3066	0.0073	0.6688	0.0227	0.1761	0.8575	9.22	43.61	0	93.0228
Average	0.06	61.06	0.02	0.01	0.05	0.03	0.01	0.26	0.69	36.82	0.01	
Standard Deviation	0.19	6.56	0.08	0.01	0.17	0.03	0.04	0.17	2.37	1.92	0.01	
Recalculated Average	0.01	62.74	0.00	0.01	0.01	0.04	0.00	0.22	0.08	36.34	0.01	
Recalculated Standard Deviation	0.02	0.55	0.01	0.01	0.01	0.03	0.01	0.04	0.17	0.39	0.01	

Bertil Carlsen

Prospecting a Structurally Complex Marble Occurrence in Vassbygda

NTNU
Norwegian University of
Science and Technology

BRØNNØY
KALK